Single-ion based quantum interfaces for quantum-network applications

Dissertation

zur Erlangung des Grades
des Doktors der Naturwissenschaften
der Naturwissenschaftlich-Technischen Fakultät
der Universität des Saarlandes

von

Reiner Pascal Eich

Saarbrücken

2019

Tag des Kolloquiums:	01.08.2019
Dekan:	Univ.-Prof. Dr. Guido Kickelbick
Berichterstatter:	Univ.-Prof. Dr. Jürgen Eschner
	Univ.-Prof. Dr. Stephan Götzinger
Vorsitz:	Univ.-Prof. Dr. Frank Mücklich
Akad. Mitarbeiter:	Dr. Elke Neu-Ruffing

Abstract

Single-atom–based quantum memories have proven to be among the most promising candidates for large-scale quantum networks. This architecture consists of material quantum memories, represented by single trapped atomic ions, interconnected by photonic quantum channels. The communication protocol requires a bi-directional interface between atomic and photonic qubits as well as the implementation of a quantum-repeater scheme for long-haul state transmission.

In the current work, I present experiments that form a fundamental step towards the realization of a quantum network, based on single trapped $^{40}Ca^{+}$ ions, in particular the implementation of an atom-photon quantum interface combined with the polarization-state–preserving single-photon conversion into the telecom regime.

The theoretical part comprises a discussion of the fundamental properties of the $^{40}Ca^{+}$ ion, followed by a treatment of the dipole emission pattern to gain a deeper understanding of the absorption and emission process.

Subsequently, the experimental implementation of two protocols for an atom-photon quantum interface at 393 nm and 854 nm is demonstrated. For the latter, I additionally demonstrate the quantum-state–preserving quantum frequency conversion of the single photon into the telecom O-band at 1310 nm.

Finally, we conducted an experiment as a first step towards a global entangling atomic two-qubit gate, represented by the Mølmer-Sørensen gate, needed for quantum-repeater applications.

Zusammenfassung

Einzelatombasierte Quantenspeicher gehören zu den aussichtsreichsten Kandidaten für ausgedehnte Quantennetzwerke. Diese Architektur besteht aus ortsgebundenen Quantenspeichern in Form gefangener atomarer Ionen, die durch photonische Quantenkanäle verbunden sind. Das Kommunikationsprotokoll benötigt eine bidirektionale Schnittstelle zwischen atomaren und photonischen Qubits sowie die Implementierung eines Quantenrepeater-Schemas für langreichweitigen Zustandstransfer.

In der vorliegenden Arbeit präsentiere ich Experimente, die einen fundamentalen Schritt hin zur Umsetzung eines auf einzelnen gefangenen $^{40}Ca^{+}$-Ionen basierenden Quantennetzwerks darstellen, insbesondere die Implementierung einer Atom-Photon-Schnittstelle, kombiniert mit polarisationserhaltender Einzelphotonenkonversion in den Telecom-Bereich.

Der theoretische Teil umfasst die Diskussion der fundamentalen Eigenschaften des $^{40}Ca^{+}$-Ions, gefolgt von einer Abhandlung der Dipolemissioncharakteristik, um ein tieferes Verständnis der Absorptions- und Emissionsprozesse zu erlangen.

Anschließend wird die Implementierung zweier Atom-Photon-Schnittstellen-Protokolle bei 393 nm, und 854 nm vorgestellt. Für letztere zeigen wir zudem die Quantenzustandserhaltende Frequenzkonversion des Einzelphotons in das Telecom-O-Band bei 1310 nm.

Letztlich zeigen wir erste Schritte zur Realisierung lokaler verschränkender Zwei-Qubit-Gatter, dargestellt durch ein Mølmer-Sørensen-Gatter, als Baustein zur Umsetzung von Qantenrepeater-Anwendungen.

Contents

Introduction

Probably one of the most important technological advancement of the last century is the development of semiconductor-based computers [1, 2] and with it the invention of the internet [3], facilitating the world-wide distribution and availability of information. Of course, the proliferation of the internet in the modern world, comprising nearly all aspects of our daily lives, makes it more and more vulnerable towards malicious cyber-attacks, requiring yet more elaborate cryptographic [4, 5] methods for secure communication. At the same time, increasingly complex data processing and computational tasks demand for increasing computational power or novel techniques.

In the early 20th century, a revolutionary new concept appeared with the development of quantum physics [6, 7, 8, 9] that represents a potential solution for both of these challenges. The emergence of quantum technologies around the end of the last and the beginning of the new century initiated a process where new applications for these technologies were sought. One of the founders of quantum computation was Richard Feynman, who, back in 1982, proposed an architecture for quantum gates for computation purposes [10, 11]. This process eventually led to the development of quantum algorithms, whereof the Deutsch-Jozsa [12], Shor [13], and Grover algorithm [14] are probably the most prominent ones, but also other implementations such as quantum simulators [15, 16, 17, 18, 19] emerged.

First important impulses towards modern quantum-information processing were given when Deutsch presented a method for the implementation of a universal quantum computer [20], based on Feynman's pioneering work.

Peter Shor realized in 1994 that quantum mechanics can be utilized to find the prime-factor decomposition and calculate discrete logarithms much more efficiently than with any classical computer. This discovery raised quite some attention as the hardness of prime-factor decomposition of large numbers and discrete logarithms were of great importance for some cryptographic principles [5].

Further progress was made when Grover developed a quantum-enhanced algorithm to find elements in an unsorted database which proved to be polynomially faster than any classical algorithm known to that point. Over the years, many other, mostly very specialized, quantum algorithms developed and are still being developed. However, for a long period in time, these algorithms remained merely theoretical constructs due to the lack of a suitable platform for the physical implementation.

In recent years, significant progress has been made concerning the control of isolated quantum systems such as single trapped ions, single atoms, or single photons, and in that context, the realization of fundamental quantum processors became possible, demonstrating for instance a basic implementation of Shor's algorithm [21] or the Grover search algo-

rithm on a programmable quantum computer [22].

Due to their controllability and good isolation from environmental influences and the comparably high flexibility and facile programmability of complex quantum gates, single trapped ions arose as one of the most promising platforms for quantum computers and closely related quantum-communication protocols. They were shown to allow for very high gate fidelities [23, 24] and coherence times while simultaneously achieving nearly unlimited storage times [25]. Single-ion–based quantum computers utilize strings of trapped ions as a quantum register [26] for quantum-information processing [27]. Important milestones were achieved with the demonstration of the Deutsch-Jozsa algorithm [28], the quantum Fourier transform [29], and the implementation of a universal quantum computer [30].

Though achieving impressive results concerning the storage and processing of quantum information on the single-ion platform, the size of the quantum registers is limited due to the repulsive interaction between the ions, inherently yielding great challenges regarding the scalability of these systems. Various approaches are pursued to tackle this limitation, including the miniaturization of the ion traps [31, 32, 33] to implement a number of quantum sub-processors [34] that are connected via photonic interaction [35, 36], or shuttling of individual ions to transfer quantum information from one sub-processor to an other [37, 38, 39, 40, 41].

Alternative to these local approaches, other strategies like non-local distributed quantum computing [42, 43], connecting small remote processing units via quantum channels to carry out quantum-computation tasks at different locations, emerged. Thinking this ansatz further results in the idea of a quantum internet as proposed by Kimble in 2008 [44]. A crucial element for distributed quantum computing (DQC) or even a fully developed quantum internet is an efficient quantum channel to establish the connection between the sub-units. For larger distances, photonic quantum channels represent the only viable possibility for fast, efficient and robust quantum communication.

Quantum communication

The link between the individual nodes of a DQC network or a general large-scale quantum network is typically established via photonic quantum channels that couple the stationary qubits either via direct quantum-state transfer [45, 46, 47], indirectly utilizing photonic interaction in a projective-Bell-state measurement (BSM) [48, 49], or via quantum teleportation [50, 51, 52]. Different strategies for the photon transfer exist, e.g. satellite-based free-space transmission [53, 54, 55] or schemes building upon the already established earth-bound fiber infrastructure [56].

Apart from applications in the context of DQC, the distribution of quantum information via photonic quantum channels opens the door to a whole range of other applications, of which quantum key distribution (QKD), a technique for the intrinsically secure generation of private keys for the encryption of information sent via (principally vulnerable) classical

communication channels, is probably the most eminent in times where the exchange of large amounts of sensitive information becomes more and more important.

The perhaps most prominent representatives of QKD protocols are BB84 [57], named after its inventors Charles H. Bennett and Gilles Brassard and the year it was first presented, and the similar protocol E91 (proposed by Artur Ekert in 1991 [58]), which shall be briefly discussed in the following. Simply spoken, E91 (and likewise BB84) exploits the no-cloning theorem of quantum mechanics to recognize an attacker eavesdropping the communication channel. For the generation of a secure encryption key, two communication partners, traditionally named Alice and Bob, share pairs of entangled particles (the original proposal for the E91 protocol assumes entangled photon pairs, but the protocol is as well applicable to other entangled systems like pairs of entangled atomic ions). Both, Alice and Bob, randomly and independently choose a measurement basis and store the outcome of the measurement for later usage. In the case of entangled photon pairs, a typical set of measurement bases are the two linear basis pairs H/V (horizontal/vertical) and D/A (diagonal/anti-diagonal). Subsequently, Alice and Bob publish their measurement bases and omit the events where the respective bases did not coincide.

The basic idea to make the protocols tap-proof is the projective nature of a quantum-mechanical measurement. Therefore, an eavesdropper – called Eve – intercepting Bob's photon, being fully ignorant of Alice's and Bob's basis choice, destroys the quantum state of the measured photon. Hence the photon state which Eve sends to Bob that mimics the original photon, is no longer correlated with Alice's photon, thus the quantum statistics measured by Alice and Bob is altered and the eavesdropper is detected when Alice and Bob communicate a (sufficiently long) random sub-set of their measured results via a classical communication channel[1].

Once the secure communication is verified, Alice and Bob generate their private keys from the remaining valid measurements (i.e. the measurements where both choose the same measurement basis), knowing their own result and hence, due to the quantum entanglement of the pairs, also the result of their communication partner. This key is utilized to encrypt a massage which is then sent through a (potentially insecure) classical communication channel. Even if the classical channel is exposed to an eavesdropping attack, the massage is still inherently secure as only the two designated communication users Alice and Bob share the key for decryption.

The ability of the QKD protocols to detect an eavesdropping attack relies on the fact that all errors, up to a certain threshold, can be attributed to an eavesdropper and not to information loss like depolarization or detector dark counts. It is therefore essential for the feasibility of the protocols to achieve low-loss photon transmission to attain a high signal-to-background ratio. However, exponential damping due to absorption or scattering in

[1] A number of methods to exploit a weakness in avalanche photo diodes to hack the in principle secure photon-based quantum-cryptography protocols have been proposed and demonstrated [59]. These vulnerabilities can in principle be avoided by, for instance, using pairs of entangled atomic ions instead of photons. However, of course, transfer and storage efficiencies then play a crucial role.

standard optical fibers impedes the fulfillment of that requirement, even in the low-loss telecom spectral regime for realistic communication distances of several hundreds of kilometers. A quantum-repeater network might represent a solution for efficient long-haul quantum communication and establishment of entanglement between remote qubits, either photonic or atomic.

Quantum repeaters

Quantum repeaters, especially quantum-memory–based quantum repeaters, provide an elegant method to counteract inevitable photon losses in long photonic quantum channels. Since simple amplification of the signal (the single photons) like in classical repeaters, i.e. the creation of an exact copy of the signal photon, is impossible due to the no-cloning theorem (which, if it wasn't impossible, would render the whole cryptography protocol useless), a solution suitable to the conditions of the quantum world has to be found.

Instead of using a single long quantum channel, the deployment of memory-based quantum repeaters allows to split the channel into separate sub-channels, whose length is reduced accordingly, connected via quantum-repeater units. These quantum-repeater units store the quantum information encoded in the photons until the corresponding partner photon has arrived and its state is mapped into the quantum memory as well. Local operations subsequent to the quantum-state storage[2] then establish a link between consecutive repeater nodes (cf. section 6.1). Eventually, entanglement (or state transfer) between the two target qubits is established. Owing to the reduced sub-quantum-channel length, the signal-transmission efficiency is, given several circumstances, increased and with it the signal-to-background ratio (SBR), crucial to the viability of the quantum-cryptography protocols.

Of course, a net gain in the SBR is only achieved if the signal-loss reduction due to the lower channel length overcompensates the non-ideal quantum-state–transfer efficiency from the photonic qubit to the repeater quantum memory. This requires reliable, efficient and high-rate quantum interfaces between the single photons and the quantum memories (represented e.g. by single trapped ions or single neutral atoms). There exists a number of different platforms for quantum-repeater memories, comprising single systems like quantum dots, defects in crystals (like nitrogen-vacancy or silicon-vacancy centers), or single atoms or atomic ions, or ensemble systems like cold atoms. For single atomic ions, several approaches exist for the implementation of quantum interfaces, comprising cavity-coupled systems [63, 64, 65, 66] or free-space coupling using high-numerical-aperture lenses [67, 68]. Due to their good isolation from environmental influences like uncontrolled interactions with nearby atoms and the relatively good controllability, we in our group decided to work with trapped single atomic ions, and hence the following description is tailored to this kind of system.

[2] The most recent results can be found, e.g., in [60, 61, 62]

The second requisite, apart from the implementation of a quantum-repeater scheme, to facilitate long-haul QKD is the reduction of channel-transmission losses between the repeater nodes. Building upon an already set-up fiber infrastructure, this means that the photon wavelength ideally lies withing the telecom range between between 1260 nm and 1625 nm, where fiber losses are particularly low. Depending on the physical system, this condition is not always fulfilled. Considering for instance single-ion–based quantum repeaters, the transition wavelengths are determined by the atom species and do very often not lie in the desired wavelength region. Nonetheless, there exist tools to resolve that obstacle. An obvious but challenging approach, which has been implemented only recently and is an active field of investigation [69, 70, 71, 72], is to deploy quantum frequency conversion to translate the wavelength of the quantum-information–bearing single photon, originally not in the telecom band, into the desired wavelength region.

This work

For the above-mentioned applications, efficient quantum interfaces between the stationary quantum-processing units and the photonic quantum channels as well as low-loss photon transmission play a crucial role for the physical implementation. This thesis primarily focuses on the conception and experimental implementation of single-photon–single-atom entanglement between a single $^{40}Ca^{+}$ ion and a telecom photon, employing high-efficiency, low-loss quantum-state–preserving single-photon quantum frequency conversion (QFC) [73, 74] to address the challenge of long-range quantum communication. Furthermore, first steps towards local entangling two-ion gates – a prerequisite for the realization of single-ion–based quantum repeaters – are presented.

The $^{40}Ca^{+}$ ion itself is the topic of the first chapter, where its level structure and all relevant transitions are presented.

The second chapter gives an overview over the experimental setup; at its heart the ion-trap apparatus – a linear Paul trap – surrounded by a complex overhead, comprising various diode-laser systems and electronic devices for experimental control. The laser systems are necessary to address the different transitions, lying in the visible and near-infrared (NIR) spectral region, of the $^{40}Ca^{+}$ ion which forms the working horse of our experiments. Of particular interest is the narrow-band qubit laser at 729 nm that coherently drives a quadrupole transition of $^{40}Ca^{+}$.

In the third chapter, coherent qubit manipulations on the quadrupole and radio-frequency transitions, as well as the effect of external fields onto the ion, like Zeeman splitting, light shifts, and magnetic decoherence are treated. Furthermore, common experimental techniques like Doppler cooling and frequency-resolved optical pumping are discussed.

Finally, single-photon-single-atom interaction and the spatial emission and absorption characteristics of dipole transitions are investigated in the fourth chapter before the experimental results are presented in the further course of the thesis.

Chapter 5 briefly recapitulates the experimental implementation of a universal, pro-

grammable quantum interface, built on the coherent manipulation of a single trapped $^{40}Ca^{+}$ ion. The interface is capable of transferring quantum information encoded in the polarization state of a single NIR photon at 854 nm onto the electronic state of the ion by controlled absorption. The process is heralded by the detection of a single 393 nm photon that signals the success of the state mapping. In a similar manner, the mapping of a qubit initially stored in the atomic state onto a single blue photon at 393 nm is realized. In addition, the interface scheme allows for the generation of an entangled atom-photon state between the ion and the emitted photon at 393 nm.

Due to the rather unfavorable wavelength of the 393 nm photon in the previous scheme, which exhibits adverse properties like strong absorption in optical fibers, an alternative interface protocol has been developed in the course of this work, presented in Chapter 6. Instead of working with single photons in the blue spectrum, we generated atom-photon entanglement and atom-to-photon state mapping in the near infrared at 854 nm. This milestone gave rise to the possibility for the implementation of quantum frequency conversion from 854 nm to 1310 nm to facilitate atom-photon entanglement between the $^{40}Ca^{+}$ ion and a photon in the low-loss telecom band.

The greater vision behind this work is the demonstration of a proof-of-principle quantum-repeater–based quantum network. Besides the photonic part and the quantum interface, which both are the topic of the previous chapters, a quantum repeater, which reduces the effective quantum-channel length, requires local entangling multi-qubit gates for the processing of quantum information between single ions[3]. The last chapter shows first steps towards this missing link based on the Mølmer-Sørensen gate, including several necessary experimental techniques like single-ion addressing, and discusses possible sources and problem-solving approaches for the observed gate imperfections.

This work forms a substantial advancement within the scope of a series of experiments and developments, which, starting various years ago, still are part of an ongoing process that will extend further into the future. Therefore, all results presented here are not the achievement of a single person, but rather represent the joint effort of a dynamically evolving team and is based on the work of generations of scientists in our group and beyond. Many enthusiastic people contributed over the years to build and improve the technical set-up this work is based upon (chapter 2). Their work formed the fundamental for all results obtained since and is described in detail in their respective theses [75, 76, 77, 78, 79, 80]. Apart from the hardware, the development of methods routinely used in the experiment was of great importance and a very valuable legacy from the former generations of students. These methods are briefly depicted in chapter 3.

Of course, the progress did not stop after these people left the group, and so further improvement was undertaken to achieve the next milestones. My dedicated part from a technical perspective was the rearrangement of the optical setup in the proximity of the ion trap, e.g. the replacement of the former photomultiplier tubes (PMT) by two avalanche

[3]Through entanglement swapping from a local pair of ions onto a remote ion pair (see section 7 for details)

photo diodes (APD) for improved detection efficiency of single 393 nm photons or the implementation of a 729 nm beam line for single-ion addressing to make the experiment suitable for future applications. In addition to the development and implementation of many new experimental sequences, I acquired and installed a new 393 nm diode laser which made most of the experiments presented in chapter 6 possible.

Efficient realization of the quantum-interface protocols treated in this thesis requires a profound understanding of the underlying absorption and emission processes. For that purpose, I did a detailed analysis of the spatial dependence of the polarization of photons emitted on an optical dipole transition, which is presented in chapter 4. Some of these results are based on the work of Philipp Müller, being described in full detail in his PhD thesis [81].

Earlier work in the context of this PhD project lead to the realization of a programmable ion-photon interface at a wavelength of 393 nm, which partially already appeared in Christoph Kurz' dissertation thesis [79] and is summarized in chapter 5 and in [82].

Chapter 6 constitutes the major content of this thesis and essentially represents my main contribution. Certainly, also other people participated in the success of that experiment. In particular, this comprises the collaboration with Matthias Bock from the group of Christoph Becher, who built and operated the frequency-converter. An overview of the quantum-frequency converter is given in that chapter. The fully-detailed description will be given in Matthias' thesis [73].

Eventually, the final chapter 7 describes first steps towards local two-ion gates. Although the chapter itself is short compared to others, Matthias Kreis and I spent a significant amount of time in the laboratory while conducting these experiments and searching for the source of the gate-fidelity reduction

Journal publications

Part of the work of this thesis has been published in refereed journals:

High-fidelity entanglement between a trapped ion and a telecom photon via quantum frequency conversion
M. Bock, P. Eich, S. Kucera, M. Kreis, A. Lenhard, C. Becher, J. Eschner
Nat. Commun. **9**, 1998 (2018)

Programmable atom-photon quantum interface
C. Kurz, P. Eich, M. Schug P. Müller, J. Eschner
Phys. Rev. A **93**, 062348 (2016)

Further associated work:

Doubly-heralded single-photon absorption by a single atom
J. Brito, S. Kucera, P. Eich, P. MÃ¼ller, J. Eschner
Appl. Phys. B, 122:36 (2016)

Telecom-heralded single-photon absorption by a single atom
A. Lenhard, M. Bock, C. Becher, S. Kucera, J. Brito, P. Eich, P. Müller, J. Eschner
Phys. Rev. A **92**, 063827 (2015)

Experimental protocol for high-fidelity heralded photon-to-atom quantum state transfer
C. Kurz, M. Schug, P. Eich, J. Huwer, P. Müller, J. Eschner
Nat. Commun. **5**, 5527 (2014)

Quantum interference in the absorption and emission of single photons by a single ion
M. Schug, C. Kurz, P. Eich, J. Huwer, P. Müller, J. Eschner
Phys. Rev. A **90**, 023829 (2014)

1. The $^{40}Ca^{+}$ ion

Singly-ionized alkaline-earth-metal atoms are a well-established quantum system for a variety of applications [19, 83, 84, 85, 86, 87, 88, 89, 90, 91, 92], in particular for quantum networks and quantum-repeaters and, very recently, even for the development of commercial quantum computers [93], due to their rather simple and well understood level structure and optical addressability of atomic transitions in the visible or (near) infrared spectral region for laser cooling and qubit manipulations.
What makes these alkaline-earth ions so exceptional is the fact that they exhibit only one valence electron which simplifies theoretical and experimental considerations significantly.

In our experiment, we work with singly-charged Calcium-40. ^{40}Ca has a nuclear spin of $I = 0$ and thus shows no hyperfine splitting. Although hyperfine splitting (as occurring for instance in $^{43}Ca^{+}$) is beneficial for certain aspects like microwave gates and the existence of clock states with long coherence times, it usually requires the presence of additional lasers for cooling and repumping, which makes it impractical for our purposes.

This chapter briefly treats the level structure of the $^{40}Ca^{+}$ ion, showing the atomic states and transitions that are relevant in the experimental framework.

1.1. Level scheme

$^{40}Ca^{+}$ shows five (easily accessible) states, $4^2S_{1/2}$, $4^2P_{1/2}$, $4^2P_{3/2}$, $3^2D_{3/2}$, and $3^2D_{5/2}$, of which two, $3^2D_{3/2}$ and $3^2D_{5/2}$, are metastable with a lifetime of more than one second. These states are further split by an external magnetic field according to the projection of their total angular momentum j, characterized by the magnetic quantum number m_j. This Zeeman splitting opens up the possibility of frequency-selective addressing of individual quadrupole transitions and coherent manipulations of the ground-state qubit and is therefore crucial for the viability of our experimental protocols, but at the same time entails vulnerability towards magnetic-field fluctuations so that additional effort has to be put into the elimination of magnetic noise.

Two short-lived states, $4^2P_{3/2}$ and $4^2P_{1/2}$, with a lifetime in the order of 7 ns, rapidly decay into either the metastable states or, most likely, into the energetic ground state $4^2S_{1/2}$ upon excitation. The short-lived states can be regarded as auxiliary states for cooling, fluorescence-assisted state discrimination on the $S_{1/2} \leftrightarrow P_{1/2}$ transition at 397 nm, and single-photon generation on the transition from $P_{3/2}$ to the meta-stable $D_{5/2}$ state at 854 nm, as explained later in this thesis. In the latter case, the $S_{1/2} \leftrightarrow P_{3/2}$ transition at 393 nm is used for excitation into the short-lived state.

Additional dipole transitions involved in the experiment are those from $D_{3/2}$ to $P_{1/2}$ at 866 nm, which is used for repumping from the meta-stable $D_{3/2}$ state during Doppler cooling (cf. section 3.1) and fluorescence generation at 397 nm, and the 850 nm transition from $D_{3/2}$ to $P_{3/2}$, which is currently used for the alignment of the quantization axis.
The quadrupole transition from $S_{1/2}$ to $D_{5/2}$ at 729 nm plays a special role in the experiment as it is used for coherent manipulations on the optical S-D qubit. For manipulations of the ground-state qubit between the two Zeeman sublevels in $S_{1/2}$, typically in the order of 8 MHz, we installed a radio-frequency coil below the trap chamber.
There exists an other quadrupole transition $S_{1/2} \leftrightarrow D_{3/2}$ which is not used in the current experiments.

All states involved in the present experiments are displayed in fig. 1.1 along with their Landé factors, the precise lifetime values, the transitions between these states and their respective (reduced) Einstein coefficients.

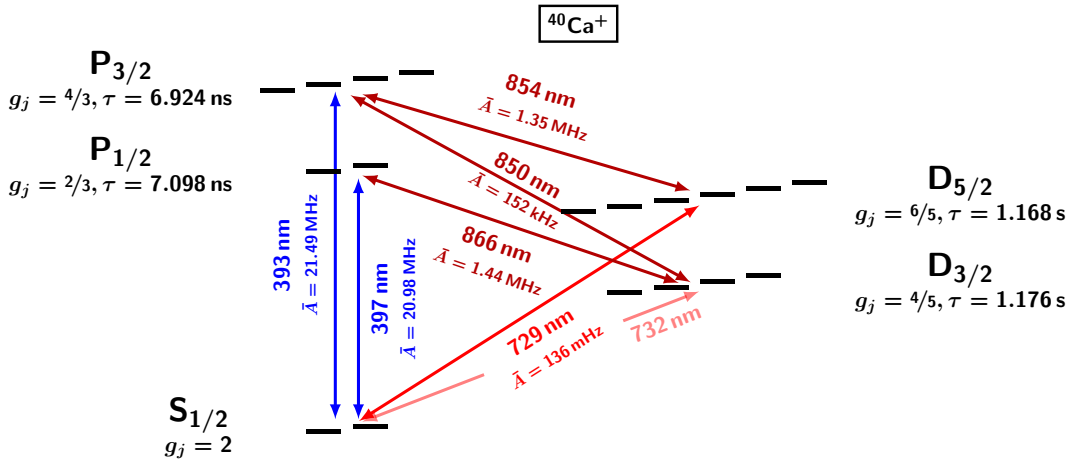

Figure 1.1.: Relevant level scheme of the $^{40}Ca^{+}$ ion. g_j and τ denote the Landé factors and the natural lifetimes of the states, respectively. Arrows depict optical transitions between the levels, together with their wavelengths and the reduced Einstein coefficients $A/2\pi$.

The Einstein coefficients correspond to the oscillator strengths for the transition from an initial state $|i\rangle$ into a state $|g\rangle$ and were measured with high precision for $^{40}Ca^{+}$ [94, 95].

The sum of all Einstein coefficients $A_{i\to g}$ for the decays from $|i\rangle$ into all other states gives the total decay rate Γ_i (where i denotes the individual states, i.e. $P_{3/2}$, $P_{1/2}$ etc.) which is directly related to the natural lifetime τ_i via $\Gamma_i = \frac{1}{\tau_i}$ (and therefore also corresponds to the linewidth of transitions coupling to the state). The ratio of the Einstein coefficients for different decays from the same excited state is called the branching ratio and represents the ratio of the probabilities for decay along the respective channels. A perhaps slightly more intuitive quantity is the branching fraction $A_{i\to g}/\Gamma$ which can be interpreted as the probability that the ion "chooses" a certain decay branch.

Non-zero branching ratios, i.e. the existence of multiple decay channels, imply a time-

bandwidth product above the Fourier limit for photons along that transition, as it is particularly the case for single photons emitted on the infrared transitions at 850 nm, 854 nm, and 866 nm. The latter can be understood intuitively in the following picture: if there is more than one decay channel, it takes on average more than one excitation cycle to generate a photon on a particular transition, while the spectral bandwidth of that photon is by the single-photon–generation time, i.e. the time for the generation of a photon on any of the transitions. This circumstance is discussed again in section 4.1.

The decay rates for the relevant levels and their transition wavelengths λ and branching fractions are summarized in tab. 1.1 (as found in [78]).

State	τ	Γ	Transitions	λ	Branching fraction
$P_{3/2}$	6.924 ns	$2\pi\cdot$22.986 MHz	$P_{3/2} \rightarrow S_{1/2}$	393.4775 nm	93.47%
			$P_{3/2} \rightarrow D_{5/2}$	854.4433 nm	5.87%
			$P_{3/2} \rightarrow D_{3/2}$	850.0361 nm	0.66%
$P_{1/2}$	7.098 ns	$2\pi\cdot$22.423 MHz	$P_{1/2} \rightarrow S_{1/2}$	396.9590 nm	93.565%
			$P_{1/2} \rightarrow D_{3/2}$	866.4515 nm	6.435%
$D_{5/2}$	1.168 s	$2\pi\cdot$136 mHz	$D_{5/2} \rightarrow S_{1/2}$	729.3473 nm	100%
$D_{3/2}$	1.176 s	$2\pi\cdot$135 mHz	$D_{3/2} \rightarrow S_{1/2}$	732.5903 nm	100%

Table 1.1.: Relevant levels, lifetimes τ and total decay rates Γ. The possible decay channels, their wavelengths and the branching fractions for the respective decays are listed.

Within the transition from one state $|i\rangle$ to another state $|g\rangle$ (e.g. from $P_{3/2}$ to $D_{5/2}$ at 854 nm), a substructure appears due to the splitting of the Zeeman sublevels by their magnetic quantum number m. The oscillator strength for the transition $|i, m_i\rangle \rightarrow |g, m_g\rangle$ (as long as it is dipole-allowed, i.e. when $\Delta m = 0, \pm 1$ is fulfilled) is then determined by the Clebsch-Gordan coefficient (CGC) for the transition $|m_i\rangle \rightarrow |m_g\rangle$. The Clebsch-Gordan coefficients arise due to the coupling of orbital angular momentum and spin and their respective magnetic quantum numbers (that is, their projections onto the quantization axis) to the total angular momentum and its magnetic quantum number. In other terms, they originate from a basis transformation from the uncoupled to the coupled eigenbases of the system. A detailed discussion is, for example, found in [96], a table of commonly appearing CGCs is given in [97]. Fig. 1.2 shows the Clebsch-Gordan coefficients for the $D_{5/2} \leftrightarrow P_{3/2}$ (854 nm) and the $P_{3/2} \leftrightarrow S_{1/2}$ (393 nm) transitions which have the highest relevance for our experimental protocols.

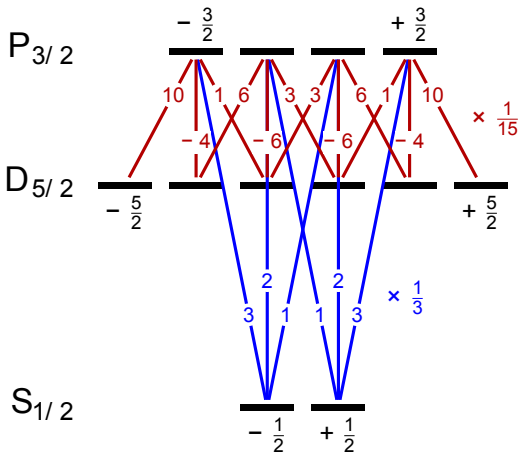

Figure 1.2.: Clebsch-Gordan coefficients for the $D_{5/2} \leftrightarrow P_{3/2}$ (854 nm) and the $P_{3/2} \leftrightarrow S_{1/2}$ (393 nm) dipole transition. Note that this representation gives the intensity of the transition, that is the square modulus of the actual CGC. A − indicates a minus sign in front of the square root. Taking for instance the transition $|P_{3/2}, +1/2\rangle \rightarrow |D_{5/2}, +1/2\rangle$, we find a Clebsch-Gordan coefficient of $-\sqrt{\frac{6}{15}}$.

2. Experimental setup

The heart and soul of each quantum-optical work is the experimental setup which usually grows organically with the complexity of the performed measurements. A (stationary) qubit constitutes the center of all quantum-optical information technology. Single atomic ions have proven to be suitable candidates as stationary qubits or quantum memories in a quantum network [98, 99, 100] due to their long coherence time [101, 102, 103], good isolation from the environment, long storage times (in the order of days to weeks, depending on the experimentalist's enthusiasm and patience), the relatively easy manipulation of quantum information stored in the ion [77, 104, 105, 106], and their ability to reliably couple to "flying" qubits, i.e. optical photons [82, 107, 108].

The ion used in the experiments presented in this thesis is $^{40}Ca^{+}$, which was discussed in more detail in chapter 1. $^{40}Ca^{+}$ exhibits six optical transitions that are addressed in the experiments. Furthermore, two additional laser systems for the photo ionization of atomic Calcium (see section 2.1.3) and our laser-locking scheme (section 2.2.2) are needed, summing up to eight laser systems in total.

In addition to the lasers needed to cool and manipulate the ion, the ion-trap apparatus, based on a linear Paul trap in a vacuum chamber, embodies the second building block for the ion experiments.

This first part of this chapter treats the linear Paul trap, including a theoretical description, the photo-ionization process of the atomic Calcium, and the optical setup surrounding the trap.
In the second part, the diode-laser systems are presented, together with the narrow-band qubit laser and our transfer-locking scheme for laser-frequency stabilization.

2.1. Ion-trap system

The key ingredient for modern single-ion–based quantum-optics technology dates back to the year 1953, when Wolfgang Paul developed an electrical quadrupole mass spectrometer [109] which was later extended to today's Paul traps [110]. The Paul trap facilitated the storage and manipulation of single ions and has thus become a widely-used tool for quantum optics [111], quantum computation [22, 112, 113], quantum simulations [114, 115, 19], and quantum metrology [116, 117].

Single atomic ions are generated by a laser-assisted two-photon photo-ionization process that will be described in the course of this section.

The integration of single ions into larger-scale quantum networks requires an optical

atom-photon interface and the ability of single- and multi-qubit manipulations of the ions. Manipulation of the trapped ions is carried out by laser and radio-frequency pulses, while coupling of the ions to single photons and collection of single photons emitted by the ions is implemented by two high-numerical-aperture laser objectives (HALO) situated in close proximity to the ions.
The description of the optical setup represents the final part of this section.

2.1.1. The Paul trap

The Paul trap consist of four electrodes aligned along the trap axis to which an oscillating radio-frequency voltage is applied, and two DC electrodes at both ends of the linear trap, generating a quasi-static potential inside the trap. A charged particle, e.g. a single atomic ion, entering the trap potential, is confined inside the trap.
The realization of a linear Paul trap in our setup, originally designed and partially manufactured in the group of Prof. Rainer Blatt at the University of Innsbruck [118], is shown in fig. 2.1. The trap is built of two pairs of electrode blades, one pair held at ground, while

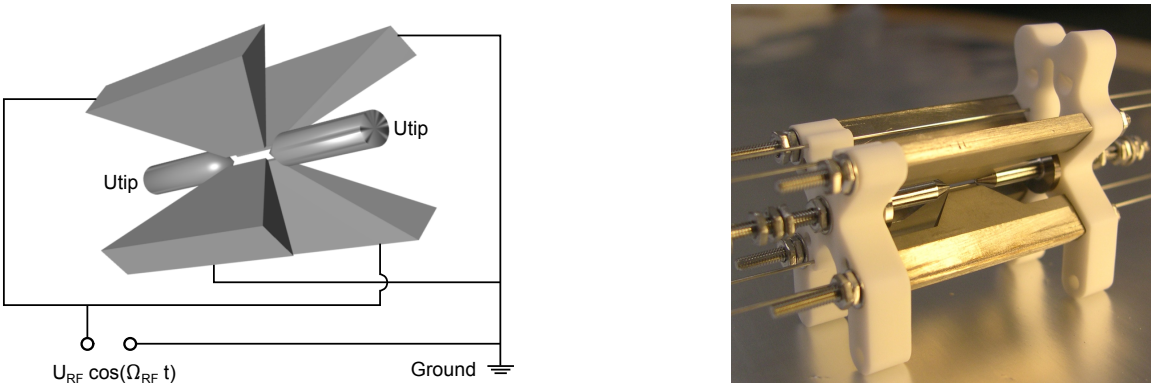

(a) (b)

Figure 2.1.: (a) Schematic depiction of the linear Paul trap, consisting of four blade electrodes for the radial and two end tips for the axial confinement of the ions. (b) Picture of the actual Paul trap. The distance between two opposite blades is 1.6 mm, the end-tip electrodes are separated by 5 mm. (From [77, 75])

an oscillating radio-frequency voltage is applied to the other blade pair. Two end-tip electrodes add a static electric field along the trap axis. The oscillating RF field and the static field sum up to a quasi-harmonic potential (see fig. 2.2) that gives rise to motional degrees of freedom of the trapped ions in axial and radial trap direction. The oscillation of the trapping field with the radio frequency leads to a fast oscillation of the ion in the trap, the so-called micromotion, that yields beneficial [119] and adverse effects [120]. A detailed description of the resulting trap potential and the experimental parameters is given in the next section. Further information about the Paul traps are found in [75].

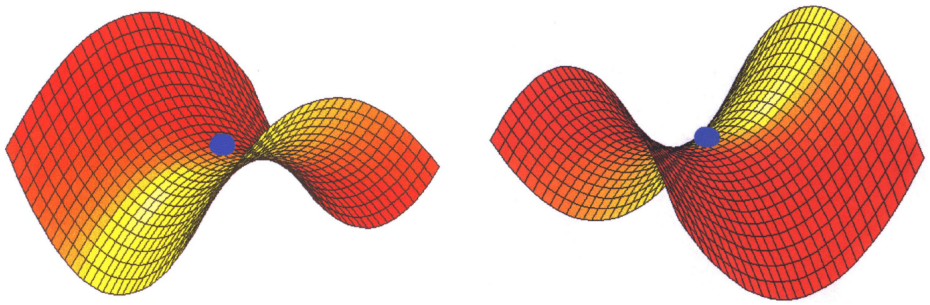

Figure 2.2.: Depiction of the oscillating quadrupole potential of the linear Paul trap. A charged particle such as a single ion (blue circle) experiences an oscillating saddle potential, here shown at two instances separated by half the period of the radio-frequency drive. (From [75])

2.1.2. Trap potential

The necessity for oscillating fields in order to trap charged particles derives from Earnshaw's theorem [121], which states that, based on Laplace's equation, there is no static magnetic or electric field that is capable of confining single charged particles in all three spatial dimensions. To overcome this limitation, the linear Paul trap, as described above, uses a combination of a static voltage, applied to the end tips, and a rotating radio-frequency voltage, applied to one pair of the blades, while the other pair is connected to ground. Defining the symmetry axis of the trap to point along the z-axis, the resulting time-dependent electric field in the vicinity of the origin is then given by

$$\Phi = \Phi_{\mathrm{RF}} + \Phi_{\mathrm{endtip}} = \frac{U_{\mathrm{RF}}}{2r_0^2}(x^2 - y^2)\,\cos(\Omega_{\mathrm{RF}} t) + \frac{\alpha'\,U_{\mathrm{endtip}}}{2\ell^2}(2z^2 - x^2 - y^2), \tag{2.1}$$

with r_0, ℓ being the distance from the center of the trap to the RF electrodes and end tips, respectively. The empirically determined geometry factor α' takes shielding effects of the electrodes into account.

Using the resulting force $\vec{F} = -e\,\nabla\Phi = m \cdot \ddot{\vec{r}}$ onto a particle of charge e, the equations of motion are derived as

$$F_x = -e\,\frac{\partial\Phi}{\partial x} = -e\left(\frac{U_{\mathrm{RF}}}{r_0^2}\cos(\Omega_{\mathrm{RF}} t) - \frac{\alpha'\,U_{\mathrm{endtip}}}{\ell^2}\right) x = m\,\ddot{x} \tag{2.2}$$

$$F_y = -e\,\frac{\partial\Phi}{\partial y} = -e\left(\frac{U_{\mathrm{RF}}}{r_0^2}\cos(-\Omega_{\mathrm{RF}} t) - \frac{\alpha'\,U_{\mathrm{endtip}}}{\ell^2}\right) y = m\,\ddot{y} \tag{2.3}$$

$$F_z = -e\,\frac{\partial\Phi}{\partial z} = -e\left(2\,\frac{\alpha'\,U_{\mathrm{endtip}}}{\ell^2}\right) z\,, \tag{2.4}$$

which can be transformed into the Mathieu equation

$$\frac{d^2 r_i}{dt^2} + \left(a_i - 2q_i\cos(\Omega_{\mathrm{RF}} t)\right)\frac{\Omega_{\mathrm{RF}}^2}{4} r_i = 0 \tag{2.5}$$

by using the substitutions

$$a_x = a_y = -\frac{1}{2}a_z = -\frac{4e\alpha' U_{\text{endtip}}}{m\ell^2\Omega_{\text{RF}}^2}, \quad q_y = -q_x = \frac{2eU_{\text{RF}}}{mr_0^2\Omega_{\text{RF}}^2}, \quad q_z = 0\,. \tag{2.6}$$

A stable (i.e. trapped) solution for eq. (2.5) is obtained for $|a|, q^2 \ll 1$ which simplifies the approximate radial solutions of the Mathieu equation to

$$r_i(t) = r_{0,i}\cos(\omega_i t)\left(1 - \frac{q_i}{2}\cos(\Omega_{\text{RF}}t)\right)\,. \tag{2.7}$$

This solution describes a slow secular motion of the ion with the radial trap frequency ω_i that is superimposed by a fast micromotion at the driving frequency Ω_{RF}. In the pseudopotential approximation [122], the fast micromotion oscillations ($\omega_i \ll \Omega_{\text{RF}}$) are averaged out to obtain the radial secular frequencies

$$\omega_x = \frac{\Omega_{\text{RF}}}{2}\sqrt{a_x + \frac{q_x^2}{2}}\,, \qquad \omega_y = \frac{\Omega_{\text{RF}}}{2}\sqrt{a_y + \frac{q_y^2}{2}}\,. \tag{2.8}$$

In a similar way, the axial trap frequency is calculated as

$$\omega_z = \frac{\Omega_{\text{RF}}}{2}\sqrt{a_z} = \sqrt{\frac{2e\alpha' U_{\text{endtip}}}{m\ell^2}}\,. \tag{2.9}$$

With eq. (2.9), (2.8) can be rewritten as

$$\omega_r = \sqrt{\omega_{0,r}^2 - \frac{1}{2}\omega_z^2}\,, \tag{2.10}$$

where $\omega_{0,r}$ denotes the bare radial frequency (i.e. for $U_{\text{endtip}} = 0$).

In the present setup, the experimental parameters $U_{\text{endtip}} = 400\,\text{V}$, $U_{\text{RF}} = 1449\,\text{V}$, $r_0 = 0.8\,\text{mm}$, $\ell = 2.5\,\text{mm}$, and $\Omega_{\text{RF}} = 26.127\,\text{MHz}$ result in the single-ion trap frequencies $\omega_z/2\pi = 1.1956\,\text{MHz}$ and $\omega_r/2\pi = 3.647\,\text{MHz}$, respectively.

In the case of two trapped ions, additional oscillation modes appear. Besides the center-of-mass mode (COM), where both ions oscillate in phase with the frequencies ω_z and $\omega_{x,y}$, respectively, the axial oscillation (which were used in later experiments) reveals an additional 'breathing' mode which exhibits a frequency of $\omega_z^{Breath} = \sqrt{3}\,\omega_z^{COM} = 2\pi \cdot 2.0708\,\text{MHz}$. Accordingly, the two-ion radial motion features four oscillation modes (two COM modes and two 'rocking' modes). In contrast to the axial motion, the higher-order radial modes (i.e. the 'rocking' modes) show lower energies than the COM modes.

2.1.3. Photo ionization

All work presented in this thesis requires the trapping of single $^{40}Ca^+$ ions. In our setup, these ions are generated in a two-photon resonance-enhanced photo-ionization process

[75], where neutral ^{40}Ca atoms evaporated from an oven are excited by laser light at 423 nm, originating from a frequency-doubled diode laser at 846 nm[1], on the $4s^2\,{}^1S_0 \rightarrow 4s4p\,{}^1P_1$ transition. Subsequent absorption of light at 390 nm, stemming from an LED[2] with an emission spectrum centered around 380 nm and a full-width at half maximum (FWHM) of 30 nm, excites the atoms into a Rydberg state from which the atom is ionized by strong electric fields within the Paul trap. Once fluorescence from a trapped ion is detected on an EMCCD camera[3] or photomultiplier tubes[4] (PMT), the photo-ionization process is interrupted to avoid trapping of further ions. With this technique, we achieve loading times on the order of several minutes.

2.1.4. Trap setup

To avoid atom loss due to collisions with background gas, the Paul trap is embedded into an ultra-high–vacuum vessel as shown in fig. 2.3.

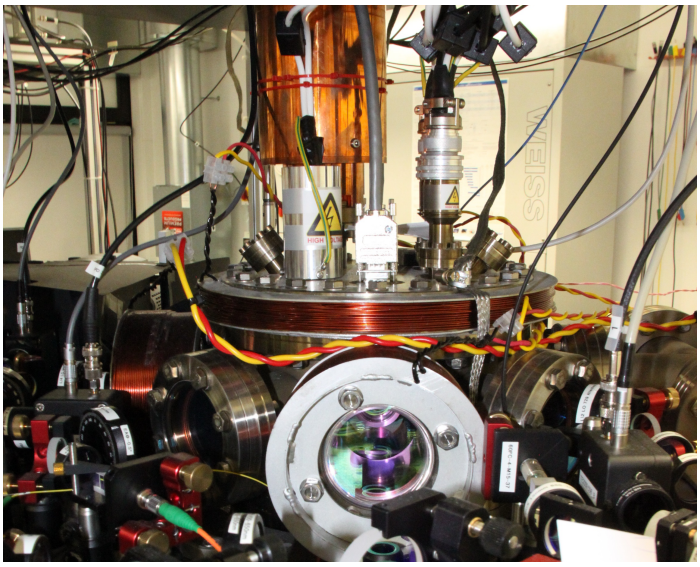

Figure 2.3.: Photograph of the vacuum chamber that contains the Paul trap.

The vacuum inside the chamber is held at a value of about 10^{-10}-10^{-11} mbar. Optical access is ensured by 8 viewports in the table plane, situated at the faces of the octagonally shaped chamber, and one additional viewport at the bottom of the vessel for the photo-ionization light. The helical resonator for the coupling of the trap radio frequency is placed on top (large copper-colored cylinder in fig. 2.3). Further details on the vacuum setup are found in [75].

[1] TOPTICA Photonics, DL pro
[2] Nichia, NCCU001-LED
[3] Andor, DV887DCS-BV
[4] Hamamatsu, H7422P-40 SEL

The trap itself is surrounded by two high-numerical-aperture laser objectives[5] (HALO) (see fig. 2.4) that serve the purpose to both, tightly focus single photons and laser beams, especially for single-ion addressing, onto the ion, as well as efficiently collecting single photons emitted by the ion. The objectives have a numerical aperture (NA) of 0.4, hence covering a solid angle of about 4%. The precise collection efficiencies for photons emitted on the different atomic transitions will be discussed in chapter 4.

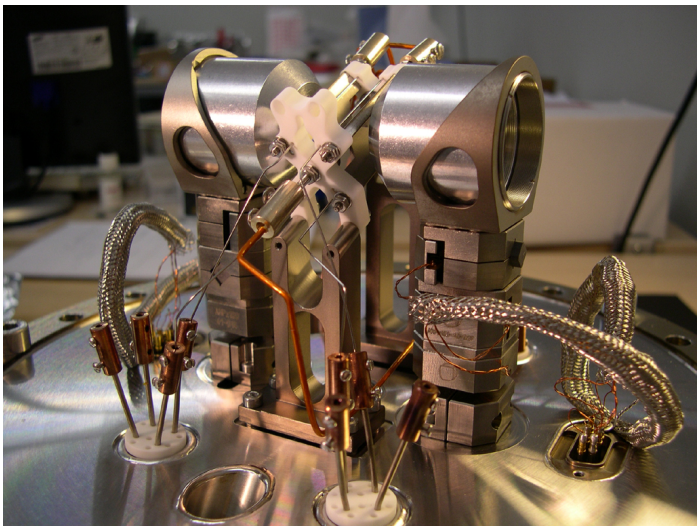

Figure 2.4.: Paul trap between the two HALOs mounted on their three-directional translation stages. (Adapted from [77])

The HALOs are mounted on three translation stages[6] for sub-micrometer positioning. The HALOs consist of an arrangement of four lenses made from different materials that are anti-reflective coated for 397 nm, 423 nm and 866 nm and yield a transmittance for the relevant wavelengths between 95.7 % for 397 nm and 98.8 % for 850–866 nm. The working distance ranges from 11.8 mm at 397 nm to 13.2 mm at 866 nm (to avoid contact of the metal housing of the HALO lenses with the RF blade electrodes) which, given[123]

$$d = 1.22 \frac{\lambda}{NA} , \tag{2.11}$$

leads to focal-spot sizes between $d = 1.2\,\mu m$ (397 nm) and $d = 2.6\,\mu m$ (866 nm).

The quantization axis is defined by a magnetic field of 2.8 G applied to the ion. This field is generated by a set of three orthogonally oriented coils or coil pairs of which one pair typically determines the main axis while the other coils are used to compensate residual magnetic fields, e.g. the magnetic field of the Earth, that otherwise distort the precise orientation of the quantization axis. In the context of the experiments presented in this thesis,

[5] Linos Photonics, HALO 25/0.4
[6] Attocube, ANPx100

the B field was aligned along the HALO axis for reasons that will become obvious in the course of this work.

Manipulations of the ion are carried out by laser and radio-frequency pulses that enter the vacuum vessel from various directions, as schematically shown in fig. 2.5.

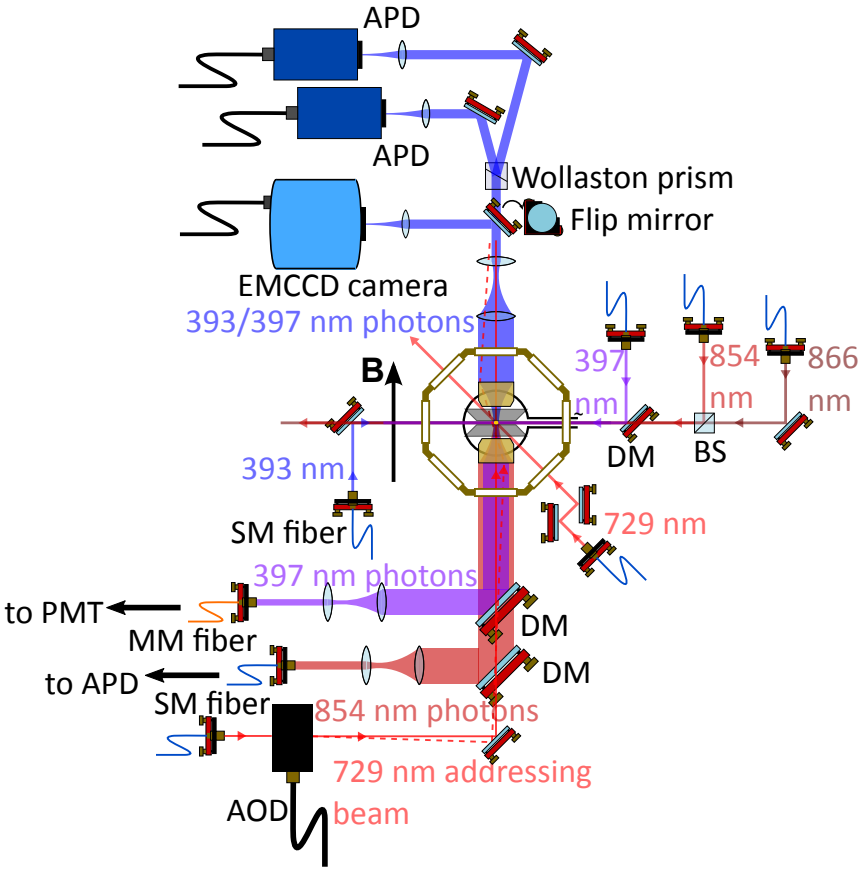

Figure 2.5.: Schematic depiction of the trap setup and its surrounding optical elements, including the beam paths for laser light and single photons. An individual description of the single elements is given in the text.

The cooling-laser beams at 397 nm and 866 nm, being overlapped at a dichroic mirror (DM), incide from 90° (where 0° is defined as parallel to the B-field direction along the HALO axis in fig. 2.5). Their polarization (vertically polarized) is chosen such that no optical pumping, i.e. decoupling from the light fields, occurs. The 854 nm repumping beam is overlapped with the 866 nm beam at a non-polarizing beam splitter (BS). An additional laser beam at 393 nm for the excitation of the $S_{1/2} \rightarrow P_{3/2}$ transition is sent from the opposite direction (270°). The focal-spot sizes for all these lasers are in the order of 100 µm, therefore the alignment of the beams is rather uncritical and robust.

Global excitation, that is, simultaneous excitation of all ions stored in the trap, of the

quadrupole qubit transition at 729 nm is realized by a beam under 45° with a spot size of about 80 µm. Tilting of the trap by 22.5° with respect to the table plane allows for the frequency-selective addressing of all motional modes, i.e. the axial and both radial modes of a single ion by tuning the laser to the respective motional sideband of the bare atomic transition.

Single-ion addressing for operating the trap with multiple ions is achieved by the "AOD beam" under 0°, i.e. through the HALO (needed to obtain the necessary small focus size), named after the acousto-optic deflector[7] (shown in the bottom of fig. 2.5). The deflection angle varies with the RF frequency applied to the AOD, thus enabling switching between the individual ions.
To ensure reliable spatial modes of all laser fields, the coupling of the beams onto the ion is realized via single-mode optical fibers for the respective wavelengths.

Besides the separate manipulation of the ions via a tightly focused laser beam, the HALOs are predominantly deployed to collect single photons emitted from the ion. Due to different diffraction indices, the focal lengths of the HALO systems differ for the different wavelengths. Therefore, the objectives have to be adjusted for the desired collection wavelength to guarantee the imaging quality of the ion image onto the photon detectors or fiber end facets. The HALO at the "Sitges" side[8] of the vacuum chamber (the bottom side of the picture) is set to collimate light at 854 nm, whereas additional correction lenses are needed for proper beam shaping of the light paths for photons at other wavelengths, particularly at 393 nm and 397 nm. 854 nm photons collected by the Sitges HALO pass the first dichroic mirror that separates red light (854 nm, 729 nm) from blue light at 397 nm and 393 nm, and are then reflected by the second dichroic mirror, which is coated to exhibit a high reflectivity at 854 nm and a high transmittance at 729 nm. A telescope, built from commercially available off-the-shelf lenses, subsequently reduces the beam diameter to meet the requirements for the following single-mode–fiber coupling. Subsequent polarization-state analysis of the photons, if employed, is performed by a usual projection setup, consisting of three waveplates ($\lambda/4$ / $\lambda/2$ / $\lambda/4$) and a polarizer, and an avalanche photo diode (APD)[9] for single-photon detection.

Atomic state detection is usually carried out by state-depedent 397 nm fluorescence of the ion. For that purpose, fluorescence is collected by the HALO on the Sitges side and coupled into a multi-mode fiber by the first dichroic mirror. As mentioned before, the telescope for the 397 nm photons has to be set up in a non-confocal configuration to compensate for the convergence of the light mode, caused by the focusing of the HALO which is optimized for 854 nm collimation. The multi-mode fiber is connected to a PMT[10] to detect the photons. Depending on the number of photon counts, the ion is either considered

[7] Gooch & Housego, R46080-3-LTD
[8] Named after the town of Sitges near Barcelona. The denotation stems from the time when the experiment was still located at ICFO at that side of the setup pointed towards Sitges. Analogously, the opposite side of the setup is called "Barcelona".
[9] Perkin Elmer, SPCM-AQR-14
[10] Hamamatsu, H7422P-40 SEL

"dark" or "bright" (see section 3.4).
Single-ion–resolved readout of the atomic state is realized by imaging the fluorescence of an ion chain (typically consisting of two ions) onto the surface of an EMCCD camera[11] through the HALO (adjusted to 393 nm collimation) on the Barcelona side. By the time the experiment was set up, hardly any to no wavelength-separation mirrors for 393 nm/397 nm where available, therefore we included a flip mirror to switch between the monitoring of 397 nm fluorescence on the camera and the projection and detection of single photons at 393 nm.

The latter is done by removing the flip mirror to let the 393 nm single photons pass through a telescope setup to reduce the diameter of the beam from about 2 cm to roughly 0.5 cm to fit the photons through the Wollaston prism[12] placed right behind the telescope[13]. The prism separates the photons according to their polarization, enabling us to project the photon polarization onto the two Eigenbases of the prism, horizontally and vertically polarized. The two polarizations are split by an angle of 20° and sent onto two APDs[14] (one per output arm).

In addition to the lasers for optical manipulation of the atom, a radio-frequency coil is installed below the trap. The coil is driven by a radio frequency that is tuned to the $|S_{1/2}, m = -1/2\rangle \leftrightarrow |S_{1/2}, m = +1/2\rangle$ transition between the two Zeeman-split sublevels of $S_{1/2}$ for coherent manipulation of the ground-state qubit.

2.2. Laser system

Singly-charged Calcium ions are nearly ideal quantum memories regarding their controllability, as they possess optical transitions in the visible or near-infrared spectral region which can easily be addressed by commercially available diode-laser systems. In the present experiments, we primarily work on four dipole transitions (393 nm, 397 nm, 854 nm, and 866 nm) with spectral widths of about 20 MHz, placing little demands on the laser linewidths. The frequency-locking scheme for these lasers is discussed later in this section.
Moreover, two ancilla lasers for photo ionization (846 nm/423 nm), B-field alignment (850 nm), and a laser that serves as master oscillator for our locking scheme (852 nm) are employed.

Aside from the dipole transitions, $^{40}Ca^{+}$ features two quadrupole transitions in the visible, $|S_{1/2}\rangle \leftrightarrow |D_{3/2}\rangle$ at 732 nm and $|S_{1/2}\rangle \leftrightarrow |D_{5/2}\rangle$ at 729 nm, of which we utilize the latter for coherent qubit manipulations. Since this transition exhibits a natural linewidth of $2\pi \cdot 136$ mHz, the requirements for a narrow-band laser linewidth in the Hz regime can no longer be fulfilled by the conventional frequency-stabilization technique applied to the

[11] Andor, DV887DCS-BV
[12] Thorlabs, WP10
[13] We learned that it is important to shine a collimated beam onto the Wollaston prism to avoid strong deformation of the beam at the outputs.
[14] Laser Components, COUNT-50B

other lasers, but a more elaborate locking setup has to be deployed. Both, the qubit laser itself as well as its stabilization are presented in the last two sections of this chapter.

2.2.1. Laser sources

The following list provides a brief overview over the laser sources that are operated in the laboratory (with the exception of the qubit laser at 729 nm which will be treated separately in a later section).
The laser sources, except for the 845 nm laser, are situated on a separate optical table, where amplitude, frequency (and phase) are adjusted. Frequency matching of the laser light with the resonance frequency of the respective transitions is obtained by tuning the laser frequency using acousto-optical modulators (AOMs) that enable us to shift the frequency in a range between 50 and 100 MHz. The light is then coupled into polarization-maintaining single-mode fibers and guided to the optical table where the ion trap is placed.

It is mentioned in the previous chapter that Doppler cooling is employed on the dipole transition $|S_{1/2}\rangle \leftrightarrow |P_{1/2}\rangle$ at 397 nm, which is also used for fluorescence generation to detect the internal state of the ion (see section 3.4). To avoid pumping into the metastable $|D_{3/2}\rangle$ manifold, an additional repumping laser at 866 nm that couples onto the $|D_{3/2}\rangle \leftrightarrow |P_{1/2}\rangle$ transition, is switched on during cooling and fluorescence generation.

Generation of single photons at 854 nm requires excitation of the ion to $|P_{3/2}\rangle$ and subsequent decay into the meta-stable $|D_{5/2}\rangle$. A diode laser at 393 nm is used for the excitation from the ground state to $|P_{3/2}\rangle$. Repumping from $|D_{5/2}\rangle$ is performed by an additional laser at 854 nm, which is also used for optical pumping (see sec. 3.2).

The frequency-stabilization scheme for the lasers resonant on the atomic dipole transitions is based on a master laser at 852 nm which is resonant on an atomic transition of a Cesium vapor cell that serves as a frequency reference. In addition, a laser at 846 nm is employed for photo ionization of the atomic Calcium atoms, and a 850 nm laser, resonant on the $|D_{3/2}\rangle$-to-$|P_{3/2}\rangle$ dipole transition, is used for the alignment of the magnetic field and thus the quantization axis.

The requirements regarding the linewidth of the lasers coupling to the dipole transitions are rather relaxed due to the atomic transition linewidth in the order of 20 MHz, hence laser widths of a few MHz or less are sufficient to achieve adequate coupling. The 729 nm laser, which couples to the narrow-band quadrupole transition $|S_{1/2}\rangle \leftrightarrow |D_{5/2}\rangle$, must be able to frequency-resolve the transitions between the different Zeeman sublevels, resulting in higher demands with concerning the spectral width. Therefore, this system is described separately in more detail in section 2.2.4.

397 nm

The $|S_{1/2}\rangle \leftrightarrow |P_{1/2}\rangle$ transition at 397 nm is used for Doppler cooling and fluorescence-based state readout.

Due to the lack of blue laser diodes at the time most of the lasers were purchased, the system[15] consists of three stages. Initially a grating-stabilized laser diode produces light at 794 nm which is then amplified by a tapered amplifier (TA) and subsequently frequency-doubled by second-harmonic generation in a nonlinear crystal inside a bow-tie cavity.
We achieve a maximum output power of 200 mW for the blue light, but reduce the power to 40 mW to increase the TA lifetime. The free-running laser linewidth is specified by the manufacturer as 300 kHz for 5 µs integration time.

866 nm

Because of spontaneous decay from $P_{1/2}$ into the metastable $D_{3/2}$ state during cooling and fluorescence integration, an additional repumping laser[16] has to be incorporated that couples to the transition from $D_{3/2}$ to $P_{1/2}$ at 866 nm. We typically work with 20 to 50 µW of 866 nm power at the ion, therefore the 30 mW direct output power of the laser diode is by far sufficient for our purposes. The free-running linewidth of 150 kHz allows for the frequency-stabilization of the laser onto an optical cavity (see section 2.2.2) without further measures.

854 nm

Repumping from the metastable $D_{5/2}$ state at the end of an experimental run and generation of single 393 nm photons is carried out by the fundamental light of a TA-SHG pro at 854 nm. The major part of the fundamental light, after amplification in a TA, is frequency-doubled to 427 nm to operate the newly built SPDC photon-pair source [124] while 10-15 mW are split off and sent to the ion. After passing two AOMs in double-pass configuration, the remaining power arriving at the ion lies in the order of 500 µW.

393 nm

The DL pro at 393 nm is the newest system in our setup. It is the first laser that is controlled by the novel DLC pro laser-control unit which features an improved temperature stability of the laser head, enabling free-running operation of the laser during the experiments, although a frequency stabilization is currently developed. The diode delivers 40 mW laser power, while the linewidth of <2 MHz is sufficiently narrow compared to the atomic linewidth ($2\pi\cdot$23 MHz) of the transition from $D_{3/2}$ to $P_{1/2}$ at 393 nm.

852 nm master laser

The laser-locking scheme, described in section 2.2.2, is based on a atomic Cesium reference

[15] TOPTICA Photonics, TA-SHG pro
[16] TOPTICA Photonics, DL pro

onto which a master laser is stabilized. The frequency stability of that laser is then transferred onto the other lasers via a locking chain. This scheme requires a laser source that is resonant on the Cs D2 line at 852 nm which is embodied by a diode-laser system [17] whose output power was measured to be around 120 mW.

846 nm photo-ionization laser

Photo ionization, as described in section 2.1.3, is assisted by a free-running laser[18] at 846 nm that delivers 120 mW of output power at a linewidth of < 1 MHz. The light is frequency doubling in a single-pass ppKTP crystal for frequency matching with the atomic transition, yielding 35 µW of light power and a bandwidth of < 2 MHz.

850 nm ancilla

The 850 nm ancilla laser[19], resonant on the $D_{3/2} \leftrightarrow P_{3/2}$ transition, is primarily used for the alignment of the quantization axis since the acquisition of the 393 nm laser. It is built of a single grating-stabilized diode.

Some details on the lasers in the context of the frequency-locking scheme and the photo ionization are found in [125] and [126], respectively. A more detailed description is found in [75] (section 2.2) and [78] (section 1.2).

2.2.2. Transfer locking

The stabilization of the lasers onto a common atomic reference requires a sophisticated locking scheme [125], built upon a chain of consecutive cavity locks to indirectly connect the laser frequency to the D2 line of the Cs reference.
The chain starts with Doppler-free absorption spectroscopy of a Cs vapor cell by the master laser at 852 nm. Prior to the spectroscopy, the laser is locked to a temperature-stabilized low-finesse cavity [76] ($\mathcal{F} = 270$, cavity linewidth $\Delta = 1.9$ MHz) via Pound-Drever-Hall technique (see section 2.2.3) using commercial electronics[20]. The light is then utilized to lock the cavity itself to the Cs line at 852.33493 nm.
The 866 nm laser is directly Pound-Drever-Hall locked to this cavity. To overcome spatial limitations[21], two additional cavities[22] are installed to bridge the gap between 852 nm and 794 nm (the fundamental laser for 397 nm light) and 854 nm, which are frequency-locked to the 852 nm laser. The lasers are locked to their respective cavities by PDH technique,

[17] *TOPTICA Photonics* DL 100
[18] TOPTICA Photonics, DL 100
[19] TOPTICA Photonics, DL pro
[20] TOPTICA Photonics, DigiLock 110
[21] Spatial separation of the individual laser beams becomes challenging for more than two beams.
[22] $\mathcal{F}_{794} \approx 100$, $\mathcal{F}_{854} \approx 100$

where feedback is applied to a piezo actuator controlling the cavity grating of the laser as well as to the diode current for fast feedback up to 5 MHz.

Frequency matching of the cavity modes and the target frequency of the laser (close to the atomic transitions) is achieved by tuning the temperature of the cavities or shifting the frequency of the 852 nm reference light with the help of an auxiliary AOM. The remaining frequency deviation from the laser light to the atomic transitions is compensated by acousto-optical modulators.

An equivalent stabilization setup for the 393 nm laser is currently being set up where stabilized 397 nm light serves as reference for the cavity lock of a blue transfer cavity.
The setup for the locking scheme, though slightly modified in the meantime, is shown in more technical detail in [76].

2.2.3. Pound-Drever-Hall technique

As mentioned in the previous section, laser locking in the present experiments is realized by the commonly used Pound-Drever-Hall technique. This technique was first developed for microwave oscillators [127] and later extended to optical frequencies [128]. Here, an optical cavity serves as a frequency-dependent phase shifter. To utilise this property, the laser light is phase-modulated by applying a modulation signal of frequency $\Omega_m/2\pi =$ 12.5 MHz or 25 MHz to the diode current or onto an external electro-optical modulator (EOM) in the case of the 729 nm laser.

Below, a brief derivation, adopted from [129], of the PDH error-signal generation is presented.
Let Φ_0 be the modulation depth, then the resulting electric laser field becomes

$$E(t) = E_0 \left(e^{i\,(\omega_c t + \Phi_0 \cdot \sin \Omega_m t)} \right) \tag{2.12}$$

with the carrier frequency ω_c of the laser and the field amplitude E_0. Using Bessel functions J_i, it is expanded to [129]

$$E(t) \approx E_0 \left(J_0(\Phi_0)\, e^{i\,\omega_c t} + J_1(\Phi_0)\, e^{i\,(\omega_c + \Omega_m)\,t} - J_1(\Phi_0)\, e^{i\,(\omega_c - \Omega_m)\,t} \right) \tag{2.13}$$

for small modulation depths Φ_0, representing a carrier and two modulation sidebands at frequencies $\pm\Omega_m$. An incident light field E_{inc} that is reflected from a (symmectric and lossless) Fabry-Pérot cavity experiences a modification of its magnitude which is characterized by the frequency-dependent reflection coefficient $F(\omega)$, defined as the ratio of incoming and reflected field

$$F(\omega) = \frac{E_{inc}}{E_{ref}} = \frac{r\,\left(\exp\left(i \frac{\omega}{\Delta\nu_{FSR}} \right) - 1 \right)}{1 - r^2 \exp\left(i \frac{\omega}{\Delta\nu_{FSR}} \right)}\,, \tag{2.14}$$

where r is the amplitude-reflection coefficient (not to be confused with the reflection coefficient $F(\omega)$) and $\Delta\nu_{FSR}$ is the free spectral range of the cavity. Applying eq. (2.14) to the modulated field (eq. (2.13)), the reflected field from the optical resonator reads

$$\begin{aligned} E_{ref} \approx\, & E_0 \left(F(\omega_c) J_0(\Phi_0)\, e^{i\,\omega_c t} \right) + F(\omega_c + \Omega_m) J_1(\Phi_0)\, e^{i\,(\omega_c+\Omega_m)\,t} \\ & - F(\omega_c - \Omega_m) J_1(\Phi_0)\, e^{i\,(\omega_c-\Omega_m)\,t} \end{aligned} \tag{2.15}$$

and accordingly, using $P_{ref} \propto |E_{ref}|^2$, the reflected power becomes

$$\begin{aligned} P_{ref} \propto\, & |E_0 J_0(\Phi_0)|^2 |F(\omega_c)|^2 + |E_0 J_1(\Phi_0)|^2 \left(|F(\omega_c+\Omega_m)|^2 + |F(\omega_c+\Omega_m)|^2 \right) \\ & + 2\sqrt{|E_0 J_0(\Phi_0)|^2 |E_0 J_1(\Phi_0)|^2} \Big[\Re\big(F(\omega_c) F^*(\omega_c+\Omega_m) \\ & - F^*(\omega_c) F(\omega_c-\Omega_m) \big) \cos\Omega_m t \\ & + \Im \left(F(\omega_c) F^*(\omega_c+\Omega_m) - F^*(\omega_c) F(\omega_c-\Omega_m) \right) \sin\Omega_m t \Big] \,. \end{aligned} \tag{2.16}$$

If the modulation sidebands are far-off resonance, $F(\omega_c \pm \Omega_m)$ becomes approximately -1 and eq. (2.16) simplifies to

$$\begin{aligned} P_{ref} \propto\, & |E_0 J_0(\Phi_0)|^2 |F(\omega_c)|^2 + 2|E_0 J_1(\Phi_0)|^2 + 2\sqrt{|E_0 J_0(\Phi_0)|^2 |E_0 J_1(\Phi_0)|^2} \Im\big(F(\omega_c) \\ & - F^*(\omega_c) \big) \sin\Omega_m t \\ & = |E_0 J_0(\Phi_0)|^2 |F(\omega_c)|^2 + 2|E_0 J_1(\Phi_0)|^2 \\ & - 4\sqrt{|E_0 J_0(\Phi_0)|^2 |E_0 J_1(\Phi_0)|^2} \Im \left(F(\omega_c) \right) \sin\Omega_m t \,. \end{aligned} \tag{2.17}$$

The reflected power is measured with a (sufficiently fast) photo diode and fed into an electronic mixer, where it is mixed with a reference oscillator at the modulation frequency Ω_m. Usually, a phase shifter has to be included to match the phases of both inputs. Low-pass filtering of the output, retaining only the $\sin\Omega_m t$ term in eq. (2.17), reveals the error signal

$$\mathcal{E}(\omega_c) \approx -4\sqrt{|E_0 J_0(\Phi_0)|^2 |E_0 J_1(\Phi_0)|^2}\, \Im \left(F(\omega_c) \right) \sin\Omega_m t \tag{2.18}$$

which features a steep slope around the cavity resonance for small deviations of the laser frequency from that resonance. Feedback onto the laser is then generated from this error signal after prior processing by a controller element, e.g. a PID controller.

2.2.4. Qubit laser

Manipulations on the optical qubit is conducted on the quadrupole transition between $S_{1/2}$ and $D_{5/2}$ at 729 nm. Due to the long lifetime of 1.17 s, the according transition reveals

a narrow linewidth of $2\pi \cdot 136\,\mathrm{mHz}$. Consequently, the width of the driving laser has to be of the same order of magnitude for efficient coherent manipulation and prevention of excitation of unwanted neighboring transitions. The transfer-locking scheme presented before no longer satisfies these requirement, which is why a different approach for the laser stabilization, namely a Pound-Drever-Hall lock onto a high-finesse cavity, presented in section 2.2.5, is adopted.

The laser itself is composed of a laser diode embedded in a grating-based feedback cavity in Littrow configuration. This way, a free-running linewidth of some 100 kHz is attained. Further reduction of the linewidth to the order of tens of Hz is achieved by a fast feedback loop acting on both, the grating for low-frequency drifts, restricted by the bandwidth of the piezo actuator that controls the angle of the grating, and the current through the diode for noise cancellation at frequencies up to some MHz.

The weak coupling strengths of the atomic quadrupole transmissions requires laser power of 10 to 100 mW. To obtain these powers, laser light coming from the diode has to be amplified by a tapered amplifier which delivers an output power of about 430 mW behind the optical isolator. Subsequently, the light is distributed among the various AOM lines that serve the different beams guided to the ion.

A small fraction of the light ($\approx 2\,\mathrm{mW}$) is split up before the TA and is used to lock the laser to an external high-finesse ULE cavity. First, the locking beam is sent through an AOM[23], running at about 290 MHz and set up in double-passage configuration, to bridge the gap between the target frequency of the laser and the nearest cavity mode. The light is then passing through a self-built EOM, running at 20 MHz, which are generated by the PDH module[24] that come with the laser, to imprint the necessary phase-modulation sideband onto the field, and then sent onto the ultra-low–expansion (ULE) cavity, described in the next section, for a PDH-type locking. Narrowing of the laser linewidth is facilitated by feedback onto the laser from a fast analog controller[25]. More details on the qubit-laser system are found in [77].

A well-known phenomenon in closed feedback loops is the emergence of so-called servo bumps. They are caused by the limited bandwidth of the servo loop that leads to a phase shift of the feedback signal for higher frequencies. Once the phase shift exceeds 180°, noise at that frequency and above is amplified instead of suppressed. In diode-laser systems, these broad servo bumps typically lie in the vicinity of 1 MHz around the carrier, coinciding with the axial trap frequency, and their magnitude lies between 25 dB and 30 dB below the carrier, if no counter measures are adopted. In the current setup, we observe the appearance of servo bumps as well. They are characterized explicitly in chapter 7 and their influence on gates that operate on the motional sidebands is investigated.

[23] Brimrose, TEF-270-100-729
[24] TOPTICA Photonics, PDD 110
[25] TOPTICA Photonics, FALC 110

2.2.5. High-finesse ULE cavity

The high-finesse ULE cavity was set up in the context of Jan Huwer's doctoral thesis [77] to enable narrow-linewidth frequency stabilization. The cavity is standing upright on three Teflon spacers to reduce thermal conductivity from the environment and minimize coupling to mechanical vibrations. To ensure passive stabilization, it is enclosed in a temperature-regulated vacuum chamber which for its part is sitting inside an isolated, temperature-stabilized Aluminum box. Mechanical perturbation is damped out by a passive vibration-damping platform[26] onto which the vacuum chamber is placed. In addition, the vacuum of about $5 \cdot 10^{-10}$ mbar provides a considerable isolation against acoustic noise. The inside of the Aluminum box can be seen in fig. 2.7.

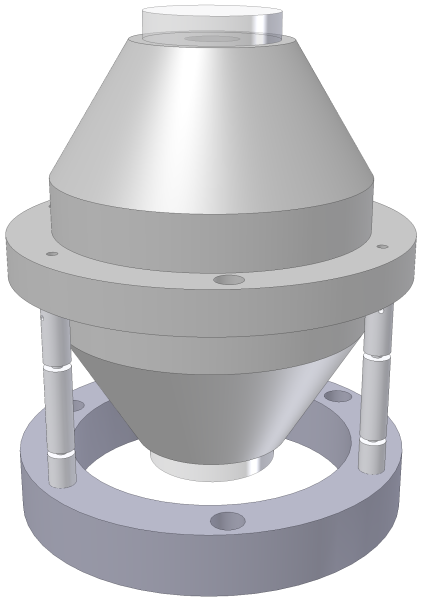

Figure 2.6.: 3D model of the high-finesse cavity. The cavity is mounted upright on three Teflon rods for mechanical and thermal decoupling. (From [77])

Figure 2.7.: A picture of the inside of the Aluminum box containing the HF cavity. The vacuum chamber is resting on a vibration-damping platform. Locking light is coupled from below. A vacuum pump, seen on the left, retains the vacuum. (From [77])

The cavity is constructed from ultra-low-expansion–glass spacer[27] with a zero-expansion point of 21° C. It is built in a Fabry-Pérot-like layout with two mirrors separated by a

[26] Minus K, 100BM-4
[27] manufactured by Corning

distance of 77.5 mm in non-confocal configuration. It consists of one planar mirror and one concave mirror with a radius of curvature (ROC) of 50 cm. The resulting free spectral range was measured to be $\Delta\nu_{FSR} = 1.935(3)$ GHz and the finesse was determined as $\mathcal{F} = 479\,000 \pm 1000$, hence

$$\Delta\nu_{cav} = \frac{\Delta\nu_{FSR}}{\mathcal{F}} \tag{2.19}$$

yields a cavity linewidth of $\Delta\nu_{cav} = 4.034(5)$ kHz.

Due to material properties of the ULE glass, the cavity exhibits a linear drift of its resonance frequency of 80 mHz/s or 7 kHz per day. Therefore, the RF-drive frequency of the compensation AOM for the laser lock is adjusted from time to time.

2.3. Experiment control

Increasing complexity in the protocols for quantum-information application demands precise control over the experimental sequences. Therefore, more and more elaborate control units are required.

We deploy a commercially available system that constitutes the second-generation version of its predecessor "HYDRA" [130] originally developed in the group. The device is manufactured and distributed by Keysight[28]. It is based on FPGA-controlled arbitrary-waveform generators (AWG) to generate RF signals of up to 1 GS/s that drive the AOMs for the individual laser beams. Additional digital-input-output (DIO) and time-to-digital–converter (TDC) modules facilitate the usage as single-photon counter with a time resolution of 150 ps, furthermore allowing for conditional operation of the experiment which leads to a tremendous speed-up of the sequential execution time, and to apply feedback to the AOMs for intensity stabilization.

[28] formerly *Signadyne*

3. Experimental methods

Even the most complex experimental sequence in the context of this work requires a comprehensive set of fundamental experimental methods for reliable initialization, manipulation, and detection of quantum states. This tool box comprises well-established techniques like Doppler cooling [131], Ramsey-type measurements [132] and fluorescence-based state discrimination.

The implementation of some of these techniques in the present experimental setup dates back to earlier work in the group; for instance the Doppler cooling presented in section 3.1 and atomic state analysis by fluorescence detection (sec. 3.4), which were already described in [75], and coherent manipulations on the optical and ground-state qubit (sections 3.3.2 and 3.3.3) as well as the usage of Ramsey experiments for the determination of the atomic coherence time (see section 3.6), that were topic of Jan Huwer's dissertation thesis [77]. A modified scheme for frequency-resolved optical pumping, presented in section 3.2, the deployment of the atomic light shift for single ion addressing, discussed in sec. 3.3.4, and an approach for the suppression of magnetic-field noise, were newly established in the course of this thesis and related work[1].

In addition, the concept of Zeeman splitting and the appearance of the (time-dependent) Larmor phase are briefly discussed in sec. 3.5 as they are essential for the understanding of some of the phenomena encountered in the following.

3.1. Laser cooling

Apart from internal electronic states mentioned in chapter 1, the overall quantum state is also characterized by its quantized motional degrees of freedom. For a single ion trapped in a linear Paul trap, these are represented by the motional quantum numbers n_{ax}, $n_{rad,x}$ and $n_{rad,y}$ for the axial and both radial trap modes, respectively.

After trapping, the ion is in a high-lying thermal state of motion whose spatial wavepacket is strongly delocalized, making laser cooling necessary.
An established cooling technique that combines high cooling rates and moderate experimental effort is Doppler cooling which will be described in the following. Even though it suffers from a minimal achievable temperature well above zero[2] and is therefore not suit-

[1] The feed-forward technique for the magnetic-noise cancellation was developed by Matthias Kreis during his Master's thesis [133].

[2] Typically, the number of motional quanta in the system after Doppler cooling lies in the order of 10, depending on the trap frequencies.

able for ground-state cooling, it has proven to be sufficient for all tasks in our context of atom-photon-interfaces so far.

In the following, the ion is assumed to be already pre-cooled to the Lamb-Dicke regime[3], where the spread of the atomic wavepacket is small compared to the wavelength of the external light field (or rather its projection onto the motional mode under consideration), or in other terms, where $\sqrt{2\langle n\rangle + 1}\,\eta \ll 1$ holds, when $\eta = k\sqrt{\frac{\hbar}{2m\omega_T}}$ is the Lamb-Dicke parameter with the laser wave number k, the ion mass m and the trap frequency ω_T, and where $\langle n\rangle$ is the mean motional quantum number.

In addition to the carrier transition, a trapped two-level atom exhibits sideband transitions at frequencies $N \cdot \omega_T$, $N \in \mathbb{N}$, from the carrier, that couple to the motional state of the ion. Hence two competing cooling/heating processes occur when the atom is driven by laser light: absorption on the red sideband (i.e. at frequency $\omega_C - \omega_T$, where ω_C is the transition carrier frequency and ω_T is the trap frequency), relieving a phonon and resulting in cooling of the ion, and absorption on the blue sideband ($\omega_C + \omega_T$) or emission on the red sideband, which counteracts the cooling and adds a phonon into the system.

It is intuitive that a net cooling is accomplished when the absorption rate on the red sideband is higher than the rate on the blue sideband. For a further understanding of the cooling dynamics, we have to distinguish between two regimes, the resolved-sideband regime, where $\omega_T \gg \Gamma$ holds so that the motional sidebands can be addressed individually, on the one hand, and the case $\omega_T \ll \Gamma$ on the other hand, where the transition is much broader than the distance of the sideband from the carrier. Doppler cooling, discussed in this chapter and deployed in the experiment, operates in the latter regime.

Ideal parameters for Doppler cooling are determined by the ratio of cooling rate vs. heating rate, i.e. we want to find a detuning Δ for the driving laser for which we achieve large cooling rates while simultaneously reducing the heating. For that purpose, an analytical expression for the cooling and heating rates has to be derived. Following the procedure in [134], we find the rates $R_\pm$ for a scattering event on the blue and red sideband, respectively, to be $R_- = nA_-$ and $R_+ = (n+1)A_+$, with the rate coefficients

$$A_\pm = \frac{\Omega^2}{\Gamma}\,\eta^2\left(\cos^2\theta\, W(\Delta \mp \omega_T) + \alpha W(\Delta)\right)\,, \tag{3.1}$$

$$W(\Delta) = \frac{1}{4\frac{\Delta^2}{\Gamma^2} + 1}\,, \tag{3.2}$$

the motional quantum number n, and the Rabi frequency Ω in the regime of weak coupling, i.e. for $\Omega \ll \Gamma$. The angle θ in eq. (3.2) represents the angle between the direction of propagation of the cooling light and the orientation of the motional mode. α describes the average component of the spontaneous-emission recoil energy on the motional axis, weighted with the dipole pattern of spontaneous emission [134, 135]. Isotropic emission

[3] which is not a necessary condition for Doppler cooling, but it simplifies the mathematical treatment by assuming that two-phonon processes are strongly suppressed.

results in $\alpha = 1/3$. The first term in $R_+(R_-)$ corresponds to absorption on the blue (red) sideband and subsequent emission on the carrier, while the second term describes absorption on the carrier and emission of a photon on the blue (red) sideband transition [134]. Note that absorption and subsequent emission on a sideband is strongly suppressed by a factor of η^2 and therefore neglected.

The mean vibrational quantum number $\langle n \rangle$ is given by

$$\langle n \rangle = \sum_{n=0}^{\infty} p_n n \,, \tag{3.3}$$

where p_n represents the probability to find the ion in $|n\rangle$ when we sum over all electronic states and is typically described by a thermal distribution. The temporal derivative of this number is then determined by the total cooling rate $R_{\text{tot}} = \sum_{n=0}^{\infty} p_n \big(R_+(n) - R_-(n)\big)$, i.e.

$$\begin{aligned} \frac{d}{dt}\langle n \rangle &= \sum_{n=0}^{\infty} p_n \big(R_+(n) - R_-(n)\big) \\ &= \sum_{n=0}^{\infty} p_n \big((n+1)A_+ - nA_-\big) = \sum_{n=0}^{\infty} p_n n (A_+ - A_-) + A_+ \\ &= (A_+ - A_-)\langle n \rangle + A_+ \,, \end{aligned} \tag{3.4}$$

where we have to take into account that the cooling efficiency, i.e. the probability for a cooling event, depends on the motional quantum number.
From eq. (3.4) we derive the temporal evolution for the mean vibrational number,

$$\langle n \rangle(t) = \langle n \rangle(0)\, e^{(A_+ - A_-)\, t} + \langle n \rangle(\infty) \left(1 - e^{(A_+ - A_-)\, t}\right) \,. \tag{3.5}$$

$\langle n \rangle(\infty)$ is the steady-state solution, assuming $A_- > A_+$, and is deduced from $\frac{d}{dt}\langle n \rangle(\infty) = 0$ as (cf. eq. (3.4))

$$\langle n \rangle(\infty) = \frac{A_+}{(A_- - A_+)} \,. \tag{3.6}$$

Minimization of eq. (3.6) leads to the optimal detuning for Doppler cooling:

$$\frac{d}{d\Delta}\langle n \rangle(\infty) \stackrel{!}{=} 0 \Rightarrow \Delta_{\text{opt}} = -\frac{\Gamma}{2} \,. \tag{3.7}$$

We see that $\langle n \rangle(\infty)$ exhibits a finite value for $\Delta = \Delta_{\text{opt}}$. This value represents the Doppler limit. Cooling below this threshold would require more advanced cooling techniques like resolved-sideband cooling [136] or EIT[4] cooling [137].

In the experimental implementation, we employ Doppler cooling on the $S_{1/2} \leftrightarrow P_{1/2}$ transition at 397 nm. Since the real ion is not an ideal two-level system, but exhibits several

[4] electromagnetically induced transparency

transitions and decay into the metastable $D_{3/2}$ manifold, an additional laser at 866 nm is required for repumping from $D_{3/2}$. As mentioned before, both lasers (397 nm and 866 nm) are vertically polarized to avoid optical pumping.
From the experimental parameters for cooling of the axial mode, $\theta = 22.5°$, $\eta = 0.163$, $\omega_T = 2\pi \cdot 1.195\,\text{MHz}$, and $\alpha = 1/3$ (assuming isotropic spontaneous emission), eq. (3.6) exhibits an expectation value for the population of the axial motional mode of $\langle n_{ax} \rangle(\infty) = 6$.

Temperature measurements using the red sidebands of the quadrupole transition[5] $S_{1/2} \leftrightarrow D_{5/2}$ reveal a mean population of the (axial) motion of $\langle n_{ax} \rangle \approx 15$. The experimental value is higher than the ideal minimum mean occupation of the motional modes after Doppler cooling. This effect is primarily traced back to the (false) assumption of an ideal two-level system in the theoretical description. In the actual implementation, the coupling of all 8 levels involved in the cooling process (two sub-levels in $S_{1/2}$, two sub-levels in $P_{1/2}$, and the four sub-levels in $D_{3/2}$) by the cooling laser at 397 nm and the repumping laser at 866 nm leads to the occurrence of dark resonances that significantly alter the conditions for the cooling dynamics. An analysis of the cooling dynamics in multi-level systems is found in Jan Huwer's dissertation thesis [77].

Although we also conducted experiments where we used resolved-sideband cooling prior to the actual experimental pulse sequence (specifically for the Mølmer-Sørensen-type two-qubit gates presented in chapter 7), we saw no improvement in the outcome and thus restricted ourselves to Doppler cooling for all measurements presented henceforth in favor of higher repetition rates.

3.2. Optical pumping

Due to a modified geometry of the trap-table setup (see chapter 2) compared to earlier experiments [77, 78, 79], polarization-selective optical pumping on the $S_{1/2} \leftrightarrow P_{1/2}$ transition at 397 nm is no longer applied to avoid damage of the single-photon detectors. For that reason, an alternative pumping scheme, based on the frequency-selective depopulation of one Zeeman sublevel of $S_{1/2}$ on the narrow quadrupole transition at 729 nm, is implemented. Repumping from $D_{5/2}$ is provided by simultaneously driving the ion with 854 nm laser light. Decay from $P_{3/2}$ to $S_{1/2}$ either transfers the ion into the target state, where it is decoupled from the 729 nm light, or into the undesired sublevel, where it undergoes the pumping cycle again until the ion eventually ends up in a pure state with high probability. The pumping procedure is again schematically shown in fig. 3.1.

To avoid a lengthy empirical optimization process for the pumping parameters, we estimate the optimal laser powers (or the respective Rabi frequencies) in advance, where we keep in mind that the potential 729 nm power is limited to avoid erroneous excitation of neighboring transitions. A typical scenario restricts the Rabi frequency of the quadrupole laser to a FWHM[6] of about $2\pi \cdot 100$ kHz and the laser power has to be chosen accordingly.

[5] for details on the temperature-measurement scheme see [77]
[6] Full width at half maximum

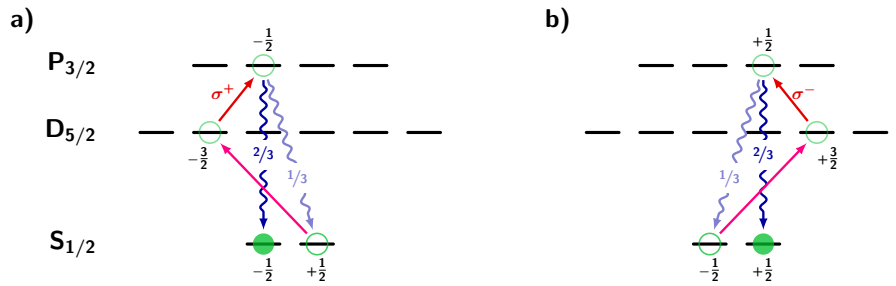

Figure 3.1.: Frequency-selective optical pumping into $|S_{1/2}, -1/2\rangle$ (a) and $|S_{1/2}, +1/2\rangle$ (b). The 854 nm repumper, incident under 90° to the quantization axis, is vertically polarized and couples exclusively to the $\sigma^{\pm}$ transitions.

The power broadened FWHM of the line is given by [138]

$$\Delta\omega_{1/2} = A_{S\to D}\sqrt{1 + 2\,\frac{\Omega_{729}^2}{A_{S\to D}^2}} \tag{3.8}$$

with $A_{S\to D} = 2\pi\cdot 136\,\text{mHz}$ being the Einstein coefficient for the $S_{1/2} \to D_{5/2}$ transition and Ω_{729} the Rabi frequency of the driving laser on said transition. If we allow for a FWHM of 250 kHz, we obtain an optimal Rabi frequency of $\Omega_{729} = 2\pi\cdot 177\,\text{kHz}$ (with the 854 nm laser switched off).

The width of the $D_{5/2}$ level is determined by its effective lifetime which is directly connected to the resonant repumping rate [78]

$$R_{D\to S} = \frac{\Omega_{854}^2}{\Gamma_{P_{3/2}}^2 + 2\Omega_{854}^2}\,A_{P\to S}\,, \tag{3.9}$$

governed by the 854 nm laser power, via $\tau_{P_{3/2}} = \frac{1}{R_{D\to S}}$ for $R_{D\to S} \gg \Gamma_{D_{5/2}}$. In analogy to eq. (3.8), Ω_{854} and $A_{P\to S}$ are the Rabi frequency ($D_{5/2} \to P_{3/2}$ transition) and the Einstein coefficient ($P_{3/2} \to S_{1/2}$ transition), respectively, and $\Gamma_{P_{3/2}}$ is the total decay rate for $P_{3/2}$. Numerical simulations show that the optimal value for the Rabi frequency on $D_{5/2} \leftrightarrow P_{3/2}$ is $\Omega_{854} = 2\cdot\Omega_{729} = 2\pi\cdot 344\,\text{kHz}$. The underlying model for the simulation is presented in section 4.1.

Assuming we start from a symmetrical mixture of both Zeeman sublevels in the $S_{1/2}$ ground state (which is not entirely true due to the more complex level structure of the cooling transitions that results in a small population imbalance) and accounting for the unequal Clebsch-Gordan coefficients of both decay paths, the minimum number of scattering events for a desired pumping efficiency η_{pump} can easily be derived as

$$N = \log_3\left(\frac{1}{2\cdot(1-\eta_{\text{pump}})}\right)\,. \tag{3.10}$$

For a target efficiency of 99.9% we obtain a minimum of 4 scattering events for our given experimental parameters which corresponds to a simulated theoretical pumping time of 33 µs (fig. 3.2). In practice we work with a moderately increased pumping time of 60 µs to 100 µs to be more robust towards imperfections. With that we achieve pumping efficiencies of typically 99.6% [139].

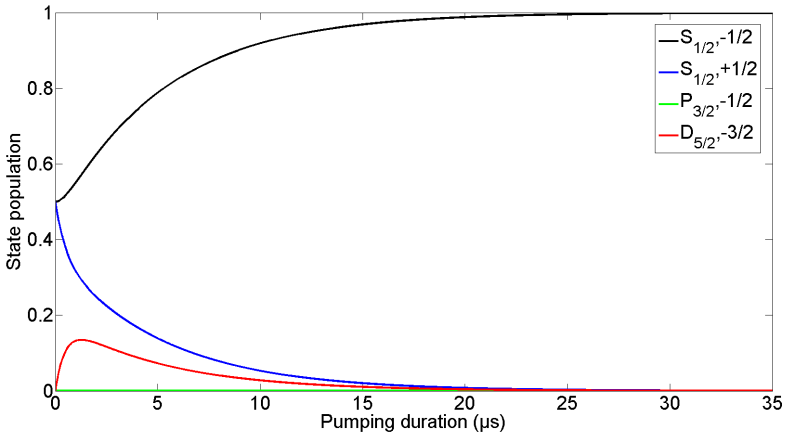

Figure 3.2.: Numerical simulation of the populations in $|D_{5/2}, -3/2\rangle$, $|P_{3/2}, -1/2\rangle$, and both ground states $|S_{1/2}, \pm 1/2\rangle$ during optical pumping in a simplified four-level system. The Rabi frequencies for the simulation were $\Omega_{729} = 2\pi \cdot 177\,\text{kHz}$ and $\Omega_{854} = 2\pi \cdot 344\,\text{kHz}$. We assume a balanced initial population in the ground states. The Clebsch-Gordan coefficients for the decay from $|P_{3/2}, -1/2\rangle$ to $S_{1/2}, \pm 1/2\rangle$ were taken into account.

The pumping efficiency is limited by off-resonant coupling to neighboring transitions.

3.3. Coherent manipulations

Optical pumping prepares the atom in a pure quantum state that forms the basis for further applications. The ability for coherent manipulation of the system plays a key role in most protocols. Over time, we have developed an elaborate quantum-mechanical tool box for these tasks which will be presented in the following sections.

3.3.1. Atomic single-qubit rotations

Despite involving some theory, understanding the atomic dynamics is of particular importance for the experimenter to gain control over its system[7]. Here we will concentrate on the effect of coherent resonant and off-resonant excitation of an ideal two-level system. Spontaneous emission is neglected for now since it plays no role in the context of quadrupole and RF transitions that are discussed later in the chapter.

[7] and, of course, also to tackle the various problems that appear in the course of an experiment.

First we treat resonant state rotations and will later see how off-resonant excitation is easily incorporated. Coherent manipulation of a single-qubit quantum state is described by rotations of the quantum-state vector on the Bloch sphere which is a representation of the states that span the one-qubit Hilbert space.

Coherent (near-)resonant excitation in the atomic reference frame (e.g. by a coherent laser field or RF drive) is described by the rotation operator

$$\begin{aligned} \hat{R}(\theta,\phi) &= \exp\left(-\frac{i}{\hbar}\vec{\theta}\vec{S}\right) = \exp\Big(-i\frac{\theta}{2}\underbrace{(\cos\phi\,\sigma_x + \sin\phi\,\sigma_y)}_{\hat{\Sigma}}\Big)\,, \text{with} \\ \vec{\theta} &= \theta\begin{pmatrix}\cos\phi\\ \sin\phi\\ 0\end{pmatrix}\,, \vec{S} = \frac{1}{2}\hbar\vec{\sigma}\,, \vec{\sigma} = \begin{pmatrix}\sigma_x\\ \sigma_y\\ \sigma_z\end{pmatrix}\,, \end{aligned} \tag{3.11}$$

acting on the (pure) qubit state $|\psi\rangle_0 = \cos\frac{\vartheta}{2}|0\rangle + e^{i\varphi}\sin\frac{\vartheta}{2}|1\rangle$. $\sigma_{x,y,z}$ are the Pauli matrices. The angle ϕ defines the orientation of the rotation axis in the equatorial plane of the Bloch sphere and θ determines the rotation angle around that axis (see fig. 3.3). In vector representation, the states $|0\rangle$ and $|1\rangle$ are written as $|0\rangle = \begin{pmatrix}1\\0\end{pmatrix}$ and $|1\rangle = \begin{pmatrix}0\\1\end{pmatrix}$.

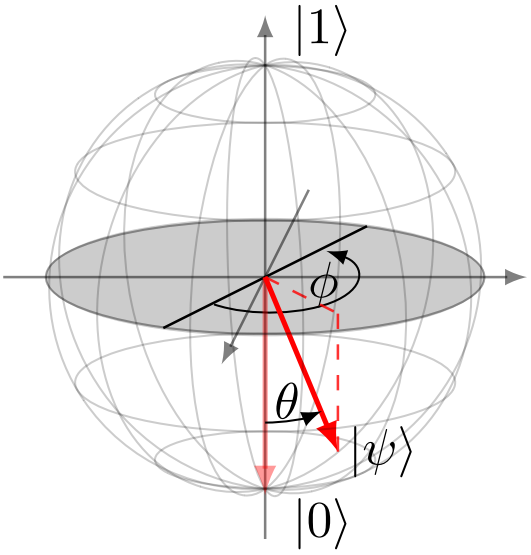

Figure 3.3.: Depiction of a state rotation on the Bloch sphere. The angle ϕ defines rotation axis in the equatorial plane, θ determines the rotation angle along that axis.

To study the effect of $\hat{R}$ on $|\psi\rangle_0$, we first rewrite $|\psi\rangle_0$ in terms of the eigenvectors of $\hat{\Sigma}$, $|s_1\rangle$ and $|s_2\rangle$:

$$\begin{aligned} |0\rangle &= \gamma_1|s_1\rangle + \gamma_2|s_2\rangle\,, & \gamma_1,\gamma_2 \in \mathbb{C} \\ |1\rangle &= \delta_1|s_1\rangle + \delta_2|s_2\rangle\,, & \delta_1,\delta_2 \in \mathbb{C}\,. \end{aligned}$$

With the eigenvalues E_1, E_2 of $\hat{\Sigma}$ defined as

$$\hat{\Sigma}|s_1\rangle = E_1|s_1\rangle \,,$$
$$\hat{\Sigma}|s_2\rangle = E_2|s_2\rangle$$

we get

$$\hat{R}|s_1\rangle = e^{-i\frac{\theta}{2}E_1}|s_1\rangle \,,$$
$$\hat{R}|s_2\rangle = e^{-i\frac{\theta}{2}E_2}|s_2\rangle$$

and hence

$$\begin{aligned}\hat{R}|\psi\rangle_0 &= \hat{R}\left(\cos\frac{\vartheta}{2}|0\rangle + e^{i\varphi}\sin\frac{\vartheta}{2}|1\rangle\right)\\ &= \hat{R}\left(\cos\frac{\vartheta}{2}\gamma_1|s_1\rangle + \cos\frac{\vartheta}{2}\gamma_2|s_2\rangle + e^{i\varphi}\sin\frac{\vartheta}{2}\delta_1|s_1\rangle + e^{i\varphi}\sin\frac{\vartheta}{2}\delta_2|s_2\rangle\right)\\ &= e^{-i\frac{\theta}{2}E_1}\left(\cos\frac{\vartheta}{2}\gamma_1 + e^{i\varphi}\sin\frac{\vartheta}{2}\delta_1\right)|s_1\rangle + e^{-i\frac{\theta}{2}E_2}\left(\cos\frac{\vartheta}{2}\gamma_2 + e^{i\varphi}\sin\frac{\vartheta}{2}\delta_2\right)|s_2\rangle \,.\end{aligned} \tag{3.12}$$

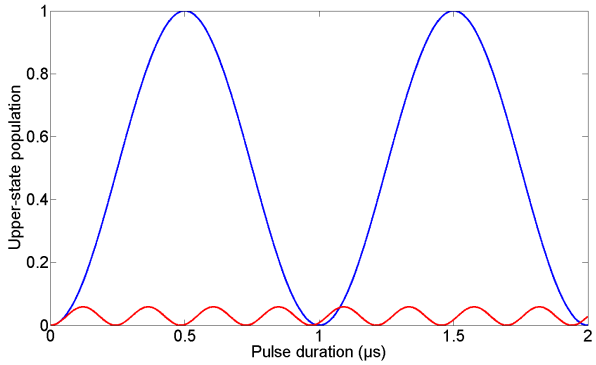

Figure 3.4.: The plot shows a simulation of a resonant single-qubit rotation (blue) with Rabi frequency $\Omega = 2\pi \cdot 1\,\mathrm{MHz}$, and an off-resonant excitation at the same Rabi frequency but detuned by $\Delta = 4\,\Omega$ (red). The off-resonant driving exhibits a fast oscillation of significantly decreased amplitude.

Eq. (3.12) is true for resonant excitation. Including off-resonant driving of the transition is simply included by making ϑ and φ (and consequently also $|s_1\rangle$ and $|s_2\rangle$) time-dependent. The time-derivative is directly given by the relation $\frac{d\vartheta}{dt} = \Omega$ with the resonant Rabi frequency Ω, while the rotation axis defined by φ oscillates in the equatorial plane. The time-varying oscillation angle depends on the detuning Δ via $\varphi(t) = \varphi_0 + \Delta \cdot t$. The system dynamics of an initial state are then deduced from these quantities. A simulation of the temporal evolution of the populations for resonant and off-resonant excitation is shown in fig. 3.4.

3.3.2. Coherent manipulations on the optical quadrupole transition

Coherent manipulations on the narrow qubit transition at 729 nm pose a very important tool for state preparation and state analysis. For the success of our protocols it is crucial to have very good control over these laser pulses and their effect on the ion.

Here we adapt the theory developed in the previous section to optical manipulations of the real system and investigate their influence onto the state dynamics. For that purpose, we prepare the ion in a defined magnetic quantum state, i.e. a specific m-state, perform a state-rotation pulse of varying length or power and read out the result by means of fluorescence detection.

Starting in a specific m-state in $S_{1/2}$, e.g. $|S_{1/2}, -1/2\rangle$, the population transfer to $D_{5/2}$ after a time τ is given by the covered pulse area $\Omega_{729} \cdot \tau$ via $p_D = \sin^2(\frac{\Omega_{729}}{2}\tau)$ with the Rabi frequency

$$\Omega_{729} = \gamma \cdot \sqrt{\frac{A_{S\to D}^2\, I_{729}}{2\, I_{\text{sat}}}} \tag{3.13}$$

on that transition. As before, $A_{S\to D} = 2\pi \cdot 136\,\text{mHz}$ is the Einstein coefficient for the $S_{1/2} \to D_{5/2}$ quadrupole transition, where the factor γ accounts for the Clebsch-Gordan coefficient on that specific transition (e.g. $|S_{1/2}, -1/2\rangle \leftrightarrow |D_{5/2}, -5/2\rangle$). I_{729} is the laser intensity at the ion and

$$I_{\text{sat}} = \frac{A_{S\to D}}{6}\frac{\hbar c}{\lambda^3} \tag{3.14}$$

is the saturation intensity of the transition. Full state transfer is performed after a pulse duration $\tau_\pi = \pi/\Omega_{729}$ (a "π pulse"). In the experiment, we usually work with a π-pulse time of 10 µs which has proven to be a good trade-off between transfer infidelity and relatively fast gate times.

To maintain the timings during the experiment, instead of scanning the pulse length, in fact the pulse duration τ is kept fix while the pulse amplitude (and hence Ω_{729}) is varied. Such a pulse-amplitude scan is presented in fig. 3.5. Optimal pulse amplitude and transfer efficiency are deduced from a fit to the data.

3.3.3. Coherent manipulations on the radio-frequency transition

Coherent manipulations on the Zeeman-split ground-state qubit in $S_{1/2}$ can be conducted by far-detuned optical Raman pulses on an electrical dipole transition [140]. In our case, we decided to directly drive the transition with the help of a magnetic RF field that is produced by a magnetic-field coil located beneath the vacuum chamber. The applied RF drive is tuned to the resonance frequency of the ground-state transition at about 8 MHz. This approach has the advantage that it is very robust and easy to control, as amplitude, frequency, duration and phase of the RF pulse are easily adjusted. Scanning the pulse-frequency over the transition reveals the resonance frequency, optimal pulse parameters for the targeted state rotation are obtained similarly to the procedure described in section

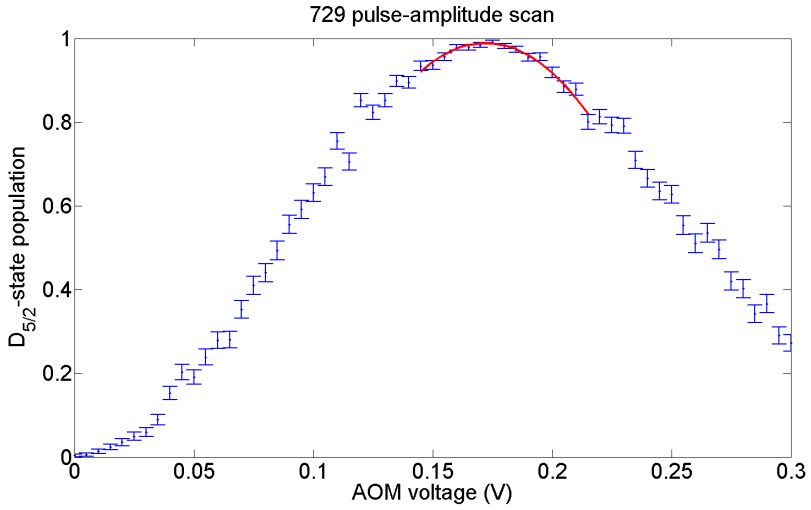

Figure 3.5.: Scan of the AOM amplitude the for a pulse resonant on the $|S_{1/2}, +1/2\rangle \rightarrow |D_{5/2}, +3/2\rangle$ transition while the pulse duration is fixed. The $D_{5/2}$ population after the optimal pulse is typically in the order of 99%, which, accounting for the pumping efficiency of 99.6%, yields a transfer efficiency of approximately 99.4%.

3.3.2, except for another "shelving" pulse at 729 nm at the end of the RF pulse. This pulse transfers the population in one of the $S_{1/2}$ Zeeman sublevels into the "dark" (i.e. decoupled from the cooling lasers and therefore dark during fluorescence detection) $D_{5/2}$ manifold. This shelving pulse is necessary for the fluorescence-based state read-out following the RF rotation.

With this technique, we achieve π-pulse times of up to 5 µs (or 2.5 µs for a $\frac{\pi}{2}$ basis-rotation pulse, mentioned in section 3.4). Again, we rather scan the RF amplitude instead of the pulse duration to obtain the optimal timing in the experimental sequences. Fig. 3.6 shows the result of a typical RF pulse-amplitude scan as performed on a daily basis in the laboratory.

3.3.4. Light shift

In section 3.3.1 we assumed the energy splitting between the eigenstates of the qubit system to be constant, hence the σ_z rotation was disregarded. However, in reality, driving a two-level system off-resonantly results in a shift of the energy levels caused by the AC Stark effect, depending on detuning Δ and (carrier) Rabi frequency Ω of the driving field, that gives rise to an additional σ_z term in the Hamiltonian describing the system. This can be understood quite intuitively: The time-dependent phase of a superposition of the eigenstates is determined by the energy difference between these states. Therefore, a change in this energy splitting results in an additional phase after a given time which corresponds to a σ_z rotation on the Bloch sphere.

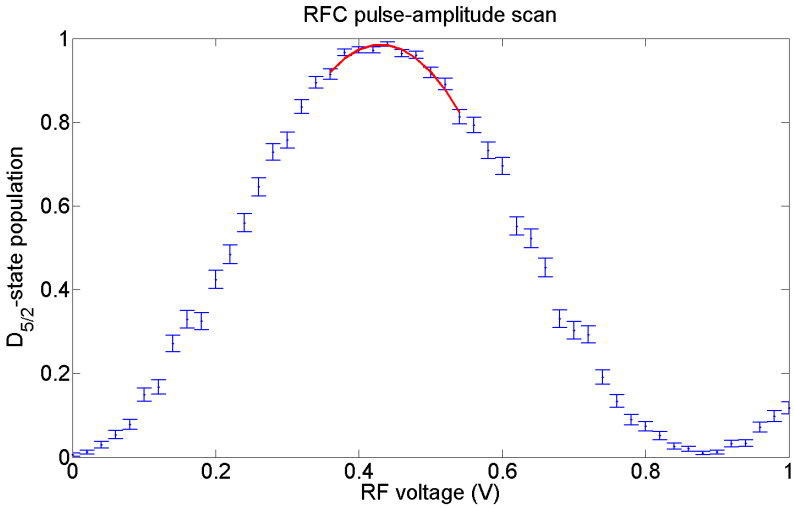

Figure 3.6.: Result of an RF pulse-amplitude scan. The maximum $D_{5/2}$ population in this scan was 98.5%. Taking pumping and shelving efficiencies into account, this corresponds to a transfer efficiency of 99.5% for the RF pulse.

The magnitude of this light shift is described by the expression [141]

$$\Delta_{AC} = -\frac{\Delta}{2} + \frac{\operatorname{sgn}\Delta}{2\sqrt{2}}\sqrt{\tilde{\Omega}^2 - \frac{\Gamma^2}{4} + \sqrt{\left(\tilde{\Omega}^2 - \frac{\Gamma^2}{4}\right)^2 + \Delta^2\Gamma^2}}, \tag{3.15}$$

with the effective Rabi frequency $\tilde{\Omega} = \sqrt{|\Omega|^2 + \Delta^2}$ and the natural transition linewidth Γ. Avoidance of unwanted excitation on the carrier is guaranteed by the condition $\Delta \gg \Omega, \Gamma$ and is necessary to achieve a pure σ_z gate.

Assuming a Rabi frequency of $\Omega = 10\,\mathrm{kHz}$, a detuning of $\Delta = 100\,\mathrm{kHz}$ and a linewidth of $\Gamma = 2\pi \cdot 136\,\mathrm{mHz}$, a phase shift of π is accumulated after a time $\tau = 1\,\mathrm{ms}$ which corresponds to a "flipping" of a superposition state in the equatorial plane.[8]

An experimental implementation of this technique is presented in chapter 7.

3.4. Atomic state analysis by fluorescence detection

Atomic state analysis usually represents the last element of an experimental cycle. In the context of our setup, it is conducted by an optional basis-rotation pulse followed by state-dependent fluorescence generation. The basis rotation is required for a full quantum-state tomography, where measurements in the σ_z basis are not sufficient. Measurements in the σ_x-σ_y bases (i.e. the superposition bases) are realized by applying a $\frac{\pi}{2}$ radio-frequency pulse prior to the state discrimination to translate the superposition phase into population of

[8] Remember that the energy shift acts on both levels in opposite direction, hence the factor of 2.

the energy eigenstates. If the qubit is encoded into an other state than the ground-state superposition, it is coherently transferred to $S_{1/2}$ before the further analysis. Fluorescence-based internal-state discrimination is facilitated by shelving the population in one of the two $S_{1/2}$ states (usually the $|+1/2\rangle$ population) into the dark $D_{5/2}$ manifold.

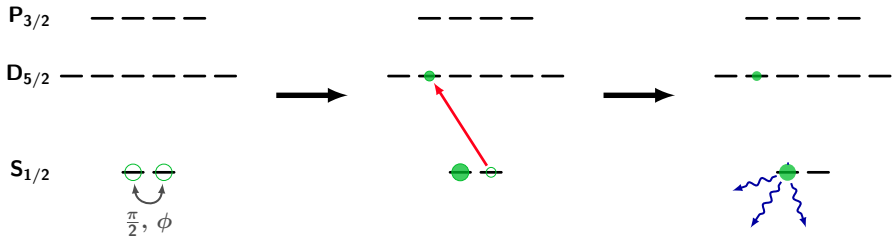

Figure 3.7.: Atomic state analysis in the ground-state qubit. If measured in a superposition basis, an (optional) radio-frequency rotation pulse, mapping the superposition phase onto the population of $|\pm 1/2\rangle$, is applied. Subsequently, a 729 nm pulse shelves the $|+1/2\rangle$ population to $D_{5/2}$. State discrimination is then performed by fluorescence detection at 397 nm under excitation with the 397nm and 866nm lasers. If the qubit is encoded in a different state (e.g. a superposition in the $D_{5/2}$ manifold), it is coherently transferred to the ground state beforehand.

Fluorescence detection itself is carried out by switching on the cooling lasers (at higher power to increase the scattering rate) and detecting the scattered 397 nm photons with a photo-multiplier tube. The fluorescence is integrated for a time τ_{int} with typical values of $\tau_{\text{int}} = 100\,\mu\text{s}$. The integrated number of counts allows for a decision whether the ion stayed in the (bright) ground state after the shelving pulse or is projected onto the (dark) $D_{5/2}$ manifold. If in $S_{1/2}$, the ion exhibits a detected fluorescence rate r_b between 135 000 and 150 000 $1/\text{s}$, while the detected dark rate r_d, consisting of detector dark counts and laser stray light, is about 100 $1/\text{s}$. The probabilistic nature of the process yields a distribution of the detected counts as illustrated in fig. 3.8.
To distinguish between both results we define a threshold n_{th} up to which the result counts as dark, i.e. the ion is assumed to be in the dark state which is decoupled from the exciting laser. If the number of detection events exceeds that threshold, the ion is assumed to be in the corresponding bright state. The goal is to find the threshold for which the decision error is minimized for a given integration time.

The error estimation is based on [79]. For integration times small compared to the natural life time of $D_{5/2}$, i.e. where we assume that the ion stays in the dark state over the whole integration process[9], and assuming no a-priori information on the atomic state and uniform temporal distribution of the detection events, the decision error is approximated as

$$\varepsilon = \frac{1}{2}\Big(F(n_{\text{th}}, \langle n_b\rangle) + \big(1 - F(n_{\text{th}}, \langle n_d\rangle)\big)\Big) \tag{3.16}$$

with the expectation values $\langle n_b\rangle = r_b\tau_{\text{int}}$ and $\langle n_d\rangle = r_d\tau_{\text{int}}$ for the number of detected

[9] a treatment including decay of the dark state is presented in [79]

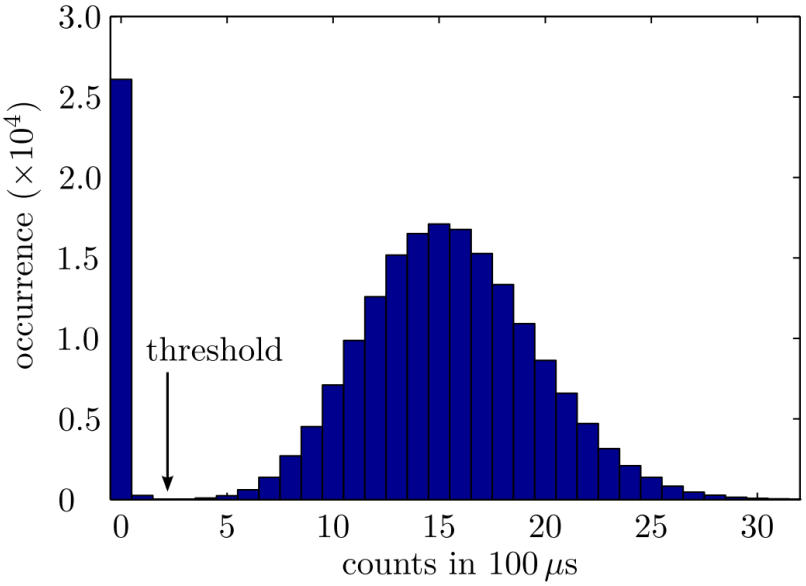

Figure 3.8.: Distribution of accumulated detection events for 100 µs integration time and bright and dark count rates of 155 000 $^1/_s$ and 100 $^1/_s$, respectively (overlayed for illustration). The computation of the optimal threshold for state distinction is discussed in the main text. (From [77])

counts in the bright and dark case and the Poisson cumulative distribution function

$$F(n_{\text{th}}, \langle n \rangle) = e^{-\langle n \rangle} \sum_{k=0}^{n_{\text{th}}} \frac{\langle n \rangle^k}{k!} \tag{3.17}$$

which describes the probability of detecting less than $n_{\text{th}} + 1$ events for a Poissonian distribution that exhibits a mean of $\langle n \rangle$ events.

For typical experimental parameters $r_b = 140\,000\,^1/_s$, $r_d = 100\,^1/_s$ and $\tau_{\text{int}} = 100\,\mu s$, we obtain an optimal threshold $n_{\text{th}} = 1$ with a decision error $\varepsilon = 3.4 \cdot 10^{-5}$.

For a reliable estimation of the populations in a certain basis, the experimental sequence followed by fluorescence detection described above is repeated a number of times. From the outcome of this experiment (k dark results) we deduce the probability p to find the atom in the dark state, that is, the probability that p correctly reproduces the observed result. Given k dark decisions, this yields the probability distribution

$$P(p|k) = \frac{P(k|p)\,P(p)}{P(k)}\,, \tag{3.18}$$

where we deployed Bayes theorem. $P(p)$ denotes the probability that p correctly describes the system. Without any initial knowledge, all p are equally probable and we set $P(p) = \text{const.} = 1$. The probability for finding k dark events, $P(k)$, is expressed as the

probability for k findings given an underlying probability p, $P(k|p)$, weighted with $P(p)$ and integrated over all p,

$$P(k) = \int_0^1 P(k|p)\, P(p)\, dp\,. \tag{3.19}$$

The probability $P(k|p)$ is described by the binomial distribution

$$P(k|p) = \binom{n}{k}\, p^k\, (1-p)^{n-k} \tag{3.20}$$

for k dark events out of n measurements.

With eq. (3.19) and (3.20), (3.18) is rewritten as

$$P(p|k) = \frac{\binom{n}{k}\, p^k\, (1-p)^{n-k}}{\binom{n}{k} \int_0^1 p^k\, (1-p)^{n-k}\, dp} = \frac{p^k\, (1-p)^{n-k}}{\int_0^1 p^k\, (1-p)^{n-k}\, dp}\,. \tag{3.21}$$

Inserting

$$\int_0^1 p^k\, (1-p)^{n-k}\, dp = \frac{\Gamma(k+1)\,\Gamma(n-k+1)}{\Gamma(n+2)} \tag{3.22}$$

with the Γ function

$$\Gamma(x) = (x-1)! \tag{3.23}$$

we obtain

$$P(p|k) = \frac{(n+1)!}{k!\,(n-k)!}\, p^k\, (1-p)^{n-k}\,. \tag{3.24}$$

From that result he expectation value for p is determined:

$$\begin{aligned} \langle p \rangle &= \int_0^1 p\, P(p|k)\, dp = \int_0^1 p\, \frac{(n+1)!}{k!\,(n-k)!}\, p^k\, (1-p)^{n-k}\, dp \\ &= \frac{(n+1)!}{k!\,(n-k)!} \int_0^1 p^{k+1}\, (1-p)^{n-k}\, dp = \frac{(n+1)!}{k!\,(n-k)!}\, \frac{(k+1)!\,(n-k)!}{(n+2)!} \\ &= \frac{k+1}{n+2} \end{aligned} \tag{3.25}$$

with the standard deviation

$$\Delta p = \sqrt{\langle p^2 \rangle - \langle p \rangle^2}\,, \tag{3.26}$$

where

$$\begin{aligned}\langle p^2 \rangle &= \frac{(n+1)!}{k!\,(n-k)!} \int_0^1 p^{k+2}\,(1-p)^{n-k}\,dp = \frac{(n+1)!}{k!\,(n-k)!}\,\frac{(k+2)!\,(n-k)!}{(n+3)!} \\ &= \frac{(k+2)(k+1)}{(n+3)(n+2)}\,.\end{aligned} \tag{3.27}$$

Equations (3.25)-(3.27) allow for the estimation of the state populations and the respective reliability for that value. As a consequence, (3.25)-(3.27) are used to compute the required number of measurement repetitions for a given desired confidence interval of the result.

3.5. Zeeman splitting and Larmor phase

The quantization axis in the present experiment is defined by a constant magnetic field aligned along the HALO axis. A collateral effect is the splitting of the respective substates of the level manifolds according to their magnetic moment in the external field due to the Zeeman effect. The frequency shift for a state of magnetic quantum number m in a field of magnitude B is given by the well-known formula

$$\Delta\nu_{\text{Zeeman}} = \frac{\mu_B}{h} \cdot g \cdot m \cdot B \tag{3.28}$$

with the Landé factor g, depending on the state manifold, and the Bohr magneton μ_B. For the $S_{1/2}$ ground state, with a Landé factor of $g \approx 2$ and magnetic quantum numbers $m = \pm 1/2$, a magnetic field of $B = 2.8\,\text{G}$ results in a ground-state splitting $\Delta\nu = 7.84\,\text{MHz}$, defining the qubit frequency. Lifting the frequency degeneracy enables coherent qubit manipulation by RF pulses resonant with the ground-state transition.

A superposition of states $|0\rangle$ and $|1\rangle$ with energies E_0 and E_1 exhibits a phase that precesses with the Larmor frequency $\omega_L = \frac{E_1 - E_0}{\hbar}$.

The radio frequency, tuned to the ground-state transition, serves as reference frame in the experiment that rotates with the atomic qubit frequency in $S_{1/2}$. However, if a distortion of the local magnetic field causes fluctuations of the qubit frequency which the experimenter is not aware of, the reference oscillator will start to rotate out of phase, causing decoherence of the system (see section 3.6).

If the qubit is encoded in a different superposition than the ground state, it acquires an additional Larmor phase according to the difference in the respective frequency splittings, until it returns to the ground state. Therefore, the precise instant of the transfer to the $S_{1/2}$ qubit has to be known so the additional phase can be taken into account for further processing. The time-dependent Larmor phase is reflected as an oscillatory behavior of the populations in $|S_{1/2}, \pm 1/2\rangle$ after the basis-rotation pulse as a function of the return time to the ground state.

3.6. Coherence time

Quantum information can only be stored as long as the coherence time of a quantum memory permits. Therefore, for larger quantum networks it is essential to obtain long coherence times to ensure reliable operation.

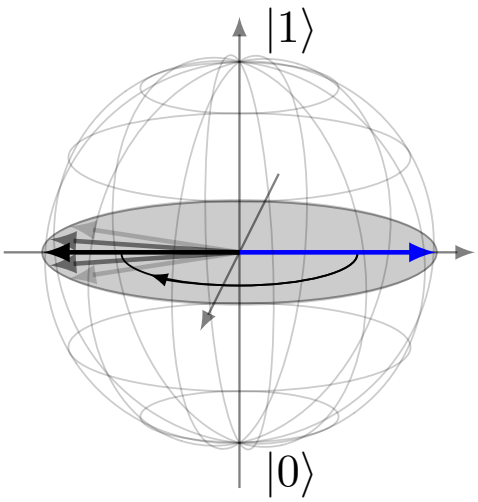

Figure 3.9.: Illustration of decoherence due to magnetic-field fluctuations. The B-field noise induces a fluctuating energy splitting between the qubit states, causing the phase of an atomic superposition (depicted as state vector on the Bloch sphere) to oscillate at different frequencies and thus to accumulate differing phases over time. If these phase deviation are unknown to the experimenter, they add up incoherently and drag the atomic state vector towards the origin of the sphere, i.e. towards a mixed state.

Decoherence, in a sense, describes the loss of knowledge over the collective quantum state of a system, e.g. due to undetected scattering of photons that carry information about the physical state, or unknown perturbations of the system Hamiltonian. In our case, the storage time of quantum information is primarily limited by the latter effect. In particular, a fluctuating local magnetic field leads to a fluctuation of the energy levels due to the Zeeman effect and thus to an additional unknown phase contribution to the superposition state in the qubit subspace, reducing the purity of the outcoming state, as depicted in fig. 3.9.

The main sources of B-field noise are the electronic overhead surrounding the trap table and noise on the current through the field coils, delivered by a DC power supply. The magnetic-field noise can be decomposed into two contributions, white noise and harmonically oscillating variations at 50 Hz and higher harmonics thereof. The latter manifests as Bessel "bumps" in visibility–vs.–waiting-time plot of Ramsey-type scans (see fig. 3.10) and is eliminated by applying a phase-shifted field of the same frequency and magnitude. A more extensive discussion of both types of B-field noise and their effect onto the coherence time is found in [77].

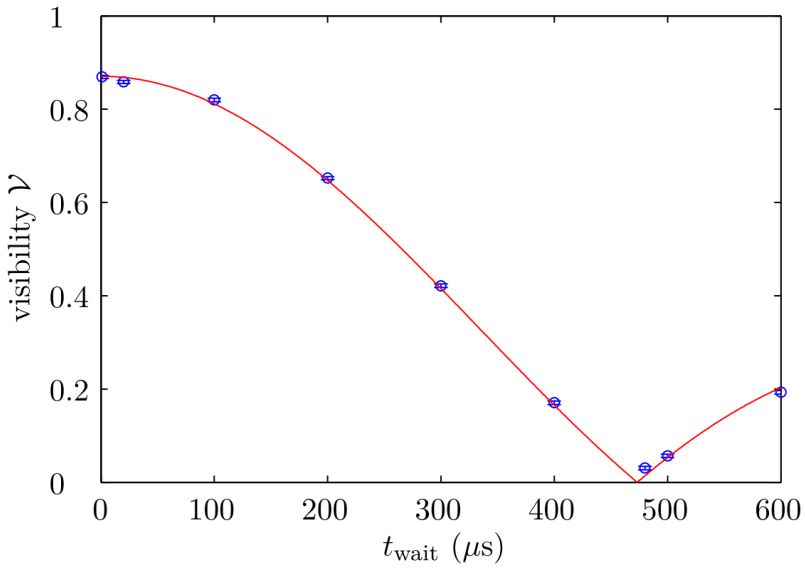

Figure 3.10.: Visibility vs. waiting time for a series of RF Ramsey scans from the "ancient days" (taken from [77]) when no B-field–noise elimination was used. The T_2^* coherence time was measured to be 279(9) µs. The Bessel fringes for higher waiting times are clearly visible.

A convenient way to deduce the coherence time is provided by a Ramsey experiment (or rather a series of Ramsey experiments). A Ramsey experiment or Ramsey phase scan consists of four steps, illustrated also in fig. 3.11. First, the ion is initialized in an energy eigenstate by optical pumping, for instance in $|0\rangle = |S_{1/2}, m = -1/2\rangle$, followed by a $\frac{\pi}{2}$ pulse of defined phase φ_0 that rotates the state into a symmetric superposition $|0\rangle + e^{i\varphi_0}|1\rangle$ on the equatorial plane of the Bloch sphere. For simplicity we assume $\varphi_0 = 0$. The superposition now evolves for a time τ_{Ramsey}, where it might pick up an undesired phase deviation caused by perturbations of the energy distance between $|0\rangle$ and $|1\rangle$. Subsequently a second $\frac{\pi}{2}$ pulse with variable phase φ is applied. The phase offset between atomic superposition and second pulse determines the resulting rotation. Fluorescence detection finally reveals the population in $S_{1/2}$ and $D_{5/2}$, respectively (explained in the previous section).

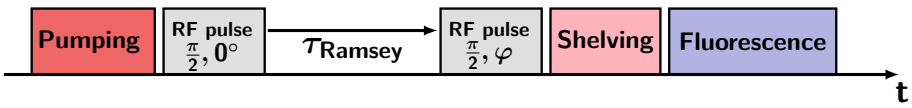

Figure 3.11.: Schematic visualization of a Ramsey sequenced as explained in the main text. The outcome of this Ramsey-type measurement is shown in fig. 3.12.

Scanning the phase of the second pulse with respect to the first one exposes an oscillatory behavior of the excited-state population (fig. 3.12) whose visibility depends on the coherence.

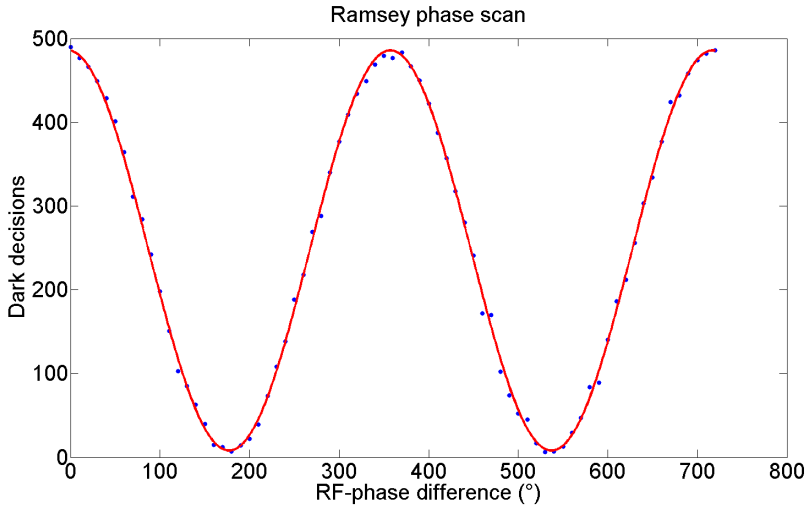

Figure 3.12.: Ramsey-type phase scan on the RF transition in $S_{1/2}$ for a waiting time of 10 µs between the consecutive RF pulses and 500 repetitions per phase point. Shown is the number of dark decisions after the shelving pulse. The slight imbalance derives from imperfect pumping and shelving.

The coherence time is then estimated by a series of these Ramsey phase scans for differing waiting times (fig. 3.10 and 3.13). We achieve a distinct increase of coherence by compensating for periodic magnetic-field noise at 50 Hz and higher harmonics, originating from the power line, by installing an additional feed-forward coil along the quantization axis. The coil is driven by an AC current at 50 Hz and 150 Hz, phase-locked to the power line, with adjustable amplitude and phase. Amplitude and phase are then optimized by maximizing the visibility of the Ramsey fringes for a particular waiting time on the first negative slope of a signal as the one shown in fig. 3.10. Detail on the feed-forward technique is found in the Master's thesis of Matthias Kreis [133] who was responsible for the conception and realization.
Applying this feed-forward technique increases the coherence time in the ground-state qubit from values as low as ≈ 200 µs to values of typically about 700 µs (as seen in fig. 3.13) or sometimes even up to 1 ms[10].

The experimental tools deduced in this chapter are widely used in the work presented in the following. Doppler cooling is employed for trapping of the ion and preparation of the thermal state that allows for coherent manipulation on the optical qubit transition and as such builds the backbone of all experiments demonstrated here. The frequency-selective optical-pumping scheme developed in the course of this thesis allows pure-state preparation of the ion independent of the spatial orientation of the (quadrupole-transition) pumping beam and forms an essential block for the quantum interface presented in chapter

[10] the actual coherence time varies from day to day and seems to depend on the overall noise on the power line, as we experienced longer coherence times on the weekends.

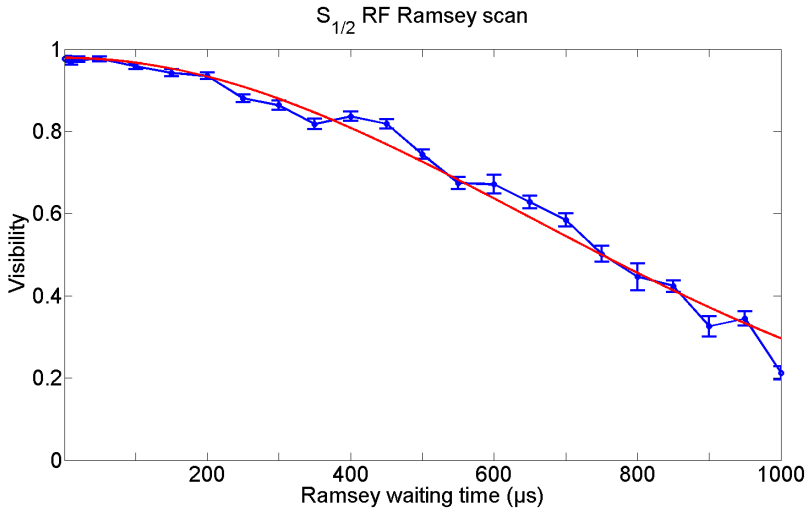

Figure 3.13.: Visibility vs. waiting time nowadays. The feed-forward compensation for magnetic-field–noise cancellation was switched on, improving the coherence time to 647(11) µs.

5 and the two-ion quantum gate (chapter 7). Coherent manipulations of the atomic qubit, either on the optical quadrupole or on the radio-frequency ground-state transition, are, in a sense, the basic tool in in our toolbox. Reliable single-qubit rotations are used for coherent-state preparation and state analysis and are therefore encountered in all of the following chapters. Future multi-ion protocols like ion-to-ion quantum-state teleportation will need (laser-phase independent) single-qubit operations in a string of two or more ions. For the implementation of the latter, we employed a scheme based on the shift of the transition frequency caused by coupling onto a light field as described in section 3.3.4. The according measurements are demonstrated in section 7.1.2. Each of the experiments shown in this work requires fluorescence-based atomic state analysis[11] described in 3.4. Prediction and reconstruction of the atomic dynamics as needed for all experimental results, presented in the chapters 5, 6, and 7, requires the understanding of the magnetic-field dependent splitting of the atomic energy levels, treated in 3.5. Finally, the ability to store quantum information or preserve entanglement in the present experiments is limited by the atomic coherence time. The mechanism for coherence-time reduction, the Ramsey phase scan as a tool for the determination of the current coherence time and measures for its improvement are briefly depicted in 3.6.

[11] Either for the evaluation of the viability of the respective operations or as part of the protocol itself, e.g. as a projective measurement.

4. Single-atom–single-photon interaction

Large-scale quantum networks, based on stationary qubits represented by atomic quantum memories for quantum-information storage and processing, and photonic quantum channels between these nodes, inherently require atom-photon interfaces that act as interconnections between flying qubits and their stationary counterpart. Therefore, accurate control over single-photon–emission and absorption processes with high fidelity is of vital interest for every future quantum-network architecture.
Understanding these processes is the key to gaining control over them and thus an essential element in the realization of a single-atom–single-photon–based quantum interface.

This chapter has two goals in particular. First, we would like to understand the process of spontaneous Raman scattering in a three-level system as an adequate model for the dynamics of the real system and develop a quantum-mechanical model for the absorption and emission of single photons by a single atomic ion. We will encounter the results of this analysis again in chapters 5 and 6 when we estimate the influence of undesired atomic decay on the final quantum state. Hence, the first part of this chapter treats spontaneous Raman scattering of a single photon in a simplified three-level model and investigates the temporal and spectral properties of the emitted photon.
The estimation of the single-process success probability for the experiments conducted in the course of this thesis, i.e. atom-to-photon state transfer, photon-to-atom state transfer, and atom-photon entanglement in chapters 5 and 6, requires knowledge about the photon collection efficiencies and, in that context, to find an analytical expression for the emission properties of an optical dipole. This represents the second goal of the present chapter. For that purpose, the absorption and emission properties of optical dipole transitions, their spatial dependence and the influence on the photon polarization is discussed in the second part of this chapter. We will derive an expression for multi-mode and single-mode photon-coupling efficiency for different atomic transitions and evaluate this expression for our experimental parameters to find the expected values in our implementation. In addition, the effect of the finite solid angle of the HALO lenses for both cases, single- and multi-mode or free-space coupling, onto the final state is discussed.

The formulation of the three-level spontaneous Raman scattering has been treated in a similar way by Michael Schug in his dissertation thesis and builds the basis for section 4.1. The calculation of the dipole-emission characteristics is inspired by the treatment in the same thesis and has been extended to complex fields and single-mode coupling for this work. The quantum-mechanical description of the single-photon emission and absorption process was originally developed by Philipp Müller and is published in [142].

4.1. Spontaneous Raman scattering in a three-level system

In most of our protocols, the atomic dynamics is well approximated by that of a three-level system in Λ configuration, which allows us to develop a simple model for the temporal behavior of the system. The Λ configuration consists of a high-lying, short-lived excited state, representing $P_{3/2}$, and two stable, low-lying ground states, representing either $S_{1/2}$ and $D_{5/2}$, or two Zeeman sublevels in $D_{5/2}$. The treatment of $D_{5/2}$ as a stable state is justified by its lifetime of more than 1 s which is large compared to the typical time scales involved in the dynamics of the system.

The evolution of atomic populations, more precisely the population of the excited state, reflects the temporal properties of the single Raman-scattered photon. The population dynamics, and hence the photonic wave packet, is modeled by means of three-level rate equations that will then be solved numerically, inspired by the treatment in [78].

In the present experiment, we will encounter three excitation schemes,

(1.) initial preparation of the ion in $D_{5/2}$, excitation to $P_{3/2}$, and generation of a single 393 nm photon on the $P_{3/2}$-to-$S_{1/2}$ transition,

(2.) initial preparation of the ion in $S_{1/2}$, excitation to $P_{3/2}$, and generation of a single 854 nm photon on the $P_{3/2}$-to-$D_{5/2}$ transition, and

(3.) initial preparation of the ion in $D_{5/2}$, excitation to $P_{3/2}$, and generation of a single 854 nm photon on the $P_{3/2}$-to-$D_{5/2}$ transition,

that will be discussed in the following.

For the **generation of single 393 nm photons (1.)**, the ion is initialized in $D_{5/2}$. A laser at 854 nm continuously excites the population to $P_{3/2}$ with the transfer rate r_{854} (fig. 4.1 (a)). From there it decays to the ground state $S_{1/2}$ with rate A_{393} by emitting a photon at 393 nm or back to $D_{5/2}$ with rate A_{854}. In addition, the stimulated transfer from $P_{3/2}$ back to $D_{5/2}$ must be taken into account. The resulting rate equations for the populations p_S, p_P and p_D for $S_{1/2}$, $P_{3/2}$ and $D_{5/2}$ are then derived as

$$\frac{d}{dt}\, p_S(t) = A_{393}\, p_P(t)\,, \tag{4.1}$$

$$\frac{d}{dt}\, p_P(t) = -(A_{393} + A_{854} + r_{854})\, p_P(t) + r_{854}\, p_D(t)\,, \tag{4.2}$$

$$\frac{d}{dt}\, p_D(t) = -r_{854}\, p_D(t) + A_{854}\, p_P(t) + r_{854}\, p_P(t)\,. \tag{4.3}$$

These rate equations are fed into a numerical simulation whose result is presented in fig. 4.1 (b), where the photon-emission rate r_{Ph} is directly proportional to the evolution of p_P via $r_{Ph,393} \propto A_{393} \cdot p_P$. It should be noted that decay into and reexcitation from other $D_{5/2}$ Zeeman sublevels is omitted in the simulation and has to be taken into account in a more realistic model, where additional losses would occur due to this effect. Mainly, it leads to a reduction of the efficiency of photon generation by a few percent.

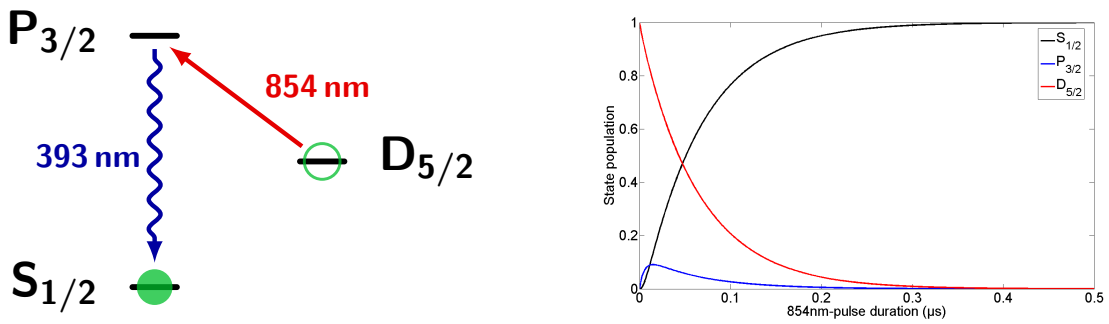

(a) (b)

Figure 4.1.: (a) Simplified level scheme for the generation of single 393 nm photons. The ion is initialized in $D_{5/2}$ and pumped into $S_{1/2}$ by applying a 854 nm laser pulse. **(b)** Temporal evolution of the populations in $S_{1/2}$ (black), $P_{3/2}$ (blue) and $D_{5/2}$ (red). The population-transfer rate r_{854} from $D_{5/2}$ to $P_{3/2}$ is chosen as $r_{854} = 2\pi \cdot 3\,\mathrm{MHz}$. The temporal shape of the 393 nm-photon wave packet is proportional to the population in $P_{3/2}$ (see main text).

The rate equations for the **generation of single 854 nm photons, starting from $S_{1/2}$ (2.)** are deduced in a similar fashion. We deploy a 393 nm laser, driving the $S_{1/2} \leftrightarrow P_{3/2}$ transition at rate r_{393}, to scatter a photon at 854 nm via decay from $P_{3/2}$ to $D_{5/2}$, as illustrated in fig. 4.2 (a). Again constraining the considerations to the three-level system, we obtain

$$\frac{d}{dt}\,p_S(t) = (A_{393} + r_{393})\,p_P(t) - r_{393}\,p_S(t)\,, \tag{4.4}$$

$$\frac{d}{dt}\,p_P(t) = r_{393}\,p_S(t) - (r_{393} + A_{393} + A_{854})\,p_P(t)\,, \tag{4.5}$$

$$\frac{d}{dt}\,p_D(t) = A_{854}\,p_P(t)\,. \tag{4.6}$$

The numerical solution for the respective populations is visualized in fig. 4.2 (b). Note that the photon length of the 854 nm photon, i.e. the decay time constant of the $P_{3/2}$ population, is substantially increased compared to the 393 nm photon for identical population-transfer rates $r_{854} = r_{393}$. This is attributed to the unequal Einstein coefficients A_{854} and A_{393}. In other words, the ion will decay back to $S_{1/2}$ several times before it eventually ends up in $D_{5/2}$. One consequence of this additional scattering is that the time-bandwidth product of the 854 nm photon will not be Fourier limited. This effect is extensively discussed in [81].

The third scheme is again the **generation of a 854 nm photon, this time starting in $D_{5/2}$ (3.)**. More precisely, we start in one of the Zeeman sublevels in $D_{5/2}$ and transfer the population into a second $D_{5/2}$ sublevel by switching on a laser at 854 nm that couples the transition from $D_{5/2}$ to $P_{3/2}$ (fig. 4.3 (a)) at rate r_{854}. It has to be mentioned that there exists an additional decay channel (shown in the previous figures), specifically the (strong) decay from $P_{3/2}$ into $S_{1/2}$ that leads to loss out of the three-level system. Therefore, this loss has

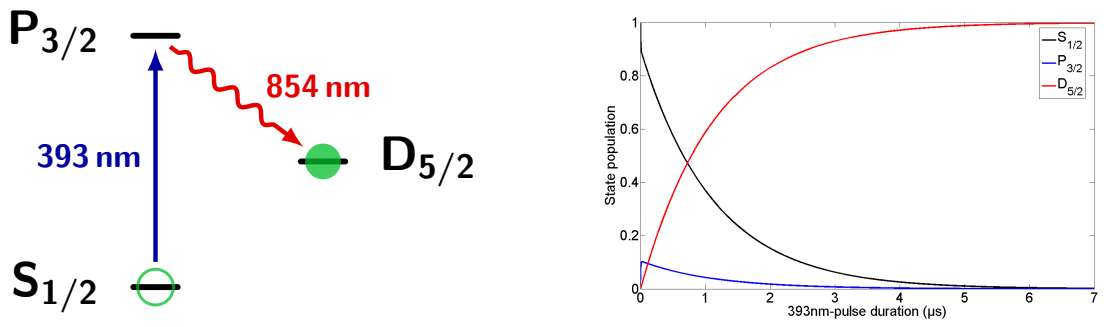

(a) (b)

Figure 4.2.: (a) The population $S_{1/2}$ is coupled to the excited, short-lived $P_{3/2}$ state via the 393 nm laser, from where it eventually decays to the meta-stable $D_{5/2}$ state by scattering a Raman photon at 854 nm. **(b)** Despite the same transfer rate $r_{393} = 2\pi \cdot 3\,\mathrm{MHz}$ of the exciting laser, the population is transferred much slower into its final state, implying an increase of the length of the Raman photon. This is traced back to the repeated decay back into the ground state before the final transfer into $D_{5/2}$, which means that the ion scatters on average a number of blue photons, corresponding to the branching ratio of both decay channels, before a red photon is emitted, repealing the Fourier limitation of the time-bandwidth product.

to be taken into account in the rate equation to reproduce reliable results. We obtain the three-level rate equations for the populations $p_{D,3/2}$, p_P, and $p_{D,5/2}$ of $|D_{5/2}, +3/2\rangle$ (initial state), $P_{3/2}$, and $|D_{5/2}, +5/2\rangle$ (final state), respectively:

$$\frac{d}{dt}\, p_P(t) = r_{854}\, p_{D,3/2} - (A_{393} + A_{854} + r_{854})\, p_P(t)\,, \tag{4.7}$$

$$\frac{d}{dt}\, p_{D,3/2}(t) = (\frac{4}{15}\, A_{854} + r_{854})\, p_P(t) - r_{854}\, p_{D,3/2}\,, \tag{4.8}$$

$$\frac{d}{dt}\, p_{D,5/2}(t) = \frac{10}{15}\, A_{854}\, p_P(t)\,, \tag{4.9}$$

where we included the Clebsch-Gordan coefficients for the $P_{3/2} \leftrightarrow D_{5/2}$ transitions and the loss into $S_{1/2}$ given by the term $-A_{393}\, p_P(t)$ in eq. (4.7). Loss into a third $D_{5/2}$ Zeeman sublevel is indirectly included in the model by using the full Einstein coefficient for the 854 nm decay in eq. (4.7). Looking at the outcome of the simulation (fig. 4.3 (b)), an interesting effect arises: The time-bandwidth product of the outgoing 854 nm photon wave packet is again (nearly) Fourier limited, as it is apparent from the fact that the wave-packet length at identical coupling rates for 854 nm coincides with the Fourier-limited wave packet at 393 nm from the first scheme, albeit at the cost of efficiency. From the simulation, we deduce a generation efficiency of approximately 4% for 854 nm photons on the desired $|P_{3/2}, +3/2\rangle \rightarrow |D_{5/2}, +5/2\rangle$ transition.

The aforementioned model can be extended by coupling both ground states via a driving field (e.g. a laser field at 729 nm), as it has been done to simulate the pumping dynamics in

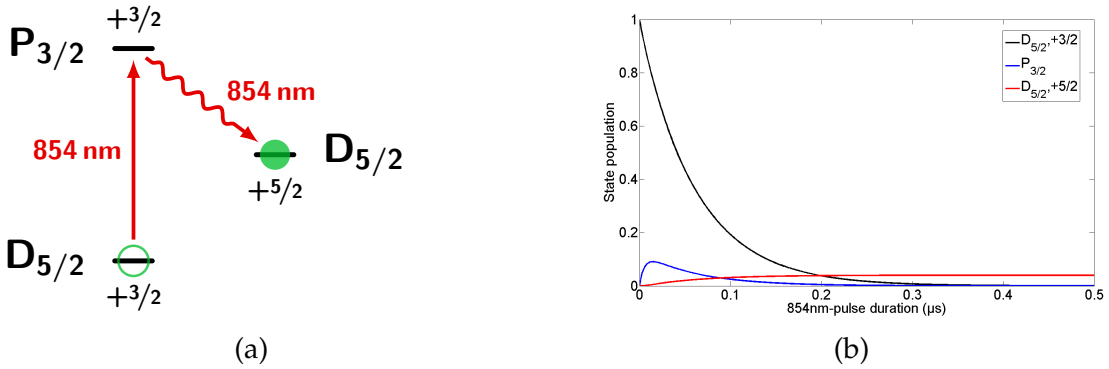

(a) (b)

Figure 4.3.: (a) Population in one Zeeman sublevel of $D_{5/2}$ is depleted by the laser field at 854 nm. Deacy into a second $D_{5/2}$ sublevel re-emits a red photon. **(b)** Numerically solving eqs. (4.7)–(4.9) for a transfer rate of $r_{854} = 2\pi \cdot 3\,\mathrm{MHz}$ reveals the population of the considered states over time. It is noticeable that the length of the photon wave packet (directly proportional to the population in $P_{3/2}$) is of the same length as in fig. 4.1, while the overall transfer efficiency, reflected in the steady-state population in the final $D_{5/2}$ substate (red) is significantly decreased due to population loss into $S_{1/2}$.

section 3.2. In that case, eqs. (4.1)–(4.3) have to by modified and we obtain the four-level rate equations

$$\frac{d}{dt}\,p_{S,+}(t) = \frac{2}{3}\,A_{393}\,p_P(t)\,, \tag{4.10}$$

$$\frac{d}{dt}\,p_{S,-}(t) = \frac{1}{3}\,A_{393}\,p_P(t) - r_{729}\,p_{S,-}(t) + r_{729}\,p_D(t)\,, \tag{4.11}$$

$$\frac{d}{dt}\,p_P(t) = r_{854}\,p_D(t) - (A_{854} + r_{854} + \frac{2}{3}\,A_{393} + \frac{1}{3}\,A_{393})\,p_P(t)\,, \tag{4.12}$$

$$\frac{d}{dt}\,p_D(t) = r_{729}\,p_{S,+}(t) + (r_{854} + A_{854})\,p_P(t) - (r_{729} + r_{854})\,p_D(t)\,, \tag{4.13}$$

with the populations $p_{S,\pm}$ for both ground states $S_{1/2}, \pm 1/2\rangle$, and p_P and p_D for the populations in $P_{3/2}$ and $D_{5/2}$, respectively. The transition from $S_{1/2}, +1/2\rangle$ to $D_{5/2}$ at 729 nm is driven at rate r_{729} and the CGCs for the decay from $P_{3/2}$ into the respective ground states are taken into account.

The rate equations presented here produce reliable results as long as the coupling to transitions or decay into states not regarded in the model is negligible and effects like light shifts or interference between individuals transition paths [143] do not occur or have negligible influence. This assumption is justified for the scenarios presented in this section, at least for reasonably low coupling strength of the driving laser and proper polarization adjustment, such that the coupling to neighboring transitions is very weak. For more complex level schemes, an 18-level Bloch-equation simulation [81] was developed in the group.

4.2. Emission properties of optical dipoles

Aside from the temporal properties, the characterization of single photons comprises the remaining degrees of freedom, spatial direction of propagation and polarization. In the following, we will limit ourselves to photons absorbed and emitted on optical dipole transitions. The dipole-allowed transitions are discussed and their influence on the photon polarization for different directions of observation are investigated. Eventually, the collection efficiencies in our setup for free-space collection and single-mode–coupled photon collection are calculated theoretically from the previously-derived models.

The calculations presented in this section are closely related to those in [144] and then extended to a full amplitude-based description, following the recipes mentioned in [100] and [145].

4.2.1. Optical dipole transitions

The probability for spontaneous transition from state i to k in a unit time interval is proportional to the Einstein coefficient [146]

$$A_{ik} = \frac{2}{3}\,\frac{e^2 8\pi^3 \nu_{ik}^3}{\varepsilon_0\, c^2\, h}\,|M_{ik}|^2 \tag{4.14}$$

with the electron charge e, the transition frequency ν_{ik} and the transition dipole moment

$$M_{ik} = \int \psi_i^*\,\vec{r}\,\psi_k\,d^3r\,. \tag{4.15}$$

$\psi_{i,k}$ denote the electron's wave function for the states i and k, respectively.

In spherical representation, the electronic wave function $\psi_{n\ell m}(\vec{r})$ for the principal quantum number n, the angular momentum quantum number ℓ and the magnetic quantum number m, can be decomposed into a radial component $R_{n\ell}(r)$ and an angular component $Y_{\ell m}(\theta,\varphi)$, i.e. $\psi_{n\ell m}(\vec{r}) = R_{n\ell}(r)\cdot Y_{\ell m}(\theta,\varphi)$. $R_{n\ell}(r)$ and the spherical harmonics $Y_{\ell m}(\theta,\varphi)$ are given by

$$R_{n\ell}(r) = \sqrt{\left(\frac{2Z}{na_0}\right)^3 \frac{(n-\ell-1)!}{2n\cdot(n+1)!}}\; e^{-\rho/2}\,\rho^\ell \cdot L_{n-\ell-1}^{2\ell+1}(\rho) \quad,\ \rho = \frac{2Zr}{n\,a_0} \tag{4.16}$$

with the Bohr radius a_0, the proton number Z and the generalized Laguerre polynomials $L_{n-\ell-1}^{2\ell+1}$, and

$$Y_{\ell m}(\theta,\varphi) = \frac{1}{\sqrt{2\pi}}\,P_\ell^m(\cos\theta)\,e^{i\,m\phi}\,, \tag{4.17}$$

where $P_\ell^m(\cos\theta)$ is the associated Legendre polynomial.

A (partially) quite lengthy calculation, which is beyond the scope of this section, reveals the selection rules for optical dipole transitions,

$$\Delta\ell = \ell_i - \ell_k = \pm 1 \tag{4.18}$$

$$\Delta m = m_i - m_k = 0, \pm 1 \,. \tag{4.19}$$

For other combinations of $|i\rangle = |n_i\, \ell_i\, m_i\rangle$ and $|k\rangle = |n_k\, \ell_k\, m_k\rangle$, eq. (4.15) vanishes and hence the transition is "dipole-forbidden". If we additionally demand that $\Delta s = 0$ for the change in the spin quantum number, we obtain in spin-orbit coupling

$$\Delta j = 0, \pm 1 \tag{4.20}$$

for the total angular momentum $\vec{j} = \vec{\ell} + \vec{s}$, whereby $j = 0 \to j = 0$ is forbidden.

The case $\Delta m = 0$ (π transition) in eq. (4.19) corresponds to the non-vanishing z component of the transition dipole moment ($(M_{ik})_x = (M_{ik})_y = 0$), i.e. to an atomic dipole oriented along the quantization axis, whereas $\Delta m = \pm 1$ ($\sigma^{\pm}$ transition) correspond to $(M_{ik})_x \pm i\,(M_{ik})_y$, i.e. dipoles that rotate (counter-)clockwise in the x-y plane perpendicular to the quantization axis. This geometrical interpretation will help to gain an intuitive picture of the directionality of the polarization properties discussed in the next section.

4.2.2. Spatial dependence of the photon polarization

The goal of this section is the development of a formalism to derive the photon polarization measured in the reference frame of the observer for a given orientation of the atomic dipole. A detailed calculation is given in appendix A.1.1, the key results are summarized in this section.

Naturally there are two reference frames involved in the consideration, the atomic (at) and photonic (ph) frame, which are defined such that $\hat{e}_z^{(\mathrm{at})}$ is oriented along the quantization axis and $\hat{e}_x^{(\mathrm{at})}$ lies in the table plane, and $\hat{e}_z^{(\mathrm{ph})} \parallel \vec{k}$, with the photonic wave vector $\vec{k}$ being parallel to the propagation direction of the light, as depicted in fig. 4.4.

Defining the right- and left-hand circular-polarization unit vectors $\hat{e}_+^{(\mathrm{ph})}$ and $\hat{e}_-^{(\mathrm{ph})}$, respectively, the horizontal and vertical polarizations are written as

$$\hat{e}_H^{(\mathrm{ph})} = -\frac{1}{\sqrt{2}}\left(\hat{e}_+^{(\mathrm{ph})} - \hat{e}_-^{(\mathrm{ph})}\right) \text{, and } \quad \hat{e}_V^{(\mathrm{ph})} = i\,\frac{1}{\sqrt{2}}\left(\hat{e}_+^{(\mathrm{ph})} + \hat{e}_-^{(\mathrm{ph})}\right) . \tag{4.21}$$

The relation between both reference frames, i.e. the transformation from the atomic to the photonic frame, is described by (c.f. [144])

$$\hat{e}_{q'}^{(\mathrm{at})} = e^{iq'\varphi} \sum_{q=-1}^{1} d^1_{q',q}(-\theta)\, \hat{e}_q^{(\mathrm{ph})} \,. \tag{4.22}$$

d describes the Wigner (small) matrices $d^j_{q',q}(\vartheta)$, and the (atomic) unit vectors are given by

$$\hat{e}_0^{(\mathrm{at})} = \begin{pmatrix} 0 \\ 0 \\ 1 \end{pmatrix} \text{ and } \hat{e}_+^{(\mathrm{at})} = -\frac{1}{\sqrt{2}}\begin{pmatrix} 1 \\ i \\ 0 \end{pmatrix} , \hat{e}_-^{(\mathrm{at})} = \frac{1}{\sqrt{2}}\begin{pmatrix} 1 \\ -i \\ 0 \end{pmatrix} . \tag{4.23}$$

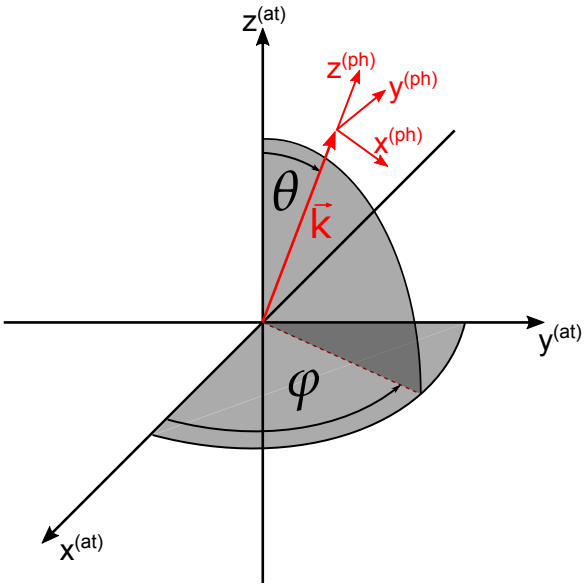

Figure 4.4.: Coordinate systems for the atomic (at) and photonic (ph) reference frame. The wave vector $\vec{k}$ coincides with the direction of observation. The transformation rule from the atomic into the photonic frame is described in the main text.

That formalism allows to derive the direction-dependent polarization amplitudes for a given orientation of the atomic dipole, i.e. for a given atomic transition, of which the π transition, corresponding to $\hat{e}_0^{(\mathrm{at})}$, and the σ^+ and σ^-, corresponding to $\hat{e}_+^{(\mathrm{at})}$ and $\hat{e}_-^{(\mathrm{at})}$, respectively, are relevant for the present treatment.

A brief calculation (see A.1.1) reveals the (un-normalized) polarization amplitude $\vec{A}_\pi^{(\mathrm{ph})}$ for the atomic π transition in the basis of the linear photonic polarizations H and V:

$$\vec{A}_\pi^{(\mathrm{ph})} = -\sin\theta\,\hat{e}_H^{(\mathrm{ph})}\,. \tag{4.24}$$

Eq. (4.24) shows that light emitted on a π transition exhibits solely a horizontal polarization component (in the photonic frame). The spatial intensity characteristic features a toroidal (or "doughnut"-like) shape, i.e. the intensity of the light is maximal perpendicular to the orientation of the atomic dipole, while emission into the direction of the symmetry axis is entirely suppressed.

Analogously, the polarization amplitudes for the atomic $\sigma^\pm$ transitions, as seen by a observer whose direction of observation is determined by the angles θ and φ, are found as[1]

$$\vec{A}_{\sigma^+}^{(\mathrm{ph})} = \frac{e^{i\varphi}}{\sqrt{2}}\left(\cos\theta\,\hat{e}_H^{(\mathrm{ph})} + i\,\hat{e}_V^{(\mathrm{ph})}\right) \tag{4.25}$$

[1] A detailed derivation is given in A.1.1.

and

$$\vec{A}^{(\mathrm{ph})}_{\sigma^-} = \frac{e^{-i\varphi}}{\sqrt{2}} \left(\cos\theta \, \hat{e}^{(\mathrm{ph})}_H - i \, \hat{e}^{(\mathrm{ph})}_V \right) . \tag{4.26}$$

Along the symmetry axis of the dipole (the quantization axis), we find the polarization of the photon emitted on the $\sigma^\pm$ transitions to coincide with right- and left-hand polarization R and L, thus being completely distinguishable. For observation perpendicular to the quantization, on the other hand, only vertically-polarized light is observed for both transitions, σ^+ and σ^-, leaving the observer fully unaware of which transition took place.

The emitted intensity is maximal along the quantization axis and reduced to $1/2$ of the maximum value perpendicular to the quantization axis. The overall intensity distribution obeys the law $I = \cos^2\theta + 1$, reminding of a peanut.

Including the normalization following the derivation in appendix A.1.1, we obtain the normalized polarization amplitudes in the photonic reference frame for the atomic π, σ^+ and σ^- transitions,

$$\vec{A}^{(\mathrm{ph})}_{\pi} = -\sqrt{\frac{3}{8\pi}} \sin\theta \, \hat{e}^{(\mathrm{ph})}_H , \tag{4.27}$$

$$\vec{A}^{(\mathrm{ph})}_{\sigma^+} = \sqrt{\frac{3}{8\pi}} \frac{e^{i\varphi}}{\sqrt{2}} \left(\cos\theta \, \hat{e}^{(\mathrm{ph})}_H + i \, \hat{e}^{(\mathrm{ph})}_V \right) , \text{ and} \tag{4.28}$$

$$\vec{A}^{(\mathrm{ph})}_{\sigma^-} = \sqrt{\frac{3}{8\pi}} \frac{e^{-i\varphi}}{\sqrt{2}} \left(\cos\theta \, \hat{e}^{(\mathrm{ph})}_H - i \, \hat{e}^{(\mathrm{ph})}_V \right) . \tag{4.29}$$

We have seen that the three atomic dipole transitions result in different emission characteristics, both in intensity and polarization in the photonic or observer reference frame. A π transition results in the emission purely horizontally polarized light, which fully vanishes along the quantization axis and shows maximal intensity perpendicular to it. Light emitted on the $\sigma^\pm$ transitions exhibits maximal intensity along the quantization axis, where the polarization of the photons corresponds to right- and left-hand-circular polarization and is fully distinguishable. Perpendicular to the quantization axis, the intensity is reduced by a factor of 2 and the light is vertically polarized for both cases, resulting in full indistinguishability between both transitions.

These properties are used in the later course of the work, e.g. for the generation of entangled atom-photon-states, where the correlation between atomic transition and photon polarization is employed

4.2.3. Free-space collection

With the polarization amplitudes derived in the previous section, it is now possible to calculate the collection efficiencies in our experiment for photons scattered on a certain transition. We have to distinguish between two cases, free-space collection, where the

entire power scattered into a given solid angle is integrated, and single-mode–coupled collection, where spatial interference effects have to be taken into account.

In this section, we investigate the free-space collection, which corresponds to the case where the collected photons are coupled into a multi-mode fiber or directly imaged onto the sensitive area of a single-photon detector.

For the sake of compactness, this section recapitulates the essential results and a detailed analysis is left to the appendix A.1.2.

Photons emitted by the single ion are collected by the HALO lens stack with a numerical aperture of 0.4, such that a cone with an opening angle of $2\alpha = 2 \cdot 23.75^\circ$ is covered by the collection setup. From purely geometrical considerations, this corresponds to 4.23% of the full solid angle. For the actual collection efficiency, the directionality of the dipole emission, as discussed in section 4.2.2, has to be regarded.

The normalized probability amplitude for photon emission into the direction determined by the angles θ and φ is defined as the square modulus of the probability-field amplitude, $I(\theta, \varphi) = |\vec{A}(\theta, \varphi)|^2$. Inserting the polarization amplitudes from eqs. (4.27)-(4.29) and integrating over the opening angle of the HALOs, the multi-mode-collection efficiencies for photon emission on the π and $\sigma^\pm$ transitions are derived as

$$\eta_\pi^{MM} = \int_{\theta=0}^{\alpha} \int_{\varphi=0}^{2\pi} |\vec{A}_\pi(\theta, \varphi)|^2 \sin\theta \, d\theta \, d\varphi = 2\pi \frac{3}{8\pi} \int_{\theta=0}^{\alpha=23.75^\circ} \sin^3\theta \, d\theta \approx 0.53\% \, . \tag{4.30}$$

and

$$\eta_\sigma^{MM} = \int_{\theta=0}^{\alpha} \int_{\varphi=0}^{2\pi} |\vec{A}_\sigma(\theta, \varphi)|^2 \sin\theta \, d\theta \, d\varphi = \frac{3}{8} \int_{\theta=0}^{\alpha=23.75^\circ} \left(\cos^2\theta + 1\right) \sin\theta \, d\theta \approx 6.09\% \, , \tag{4.31}$$

i.e. the collection of π light is suppressed by more than one order of magnitude with respect to the collection of σ light, while the latter is enhanced compared to the covered solid angle of the HALO by a factor of $\frac{3}{2}$, when the HALO is aligned along the quantization axis. The suppression of collection for π emission is even increased when the light is coupled into a single-mode fiber due to interference effects, as it is demonstrated in the next section.

4.2.4. Single-mode coupling

For some experiments conducted in the context of this thesis, it is of importance to investigate the influence of single-mode coupling onto the collection efficiencies for our single photons. In contrast to the previous section, interference of the individual light fields becomes important in the case of single-mode collection, i.e. when the collected photons are coupled into a single-mode fiber. This section gives an overview of the results. A more elaborate version is given in the appendix (sec. A.1.3).

For reasons of comparability, first we assume a single-mode fiber whose mode coincides exactly with the non-Gaussian light mode leaving the HALO[2]. For a more realistic treatment, the mode overlap between the (Gaussian) fiber mode and the HALO mode would have to be included, as it is presented in sec. 4.2.5.

All calculations in this section are conducted in the laboratory (atomic) reference frame, hence the superscripts $^{(\mathrm{at})}$ and $^{(\mathrm{ph})}$ are omitted.

For a non-extended light source in the focus of the HALO, which approximately represents the situation in our experiment with the ion acting as single point source, the light field leaving the HALO becomes flat. Thus, we re-write the electrical-field amplitudes[3] for atomic π and $\sigma^{\pm}$ transitions in cylindrical coordinates (z, φ, ϱ):

$$\vec{E}_{\pi} = -\frac{i}{\sqrt{f^2+\varrho^2}} \sqrt{\frac{3}{8\pi}} \frac{\varrho}{\sqrt{f^2+\varrho^2}} \hat{e}_{\varrho} \,, \tag{4.32}$$

$$\vec{E}_{\sigma^{\pm}} = \frac{i}{\sqrt{f^2+\varrho^2}} \sqrt{\frac{3}{8\pi}} \frac{e^{\pm i\varphi}}{\sqrt{2}} \left(\frac{f}{\sqrt{f^2+\varrho^2}} \hat{e}_{\varrho} \pm i\, \hat{e}_{\varphi} \right) \tag{4.33}$$

with

$$\hat{e}_{\varrho} = \begin{pmatrix} \cos\varphi \\ \sin\varphi \\ 0 \end{pmatrix} \text{ and } \hat{e}_{\varphi} = \begin{pmatrix} -\sin\varphi \\ \cos\varphi \\ 0 \end{pmatrix} . \tag{4.34}$$

Here, f denotes the focal length of the HALO. In this simplified treatment we first consider the fiber mode $\vec{G}$ [100] to perfectly match the top-hat mode of the HALO, i.e.

$$\vec{G} = \Theta(\varrho_0 - \varrho) \begin{pmatrix} \alpha \\ \beta \\ 0 \end{pmatrix} \quad , \quad |\alpha|^2 + |\beta|^2 = 1 \tag{4.35}$$

with the Heaviside function $\Theta(\varrho_0 - \varrho)$. The coupling efficiency into the single-mode fiber is determined by the overlap between the electrical-field mode $\vec{E}$ and the fiber mode: [100]

$$\eta^{SM} = \frac{\left| \int_{\varrho=0}^{\varrho_0} \int_{\varphi=0}^{2\pi} \vec{E} \cdot \vec{G}\, \varrho \cos(\theta(\varrho)) d\varrho d\varphi \right|^2}{\int_{\varrho=0}^{\infty} \int_{\varphi=0}^{2\pi} \left|\vec{E}\right|^2 \varrho \cos(\theta(\varrho)) d\varrho d\varphi \int_{\varrho=0}^{\infty} \int_{\varphi=0}^{2\pi} \left|\vec{G}\right|^2 \varrho \cos(\theta(\varrho)) d\varrho d\varphi} . \tag{4.36}$$

[2] Assuming a point source lying in the focus of the HALO, as it is approximately the case for the the properly aligned ion-HALO system.

[3] in the physical dimension of probability per solid angle

Therefore, the single-mode fiber coupling efficiency for an atomic $\sigma^{\pm}$ transition becomes

$$\eta_{\sigma^{\pm}}^{SM} = \frac{\left| \int_{\varrho=0}^{\varrho_0} \int_{\varphi=0}^{2\pi} \frac{f\varrho}{f^2+\varrho^2} e^{\pm i\varphi} \left(\frac{f}{\sqrt{f^2+\varrho^2}} \begin{pmatrix} \cos\varphi \\ \sin\varphi \\ 0 \end{pmatrix} \pm i \begin{pmatrix} -\sin\varphi \\ \cos\varphi \\ 0 \end{pmatrix} \right) \begin{pmatrix} \alpha \\ \beta \\ 0 \end{pmatrix} d\varrho d\varphi \right|^2}{\underbrace{\int_{\varrho=0}^{\infty} \int_{\varphi=0}^{2\pi} \left(\frac{f^2}{(f^2+\varrho^2)^2} + \frac{1}{f^2+\varrho^2} \right) \frac{f\varrho}{\sqrt{f^2+\varrho^2}} d\varrho d\varphi}_{=\frac{8\pi}{3}} \underbrace{\int_{\varrho=0}^{\varrho_0} \int_{\varphi=0}^{2\pi} \frac{f\varrho}{\sqrt{f^2+\varrho^2}} d\varrho d\varphi}_{=2\pi\left(f\sqrt{f^2+\varrho_0^2}-f^2\right)}} \approx 6.09\% \,. \quad (4.37)$$

Compared to the multi-mode coupling (c.f. eq. (4.31)), the single-mode collection of $\sigma^{\pm}$ photons is unchanged if assuming the idealized fiber mode.

In some experiments in this work, e.g. the atom-photon entanglement or atom-to-photon state transfer in chapter 6, it is essential to collect photons emitted in the σ transitions, while the detection of π photons reduces the final state fidelity significantly. In section 4.2.3 we have seen that, though being reduced due to the spatial emission properties of the atomic dipole, the collection-efficiency for π photons still accounts for about 10% compared to photons emitted on the σ transitions in the case of multi-mode coupling. For single-mode coupled photons, however, the collection efficiency completely vanishes:

$$\eta_{\pi}^{SM} = \frac{\left| \int_{\varrho=0}^{\varrho_0} \int_{\varphi=0}^{2\pi} \frac{1}{\sqrt{f^2+\varrho^2}} \frac{\varrho}{\sqrt{f^2+\varrho^2}} \begin{pmatrix} \cos\varphi \\ \sin\varphi \\ 0 \end{pmatrix} \Theta(\varrho_0-\varrho) \begin{pmatrix} \alpha \\ \beta \\ 0 \end{pmatrix} \frac{f\varrho}{\sqrt{f^2+\varrho^2}} d\varrho d\varphi \right|^2}{\int_{\varrho=0}^{\infty} \int_{\varphi=0}^{2\pi} \frac{\varrho^2}{(f^2+\varrho^2)^2} \frac{f\varrho}{\sqrt{f^2+\varrho^2}} d\varrho d\varphi \int_{\varrho=0}^{\varrho_0} \int_{\varphi=0}^{2\pi} \frac{f\varrho}{\sqrt{f^2+\varrho^2}} d\varrho d\varphi} = 0 \quad (4.38)$$

The latter effect can also be understood in a more intuitive picture. Due to the rotational (a-)symmetry of the field amplitude $\vec{E}_{\pi}$ with respect to the quantization axis, the field contributions for φ and $\varphi + \pi$ cancel each other, resulting in an effective destructive interference for the coupling into the single-mode fiber.

Thus, when collection of π light is unwanted, coupling of the emitted photons in a single-mode fiber offers enormous advantages as the polarization purity of the single-mode-coupled photons is significantly increased.

It will become obvious in later chapters that it is of particular interest to analyze the situation of a superposition of two atomic dipoles emerging from a σ^+ and a σ^- transition, respectively. The resulting emitted field consequently consists of a superposition of the σ^+ and σ^- field contributions and becomes

$$\vec{E}_{\sigma} = \frac{1}{\sqrt{2}} \left(\vec{E}_{\sigma^+} + e^{i\phi} \vec{E}_{\sigma^-} \right) , \quad (4.39)$$

where ϕ describes the relative phase between the dipoles. An analogue calculation as in eq. (4.37) (see also appendix A.1.3) reveals the coupling efficiency $\eta_{\sigma}^{SM} \approx 6.09\%$. We see that the collection efficiency stays unchanged and is independent of ϕ.

For the (slightly unrealistic) scenario investigated here, where we assumed single-mode coupling into a fiber whose mode coincides with the output mode of the HALO for a point source in the focus of the HALO input, we concluded that coupling of light emitted on a π transition and collected along the quantization axis is fully suppressed, while the coupling efficiency for $\sigma^{\pm}$ photons remains unaltered compared to free-space or multi-mode coupling. In addition, we investigated the coupling efficiency for a superposition of light from σ^{+} and σ^{-} transitions. The coupling efficiency for the superposition stayed unchanged compared to the case of emission on a single σ transition. This means that each superposition of light emitted on $\sigma^{\pm}$ transitions exhibits a single-mode coupling efficiency of 6.09%, independent of the superposition amplitude and phase.

4.2.5. Mode matching

In reality, the single-mode fiber is not so gracious as to provide a mode that perfectly matches our collection mode, but rather exhibits an approximately Gaussian shape. This means, for a realistic estimation of the coupling efficiency, the $\vec{G}$ used in eq. (4.35) has to be modified accordingly and we obtain [145]

$$\vec{G} = \frac{\sqrt{2}}{w_0\sqrt{\pi}}\, e^{i\psi}\, \exp\left(-\frac{\varrho^2}{w^2(z)}\right) \begin{pmatrix} \alpha \\ \beta \\ 0 \end{pmatrix} . \tag{4.40}$$

ψ denotes the Gouy phase, w_0 is the beam waist, and $w(z)$ describes the beam radius in the measurement plane. In our situation, $w(z)$ coincides with the maximum beam radius ϱ_0.

The fiber mode $\vec{G}$ exhibits a rotation symmetry and is therefore independent of φ. As in sec. 4.2.4, the field contributions of φ and $\varphi + \pi$ cancel out for light emitted on a π transition, resulting in a single-mode coupling efficiency of 0.

To evaluate the coupling efficiency into the (more realistically modeled) single-mode fiber for the case of photons originating from a $\Delta m = \pm 1$ ($\sigma^{\pm}$) transition, we have to compute eq. (4.36) for the fiber mode (4.40) and the field amplitude (4.33). The detailed analysis is given in app. A.1.4. Due to reasons of compactness, only the result is given here. We find an overall coupling efficiency of approximately 2.43% for the Gaussian fiber mode, corresponding to a mode-matching efficiency of about 40% between HALO and fiber mode.

The theoretically derived value of 2.43% overall coupling efficiency[4] for photons from a σ transition (corresponding to 40% mode-matching efficiency times 6.09% collection efficiency) is in good agreement with the value of 39% mode-matching efficiency (or 2.36% overall coupling efficiency) observed in the experiment (c.f. sec. 6.2.1), showing that the simple model is indeed too simple to reproduce realistic results, but proves to be useful to learn the fundamental concept.

[4] i.e. from ion to fiber

4.3. Quantum-mechanical formalism

In section 4.1 we introduced the spontaneous Raman scattering in single atoms and derived a model for the wave packet of the emitted single photon based on three-level rate equations. As that approach only considered the population of the states, the quantum properties of the photons remained unknown. To gain insight into the quantum mechanical phase involved in the process of single-photon scattering, here we formulate a quantum-mechanical description for the absorption and emission of single photons by a single atom [142].
The underlying motivation for the development of the quantum-mechanical description is the prediction of the expected quantum state of an atom following the absorption or emission process of a single photon in the experimental realization of the quantum-interface operations discussed in chapters 5 and 6.

For the formalism presented in this section, we assume the ion to start in a general superposition between two initial states $|i_1\rangle$ and $|i_2\rangle$, $|\psi_i\rangle = \alpha|i_1\rangle + \beta|i_2\rangle$, with $|\alpha|^2 + |\beta|^2 = 1$. Upon absorption of a single photon, the ion is transferred into an auxiliary excited state $|e\rangle$ (or a superposition of two excited states $|e_1\rangle$ and $|e_2\rangle$), from where it decays into a ground-state superposition $\alpha'|g_1\rangle + \beta'|g_2\rangle$. Again the final superposition is normalized[5] by the condition $|\alpha'|^2 + |\beta'|^2 = 1$.
For varying experimental conditions, like different start or end levels, the model is modified accordingly.

In an alternative form, the complex amplitudes α and β of the initial superposition state $|\psi_i\rangle$ can be written in terms of the populations $p_{i,1}$ and $p_{i,2}$ and the (time-dependent) relative phase $\phi_i(t)$ between the states,

$$|\psi_i\rangle = \sqrt{p_{i,1}}\,|i_1\rangle + e^{i\phi_i(t)}\sqrt{p_{i,2}}\,|i_2\rangle\,. \tag{4.41}$$

Henceforth we assume absorption from and emission into a well-defined spatial direction and effects of the finite solid angle due to light collection with the HALO are so far neglected.

To account for single-photon absorption, we extend the system under investigation and find the joint atom-photon state

$$|\Psi_i^{AP}\rangle = |\psi_i\rangle \otimes |\psi_{Ph}^{ab.}\rangle\,, \tag{4.42}$$

with the polarization state $|\psi_{Ph}^{ab.}\rangle$ of the incoming photon, described by

$$|\psi_{Ph}^{ab.}\rangle = \cos\frac{\vartheta}{2}\,|+\rangle^{(\mathrm{ph})} + e^{i\phi_{Ph}}\sin\frac{\vartheta}{2}\,|-\rangle^{(\mathrm{ph})} \tag{4.43}$$

[5] The normalization assumes an ideal situation where no decay into levels not taken into account in the model occurs. For the case when loss channels are considered, attenuation of the state populations is incorporated by reducing the factor accordingly, i.e. $|\alpha|^2 + |\beta|^2 < 1$.

with the photonic states $|\pm\rangle^{(\mathrm{ph})}$, corresponding to $\hat{e}_{\pm}^{(\mathrm{ph})}$ from section 4.2.2, and the polarization angle ϕ_{Ph}. Following the treatment in [142], we model the absorption of a single photon utilizing the absorption operator[6]

$$\hat{A} = \sum_{m_i, m_e} C_{m_i, m_{Ph}^{(ab.)}, m_e} |m_\mathrm{e}\rangle\langle m_\mathrm{i}|\langle m_{Ph}^{(ab.)}| \,, \tag{4.44}$$

where m_i and m_e denote the magnetic quantum numbers of the initial and excited state and the photonic spin projection $m_{Ph}^{(ab.)}$ is determined by $m_{Ph}^{(ab.)} = m_e - m_i = \pm 1$ (depending on m_i and m_e). The $C_{m_i, m_{Ph}^{(ab.)}, m_e}$ are the Clebsch-Gordan coefficients for the transition $|i, m_i\rangle \rightarrow |e, m_e\rangle$.

In general, the absorbed photon can be off-resonant to the transition from m_i to m_e by a detuning δ, therefore eq. (4.44) has to be expanded by including a factor

$$c_{m_i, m_e}(\delta) = a(\delta)\, e^{i\phi_\delta(\delta)} \tag{4.45}$$

with the detuning-dependent real amplitude factor $a(\delta)$ and an additional phase term $e^{i\phi_\delta(\delta)}$. In sum, the combined absorption operator becomes

$$\hat{A} = \sum_{m_i, m_e} C_{m_i, m_{Ph}^{(ab.)}, m_e}\, c_{m_i, m_e}(\delta)\, |m_\mathrm{e}\rangle\langle m_\mathrm{i}|\langle m_{Ph}^{(ab.)}| \,. \tag{4.46}$$

For the sake of coherence of the theoretical description, it is more convenient to introduce a detuning Δ from the "line center" between two manifolds, i.e. the transition frequency for a vanishing external magnetic field. With that, the absorption operator becomes

$$\hat{A} = \sum_{m_i, m_e} C_{m_i, m_{Ph}^{(ab.)}, m_e}\, c_{m_i, m_e}(\Delta)\, |m_\mathrm{e}\rangle\langle m_\mathrm{i}|\langle m_{Ph}^{(ab.)}| \,. \tag{4.47}$$

In a similar way, the emission of a photon during decay from the excited-state superposition into the ground-state manifold is formulated. The emission operator describing the transition from $|e\rangle$ to $|g\rangle$ and the generation of a single photon is written as

$$\hat{E} = \sum_{m_g, m_e} C_{m_e, m_{Ph}^{(em.)}, m_g} |m_{Ph}^{(em.)}\rangle |m_g\rangle\langle m_e| \tag{4.48}$$

with the spin projection $m_{Ph}^{(em.)} = m_g - m_e$ of the emitted single photon.

The effect of a photon absorption followed by emission on an initial joint atom-photon state

$$\begin{aligned} |\Psi_i^{AP}\rangle &= |\psi_i\rangle \otimes |\psi_{Ph}^{ab.}\rangle \\ &= \left(\sqrt{p_{i,1}}\,|m_{i,1}\rangle + e^{i\phi_i(t)}\sqrt{p_{i,2}}\,|m_{i,2}\rangle\right) \cdot \left(\cos\frac{\vartheta}{2}\,|+\rangle^{(\mathrm{ph}),ab.} + e^{i\phi_{Ph}}\sin\frac{\vartheta}{2}\,|-\rangle^{(\mathrm{ph}),ab.}\right) \end{aligned} \tag{4.49}$$

[6] We assume the photon to be absorbed along the quantization axis, so that only the $\sigma^{\pm}$ transitions are addressed, i.e. $|\pm\rangle^{(\mathrm{ph})}$ directly correspond to the atomic $\sigma^{\pm}$ dipoles. For absorption under an arbitrary angle, the photon state (in the atomic reference frame) has to be modified accordingly, as discussed in section 4.2.2.

is then

$$\hat{E}\hat{A}|\Psi_i^{AP}\rangle = \hat{E}\Big(\sum_{m_i,m_e} C_{m_i,m_{Ph}^{(ab.)},m_e}\, c_{m_i,m_e}(\Delta)\, |m_\mathrm{e}\rangle\langle m_\mathrm{i}|\langle m_{Ph}^{(ab.)}|\, \Big(\sqrt{p_{i,1}}\,|m_{i,1}\rangle + e^{i\phi_i(t)}\sqrt{p_{i,2}}\,|m_{i,2}\rangle\Big)\cdot \Big(\cos\frac{\vartheta}{2}\,|+\rangle^{(\mathrm{ph}),ab.} + e^{i\phi_{Ph}}\sin\frac{\vartheta}{2}\,|-\rangle^{(\mathrm{ph}),ab.}\Big)\Big) \tag{4.50}$$

and likewise for the application of the emission operator. For a typical experimental scenario, most transitions do not exist or are not allowed, hence most CGC become zero, simplifying the situation significantly, e.g. to the one depicted in fig. 4.5.

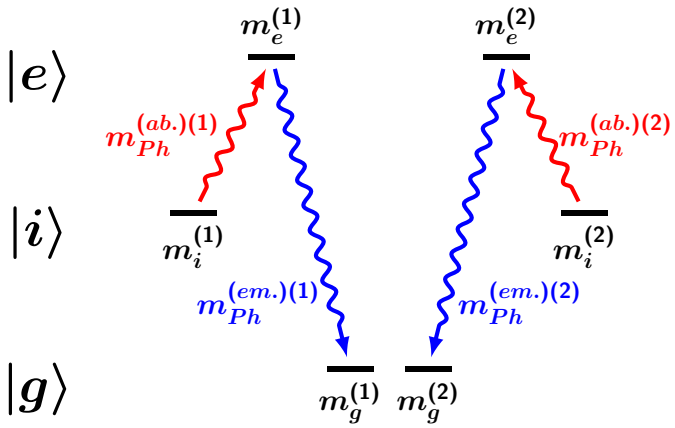

Figure 4.5.: Example for a photon-absorption and subsequent emission process inspired by one of the schemes used in the experiment. The atom is initialized in a superposition in $|i\rangle$ and transferred into an excited-state superposition via absorption of a single photon in the polarization state $|\psi_{Ph}^{ab.}\rangle$. Note that there exist only two allowed excitation paths (but the sublevels in the respective manifolds may be non-degenerate). Subsequent decay to the ground-state manifold releases a second single photon. The resulting atom-photon state is derived in the main text.

In that case, the resulting state after photon absorption becomes

$$\begin{aligned}\hat{A}|\Psi_i^{AP}\rangle = &\sum_{m_i,m_e} C_{m_i,m_{Ph}^{(ab.)},m_e}\, c_{m_i,m_e}(\Delta)\, |m_\mathrm{e}\rangle\langle m_\mathrm{i}|\langle m_{Ph}^{(ab.)}|\, \Big(\sqrt{p_{i,1}}\,|m_{i,1}\rangle + e^{i\phi_i(t)}\sqrt{p_{i,2}}\,|m_{i,2}\rangle\Big)\cdot \\ &\Big(\cos\frac{\vartheta}{2}\,|+\rangle^{(\mathrm{ph}),ab.} + e^{i\phi_{Ph}}\sin\frac{\vartheta}{2}\,|-\rangle^{(\mathrm{ph}),ab.}\Big)\Big) \\ &= C_{m_{i,1},+1,m_{i,1}+1}\, c_{m_{i,1},m_{i,1}+1}(\Delta)\,\sqrt{p_{i,1}}\,\cos\frac{\vartheta}{2}\,|e,m_{i,1}+1\rangle \\ &+ C_{m_{i,2},-1,m_{i,2}-1}\, c_{m_{i,2},m_{i,2}-1}(\Delta)\,\sqrt{p_{i,2}}\,e^{i\phi_i(t)}\,e^{i\phi_{Ph}}\,\sin\frac{\vartheta}{2}\,|e,m_{i,2}-1\rangle\end{aligned} \tag{4.51}$$

for $m_{Ph}^{(ab.)(1)} = +1$ and $m_{Ph}^{(ab.)(2)} = -1$. The subsequent decay on the channels $|e,m_e^{(1)}\rangle \rightarrow$

$|g, m_g^{(1)} = m_e^{(1)} + 1\rangle$ and $|e, m_e^{(2)}\rangle \rightarrow |g, m_g^{(2)} = m_e^{(2)} - 1\rangle$ creates the atom-photon state

$$\begin{aligned}\hat{E}\hat{A}|\Psi_i^{AP}\rangle &= \sum_{m_g, m_e} C_{m_e, m_{Ph}^{(em.)}, m_g} |m_{Ph}^{(em.)}\rangle |m_g\rangle \langle m_e|\hat{A}|\Psi_i^{AP}\rangle \\ &= C_{m_{i,1}+1,-1,m_{i,1}+2} C_{m_{i,1},+1,m_{i,1}+1}\, c_{m_{i,1},m_{i,1}+1}(\Delta)\, \sqrt{p_{i,1}}\, \cos\frac{\vartheta}{2}\, |g, m_{i,1}+2\rangle |-\rangle^{(\mathrm{ph}),em.} \\ &+ C_{m_{i,2}-1,+1,m_{i,2}-2} C_{m_{i,2},-1,m_{i,2}-1}\, c_{m_{i,2},m_{i,2}-1}(\Delta)\, \sqrt{p_{i,2}}\, e^{i\phi_i(t)}\, e^{i\phi_{Ph}}\, \sin\frac{\vartheta}{2}\, |g, m_{i,2}-2\rangle |+\rangle^{(\mathrm{ph}),em.}\,,\end{aligned} \tag{4.52}$$

where we assumed $m_{Ph}^{(em.)(1)} = -1$ and $m_{Ph}^{(em.)(2)} = +1$. For $\langle g, m_{i,1}+2 | g, m_{i,2}-2\rangle = 0$ and photon collection along the quantization axis, eq. (4.52) describes an entangled atom-photon state whose phase is determined by both, the initial atomic state and the polarization of the absorbed photon.

The formalism developed here will be adapted to problems treated in the later course of this work to predict the expected quantum state of an atom following the absorption or emission process of a single photon.

4.4. Influence of the polarization directionality

Entanglement and state transfer in the experiment is carried out by mapping atomic transitions onto photonic polarizations. In section 4.3 we developed a formalism to describe the generation of an entangled atom-photon state, where collection perfectly along the quantization axis was assumed. In a realistic implementation, the finite collection angle has to be considered. Here we investigate the impact of the off-axis collection onto the mapping process. Ideally, decay on a $\sigma^{\pm}$ transition will be translated into right- and left-hand–circular polarization.

From section 4.2.2 we know that $|\sigma^{\pm}\rangle$ transforms into the polarization states

$$|\sigma^{\pm}\rangle = \sqrt{\frac{3}{8\pi}}\, \frac{e^{\pm i\varphi}}{\sqrt{2}}\, \left(\cos\theta\, |H\rangle^{(\mathrm{ph})} \pm i\, |V\rangle^{(\mathrm{ph})}\right)\,. \tag{4.53}$$

With the definitions for right- and left-hand circular light,

$$|R\rangle^{(\mathrm{ph})} = -\frac{1}{\sqrt{2}}\left(|H\rangle^{(\mathrm{ph})} + i\, |V\rangle^{(\mathrm{ph})}\right) \;\text{ and }\; |L\rangle^{(\mathrm{ph})} = \frac{1}{\sqrt{2}}\left(|H\rangle^{(\mathrm{ph})} - i\, |V\rangle^{(\mathrm{ph})}\right)\,, \tag{4.54}$$

we derive the projections of the ideal onto the actual polarization of the collected photon:

$$\begin{aligned}\langle R|\sigma^{+}\rangle &= -\sqrt{\frac{3}{32\pi}}\, e^{i\varphi}\, \left(\langle H| - i\, \langle V|\right)\left(\cos\theta\, |H\rangle + i\, |V\rangle\right) \\ &= -\sqrt{\frac{3}{32\pi}}\, e^{i\varphi}\, \left(\cos\theta + 1\right)\end{aligned} \tag{4.55}$$

and

$$\begin{aligned}\langle L|\sigma^-\rangle &= \sqrt{\frac{3}{32\pi}}\, e^{-i\varphi}\ \left(\langle H| + i\langle V|\right)\left(\cos\theta\,|H\rangle - i\,|V\rangle\right)\\ &= \sqrt{\frac{3}{32\pi}}\, e^{-i\varphi}\ \left(\cos\theta + 1\right)\ .\end{aligned} \tag{4.56}$$

Likewise, we obtain the projections onto the unwanted polarizations:

$$\begin{aligned}\langle L|\sigma^+\rangle &= \sqrt{\frac{3}{32\pi}}\, e^{i\varphi}\ \left(\langle H| + i\langle V|\right)\left(\cos\theta\,|H\rangle + i\,|V\rangle\right)\\ &= \sqrt{\frac{3}{32\pi}}\, e^{i\varphi}\ \left(\cos\theta - 1\right)\end{aligned} \tag{4.57}$$

and

$$\begin{aligned}\langle R|\sigma^-\rangle &= -\sqrt{\frac{3}{32\pi}}\, e^{-i\varphi}\ \left(\langle H| - i\langle V|\right)\left(\cos\theta\,|H\rangle - i\,|V\rangle\right)\\ &= -\sqrt{\frac{3}{32\pi}}\, e^{-i\varphi}\ \left(\cos\theta - 1\right)\ .\end{aligned} \tag{4.58}$$

With eqs. (4.57) and (4.58) we find the probability for a false projection as

$$\begin{aligned}p_f &= \int_{\theta=0}^{\alpha=23.75^\circ}\int_{\varphi=0}^{2\pi} |\langle R|\sigma^-\rangle|^2\,\sin\theta\,d\theta\,d\varphi = \int_{\theta=0}^{\alpha=23.75^\circ}\int_{\varphi=0}^{2\pi} |\langle L|\sigma^+\rangle|^2\,\sin\theta\,d\theta\,d\varphi\\ &= \frac{3}{32\pi}\int_{\theta=0}^{\alpha=23.75^\circ}\int_{\varphi=0}^{2\pi} \left(\cos\theta - 1\right)^2\,\sin\theta\,d\theta\,d\varphi \approx 0.0038\%\ .\end{aligned} \tag{4.59}$$

The result shows that the contribution of collection of wrong polarizations to the infidelity of a quantum process is negligible compared to other experimental error sources.

To summarize, two main topics were discussed in this chapter. The first part consisted of a derivation of the expected temporal shape of the single-photon wave-packet, based on three-level rate equations, for three excitation schemes that are used in the later course of the work:
For the first scheme, i.e. the initial preparation of the ion in $D_{5/2}$, excitation to $P_{3/2}$, and generation of a single 393 nm photon on the $P_{3/2}$-to-$S_{1/2}$ transition, we obtained a nearly Fourier-limited photon with a generation efficiency close to 1, but at an unfavorable wavelength of 393 nm.
The second scheme, where the ion is initially prepared in $S_{1/2}$, excited to $P_{3/2}$, followed by the generation of a single 854 nm photon on the $P_{3/2}$-to-$D_{5/2}$ transition, exhibits a photon wavelength in the infra-red regime, more favorable for long-range transmission, and generation efficiency close to 1, but the generated photon is not Fourier-limited due to decay

back to the ground state $S_{1/2}$.
The initial preparation of the ion in $D_{5/2}$, excitation to $P_{3/2}$, and generation of a single 854 nm photon on the $P_{3/2}$-to-$D_{5/2}$ transition represents the third scheme. Here the photon is in the infra-red regime at 854 nm and Fourier-limited, but at the cost of a lowered generation efficiency in the order of 4%.

The second part of this chapter treats the spatial characteristics of the atomic dipole emission (sec. 4.2.2) and its influence on the photon-collection efficiency (sections 4.2.3 to 4.2.5) and the process fidelity (sections 4.3 and 4.4). For free-space or multi-mode collection along the quantization axis, as utilized in the experiment, we find collection efficiencies of approximately 6.1% for photons emitted on atomic $\sigma^{\pm}$ $(\Delta m = \pm 1)$ transitions and about 0.5% for (in our case unwanted) photons emitted on a π $(\Delta m = 0)$ transition. It is then shown that photon coupling into a single-mode fiber enables full suppression of π-photon collection while the coupling efficiency for photons from the $\Delta m = \pm 1$ is only reduced by a factor of 2.5 to 2.43%. This provides significant potential for the improvement of the photon-state purity as long as the detection of photons with the wrong polarization (and not detector dark counts) represents the limiting factor for the purity in the experiment.

The results derived here are used in chapters 5 and 6 to estimate the expected state fidelity and the success rate for the implementation of the quantum-interface protocols discussed there.

5. Programmable atom-photon interface

The distribution of quantum information within a quantum network requires an interface to connect stationary qubits that serve for storing and processing the quantum information to photonic flying qubits that transfer information between the nodes. These interfaces have to fulfill three requisites to represent a fully operational bidirectional connection between node and communication channels:

- Quantum-state transfer from the memory onto the photon,
- Re-conversion from the quantum information stored in the photonic degrees of freedom into information stored in the memory, and
- Generation of entanglement between the memory and the photon.

In single-atom–based systems, several approaches have been used to address these issues, including deep parabolic mirrors [147, 148], optical resonators [149, 150], and high-numerical-aperture objectives [151, 152]. We deploy the latter for the implementation of our interface.

In the following, the realization of a comprehensive programmable atom-photon quantum interface [82], based on a single trapped ion and high-numerical-aperture optics, is presented. Depending on its mode of operation, the interface allows for photon-to-atom quantum-state transfer, atom-to-photon state transfer, and the generation of atom-photon entanglement.

The measurements were conducted primarily in collaboration with Christoph Kurz, who also wrote the evaluation, and are published in [153] and [82], although a lot of group members contributed to the experiments, ranging from discussions during the conceptional phase to building the basic experimental setup. A comprehensive re-evaluation of the results was performed by Philipp Müller and will be presented in his thesis [81].
In this thesis, a complete summary of the full interface operation, together with a theoretical description of the protocol, is given.

5.1. Atom-photon interface

The basis for the atom-photon quantum interface is the development of our versatile interface protocol, employing a coherent superposition in the metastable $D_{5/2}$ manifold, followed by single-photon absorption and emission. The protocol was initially implemented for high-fidelity heralded transfer of a photonic polarization qubit onto the qubit state of

a single ion [153] and has later been extended to a programmable, bidirectional interface between a single ion and single photons in order to fulfill the aforementioned conditions.

For each operation mode – atom-to-photon state transfer, photon-to-atom state transfer, and atom-photon entanglement – the ion is initially prepared in a superposition of the two Zeeman sublevels $|\pm 5/2\rangle$ (or $|\pm 3/2\rangle$) in $D_{5/2}$. The state initialization is carried out by optical pumping into a pure state, typically into the $|-1/2\rangle$ sublevel of the ground state, followed by a radio-frequency pulse, resonant on the transition frequency between both ground-state sublevels, of adjustable phase and pulse area (**(1)** in fig. 5.1 (a)). The phase of the radio frequency is synchronized with the clock of the control electronics. Thus, the atomic superposition is also in phase with the RF drive (as long as the ion stays in the ground-state superposition and the RF drive is resonant on the ground-state transition). Subsequent application of two resonant π pulses on the narrow-band quadrupole transition at 729 nm coherently transfers the state into $D_{5/2}$ (**(2)** and **(3)** in fig. 5.1 (a)). The initial phase of the $D_{5/2}$ superposition depends on the phase of the RF drive and the phase difference between the two 729 nm pulses and is controllable via these magnitudes. Depending on the desired application (atom-to-photon state transfer, photon-to-atom state transfer, or atom-photon entanglement), the qubit is either encoded into the atomic state or we start with a known, fixed state, as it will be explained in more detail later.

Once the atom state is transferred to $D_{5/2}$, the ion is able to absorb photons resonant on the $D_{5/2} \leftrightarrow P_{3/2}$ transition at 854 nm (see fig. 5.1 (b)).

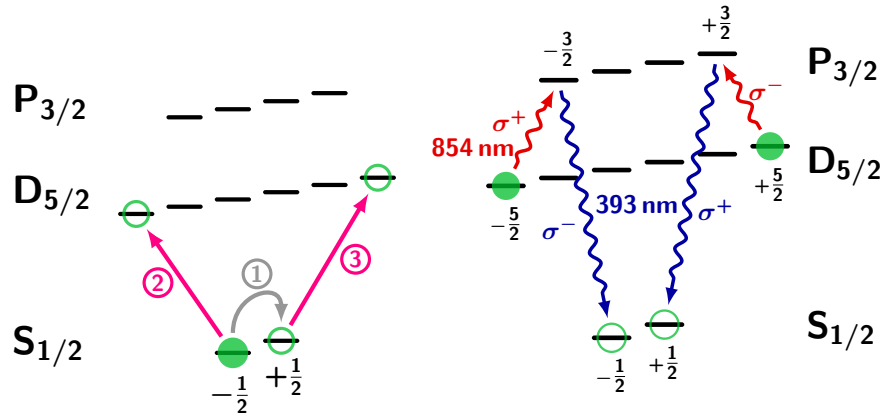

Figure 5.1.: (a) Scheme for the atomic state preparation. The details are explained in the main text. **(b)** Scheme for the interface protocol. Initially, the ion is prepared in a general superposition in the two $\pm 5/2$ Zeeman sublevels of the metastable $D_{5/2}$ state, followed by absorption of a resonant photon at 854 nm in the polarization state $|\psi_{854}\rangle$. Decay from the excited $P_{3/2}$ state transfers the ion into the ground-state qubit $|\psi_S\rangle$ in $S_{1/2}$ and leads to the emission of a single blue photon at 393 nm of polarization $|\psi_{393}\rangle$. The mode of operation decides which states are fixed, projected, or used as carrier of quantum information.

Following the formalism from section 4.3, an absorption event is described by applying the absorption operator $\hat{A}$ onto the initial atomic statestate [1] (or, to be more precise, onto the combined initial atom-photon state)

$$|\psi_{\mathrm{D}}\rangle = \cos\frac{\vartheta_{\mathrm{D}}}{2}|\mathrm{D},-5/2\rangle + \sin\frac{\vartheta_{\mathrm{D}}}{2}\,e^{i\varphi_{\mathrm{D}}}|\mathrm{D},+5/2\rangle\ . \tag{5.1}$$

With the polarization state of the absorbed red photon,

$$\begin{aligned}|\psi_{854}\rangle &= \cos\frac{\vartheta_{854}}{2}|854,\mathrm{R}\rangle + \sin\frac{\vartheta_{854}}{2}e^{i\varphi_{854}}|854,\mathrm{L}\rangle \\ &= \cos\frac{\vartheta_{854}}{2}|854,+\rangle + \sin\frac{\vartheta_{854}}{2}\,e^{i\varphi_{854}}|854,\text{-}\rangle\end{aligned} \tag{5.2}$$

in the left- and right-hand–circular polarization basis and absorption along the quantization axis[2], $\hat{A}$ becomes

$$\hat{A} = |\mathrm{P},+3/2\rangle\langle\mathrm{D},+5/2|\langle 854,\mathrm{L}| + |\mathrm{P},-3/2\rangle\langle\mathrm{D},-5/2|\langle 854,\mathrm{R}|\ , \tag{5.3}$$

and hence

$$\hat{A}|\psi_{\mathrm{D}}\rangle|\psi_{854}\rangle = \cos\frac{\vartheta_{854}}{2}\cos\frac{\vartheta_{\mathrm{D}}}{2}|\mathrm{P},-3/2\rangle + \sin\frac{\vartheta_{854}}{2}\sin\frac{\vartheta_{\mathrm{D}}}{2}\,e^{i\varphi_{\mathrm{D}}}e^{i\varphi_{854}}|\mathrm{P},-3/2\rangle\ . \tag{5.4}$$

The detuning-dependent factor in the absorption operator has been neglected as the photon frequency is constant and equally detuned from the both atomic transitions, such that $c(\Delta)$ just gives a constant known phase offset. A detailed analysis of the photon-frequency dependency of the final atomic state is found in [141].

Decay on the $\sigma^{\pm}$ transitions into a superposition into $\mathrm{S}_{1/2}$ triggers the emission of a single photon at 393 nm. The polarization of the blue photon is connected to the transition on which it was emitted, thus the photon state is correlated to the state of the $\mathrm{P}_{3/2}$ superposition or, eventually, to the final atomic ground-state qubit. In a mathematical sense, this process is described by the emission operator $\hat{E}$, which is in that case represented by

$$\hat{E} = |393,\mathrm{L}\rangle|\mathrm{S},-1/2\rangle\langle\mathrm{P},-3/2| + |393,\mathrm{R}\rangle|\mathrm{S},+1/2\rangle\langle\mathrm{P},+3/2|\ . \tag{5.5}$$

for emission along the quantization axis[3], where the polarizations are defined along the

[1] In the situation when the ion is initially prepared in a superposition of $|\pm 3/2\rangle$ instead of $|\pm 5/2\rangle$, the according $\mathrm{D}_{5/2}$ sub-states have to be substituted.

[2] For absorptions from other directions, the operator has to be modified accordingly. For instance, exciting the $\mathrm{D}_{5/2} \leftrightarrow \mathrm{P}_{3/2}$ transition under 90° with respect to the quantization axis leads to an equivalent expression as (5.3) for vertically polarized photons, while the projection of the input photons onto horizontal polarization couples to the π transition which does not exist in this scheme.

[3] We have seen in section 4.4 that the effect of the finite collection angle due to the HALO onto the resulting polarization of the collected photons is negligible, thus it is legitimate to assume collection solely on the quantization axis for the moment.

direction of propagation. With (5.5), we obtain the resulting joint atom-photon state

$$\begin{aligned} |\psi_{\text{final}}\rangle &= \hat{E}\hat{A}|\psi_{\text{D}}\rangle|\psi_{854}\rangle \\ &= \cos\frac{\vartheta_{854}}{2}\cos\frac{\vartheta_{\text{D}}}{2}|393,\text{L}\rangle|\text{S},-1/2\rangle \\ &\quad + \sin\frac{\vartheta_{854}}{2}\sin\frac{\vartheta_{\text{D}}}{2}\,e^{i\varphi_{\text{D}}}e^{i\varphi_{854}}|393,\text{R}\rangle|\text{S},+1/2\rangle\ . \end{aligned} \tag{5.6}$$

It is evident that the amplitudes and the phase, i.e. ϑ_{D} and φ_{D}, of the initial atomic state as well as the polarization state of the absorbed photon, i.e. ϑ_{854} and φ_{854}, enter into the final atom-photon state. This state forms the basis for the protocol, as we will see in the following sections.

For certain operational modes it is mandatory to project the atomic state via fluorescence-based state detection onto a basis that leaves us ignorant of the qubit states of the remainder of the quantum system, i.e. the polarization state of the blue photon, or vice versa. Very generally, even if no atomic projection is necessary, atomic state analysis has to be conducted in order to evaluate reliability or fidelity of the quantum process or the generated entangled state.

The process of atomic state analysis is depicted in fig. 5.2. After the qubit superposition

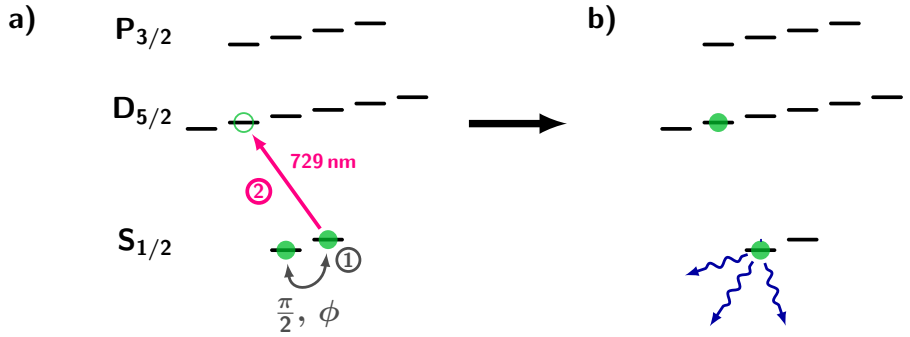

Figure 5.2.: Atomic state analysis for state projection and state tomography. An optional basis-rotation pulse, resonant on the transition between the ground-state sublevels, transforms the superposition phase into populations of $|\pm 1/2\rangle$ for projective measurements in the σ_x and σ_y bases. A 729 nm π pulse transfers the population in $|+1/2\rangle$ into the $D_{5/2}$ manifold, followed by fluorescence-based state discrimination. For a full tomography, the atom is measured in the three different σ_x, σ_y, and σ_z bases.

is formed in the ground-state manifold, an optional $\frac{\pi}{2}$ radio-frequency pulse with phase ϕ is applied to facilitate measurements in the σ_x and σ_y superposition bases. This pulse translates the atomic superposition phase into populations in $|S_{1/2}, m = \pm 1/2\rangle$ (see section 3.3.1), depending on the relative phase between RF and atomic superposition. State read-out is then conducted by shelving the population in one of the two substates, typically

$|+1/2\rangle$, into the meta-stable $D_{5/2}$ state and subsequently performing the state discrimination by fluorescence detection, as described in section 3.4. Full atomic state tomography is carried out by measuring in the three different σ_x, σ_y, and σ_z bases, where the RF pulse is switched off for the σ_z measurement to solely obtain the state occupations. The reconstructed atomic state is then deduced from the outcome of these measurements (explained in more detail in A.2).

5.2. Photon-to-atom state transfer

The first operation under investigation is the transfer of a photonic qubit, imprinted into the polarization state of the photon, onto the stationary node of the quantum network, i.e. onto the state of the single ion. The work is presented in detail in Christoph Kurz' dissertation thesis [79] and [153], but presented briefly here for reasons of completeness. Additionally, the ideas developed for the evaluation of the state-transfer protocol are fundamental for the understanding of the evaluation process for other experiments.

To prove the viability of our interface, we used laser photons as carriers for the polarization state to be transferred [153]. Photon-state transfer with heralded single photons, originating from a photon-pair source based on spontaneous parametric down conversion (SPDC) are presented in [154], [155], and [124].

In the present experiment, a laser beam along the quantization axis provides polarized photons at 854 nm. In fact, the quantization axis was rotated by 90° with respect to the HALO axis for the present demonstration, as shown in fig. 5.3. This configuration poses no fundamental difference to the usual alignment, where the quantization axis points along the HALO axis, as we could as well have oriented the B field along the HALOs and sent the laser beam through the same, but that beam was not set up at the time the experiment was conducted.

A PBS and two waveplates are inserted into the 854 nm beam to adjust the photonic polarization state. The experimental sequence starts, as described before, with optical pumping of the ion into the $|S_{1/2}, m = -1/2\rangle$ Zeeman sublevel, followed by coherent state preparation in a (fixed) superposition in $D_{5/2}$ (see section 5.1). Once the atom is initialized, it is exposed to photons resonant on the $D_{5/2} \leftrightarrow P_{3/2}$ transition, stemming from the laser beam mentioned before. Upon absorption of a photon, the ion is excited into $P_{3/2}$, from where it rapidly decays to the ground state via the emission of a single photon at 393 nm, leaving the atom-photon system in an entangled spin-polarization state. To map the state of the absorbed photon onto the atomic state, the polarization state of the blue photon has to be projected out. The photonic state projection is realized by an adjustable optical polarizer that, conditioned on detection, projects the 393 nm photon onto a linear polarization, i.e. a superposition of right- and left-hand circular polarization, such that no information on the atomic state is gained due to the photon detection. In addition, the photon detection serves as a herald for a successful transfer event. The latter allows for high-fidelity gate operation even for the low photon-detection efficiencies, typically in the order of 1%, which would

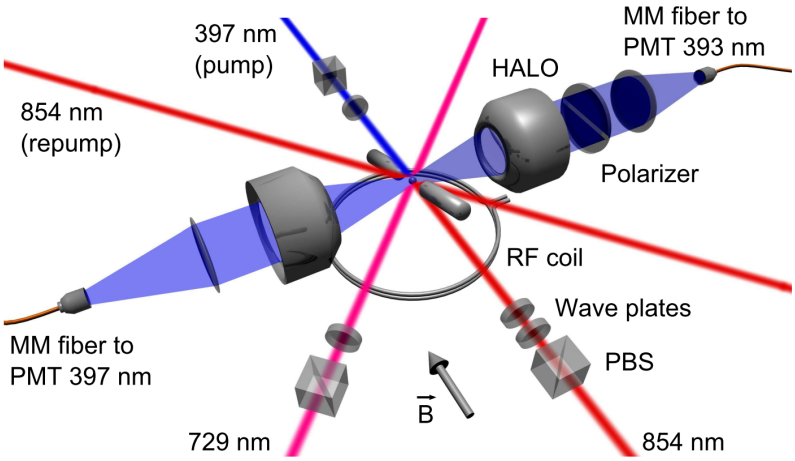

Figure 5.3.: Experimental setup for the photon-to-atom state transfer. The quantization axis, given by the B field, is oriented perpendicular to the HALOs to be parallel to the propagation direction of the 854 nm laser photons. A polarizing beam splitter (PBS) and two waveplates ($\lambda/2$ and $\lambda/4$) are used to adjust the polarization of the 854 nm beam for state transfer. State projection of the scattered 393 nm photons is carried out by a polarizer before they are detected by a photo-multiplier tube (PMT). (taken from [79]).

otherwise (i.e. without heralding) lead to nearly complete loss of information and hence to a nearly entirely mixed final state.
The protocol used here is a slight variation of the one presented in fig. 5.1 as the atomic qubit is imprinted in a superposition in $|D_{5/2}, \pm 3/2\rangle$ to increase the coherence time, but the operational principle stays the same.

The transfer scheme is again summarized in fig. 5.4.

The heralding property of the detection of the blue photon serves a second purpose that has not been mentioned so far. In eq. 5.6 we have neglected the time dependency due to the Larmor precession. In fact, the atomic-phase term $e^{i\varphi_D}$ consists of a constant (and experimentally controllable) part $e^{i\varphi_{D,0}}$ and a temporally oscillating phase contribution $e^{i\varphi_L}$ caused by the Zeeman splitting between both $D_{5/2}$ sub-levels. Since the experimental reference frame oscillates with the radio frequency resonant on the ground-state transition, the atom acquires a Larmor phase (relative to the experimental reference) until it returns to the ground-state superposition due to absorption of a 854 nm photon, followed by the emission of a 393 nm photon. Hence, the additional Larmor phase depends on the moment of the photon emission. Without heralding by detection of the 393 nm photon, we are entirely ignorant of the instant when the ion is transferred into the ground-state superposition, leading to incoherent mixing of the Larmor phases and thus to a statistical mixture for the final atomic state. Therefore, it is a vital requirement to precisely know when the transfer happened, so we can either correct for the acquired Larmor phase by an additional phase-rotating pulse, or take the additional phase into account for further operations. In this experiment, we pursue the second approach. Thus, the phase of the final superposi-

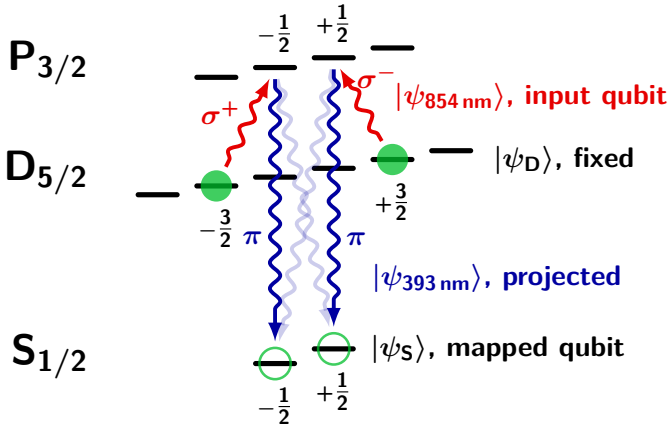

Figure 5.4.: Schematic protocol for the photon-to-atom state transfer. The qubit is encoded in the polarization of the red photons at 854 nm. The ion starts in a fixed superposition in $|D_{5/2}, \pm 3/2\rangle$, enabling the absorption at the $D_{5/2} \leftrightarrow P_{3/2}$ transition. Upon absorption, the ion releases a photon at 393 nm which transfers the ion into the ground-state superposition. Projection of the blue photon onto horizontal polarization maps the photonic input state onto the spin qubit in the ground state.

tion state oscillates, depending on the detection time of the blue photon which projects the atom into the ground state. For a fixed angle of the polarizer, this results in an oscillatory pattern in the arrival-time distribution (ATD) of the photon when the polarization is projected onto H (atomic π transitions) and detection events are conditioned on the projection of the ion onto two orthogonal superposition bases, i.e. on a bright or dark fluorescence detection after RF and 729 nm pulse. A representative photon wave form is shown in fig. 5.5 [153]. As a side-effect, the sharp temporal projection of the photon arrival time erases the spectral distinguishability of the photons scattered on the different decay channels.

Knowing the oscillation period, given by the splitting of the Zeeman states, allows us to merge the detection events into bins of equal phase and calculate the state probabilities (i.e. the probabilities to end up in $\pm 1/2$ following the basis-rotation pulse) to obtain a histogram as shown in fig. 5.6. To reduce the effect of erroneous multi-photon absorptions in the case of laser excitation and improve the signal-to-background ratio while simultaneously maintaining reasonable success probabilities, we only take the first 450 ns of the photon wave packet into consideration.

From the visibility $\mathcal{V}$ of the oscillating fringes shown in fig. 5.6 we deduce the projection of the resulting atomic state after the transfer process onto a perfectly symmetric and coherent superposition of the two energy Eigenstates $|\pm 1/2\rangle$. The phase of the atomic state after the transfer is directly reconstructed from the phase of the oscillation fringe. For linear input polarizations, we expect an ideal mapping onto the symmetric atomic superpositions $|\psi_S\rangle = |-1/2\rangle + e^{i\phi}|+1/2\rangle$. From that we finally extract the overlap fidelity $\mathcal{F}$ of

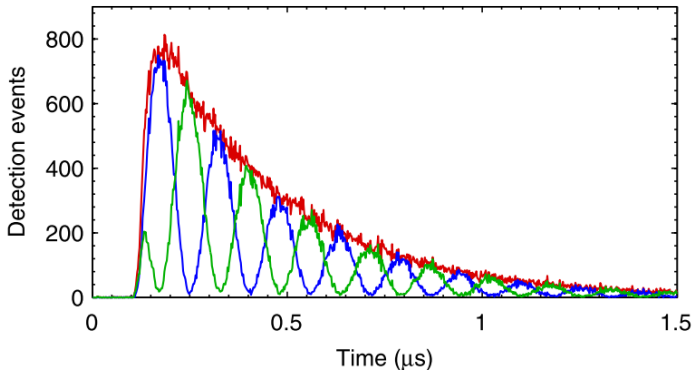

Figure 5.5.: Arrival-time distribution of the emitted 393 nm photon, conditioned on the outcome of the atomic state projection onto two orthogonal superposition bases for linearly polarized 854 nm photons. The prominent oscillation is used to reconstruct the projection of the resulting atomic output state onto the equatorial plane of the Bloch sphere, as explained in the main text (from [153]).

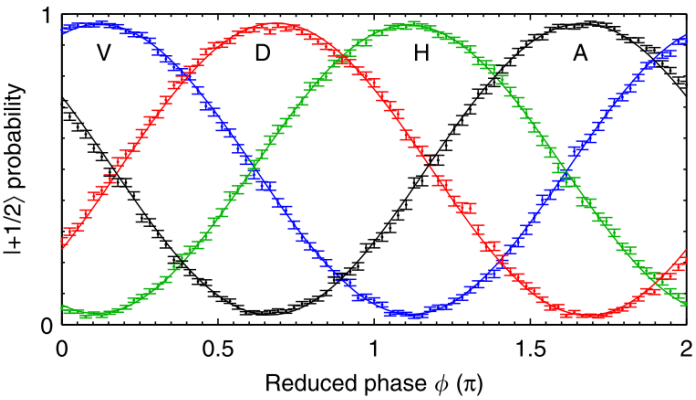

Figure 5.6.: Probability to find the ion in $|+1/2\rangle$ after the basis-rotation RF pulse as a function of the phase equivalent to the arrival time of the heralding photon for different input polarizations. The solid lines represent sinusoidal fits (from [153]).

the resulting states with respect to the atomic target states,

$$\mathcal{F} = \frac{1}{2}\left(\mathcal{V} + 1\right) \ . \tag{5.7}$$

Since we consider deviations between the measured and expected phase values not to result from the mapping process itself, only the fringe visibility enters into the fidelity of the atomic state [79]. For the four linear photonic-qubit polarizations H, V, D, and A, we achieve fidelities of 96.4(1)%, 96.7(1)%, 97.0(2)% and 96.9(1)%, respectively.

For measurements in the σ_z basis, the RF pulse is simply skipped and the projection onto the energy eigenstates is derived in the same way as explained in section 3.4. A typical arrival-time distribution, analyzed in the σ_z basis, for right-hand circularly polarized

854 nm photons is shown in fig. 5.7. The full atomic state for a given photonic input state

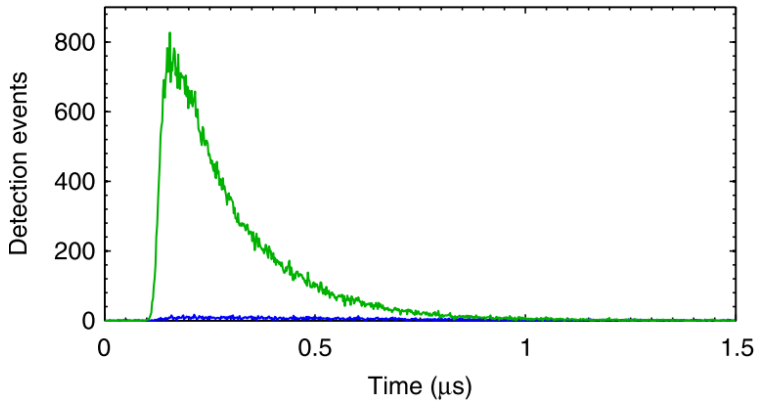

Figure 5.7.: Projection onto $|+1/2\rangle$ (blue) and $|-1/2\rangle$ (green) for right-hand–circular input polarization without basis-rotation pulse (from [153]).

is reconstructed from the combination of both measurements (see [156] and section A.2).

Including the measurements for the circularly polarized input states, whose fidelities are analogously to (5.7) given by the probabilities $p_{\pm 1/2}$ to find the ion in the energy eigenstates $|\pm 1/2\rangle$, as

$$\mathcal{F}_{\pm 1/2} = p_{\pm 1/2}\,, \tag{5.8}$$

we obtain an average state-transfer fidelity $\bar{\mathcal{F}}$ of 96.9(1)%.

For the characterization of the transfer process, the mapped atomic state is evaluated for four different photonic input polarizations (H, D, R, and L) and the quantum-process matrix χ is derived from the results. χ describes the modification of an initial quantum state due to a quantum process and is defined by the completely positive map $\varepsilon(\rho)$ that fully characterizes the transformation of the input state ρ into the output state $\varepsilon(\rho)$ after undergoing the quantum process. ε itself can be re-written in terms of χ as

$$\varepsilon(\rho) = \sum_{i,j=1}^{4} \chi_{i,j}\,\sigma_i\,\rho\,\sigma_j \tag{5.9}$$

with the Pauli matrices σ_i and $\sigma_1 = \mathbb{1}$. From the data of the four input polarizations H, D, R, and L, the quantum-process matrix shown in fig. 5.8 is computed following the procedure described in [157].

Ideally, a quantum process does not alter the state of a system, therefore we define the identity contribution of the process-tomography matrix, χ_{11}, as the quantum-process fidelity. From the process matrix, we find a quantum-process fidelity of 95.0(2)%.

Note that the average state fidelity and the process fidelity are generally linked by the relation [81]

$$\bar{\mathcal{F}} = \frac{2\,\chi_{11} + 1}{3}\,. \tag{5.10}$$

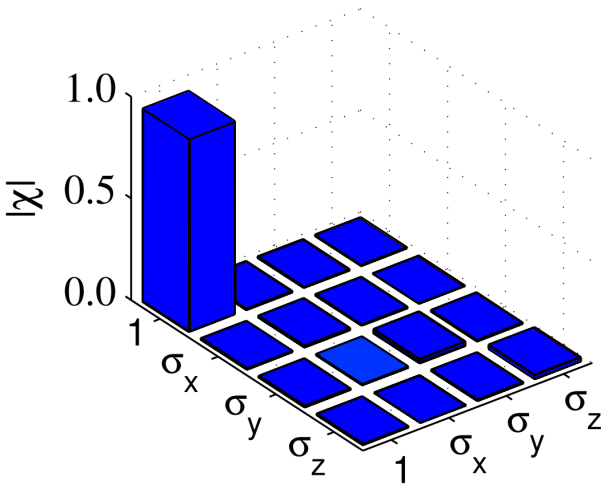

Figure 5.8.: Moduli of the entries of the quantum process-tomography matrix for the photon-to-atom state transfer. The identity contribution, χ_{11}, is defined as the quantum-process fidelity (adopted from [79]).

The discrepancy between the measured values for $\bar{\mathcal{F}}$ and χ_{11} derives from the fact that, in the present evaluation, the average state fidelity was evaluated from all six input states, while only four input states entered into the calculation for the process fidelity.

In analogy to the detailed treatment given in chapter 6, decay from $P_{3/2}$ back to $D_{5/2}$, releasing an undetected 854 nm photon, followed by re-excitation results in an incoherent contribution to the final $S_{1/2}$ qubit. Neglecting decay to $D_{3/2}$, this effect accounts for a reduction in the process fidelity of 1.4% for a 450 ns time window and the given photon-wave-packet length (see [153] and [79]).

In addition, detector dark counts that mimic the detection of a blue photon leave us ignorant of the actual time, direction, and polarization of the emitted photon, dragging the transferred state towards a statistical mixture and thus further degrade the transfer fidelity. Overall, another 1.7% decrease of the process fidelity is attributed to dark-count events (see [153, 79]).

The remaining reduction of the process fidelity is attributed to decoherence due to magnetic-field noise as discussed in 3.6. Briefly estimated, the expected transfer-fidelity reduction in the 450 ns time window and a state-preparation time of about 20 µs for the observed atomic-qubit coherence time of about 670 µs (c.f. [79], section 4.1.9, keeping in mind that the sensitivity against magnetic-field noise is reduced to 60% for the scheme treated here and assuming a coherence time of 400 µs for the σ scheme presented in [79]) is 1.5%. From eq. (5.10) and assuming linearity[4], this value corresponds to a process-fidelity reduction of 2.2%.

Further error contributions, like the decay to $D_{3/2}$ during the excitation process or the

[4]Which is justified for the small values treated here.

erroneous detection of light scattered on the σ transitions that passes the polarizer due to the finite collection angle of the HALO and the spatial emission characteristics of an optical dipole, have no significant influence on the state fidelity and are neglected.
Linearly adding up the error contributions, we obtain an overall process-fidelity reduction of 5.3%, which is in good agreement with the experimental results.

5.3. Atom-to-photon state transfer

Bidirectional operation of the quantum interface requires the ability to release a photon that carries the quantum information formerly encoded in the atom for storage and processing. Again we employ the protocol presented in 5.1. The qubit, initially stored in the ground-state manifold, is coherently transferred into a superposition in $|D_{5/2}, \pm 5/2\rangle$ by two resonant laser pulses at 729 nm. A laser at 854 nm, driving the transition from $D_{5/2}$ to $P_{3/2}$, of fixed linear polarization and incident under 90° to the quantization axis, triggers the emission of a single photon at 393 nm which is at first entangled with the ion. Projection of the atomic state onto a fixed symmetric superposition of both Zeeman sublevels $|\pm 1/2\rangle$ maps the atomic state onto the polarization state of the scattered 393 nm Raman photon. Fig. 5.9 shows the experimental setup for the atom-to-photon state transfer.

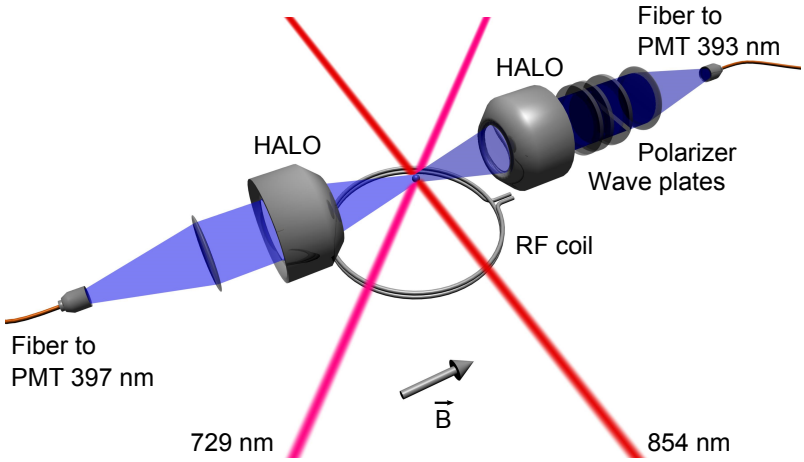

Figure 5.9.: Experimental setup for the atom-to-photon state transfer. The quantization axis, given by the B field, is oriented along the HALO axis. Upon absorption of a vertically polarized laser photon at 854 nm from 90° to the quantization axis, the ion is excited on the $D_{5/2} \leftrightarrow P_{3/2}$ transition and subsequently releases a single blue photon at 393 nm. For the characterization of the state transfer, two waveplates ($\lambda/2$ and $\lambda/4$) and a polarizer facilitate photonic-polarization projection before photon detection on the PMT (from [82]).

The general principle is depicted again in fig. 5.10.

The characterization of the state-transfer process is performed by preparing the atom in both energy eigenstates $|D_{5/2}, \pm 5/2\rangle$ and in a superposition of variable phase and mea-

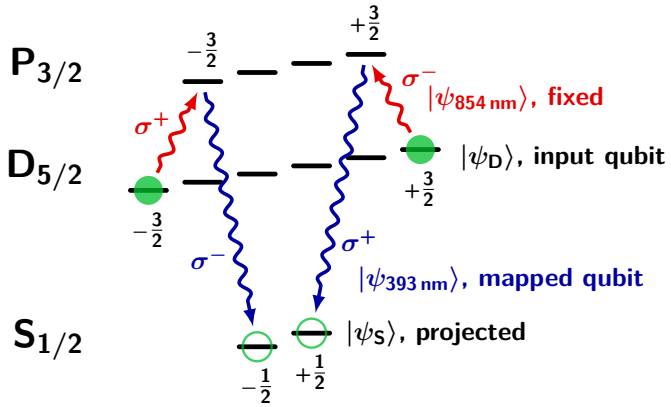

Figure 5.10.: The atomic qubit, initially stored in $S_{1/2}$, is coherently transferred into a superposition in $D_{5/2}$, $|\psi_D\rangle = \alpha\,|-5/2\rangle + \beta\,|+5/2\rangle$ (full green circles). Absorption of a photon at 854 nm of fixed linear polarization, originating from a laser beam from 90° with respect to the quantization axis, triggers the emission of a single photon at 393 nm. After projection of the atomic state onto a symmetric superposition basis with the help of a basis-rotation RF pulse and fluorescence-based state detection, the emitted photon carries the atomic qubit state (together with a known additional phase).

suring the polarization state of the Raman photon. The overall atomic phase in $|D_{5/2}\rangle$ before photon emission is composed of a fixed and experimenter-defined contribution that originates from the state preparation and an temporally oscillating part due to the energy splitting of both $|D_{5/2}\rangle$ sublevels. Consequently, the phase of the atomic superposition and hence the phase of the entangled atom-photon state after emission (see eq. (5.6)) depends on the duration between preparation and return into the ground state, i.e. the time between state transfer to $D_{5/2}$ and detection of the blue photon[5], and also a known and fixed contribution from the polarization of the absorbed 854 nm photon. Projecting the ion onto a symmetric superposition state in $S_{1/2}$ by applying a basis-rotation RF pulse of known phase and a shelving pulse at 729 nm as before thus maps the atomic qubit state in the $D_{5/2}$ superposition onto the polarization state of the blue photon. Depending on the result of the projection measurement, i.e. which of the two orthogonal ground-state superpositions the ion has been projected on, an additional but known phase of π is imprinted on the mapped photonic state (which becomes evident when we re-write the atomic contribution in eq. (5.6) in the superposition basis and apply a projection onto either of the two possible superposition states $|S,-1/2\rangle \pm e^{i\varphi_D}\,|S,+1/2\rangle$, while ϑ_{854} and φ_{854} are kept constant).

For atomic qubits purely encoded into one of the two energy eigenstates $|\pm 5/2\rangle$, it is obvious that the mapped photonic qubit also exhibits purely circular polarization as

[5]Since the radio frequency, being resonant on the transition between both ground-state sublevels, serves as reference oscillator, the atom effectively does not acquire a phase while residing in the ground-state superposition.

there are no other decay channels to $S_{1/2}$. This result becomes apparent when writing down the effect of the absorption and emission operator from section 5.1 onto the initial state (c.f. eq. (5.6)) and projecting the 393 nm polarization onto $|\psi_{393}\rangle = \cos\frac{\vartheta_{393}}{2}|393,\mathrm{L}\rangle + \sin\frac{\vartheta_{393}}{2}e^{i\varphi_{393}}|393,\mathrm{R}\rangle$:

$$\langle\psi_{393}|\hat{E}\hat{A}|\mathrm{D},+5/2\rangle|\psi_{854}\rangle = \sin\frac{\vartheta_{393}}{2}\sin\frac{\vartheta_{854}}{2}e^{i\varphi_{393}}|\mathrm{S},+1/2\rangle \tag{5.11}$$

and

$$\langle\psi_{393}|\hat{E}\hat{A}|\mathrm{D},-5/2\rangle|\psi_{854}\rangle = \cos\frac{\vartheta_{393}}{2}\cos\frac{\vartheta_{854}}{2}|\mathrm{S},-1/2\rangle\ , \tag{5.12}$$

where the factors $\cos\frac{\vartheta_{854}}{2}$ and $\sin\frac{\vartheta_{854}}{2}$ reflect the relative absorption probabilities in dependence of the polarization of the 854 nm photon.

If, however, the atom starts in a superposition between $|\pm 5/2\rangle$, the 393 nm polarization should be in a superposition of R and L after atomic state projection according to (5.6). The polarization angle of the photonic superposition is determined by the atomic phase upon photon absorption. This should manifest as a detection-time–dependent rotation of the blue polarization or an oscillation when the photon is projected onto a linear polarization. In the theoretical description, the respective (normalized) expression according to (5.6) becomes

$$\begin{aligned}\sqrt{\frac{1}{2}}\Big(\langle 393,\mathrm{L}| + \langle 393,\mathrm{R}|\Big)\hat{E}\hat{A}|\psi_{\mathrm{D}}\rangle|\psi_{854}\rangle = &\ \cos\frac{\vartheta_{\mathrm{D}}}{2}|\mathrm{S},-1/2\rangle \\ &+ \sin\frac{\vartheta_{\mathrm{D}}}{2}\,e^{i\varphi_{\mathrm{D}}}e^{i\varphi_{854}}|\mathrm{S},+1/2\rangle\end{aligned} \tag{5.13}$$

with the temporally oscillating phase $e^{i\varphi_{\mathrm{D}}}$ and $\cos\frac{\vartheta_{\mathrm{D}}}{2}, \sin\frac{\vartheta_{\mathrm{D}}}{2} \neq 0$ for projection onto the linear polarizaztion $\sqrt{\frac{1}{2}}\Big(|393,\mathrm{L}\rangle + |393,\mathrm{R}\rangle\Big)$ (and analogously for he other linear polarizations). In the experiment, we see exactly that oscillating behavior, as shown in fig. 5.11. In analogy to section 5.2, we calculate the reduced phase for the oscillation inherent in the photon from the Larmor period of about 64 ns to deduce the phase histogram presented in fig. 5.12. As a trade-off between state fidelity and detection efficiency, we choose a time window of 450 ns of the photonic wave-packet (gray shade in fig. 5.11).

Amplitude and phase of the oscillations for the linear bases reveal the projection of the photonic state onto the plane spanned by the linear polarizations in the Poincaré sphere. As expected, the oscillation for projections onto the circular polarizations is nearly completely suppressed, which is seen on the resulting atom-photon state after absorption of the red and subsequent emission of the 393 nm photon, followed by projection onto the circular polarizations $|393,\mathrm{R/L}\rangle$:

$$\langle 393,\mathrm{R}|\hat{E}\hat{A}|\psi_{\mathrm{D}}\rangle|\psi_{854}\rangle = \sin\frac{\vartheta_{\mathrm{D}}}{2}\sin\frac{\vartheta_{854}}{2}e^{i\varphi_{\mathrm{D}}}|\mathrm{S},+1/2\rangle \tag{5.14}$$

and

$$\langle 393,\mathrm{L}|\hat{E}\hat{A}|\psi_{\mathrm{D}}\rangle|\psi_{854}\rangle = \cos\frac{\vartheta_{\mathrm{D}}}{2}\cos\frac{\vartheta_{854}}{2}|\mathrm{S},-1/2\rangle\ . \tag{5.15}$$

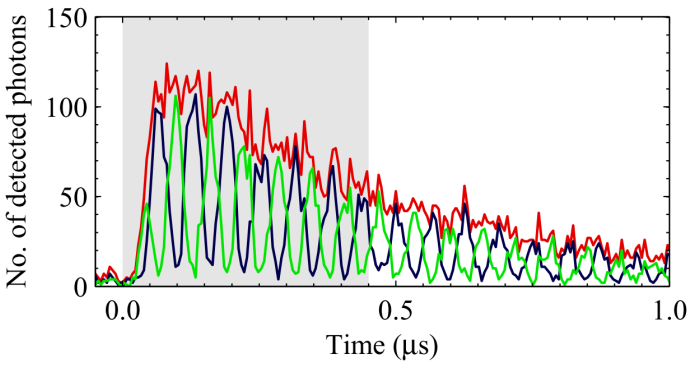

Figure 5.11.: Photon arrival-time histogram for projection of the photon onto the polarization bases H (blue) and V (green). The events are conditioned on the atomic-state projection onto the $|+1/2\rangle$ state following the RF basis-rotation pulse. The red curve represents the sum of both histograms and corresponds to the unconditioned arrival-time distribution. The gray-shaded area indicates the time windows of 450 ns used in the evaluation (from [82]).

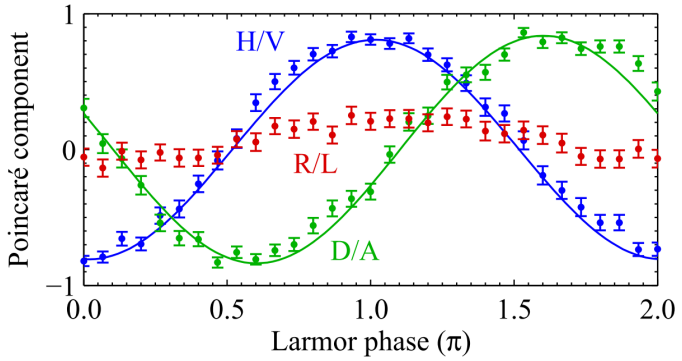

Figure 5.12.: Poincaré components of the resulting photon state vs. reduced Larmor phase for the atom prepared in a linear superposition in $D_{5/2}$, extracted from measurements shown in fig. 5.11. The ellipticity of the polarization (R/L component) is close to zero, with a slightly visible oscillation originating from an imperfect calibration of the wave plates. The solid lines are sinusoidal fits (from [82]).

From the measurements in the circular and linear bases we perform a full state tomography to reconstruct the mapped photonic states for the different atomic input qubit states (in both energy eigenstates and the symmetric superpositions thereof with the starting phases $\varphi_D = 0, \frac{\pi}{2}, \pi, \frac{3}{2}\pi$) to obtain the characterization of the quantum process in the same manner as described in 5.2.

The quantum process-tomography matrix, calculated as described in [153], (fig. 5.13) exhibits a χ_{11} component, identified as the process fidelity, of 90(1)%. Averaged over all six input states, the average state fidelity of the transferred state is 92.4(3)%, which, within the error, agrees to the expected value according to eq. (5.10).

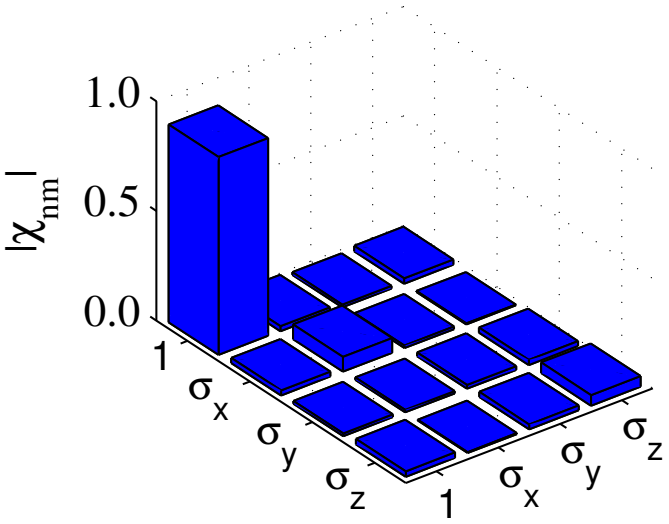

Figure 5.13.: Moduli of the quantum-process matrix characterizing the state mapping. The quantum-process tomography is depicted in the main text (section 5.2) and explained in detail in the appendix. The identity contribution χ_{11}, defined as the process fidelity, is found to be 90(1)% in the present experiment (from [82]).

The main contributions to the infidelity are discussed in the following:

At the time the experiment was conducted, the feed-forward compensation of magnetic-field fluctuations was not yet installed, magnetic-field noise during the storage time of the atomic state of about 30µs has a non-negligible influence on the state-transfer fidelity. Further sources of infidelity are the decay from $P_{3/2}$ back to $D_{5/2}$, which contributes 1.4%, and detector dark counts that account for additional 1.7% for the 450 ns time window. The remaining infidelity is attributed to imperfect calibration of the 393 nm waveplates. It has been shown in section 4.4 that the influence of collection of the wrong polarization is negligible. Collection of π light is irrelevant as a π transition simply does not appear in this scheme.

One way to improve the quality of the state transfer is the implementation of a magnetic-field stabilization, which has been realized in the meantime. The influence of decay back to $D_{5/2}$ can be reduced by decreasing the photon time window, which however reduces the success probability at the same time.

More recently, we developed a protocol for atom-to-photon state transfer onto a photon at 854 nm, presented in the next chapter, that allows for conversion of the photonic qubit into the low-loss telecom regime at 1310 nm and inherently exhibits a higher transferred-state fidelity (see section 6.5).

5.4. Atom-photon entanglement at 393 nm

We have demonstrated the transfer of quantum information from a photon onto a stationary trapped ion on the one hand and the reverse operation, the atom-to-photon state transfer, on the other hand. What remains to show is the entanglement between atom and photon, like it is required as a resource for certain schemes for entanglement distribution within a quantum network [158].

Our protocol is intrinsically capable of providing atom-photon entanglement. In fact, in the atom-photon state transfer shown in section 5.3, we already generated atom-photon entanglement, where we had to project the atomic state in order to map the state onto the photon.

In this section we investigate the resulting entangled state when neither the atom, nor the photon is projected. It is not surprising that the experimental setup for the entanglement operation resembles the one shown in fig. 5.9, although it has to be mentioned that the waveplates for the polarization analysis of the 393 nm photons were replaced in between. Actually, in a chronological sense, the entanglement measurement was performed earlier and the waveplates were replaced for the state-transfer measurement by a set of more reliable ones after we found out that they acted as a source of infidelity.

We begin by preparing a fixed symmetric superposition in the $|\pm 5/2\rangle$ sublevels in $D_{5/2}$ in the usual manner, i.e. by optically pumping the ion into $|S_{1/2}, -1/2\rangle$, generating the coherent superposition in $S_{1/2}$ by a $\frac{\pi}{2}$ RF pulse and subsequently coherently transferring the superposition into $D_{5/2}$ by two consecutive pulses at 729 nm.

After the preparation, a vertically polarized 854 nm laser pulse initiates the emission of a single 393 nm photon, whose polarization is entangled with the spin state of the atom after emission, i.e. in the ground-state manifold (see fig. 5.14).

The viability of the entanglement operation is verified by standard two-qubit tomography, following the instruction in [156], through correlation measurements in the product bases of photonic and atomic qubits. The tomography is explained again in detail in appendix A.3, but shall be briefly recapitulated here.

Generally, a two-qubit state, described by the density matrix

$$\hat{\rho} = \frac{1}{4} \sum_{i_1,i_2=1}^{3} r_{i_1}\, r_{i_2}\, \hat{\sigma}_{i_1} \otimes \hat{\sigma}_{i_2}\,, \qquad\qquad r_{i_1}, r_{i_2} \in \mathbb{R}\,, \tag{5.16}$$

where $\hat{\sigma}_{i_k}$ denotes the i-th Pauli matrix for the k-th qubit, and $\otimes$ denotes the tensor product, can be reconstructed by 16 measurements $\hat{\mu}_i \otimes \hat{\mu}_j$ $(i, j = 0, 1, 2, 3)$. A typical set of measurement bases is given in A.3.

Relabeling the 16 measurement bases $\hat{\sigma}_i \otimes \hat{\sigma}_j = \hat{\Gamma}_\nu, \nu = 1, ..., 16$ according to [156], appendix A, we find the matrices $\hat{M}_\nu$ defined in [156], appendix B, and derive the linearly reconstructed density matrix

$$\hat{\rho} = \sum_{\nu=1}^{16} \hat{M}_\nu n_\nu / \sum_{\nu=1}^{4} n_\nu \tag{5.17}$$

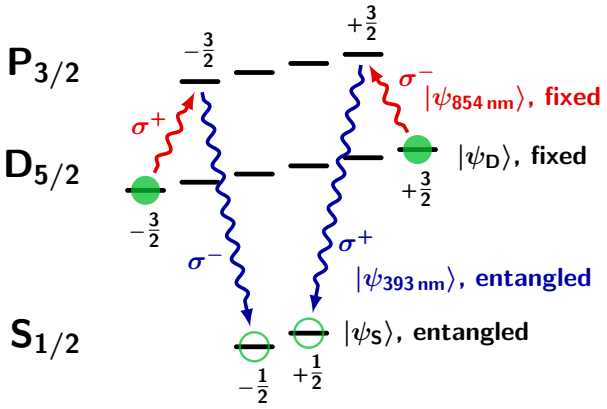

Figure 5.14.: Protocol for the generation of atom-photon entanglement as part of the programmable atom-photon quantum interface. Both input states, the atomic and photonic, are fixed in a symmetric superposition of $|D_{5/2}, \pm 5/2\rangle$ and R/L, respectively. Absorption of the 854 nm and subsequent emission of a 393 nm photon transfers the ion into the ground-state manifold, whose spin state is entangled with the polarization state of the emitted photon.

from the experimentally obtained coincidence counts n_ν. $\nu = 1$ to $\nu = 4$ correspond to the coincidence measurements in the bases $\langle HH|\hat{\rho}|HH\rangle$, $\langle HV|\hat{\rho}|HV\rangle$, $\langle VV|\hat{\rho}|VV\rangle$, and $\langle VH|\hat{\rho}|VH\rangle$[6].

We employ a maximum-likelihood approach (described in A.4) to reconstruct the physical quantum state which produces the experimental data with the highest probability.

From the theoretical treatment in 5.1, we expect the ideal entangled state

$$|\psi_{\text{ideal}}\rangle = \frac{1}{\sqrt{2}}|393,\text{L}\rangle|\text{S},-1/2\rangle - \frac{1}{\sqrt{2}}e^{i\varphi_\text{D}}|393,\text{R}\rangle|\text{S},+1/2\rangle \tag{5.18}$$

according to eq. 5.6.

The experimentally derived atom-photon density matrix after maximum-likelihood reconstruction is shown in fig. 5.15. From the experimental outcome, we find an overlap fidelity with the expected state (5.18) of 84.6(2)% for the photon time window of 450 ns, which clearly exceeds the classical threshold of $\frac{2}{3}$ by more than 80 standard deviations.

The reduction in fidelity is traced back to, once again, primarily the lack of magnetic-field stability that accounts for a significant amount of phase insecurity. For our qubit storage time of about 30 µs, we estimate a decrease in fidelity to about 96%. Another 1.4% loss in fidelity result from decay from $P_{3/2}$ back to $D_{5/2}$, and further 1.9% originate from detector dark counts (taking into account that signal-to-background ratio is decreased by a

[6]The notations $|H\rangle$ and $|V\rangle$ do not necessarily only describe the photonic polarizations, but generally denote the superpositions between the qubit eigenstates $|0\rangle$ and $|1\rangle$, $|H\rangle = |0\rangle + |1\rangle$ and $|V\rangle = |0\rangle - |1\rangle$

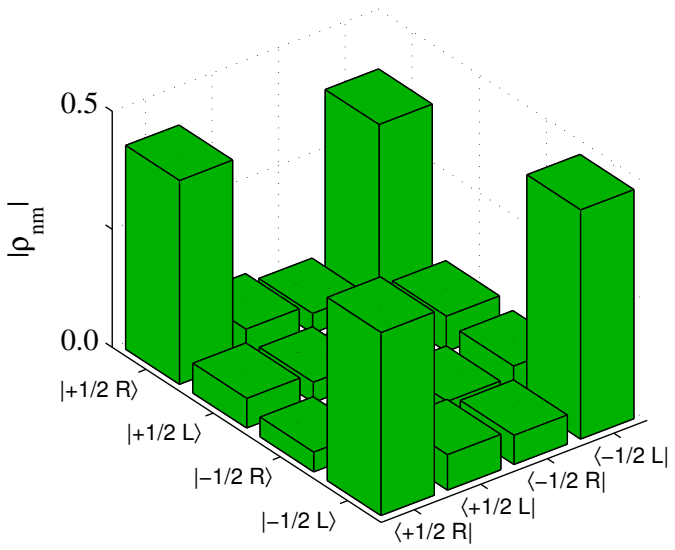

Figure 5.15.: Moduli of the density matrix for the entangled ion-photon state. The generated state exhibits an overlap fidelity with the targeted maximally entangled Bell state of $\mathcal{F} = 84.6(2)\%$. The sources of infidelity are discussed in the main text.

factor of two due to the transmission of photons (signal) through the polarization-analysis setup that result in a signal attenuation of 50%). The remaining infidelity is attributed to imperfect calibration of the waveplates for photonic state analysis, especially for the circular bases.

The photon-detection efficiency for this experiment amounts to 0.353(1)%, including that only 50% of the arriving photons are transmitted through the polarization analyzer. With a sequence-repetition rate of 11 kHz and the quantum efficiency of 28(1)% of the PMT, we obtain 140(5) fiber-coupled photons per second.

In conclusion, we demonstrated a proof-of-principle implementation of a fully programmable atom-photon quantum interface, a key ingredient for a photon-coupled quantum network. The interface offers three operational modes: atom-to-photon state transfer (from the atom onto a 393 nm photon), photon-to-atom state transfer (from a 854 nm photon onto the atom), and the generation of atom-photon entanglement (between atom and 393 nm photon). All operations begin with the controlled generation of a coherent superposition in the meta-stable $D_{5/2}$ manifold with adjustable population amplitude and phase[7], followed by the heralded absorption of a photon at 854 nm (either in e known polarization state in the case of atom-to-photon state transfer and atom-photon entanglement or carrying quantum information encoded in its polarization state in the case of photon-to-atom state transfer).

[7] In an implementation of the atom-to-photon state transfer within a larger quantum network, the atomic qubit state might already be stored in the ion instead of being generated for the purpose of process characterization.

Projection of the atomic state onto a symmetric superposition offers the mapping of the initial atomic state onto the blue photon (for the atom-to-photon transfer) or vice versa (for the photon to atom transfer). If the generation of atom-photon entanglement is intended, no projection is conducted and the atom-photon system remains in an entangled state.

In the next chapter, an enhanced variation of such an interface is presented that allows for quantum-interface operations (photon-to-atom state transfer, atom-to-photon state transfer, atom-photon entanglement) in the spectral telecom range at 1310 nm, appropriate for long-haul quantum communication due to strongly decreased loss in optical fibers.

6. Experiments for quantum-repeater applications

Long-distance quantum communication or distribution of entanglement amongst a large-scale quantum network requires reliable, low-loss transmission of quantum information. Unfortunately, this requisite is obstacled by losses within the quantum channel, e.g. due to photon loss or depolarization, resulting in dramatically reduced rate of information transmission at long distance. For example, the attenuation in optical fibers in the near-infrared region at 854 nm is already 1.3 dB/km. That means that a single photon as a carrier of quantum information, emitted in Saarbrücken and sent to the closest $^{40}Ca^{+}$ experiment in Mainz, situated a bit more than 100 km to the north-east, would suffer losses of 130 dB, i.e. the probability to detect the photon is 0.00000000001%. It is obvious that it would require generations of PhD students to even transmit one single photon, not to mention the signal-to-background ratio for that kind of experiment. All in all, this approach seems not to be practical.

To overcome these limitations, it would be desirable to find a quantum-mechanical analog to a classical signal repeater used in communication technology to break down the long communication channel into a number of shorter channels, coupled by quantum-repeater nodes. Due to the no-cloning theorem of quantum physics, the sent photon cannot simply be amplified, but alternative approaches have emerged that will be presented in the next section.

Of course, a realistic quantum repeater suffers from imperfections, thus the fidelity of the transferred information will be lower the larger the number of required repeater nodes becomes. Therefore, a feasible repeater-assisted communication channel is only applicable if the overall channel losses can be drastically decreased. This is facilitated by the conversion of the photonic qubits into the low-loss telecom spectral range. An atom-photon quantum interface that couples single trapped $^{40}Ca^{+}$ ions and photons in the telecom region is the topic of this chapter.

Our attempt of local two-qubit gates with trapped ions, necessary for single-ion–based quantum repeaters, is presented in chapter 7.

This chapter is split into four major parts. After a brief depiction of the concept of a single-ion based quantum repeater in section 6.1, I present the realization of atom-photon entanglement in the near-infrared regime at 854 nm. The developement and experimental realization of this entanglement protocol, together with the conception and implementation of atom-to-photon state transfer at 854 nm, described in section 6.5, constitutes mainly my contribution to this experiment. All experiment presented in this chapter were

conducted in collaboration with Matthias Bock (a member of the quantum optics group of Christoph Becher), who also built and operated the setup used for polarization-state-preserving single-photon conversion. The latter is briefly depicted in section 6.3. Atom-photon entanglement in the telecom range (section 6.4), employing single-photon quantum frequency conversion, represents the main result of the present chapter. An alternative numerical evaluation for the reconstruction of quantum processes was written by Stephan Kucera. The evaluation is summarized in sec. 6.5.2 and briefly described in Stephan's dissertation thesis [124]. A more detailed description is found in Philipp Müller's dissertation thesis [81].

The results derived in this chapter were published in [159]. The quantum frequency conversion and the converter setup are treated in detail in [73, 80].

6.1. The quantum repeater

The concept of a quantum repeater was first proposed by Briegel, Dür, Cirac and Zoller in 1998 [160]. The original proposal employs a combination of entanglement swapping and purification to overcome the limitation of exponential scaling of the error probability in noisy quantum channels. The initial channel is divided into a number of sub-channels between individually entangled Einstein-Podolsky-Rosen (EPR) pairs. Entanglement swapping is repetitively applied to finally obtain entanglement between both end-points of the quantum channel. As a drawback, the protocol requires the generation of a number of copies of each EPR pair for entanglement purification.

Over time, various approaches for quantum repeaters emerged [161], of which those employing quantum memories as intermediate nodes [162] proved to be among the most promising [163, 164]. In our experiment, we pursue the latter approach. The principle of these protocols is depicted in the following.

A common method for the generation of remote entanglement is a projective Bell-state measurement (BSM) on the photonic part of two pairs of entangled atom-photon pairs [48], as indicated in fig. 6.1 (a). Assuming, for simplicity, only photon loss, a node-node distance ℓ implies a photon-arrival probability of $e^{-\lambda\frac{\ell}{2}}$ from one node to the Bell-measurement device, where λ denotes the attenuation factor of the photonic channel. The probability to detect a coincidence of photons from both nodes is then $p_{\text{coinc}} = e^{-\lambda\ell}$. If we generate entangled atom-photon pairs at rate r, we obtain an atom-atom-entanglement rate

$$R = \eta_{\text{APE}} p_{\text{coinc}} \frac{r}{2} = \eta_{\text{APE}} \frac{r}{2} e^{-\lambda\ell} , \tag{6.1}$$

Where the factor $\frac{1}{2}$ derives from the projection-measurement efficiency for a typical BSM setup, consisting of a non-polarizing beam splitter, two polarizing beams splitters and four single-photon detectors, and η_{APE} is the atom-photon-entanglement-generation efficiency (determined e.g. by the photon-collection efficiency and fiber coupling). For larger distances, the rate rapidly drops below any viability threshold, rendering the entanglement distribution impractical.

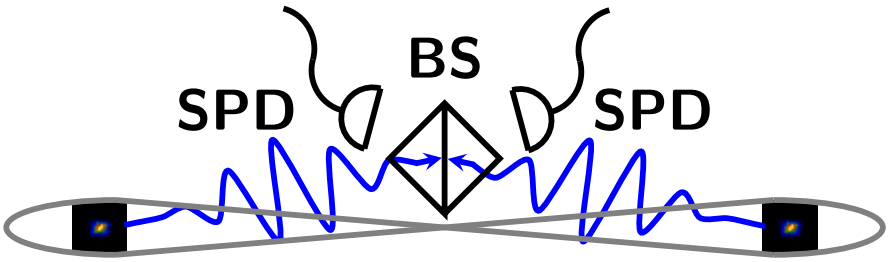

(a) Naive approach for the entanglement of two remote atoms. Both atoms generate a photon, entangled with the respective atom, which are subsequently sent to a projective Bell-state measurement to swap the entanglement onto the atom-atom pair. The entanglement probability suffers from the necessity for simultaneous incidence of the photons at the BSM setup, which is drastically reduced for longer atom-atom distances due to photon loss.

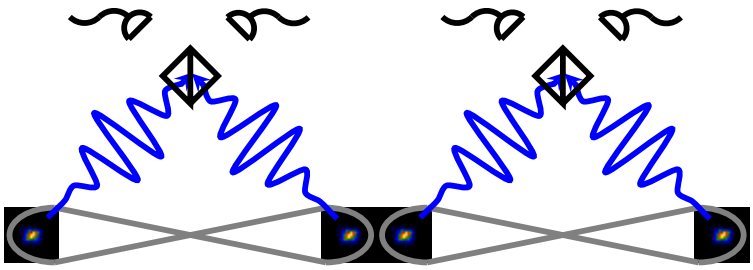

(b) Inclusion of a pair of quantum memories in the middle of the quantum channel facilitates the separation of the quantum-channel between both target nodes into two sub-channels of half length, resulting in a reduction of the channel losses by a factor of $e^{1/2}$. Once entanglement between two nodes is established, it is stored until the whole channel is finally entangled.

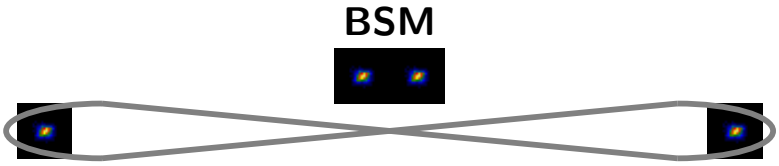

(c) Eventually, a local atomic Bell-state measurement between both ancilla nodes swaps the entanglement onto both target nodes.

Figure 6.1.: Simple example of the working principle of a quantum-memory–based quantum repeater. In a realistic scenario, the chain of sub-channels can be extended according to the desired communication length.

Including a number of N intermediate atomic ancilla nodes (see fig. 6.1 (b)) reduces the inter-node distance to $\ell' = \ell/(N+1)$. The modified entanglement-generation rate between two auxiliary nodes becomes

$$R_{\text{anc}} = \eta_{\text{APE}}^{N}\, p'_{\text{coinc}}\, \frac{r}{2} = \eta_{\text{APE}}^{N}\, \frac{r}{2}\, e^{-\lambda \ell'} = \eta_{\text{APE}}^{N}\, \frac{r}{2}\, e^{-\lambda \ell/(N+1)}\,. \tag{6.2}$$

Since the entanglement between two qubits along a sub-channel is stored once it is established, the individual entanglement generations become independent. Once entanglement between all subsets of ancilla nodes is established, entanglement between both target nodes is generated by repetitive application of entanglement swapping by local two-atom Bell-state measurements (fig. 6.1 (c)). Thus, the rate at which entanglement between both end nodes is generated, is enhanced by the factor $\gamma = \eta_{\text{APE}}^{(N-1)}\, e^{\lambda \ell \frac{N}{(N+1)}}$.

Of course, two-atom–gate infidelities limit the number of auxiliary nodes to not distort the final entangled state between both target nodes too much. Additionally, the entanglement fidelity of the generated intermediate atom-photon pairs, and the photon loss between the ancilla nodes, have a strong impact on the resulting entanglement-transfer fidelity and rate. In the next sections, we will present an implementation of an atom-photon quantum interface, extended by a single-photon frequency-converter setup, to address the latter two challenges.

6.2. Atom-photon entanglement at 854 nm

The implementation of the aforementioned quantum-repeater scheme requires three main building blocks: the generation of entanglement between a quantum memory and a photon, the conversion of the photon into the telecom-wavelength band to overcome high losses in the fiber infrastructure for node-to-node communication, and local entangling two-atom gates. This chapter covers the first two points, while a possible realization of the local gates is described in the next chapter.

First steps have been undertaken to connect the ultra-violet (UV) and telecom band [165], but these devices still suffer from comparatively low conversion efficiency and relatively high background count rates, and still lack the possibility for down-conversion from the UV to the telecom spectrum. Therefore we decided to pursue a different strategy: instead of converting the single photons at 393 nm presented in chapter 5, we create entanglement between the ion and single photons at 854 nm, which can be converted much more easily. This entangled state serves as the foundation for our protocol [159].

6.2.1. Generation of an entangled atom-photon state at 854 nm

One prerequisite for our protocol is the generation of atom-photon entanglement in the near infrared (NIR). At first glance, the $P_{3/2} \leftrightarrow D_{5/2}$ transition at 854 nm seems quite unsuitable for that task due to the disadvantageous branching ratios between $P_{3/2} \leftrightarrow D_{5/2}$

and $P_{3/2} \leftrightarrow S_{1/2}$, which strongly favors the emission of a blue photon at 393 nm over the decay to $D_{5/2}$. In fact, this circumstance appeared discouraging also for us in the beginning. The key to overcome this obstacle lies in the projective nature of a quantum-mechanical measurement.

Since the benefits from optical pumping into a single substate of $S_{1/2}$ are marginal in the current implementation, the sequence directly starts by 8 µs of Doppler cooling and repumping from $D_{5/2}$, leaving the ion in a mixture between the $|m = \pm 1/2\rangle$ Zeeman substates in $S_{1/2}$. Starting from that mixed states, the ion is excited to $P_{3/2}$ by a 5 µs long horizontally polarized laser pulse at 393 nm, incident under 90°, which couples solely to the π transitions $|-1/2\rangle \rightarrow |-1/2\rangle$ and $|+1/2\rangle \rightarrow |+1/2\rangle$ (see figures 6.2 and 6.3). Back-decay into $S_{1/2}$ simply causes re-excitation until the ion ultimately ends up in $D_{5/2}$ with a few exceptions when a decay into $D_{3/2}$ appears (11.1% of the cases). The wave-packet of the 854 nm photon emitted during the process has already been simulated in section 4.1.

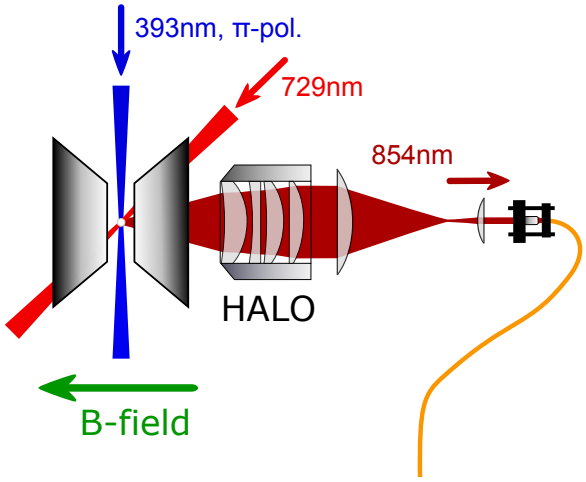

Figure 6.2.: Atom-photon entanglement is generated between a single trapped $^{40}Ca^{+}$-ion confined in a linear Paul trap and a single photon at 854 nm. The photons are collected through a HALO ("High numerical-Aperture Laser Objective") and coupled to a single mode fiber. A 729 nm laser beam under 45° is used for coherent manipulation on the narrow-band quadrupole transition. Single-photon generation is facilitated by a horizontally-polarized 393 nm laser perpendicular to the quantization axis.

Each excitation path exhibits three decay channels,
$|P_{3/2}, -1/2\rangle \rightarrow |D_{5/2}, -3/2\rangle$, $|P_{3/2}, -1/2\rangle \rightarrow |D_{5/2}, -1/2\rangle$, and $|P_{3/2}, -1/2\rangle \rightarrow |D_{5/2}, +1/2\rangle$ (or $|P_{3/2}, +1/2\rangle \rightarrow |D_{5/2}, -1/2\rangle$, $|P_{3/2}, +1/2\rangle \rightarrow |D_{5/2}, +1/2\rangle$, and $|P_{3/2}, +1/2\rangle \rightarrow |D_{5/2}, +3/2\rangle$ for excitation to $|P_{3/2}, +1/2\rangle$). Since the photon is collected along the quantization axis and coupled into a single-mode fiber, collection of photons emitted on the π transitions is suppressed and we effectively end up with photon emission on both σ transitions with orthogonal photon polarization R and L, such that the final atomic state is entangled with the photon polarization. As the ion starts in a mixture in the ground state, the final state

also will consist of a mixture of two entangled atom-photon states, as indicated in fig. 6.3. Therefore, we have to eliminate one of these two states by projecting the ion onto the desired superposition by means of fluorescence-based state discrimination. For that purpose, we apply two resonant pulses at 729 nm of 50 µs length[1] to transfer the population in the unwanted superposition ($|-1/2\rangle$ and $|+3/2\rangle$) into the ground state, and subsequently switch on the cooling lasers for 200 µs of fluorescence detection. If the ion stays dark, it is projected onto the desired superposition of $|-3/2\rangle$ and $|+1/2\rangle$, otherwise the data is discarded and the sequence is restarted. A successful generation of an entangled pair is followed by atomic and photonic state analysis.

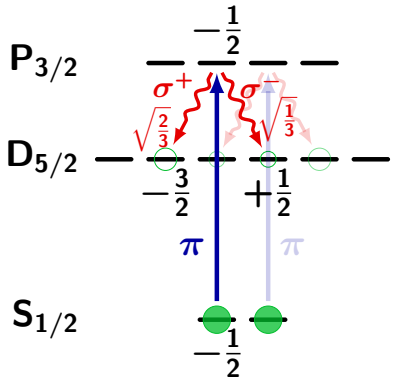

Figure 6.3.: Schematic depiction of the principle for the generation of atom-photon entanglement. Initially in a statistical mixture in $S_{1/2}$, the ion is excited to $P_{3/2}$ by a 393 nm laser pulse whose polarization is adjusted to drive only the π transitions. Upon emission of a 854 nm photon, the ion arrives in one of two possible superpositions (depending on the initial state).

Conditioning of the state-analysis process onto the detection of the red photon and short cooling times allow for high repetition rates of 58 kHz. Taking into account the collection efficiency of 6%[2], single-mode–fiber coupling of 39%, a correction factor of 89.9% due to the decay into $D_{3/2}$[3] (which is projected out afterwards if the 866 nm laser is switched off during the generation), a factor of 1/2 caused by the fact that we start in a mixed state, and an additional factor of 65% as we take only a part of the photon wave-packet into consideration, we expect a success rate of 238 1/s fiber-coupled entangled atom-photon pairs. In the experiment, we measure 27.6 1/s pairs after projection and detection (with an additional factor of 1/2 due to the polarization projection), corresponding to 236 1/s entangled

[1] We choose the large pulse length to avoid excitation of neighboring transitions and ensure reliable population transfer.

[2] Note that this collection efficiency describes the collection conditioned on the emission of a σ polarized photon. If decay along the π transition is taken into account, the resulting collection efficiency reduces to 3.6%.

[3] The ratio of generated 854 nm compared to the generation of 850 nm photons is given by $\eta_{854} = \frac{A_{854}}{A_{854}+A_{850}} = 0.899$.

fiber-coupled pairs, which compares well with other trapped-ion systems [166]. Here we assumed a quantum efficiency of the APDs of 30%, a transmission of 78% through the polarizer and a factor of 50% as the emitted photons are (mostly) unpolarized. A summary of the efficiency factors is given in table 6.1.

Probability for photons on σ transitions	60%
Collection efficiency for photons emitted on σ transitions	6%
Single-mode–fiber coupling	39%
Correction factor due to the decay into $D_{3/2}$	89.9%
Correction factor due to initially starting in a mixed state	50%
Fraction of the photon wave-packet taken into consideration	65%
Polarization projection	50%
Transmission of polarizer	78%
APD quantum efficiency	30%
Σ	0.05%

Table 6.1.: Efficiency factors for the detection of single 854 nm photons in the context of atom-photon entanglement. The photons are collected along the quantization axis, coupled into a single-mode fiber, and subsequently measured in different polarization bases using a polarizer setup and a APD for single-photon detection. The resulting overall detection efficiency is 0.05%. For a repetition rate of 58 kHz, we expect 29.75 $1/s$ detection events.

Close examination reveals an imbalance in the transition probability for the two decay channels caused by different Clebsch-Gordan coefficients, as displayed in fig. 6.3. This imbalance results in a distinguishability of both decay channels as the decay along one channel is more probable than the decay along the other one, hence the expected overlap fidelity with a maximally entangled Bell state is reduced. For a quantitative analysis, we first derive the expected state after photon emission. Assuming the atom to start in $|S_{1/2}, -1/2\rangle$, excitation to $P_{3/2}$ on the π transition and subsequent decay into $D_{5/2}$ leaves the joined atom-photon system in the state

$$|\psi_{\text{exp}}\rangle = \sqrt{\frac{2}{3}}\,|-3/2, \sigma^+\rangle + \sqrt{\frac{1}{3}}\,|+1/2, \sigma^+\rangle \tag{6.3}$$

for single-mode photon collection along the quantization axis. As a figure of merit, we

calculate the overlap fidelity with the maximally entangled Bell state $|\Phi^+\rangle = \sqrt{\frac{1}{2}}|-3/2,\sigma^+\rangle + \sqrt{\frac{1}{2}}|+1/2,\sigma^+\rangle$ as

$$\begin{aligned} |\mathcal{F}_{\text{exp}}\rangle &= \langle\Phi^+|\rho|\Phi^+\rangle = \langle\Phi^+|\psi_{\text{exp}}\rangle\langle\psi_{\text{exp}}|\Phi^+\rangle \\ &= \frac{1}{2}\left(1+\frac{2\sqrt{2}}{3}\right) \approx 97\% \,, \end{aligned} \tag{6.4}$$

which is surprisingly large regarding the fact that the imbalance in the CGCs is 1:2. To circumvent the limitation of the fidelity by different CGCs, we might think of attenuating the stronger decay path by a factor of two, lifting the distinguishability and thus obtaining an (ideally) maximally entangled atom-photon state. This strategy was implemented in a later experiment where single-photon frequency conversion into the telecom band was included.

In the present realization, we conducted two slightly different experimental sequences, where the difference lies in the application of 866 nm light during the generation of the 854 nm photon. The reason is the generation of 850 nm photons that are collected and mimic the detection of a 854 nm photon, resulting in an additional mixed contribution in the final state. Switching the 866 nm laser off during the generation leaves the atom in $D_{3/2}$ after the emission of a 850 nm photon and the events are filtered out during the fluorescence generation for the discrimination of the wrong superposition[4]. The results for both sequences are presented in sec. 6.2.2.3.

6.2.2. Atom-photon state tomography

In the actual experiment, we additionally perform atomic state analysis to characterize the entanglement process. To avoid significant decoherence, the (optional) state rotation is performed prior to the projection for elimination of the wrong state. As before, the desired superposition is coherently transferred into the ground-state manifold by two resonant 729 nm pulses (fig. 6.4). A $\pi/2$ radio-frequency pulse, resonant on the transition between both ground-state sub-levels, of varying phase facilitates the measurement in the atomic superposition bases, as it translates the superposition phase into population of both Zeeman levels. Afterwards, the population is transferred back to $D_{5/2}$. The populations of $|D_{5/2},-3/2\rangle$, $|D_{5/2},-1/2\rangle$, $|D_{5/2},+1/2\rangle$, and $|D_{5/2},+3/2\rangle$ are then determined by a series of four consecutive 729 nm π pulses, tuned to the respective transition from each of the four $D_{5/2}$ Zeeman sub-levels to the $S_{1/2}$ ground state and with adjusted pulse areas, each followed by fluorescence detection.

[4]Since both, the 397 nm and the 866 nm laser are switched on during the fluorescence generation, any population in $D_{3/2}$ results in a "bright" ion, i.e. the generation of 397 nm photons.

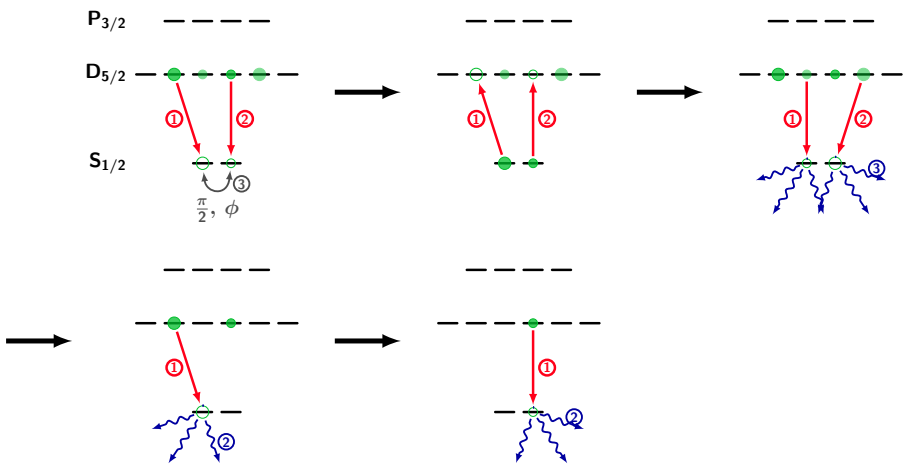

Figure 6.4.: Atomic state analysis is performed by measurements of the desired superposition ($|-3/2\rangle$,$|+1/2\rangle$) in the usual six atomic bases. For measurements in the superposition bases, the atomic state is coherently transferred into the ground state and a $\pi/2$ RF pulse of variable phase is applied before the superposition is brought back to $D_{5/2}$. Decay events into the wrong superposition are evaded by fluorescence detection after the population in these states is transferred to $S_{1/2}$. If the ion stays dark, the desired superposition is finally analyzed in the usual way.

6.2.2.1. State reconstruction

To perform quantum-state tomography, ion and photon are measured in all 9 combinations of the Pauli operators σ_x, σ_y, and σ_z for photon and ion (corresponding to the projection onto $(2 \cdot 3)^2 = 36$ eigenstates), where σ_z represents the eigenbasis ($|R\rangle/|L\rangle$ for the photon and $|-3/2\rangle/|+1/2\rangle$ for the ion) and σ_x/σ_y the superpositions of the latter. The tomography setup for 854 nm photons is inserted into the beam path via a flip mirror and consists of QWP, HWP, polarizer and a silicon APD. The APD [5] has a quantum efficiency of η_{APD} = 30% and a dark-count rate of $\gamma_{\mathrm{DC,\,APD}} = 117.7$ counts/s. The waveplates are motorized and remote-controlled via Ethernet to allow for automation of the measurement. The atomic state analysis is conducted in the usual way, i.e. by coherently transferring population using the quadrupole transition at 729 nm and applying an optional radio-frequency pulse for basis rotation in the ground-state qubit, followed by fluorescence detection for state discrimination (see Fig. 6.4). The joint atom-photon state, represented by its density matrix, is then reconstructed from the combination of measurements in different atom-photon bases via linear state reconstruction[6] and subsequent application of the maximum-likelihood technique.

[5] *Perkin Elmer*, SPCM-AQR-14

[6] From the 9 combinations of the Pauli operators σ_x, σ_y, and σ_z for both, ion and photon, we obtain 36 values for the projections onto the eigenstates of the respective Pauli operators (see main text), from which we deduce the relative frequencies used to calculate the joint-state expectation values.

The state reconstruction is adapted from [153, 82, 156] while the MATLAB program for the evaluation is based on a script written by Stephan Kucera [124].

We measure the atom-photon system in the 9 combinations of photonic polarization bases $|H\rangle/|V\rangle, |D\rangle/|A\rangle, |R\rangle/|L\rangle$ and atomic bases, represented by the Pauli matrices $\pm\sigma_x$, $\pm\sigma_y$, and $\pm\sigma_z$. Specifically this means that we obtain 36 values for the coincidence events between photon detections in the mentioned polarization states and projection of the ion in the respective atomic states (facilitated by fluorescence-based state detection preceded by an optional RF basis-rotation pulse). Two exemplary measurements are shown in Fig. 6.5. Fig. 6.5 a) shows the photonic arrival-time distribution (ATD) for projection onto $|L\rangle$, conditioned on the measurement of the atomic state in the two σ_z eigenbases $|m = -3/2\rangle$ (red curve) and $|m = 1/2\rangle$ (blue curve), respectively. In Fig. 6.5 b), the photon is projected onto a linear polarization, namely onto $|V\rangle$, and its ATD is conditioned on simultaneous projection of the atom onto the superposition bases, determined by the relative phase between basis-rotation pulse and atomic superposition phase. The latter can be understood by keeping in mind that the absolute phase of the RF pulse, as well as the instant it is applied, is fixed, while the atomic phase starts to oscillate as soon as the photon is emitted and the entanglement is established. The oscillation in the ATD, caused by the Larmor precession of the atom, can then be viewed as an emission-time–dependent atomic phase, or, from a different perspective, as measurements in different superposition bases.

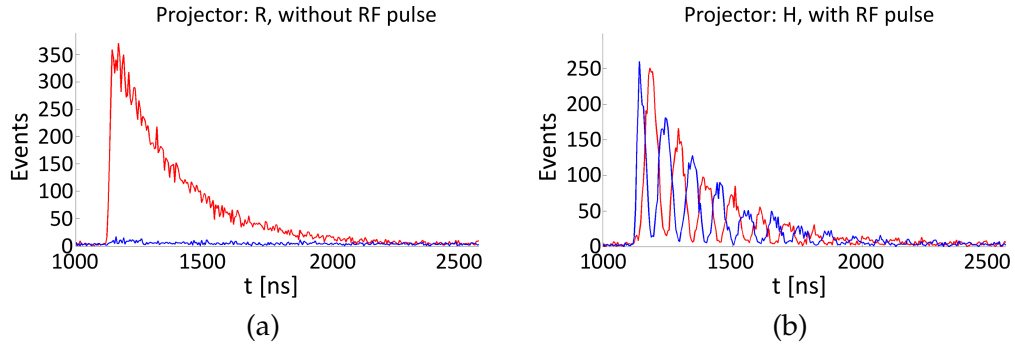

Figure 6.5.: Coincidences between 854 nm photon-detection events and bright events from the atomic state analysis. **(a)** 854 nm photon and ion are projected onto one of the eigenbases, i.e. the photon is projected to $|R\rangle$ and the ion to σ_z. Thus, no $\pi/2$ radio-frequency (RF) pulse resonant to the $|S_{1/2}, m = -1/2\rangle \rightarrow |S_{1/2}, m = +1/2\rangle$ transition is applied. **(b)** Projection into one of the superposition bases, i.e. the photon is projected to $|H\rangle$ and the ion to σ_x/σ_y, realized by the RF $\pi/2$-pulse.

From these measurements, we evaluate the joint expectation values $S_{i,j} = \langle \sigma_i \otimes \sigma_j \rangle$ with the Pauli matrices $\{\mathbb{1}, \sigma_x, \sigma_y, \sigma_z\}$. For the atomic eigenbases (σ_z), the expectation values correspond to the number of coincidences in the 300 ns time window, while for the atomic superpositions, the expectation values are extracted from the amplitude and phase of the Larmor fringes, obtained from a fit to the data, analogue to the method described in section

5.2. With the $S_{i,j}$ we get the density matrix

$$\rho = \frac{1}{4} \sum_{i,j=0}^{3} S_{i,j} \sigma_i \otimes \sigma_j \, . \tag{6.5}$$

To ensure that the density matrix is physical, a maximum-likelihood estimation is performed afterwards with the linear reconstructed matrix as initial guess. This final density matrix is utilized to calculate the fidelities and purities stated in section 6.2.2.3. The error bars of the latter are derived via a finite difference-quotient method assuming a Poissonian distribution of the detection events.

6.2.2.2. Maximum-likelihood estimation

The linear reconstruction of the density matrix may deliver states that are not physical, i.e. states that violate the properties of positivity, Hermiticity, or normalization. These reconstructed state are obviously not a plausible representation of the underlying physical state. The idea behind the maximum-likelihood estimation [156] (MLE) is to find the physical state which reproduces the measured experimental data with the highest probability. For that purpose, we define a two-qubit density matrix $\hat{\varrho}_P(t_1, ..., t_{16})$ which is physical by construction, and formulate that 4×4 matrix as a function of 16 real parameters $t_1, ..., t_{16}$ (see A.4 for details), of which 15 are independent.

Assuming a Gaussian distribution of the coincidence counts, one obtains a likelihood function which reflects the probability that the measurement result is correctly predicted by the current density matrix. For reasons of computational speed-up, we do not maximize the direct likelihood function, but use its (negative) logarithm

$$\mathcal{L}(t_1, ..., t_{16}) = \sum_{\nu=1}^{16} \frac{\left(\mathcal{N} \langle \psi_\nu | \hat{\varrho}_P(t_1, ..., t_{16}) | \psi_\nu \rangle - n_\nu\right)^2}{2\mathcal{N} \langle \psi_\nu | \hat{\varrho}_P(t_1, ..., t_{16}) | \psi_\nu \rangle} \, , \tag{6.6}$$

which ought to be minimized in order to find the physical state that optimally reproduces the experimental data. $\mathcal{N} = \sum_{\nu=1}^{4} n_\nu$ is the normalization factor that we already encountered in sec. 5.4, ψ_ν is the vector representation of the measurement basis (i.e. $|HH\rangle$, $|HV\rangle$ and so on), and n_ν describes the number of coincidence counts for the measurement in the ν-th basis. Minimization of (6.6) reveals the density matrix $\hat{\varrho}_{P,\text{opt.}}(t_{1,\text{opt.}}, ..., t_{16,\text{opt.}})$ of the optimal physical state.

The current evaluation exhibits, based upon a MATLAB script written by Stephan Kucera, slight modifications to this method, described in more detail in sec. A.4.

6.2.2.3. Experimental results

The results presented in this section are also summarized in [159]. To determine the quality of our quantum interface, we perform standard atom-photon state tomography subsequent to the entanglement generation, as described in the previous section. Conditioned

on the detection (and prior polarization projection) of the 854 nm photon, the atomic state is read out as described in section 6.2.2. For measurements in the atomic superposition bases ($\sigma_{x,y}$), an additional RF $\pi/2$ pulse is applied to obtain an oscillatory fringe in the conditioned photon-arrival-time distribution (see fig. 6.5 (b)) when the photon is projected onto a linear polarization due to the Larmor precession. Knowing the oscillation period, which is given by the Zeeman splitting, we can sum up the detection events into a phase histogram like the one shown in fig. 6.6. From the histogram, we deduce the visibility and the phase from a fit to the data, and hence can derive the projection of the resulting atomic state onto the equatorial plane of the Bloch sphere.

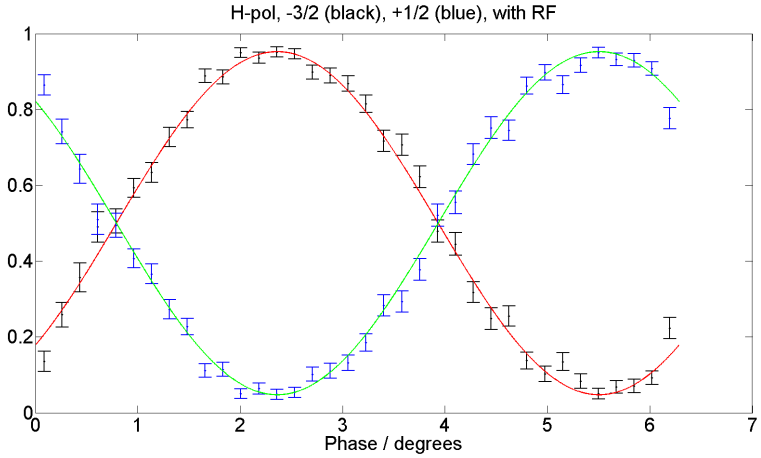

Figure 6.6.: Atomic-state projection onto the eigenstates $|-3/2\rangle/|+1/2\rangle$ after the application of the $\pi/2$ radio-frequency pulse as a function of the reduced phase, calculated from the photon-arrival time, for the photonic-state projection onto horizontal polarization. Visibility and phase, used for the reconstruction of the projection onto the equatorial plane of the Bloch sphere, are derived from a sinusoidal fit.

We perform this measurement for all photonic state projections ($|H\rangle$, $|V\rangle$, $|D\rangle$, $|A\rangle$, $|R\rangle$, and $|L\rangle$) each time in the atomic eigenbases ($|-3/2\rangle$, $|+1/2\rangle$) and in the superposition bases.

As mentioned earlier, we employed two slightly different implementations of this experiment, which differ by the application (or lack thereof) of 866 nm laser light during the generation of the 854 nm photon[7]. The difference in these two schemes lies in the generation, detection and consideration of 850 nm photons emitted in the course of the 854 nm generation.

[7]From a chronological point of view, we first ran the sequence with the 866 nm laser switched on, then included the single-photon conversion, explained later in the course of this chapter, where we experienced a significant improvement of the entanglement fidelity, and then concluded that the 850 nm photons that might be emitted during the generation process have a larger effect than we expected. Thus, we decided to switch the 866 nm laser off and perform the entanglement measurement without conversion once again.

With the Einstein coefficients for the transitions at 854 nm and 850 nm, the ratio between decay along these two channels is $r_{850} = \frac{A_{850}}{A_{850}+A_{854}} = 10.1\%$, that is the probability to experience an erroneous decay is about 10%. Detection of the emitted 850 nm photon mimics the detection of a photon at 854 nm, thus mixing the resulting state. If the 866 nm laser is switched off during the photon generation, the ion will remain in $D_{3/2}$ after the emission of a 850 nm photon, hence we will see a fluorescence signal in the course of the elimination of the undesired superposition states, and the events will be ignored. If, however, the 866 nm is switched on, the ion will be transferred back to the ground-state after decay into $D_{3/2}$, re-excited and might finally end up in the "right" superposition (by emitting an undetected 854 nm photon), but with random phase and therefore results in a mixed-state contribution to the final atomic state.

First we examine the resulting atom-photon state when the 866 nm laser is switched on, and then repeat the measurement with the laser switched off to see if we achieve an improvement in the state fidelity and purity.

Applying the aforementioned atom-photon–state tomography onto the joint atom-photon state (866 nm laser switched **on**), we obtain the reconstructed density matrix shown in 6.7. The imbalance of the two Clebsch-Gordan coefficients is clearly visible in the different

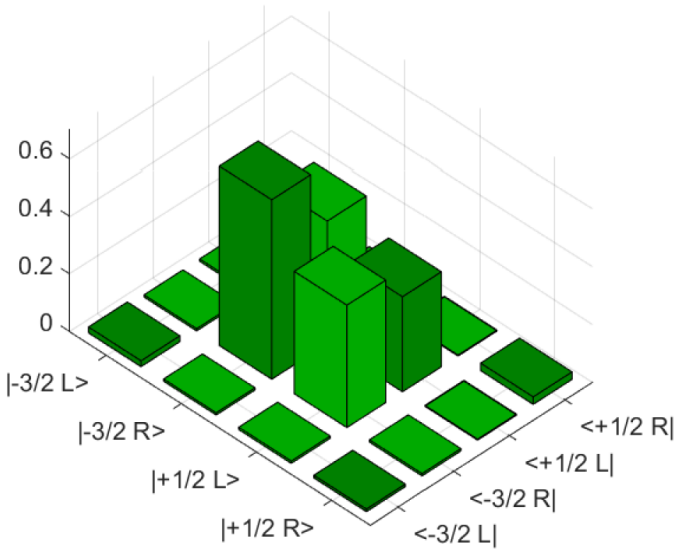

Figure 6.7.: Reconstructed atom-photon density matrix for the atom-photon entanglement at 854 nm. The 866 nm laser was switched on during the photon generation. Shown are the moduli of the matrix entries.

heights of the diagonal elements (i.e. the populations of $|-3/2, \sigma^+\rangle$ and $|+1/2, \sigma^+\rangle$, respectively). Maximum-likelihood reconstruction reveals an overlap fidelity $F = \langle\psi_{\text{Bell}}|\rho|\psi_{\text{Bell}}\rangle$ of 90.2(2)% with the maximally entangled target Bell state $|\psi_{\text{Bell}}\rangle = \sqrt{\frac{1}{2}}|-3/2, \sigma^+\rangle + \sqrt{\frac{1}{2}}|+1/2, \sigma^+\rangle$, which, of course, is reduced by the imbalanced CGCs. It is therefore also

of interest to know the overlap with the expected state $|\psi_{\text{exp}}\rangle = \sqrt{\frac{2}{3}}|-3/2, \sigma^+\rangle + \sqrt{\frac{1}{3}}|+1/2, \sigma^+\rangle$ in order to estimate the quality of our operation. In that case, the overlap fidelity is increased to 92.7(2)%.

Another quantity of interest is the purity $P = tr(\rho^2)$ as a measure for the depolarization of the quantum state. In the present experiment, we obtain a state purity of (86.1 ± 1.2)% for the sequence without switching off the 866 nm laser.

Note that the numbers presented here are obtained after subtracting the detector dark counts as we are interested in the viability of the protocol itself rather than that of the whole experimental setup. Including the current setup into a realistic repeater scenario, the detector dark counts have to be included. Without the dark-count subtraction, the fidelities become 90.2(2)% and 87.9(2)% for the overlap with the expected state and the Bell state, respectively, and the purity reduces to (81.7 ± 1.2)%.

Switching off the 866 nm laser results in a considerable increase in the fidelities and purities. In that case, the generated state, presented in 6.8, exhibits overlap fidelities of 95.5(3)% and 98.3(3)% for the overlap with the Bell state and the expected state, and a purity of (96.7 ± 1.6)%.

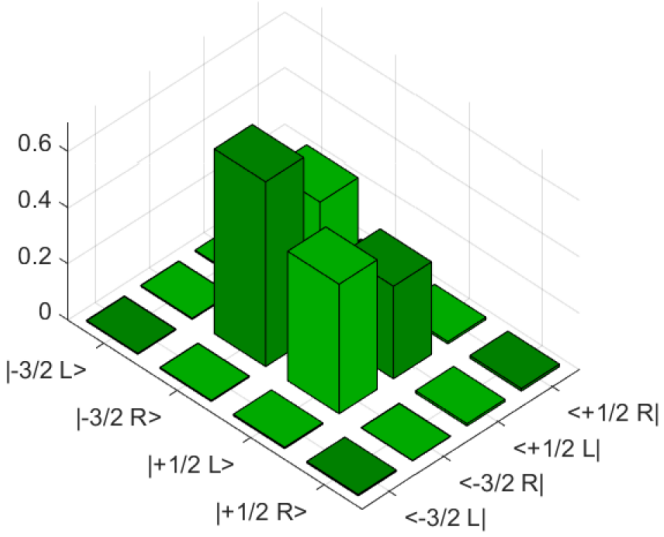

Figure 6.8.: Moduli of the reconstructed density matrix for the atom-photon entanglement at 854 nm with the 866 nm laser switched off during the photon generation.

An upper bound of the fidelity for a given purity is $F_{\text{max}} = \frac{1}{2}(1+\sqrt{2P-1}) = 98.3\%$, indicating that the fidelity is solely limited by depolarization and not by undesired unitary rotations of the state [167]. The sources for depolarization are discussed in the next section. Without background subtraction, we achieve overlap fidelities of 93.3(3)% and 95.9(3)% and a state purity of (92.1 ± 1.6)%.

The experimentally achieved entanglement-generation rate was determined from a total

number of 114,200 photon-detection events in an overall measurement time of 4,123 s. Only the signal events excluding the APD dark counts are considered for the generation rate. The photon-detection window is 300 ns corresponding to 65% of the photonic wavepacket. Thus we get for the detected entanglement rate after projection

$$\gamma_{854,\mathrm{det}} = \frac{114,200\,\mathrm{events}}{4132\,s} = 27.64\,\mathrm{events/s}\,. \tag{6.7}$$

The generated rate is calculated to

$$\gamma_{854,\mathrm{gen}} = \frac{27.6\,\mathrm{events/s}}{\eta_{\mathrm{Pol,trans}} \cdot \eta_{\mathrm{Pol,ab}} \cdot \eta_{\mathrm{APD}}} = 236\,\mathrm{events/s} \tag{6.8}$$

which is in very good agreement with the theoretically derived value of 238 events/s (see 6.2.1). Here we used the transmission of the polarizer $\eta_{\mathrm{Pol,trans}}$ = 78%, the quantum efficiency of the APD η_{APD} = 30%, and an additional factor $\eta_{\mathrm{Pol,ab}}$ = 50% accounting for the fact that the photons are unpolarized (due to the entanglement), resulting in the transmission of only 50% of the photons.

From the number of S_{854} = 114,200 signal events and BG_{854} = 3,868 background events (inside the 300 ns time window) in a total of 4,132 s measurement time, we calculate a signal-to-background ratio of 29.5. The background originates solely from APD dark counts, as it becomes apparent when we calculate the expected number of background events,

$$\mathrm{BG}_{854,\,\mathrm{theo}} = \mathrm{DC}_{\mathrm{APD}} \cdot 300\,\mathrm{ns} \cdot \eta_{\mathrm{Mix}} \cdot \eta_{850} \cdot \gamma_{\mathrm{rep}} \cdot 4,132\,s = 3,803\,, \tag{6.9}$$

being in good agreement with the experimentally determined background. DC_{APD} denotes the APD dark-count rate of 117.7 photons/s, γ_{rep} is the sequence-repetition rate of 58 kHz, η_{Mix} accounts for the already mentioned reduction by a factor of 1/2 due to the fact that the ion starts in a mixture in $S_{1/2}$ instead of a pure state, and $\eta_{850} = \frac{A_{854}}{A_{850}+A_{854}} = 89.9\%$ is derived from the branching ratio between 854 nm and (undesired) 850 nm decay.

6.2.2.4. Error budget

As stated in section 6.2.2.3, the infidelities in the present experiment are primarily traced back to depolarization of the 854 nm photon. Depolarization is mainly caused by polarization-dependent loss in the optics behind the ion trap and loss of atomic coherence due to magnetic-field noise; minor contributions arise from non-perfect readout pulses. The effect of decoherence is estimated by an independent measurement of the coherence time of the ground-state qubit and then extrapolated to our situation. From the ground-state coherence time of approximately 800 µs (varying during the measurement due to changing conditions), derived from a Ramsey measurement, we estimate a contribution to the infidelity of 0.5% within the 108 µs from the state generation to the RF basis-rotation pulse (3 µs generation, 2×50 µs for both 729 nm pulses, 5 µs RF pulse).

6.3. Quantum frequency conversion

So far we have presented a method for the generation of atom-photon entanglement in the near infrared spectral region at 854 nm. Though doubtlessly highly interesting from a technological and fundamental point of view, its practical applicability in a large-scale quantum network is limited by the still rather large losses inside optical fibers of 1.3 dB/km that makes the NIR wavelengths unsuitable for long-haul fiber-communication channels (see fig. 6.9).

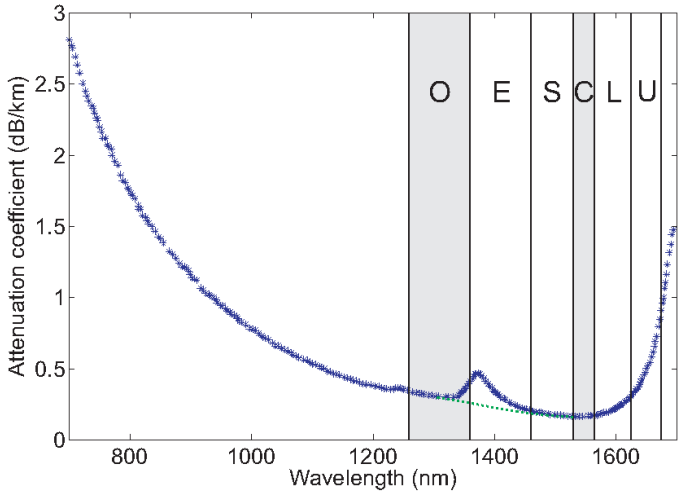

Figure 6.9.: Signal attenuation in standard optical fibers as a function of the photon wavelength. The figure is adopted from [168].

Significantly lower fiber attenuations are achieved in the so-called telecom bands between 1260 nm and 1625 nm. Here two bands are of particular interest, the C band which shows the lowest loss factor, and the telecom O band that exhibits the lowest dispersion.

However, the transition wavelengths of the ion are a fundamental property and can not be changed (at least not by the amount that would be necessary to shift it into the telecom range). Therefore, we have to find a way to convert the frequency of the emitted single photon from the NIR into the telecom regime, ideally without altering its other degrees of freedom, like polarization or the spectro-temporal properties.

An effective method to perform this task is given by the quantum frequency conversion (QFC) which was realized and implemented by Matthias Bock and will be described in detail in his dissertation thesis [73]. A brief description of the concept of QFC shall be given in the next sections.

6.3.1. Theory

The theory presented in this section is a short recapitulation of the respective chapter found in Andreas Lenhard's dissertation thesis [80]. The QFC we employ is based on difference-

frequency generation (DFG) [74] in a periodically-poled Lithium-niobate (PPLN) ridge waveguide [169], where we employ the DFG process $\frac{1}{854\,\mathrm{nm}}$ - $\frac{1}{2456\,\mathrm{nm}}$ = $\frac{1}{1310\,\mathrm{nm}}$ which is depicted in fig. 6.10.

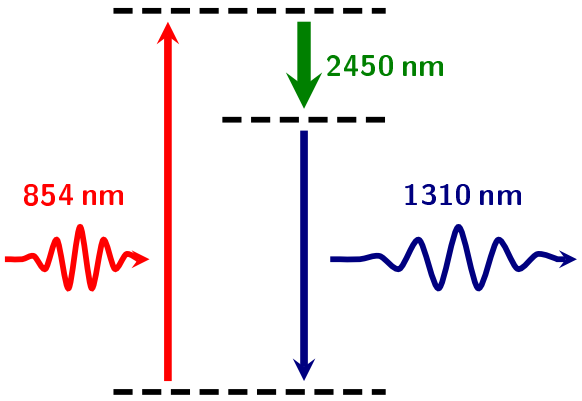

Figure 6.10.: "Level scheme" for the DFG process in the PPLN waveguide. A strong pump field at 2450 nm, stemming from a home-built optical parametric oscillator, stimulates the splitting of the higher-energy photon at 854 nm (called *signal*) into two photons at 1310 nm (*idler*) and 2450 nm (*pump*).

Stimulated by a strong light field at 2450 nm, the input photon at 854 nm (*signal*) is split into two photons at 1310 nm (*idler*) and 2450 nm (called *pump*). Following the description in [80] (which itself is based on [170]), the interaction Hamilton operator for the three light fields inside the waveguide is expressed as

$$\hat{H} = i\hbar\eta\hat{a}_s\hat{a}_p^\dagger\hat{a}_i^\dagger - i\hbar\eta^*\hat{a}_s^\dagger\hat{a}_p\hat{a}_i \,, \tag{6.10}$$

or

$$\hat{H} = i\hbar\eta\hat{a}_s A_p^*\hat{a}_i^\dagger - i\hbar\eta^*\hat{a}_s^\dagger A_p\hat{a}_i \tag{6.11}$$

if we replace the pump photons by the amplitude A_p of the classical pump field, which is justified due to its high power. $\hat{a}_s$, $\hat{a}_p$, and $\hat{a}_i$ are the annihilation operators of the three fields involved, i.e. of the signal-, pump-, and the idler field, respectively, and η is the coupling constant of the process. Solving the dynamics described by the "equations of motion" of the time-dependent photon operators, derived from the Heisenberg relation

$$\frac{d\hat{a}_{s,i}}{dt} = \frac{i}{\hbar}\left[\hat{H}, \hat{a}_{s,i}\right] \,, \tag{6.12}$$

yields

$$\hat{a}_s(t) = \hat{a}_s(0)\,\cos(|\eta A_p|\,t) - e^{i\Phi_p}\,\hat{a}_i(0)\,\sin(|\eta A_p|\,t) \qquad \text{and} \tag{6.13}$$

$$\hat{a}_i(t) = \hat{a}_i(0)\ \cos(|\eta A_p|\, t) + e^{i\Phi_P}\, \hat{a}_s(0)\ \sin(|\eta A_p|\, t)\ , \tag{6.14}$$

where Φ_P is the phase of the pump field. After the time $\tau = \pi/2|\eta A_p|$, an initial Fock state with one photon in the signal mode and zero photons in the idler mode is ideally completely converted into the inverted state with one photon in the idler and no photon in the signal mode.

6.3.2. Converter setup

The setup for the single-photon conversion, designed by Andreas Lenhard and Matthias Bock and described in their respective theses [80, 73] and in [159], is shown in the right part of fig. 6.11. The incoming photon, after passing the 99:1 beam splitter used for the stabilization of the setup, is split according to its polarization (i.e. the horizontal and vertical components) at the first polarizing beam splitter (PBS). Both "half" photons are separated by a dichroic mirror and guided into the periodically-poled Lithium-niobate waveguide from two opposite directions, where the polarization of the part transmitted at the PBS (horizontally polarized) is rotated to vertical polarization using a half-wave plate (HWP) to match the polarization of the pump light at 2456 nm. The latter is guided and focused into the waveguide chip by a ZnSe aspherical lens. The transmitted pump light through the waveguide is back-reflected and recoupled into the chip by a second aspherical lens. The pump power, controlled via a HWP and a polarizer, is chosen such that the conversion efficiencies are equal for both directions (see [159] for details on the optimization process). Coupling the pump field back from the opposite direction facilitates the polarization-independent single-photon conversion as both polarization components of the 854 nm photon, incident from both sides into the waveguide, are converted with equal probability and are therefore not distinguishable after the conversion. The generated 1310 nm photons are subsequently separated by two dichroic mirrors, that also filter out the pump light, and superimposed at a second PBS. To reconstruct the original polarization state, the polarization of the "left" part of the photon, i.e. the part that was transmitted at the first PBS, is rotated back to horizontal before it's overlapped with the reflected path at the second PBS. Following the recombination, the 1310 nm photon passes a band-pass filter centered around 1300 nm (and a width of 25 nm) and a telescope setup to mode-match the photon mode into a single-mode fiber. A tunable fiber Bragg grating (FBG) with an FWHM (full width at half maximum) of 25 GHz is utilized to additionally clean the telecom photons from residual background from the conversion process.

A second 99:1 beam splitter, designed for 1310 nm, behind the second PBS, is used to split a small fraction of the laser light sent during the stabilization period onto the optical-pathway analysis, consisting of a quarter-wave plate (at 22.5°), a PBS and two InGaAs photo diodes. A change in the path length between both arms is related to a variation of the phase between both polarization components H and V and is observed by measuring the signal at both photo diodes. The resulting change in the contrast $\left(\frac{I_1-I_2}{I_1+I_2}\right)$ of the measured

intensities at the two photo diodes is used as the error signal for a PID lock, which is then fed back onto a piezo actuator at the mirror right behind the first PBS.

The chopper wheel is needed to block the laser light during the conversion period to avoid exposure of the single-photon detectors.

The strong pump field at 2456 nm, needed for the DFG process, is produced by a home-built continuous-wave optical parametric oscillator (OPO) which is described in more detail in [74, 80, 159].

The converter setup exhibits an external conversion efficiency (defined as the "fiber-to-fiber" efficiency) of 26.5% for both polarizations, which can, compared to other QFC experiments [171, 172, 70], be regarded as state of the art.

6.3.3. Polarization-independent single-photon conversion

The conversion process is characterized using a laser to perform a full process tomography [157]. Four different input states $\{H, V, D, L\}$ were prepared and the Stokes vector of the output state for each of the input states were measured. The process matrix χ in the usual Pauli basis is calculated from the results. In the ideal case, χ possesses only one single non-zero entry χ_{11}, denoting the identity operation. This entry can be identified as process fidelity, which in our case is $F = (99.75 \pm 0.18)\%$, confirming the coherent conversion of the polarization state. The error in F is deduced from a Poissonian distribution and arises from power fluctuations of the input and the pump field. Details on the characterization are found in [159].

6.4. Atom-photon entanglement in the telecom band

With all tools at hand, the next consequent step is the interconnection of ion- and converter setups to implement a combined quantum interface for the generation of entangled atom-photon pairs in the telecom regime. The full setup, comprising the ion, situated in our laboratory, and the converter part, set up in the laboratory of the group of Christoph Becher and operated by Matthias Bock, is shown in fig. 6.11.

Generation of entanglement between the atom and the NIR photon at 854 nm is employed as before (see section 6.2.1). The fiber-coupled single photons are first sent to an ancilla setup from where they are either guided to the state-analysis setup for 854 nm, including the APDs (see sec. 6.2.2.3), or coupled into a 90 m long single-mode fiber (polarization-isotropic) that connects the ion laboratory with the converter laboratory. Three wave plates ($\lambda/4$, $\lambda/2$, $\lambda/4$) are utilized to compensate for polarization rotations occuring on the photon's way from the ion to the polarization-analysis setup. For that purpose, a laser beam of known polarization is sent along the same path and the three wave plates are adjusted such that the resulting laser polarization at the analysis setup corresponds to its original polarization state. In addition, a fraction of the laser light at 854 nm is also sent to the same lab for the stabilization of the converter setup. Both, the photons and the laser beam are

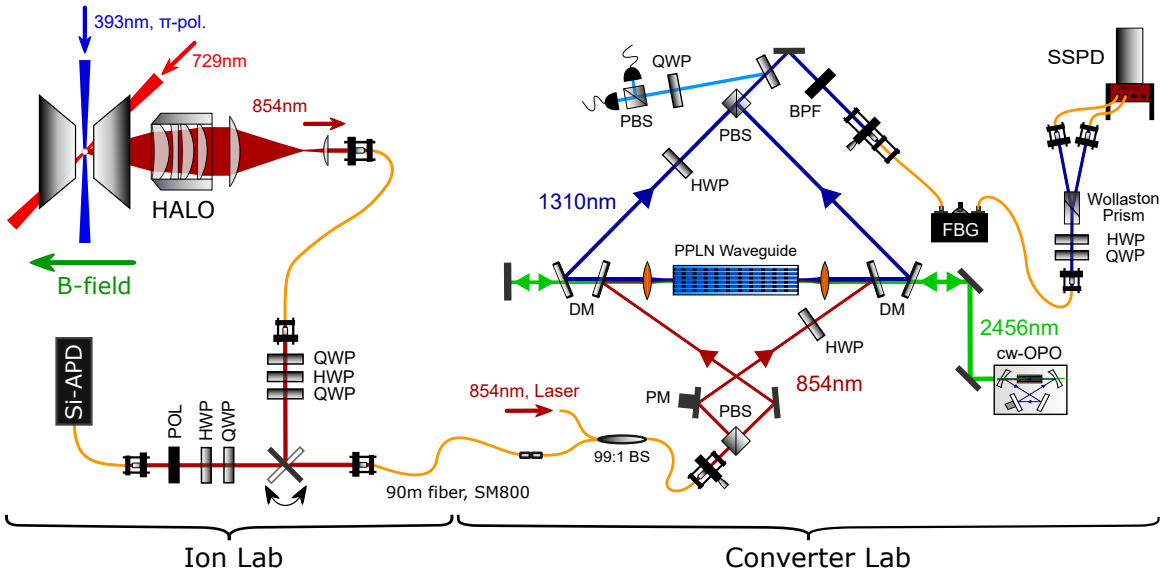

Figure 6.11.: Combined full setup for generation and analysis of atom-photon entanglement at 854 nm (lower left part of the setup) and 1310 nm (right part of the setup) (from [159]). More details on the setup are found in the main text.

passing through a non-polarizing 99:1 beam splitter, while a chopper wheel ensures that either the laser light or the single photons are sent through the converter.

Following the polarization-independent and state-preserving conversion process, described in the previous section, both polarization components of the single incident photons are recombined at the second PBS, pass a band-pass filter (BPS), and are coupled into a single-mode telecom fiber. The fiber-coupled telecom photons are frequency-filtered by a fiber Bragg grating to eliminate background from the conversion process and subsequently guided through a polarization-tomography setup, consisting of two wave plates ($\lambda/4$ and $\lambda/2$ as seen from the converter) and a Wollaston prism serving as a polarizer. Both output arms of the prism are fiber-coupled again and sent to two superconducting single-photon detectors[8] (SSPD) with quantum efficiencies of 70(2)% and 62(2)%, respectively, and dark-count rates of 58.7 $\frac{1}{\mathrm{s}}$ and 56.4 $\frac{1}{\mathrm{s}}$.

Apart from the obvious advantages of the quantum frequency conversion, another beneficial effect is the fact that we do not have to take 850 nm photons, emitted during the generation of 854 nm photons, into consideration, as the conversion of these is strongly suppressed and therefore a filtering comes with the process for free.

The atomic and photonic state analysis are not different for both operations, i.e. for the entanglement generation at 854 nm or 1310 nm, and hence also the two-qubit state tomography presented in sec. 6.2.2 can directly be applied to the case with single-photon conversion implemented.

[8] Single Quantum

The density matrix of the ion-photon state after photon conversion is shown in Fig. 6.12.

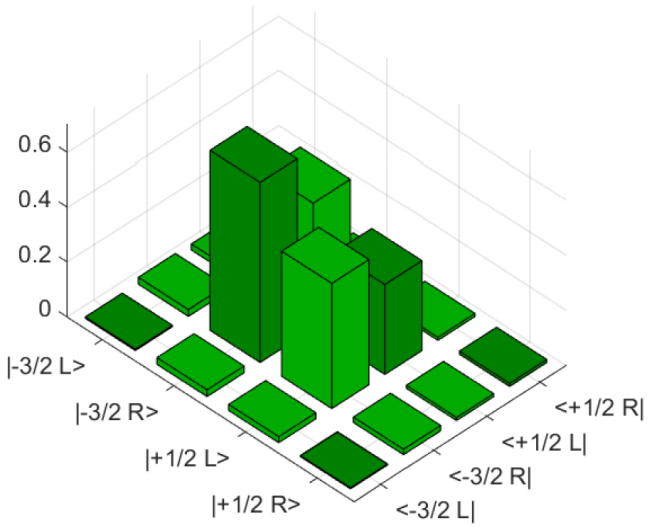

Figure 6.12.: Absolute values of the density-matrix entries for the atom-photon state after single-photon conversion. The density matrix is derived by standard state tomography, described in sec. 6.2.2. The unequal transition probabilities for σ^+ and σ^- are manifested as different heights of the diagonal elements.

As the typical figures of merit, we compute the overlap fidelity with the target Bell state, F_{Bell}, the overlap fidelity with the expected state (6.3), F, and the obtained purity $P = tr(\rho^2)$. The generated state yields $F = (97.7 \pm 0.2)\%$, F_{Bell} = (94.8 $\pm$ 0.2)%, and $P = (95.8 \pm 1.3)\%$. Excluding the background subtraction, the fidelities and the observed purity are reduced to $F = (94.8 \pm 0.2)\%$, F_{Bell} = (92.2 $\pm$ 0.2)%, and $P = (90.3 \pm 1.2)\%$. The created Bell state exhibits, within the error, the same purity as the originally generated atom-photon state, indicating that the conversion process does not significantly alter the polarization of the photon. The fidelity reduction of 0.6% compared to the unconverted ion-photon state is higher than one would expect from the process fidelity[9]. This is attributed to power fluctuations of the pump laser and long-term polarization drifts in the fiber connecting the setups [159].

We achieve an entanglement-generation rate of 43.5 pairs/s (corresponding to 24.8 projected and detected photons per second), with a signal-to-background ratio of 24.3 (29.5 for the protocol without conversion), where the background is primarily resulting from SSPD dark counts (93.5%) and only a minor part (6.5%) is originating from conversion-induced background photons. The comparatively small reduction in the SBR derives from the fact that the conversion loss is partially compensated by the increased detection efficiency and

[9] Although one should note that, taking into account the error bars, the numbers for the purity before and after conversion are almost in accordance.

the decreased background of the SSPDs compared to the APDs.

A slight drawback of all above-mentioned protocols is the limitation of the maximally achievable fidelity due to the imbalanced Clebsch-Gordan coefficients for both decay channels at the 854 nm transition. The converter setup provides a way to overcome this limitation by introducing polarization-dependent loss in the conversion process, thus allowing for a better approximation to a fully-entangled atom-photon state. For that purpose, right- and left-hand circular polarized 854 nm photons emitted by the ion are rotated to possess vertical and horizontal polarization at the input PBS of the converter setup in fig. 6.11 with the help of the three rotation-compensation wave plates, such that the R and L components of the polarization of the emitted photon correspond to both interferometer arms of the converter setup. After being split up according to their polarization (where photons emitted on the σ^- transition take the "left" path through the waveguide and vice versa for the part of the photon emitted on the σ^+ transition) and being converted in the waveguide, both branches are again superimposed at the second PBS. The CGC compensation occurs at this second PBS. The half-wave plate in the left branch of the interferometer is set to rotate the photon to an (anti-)diagonal polarization, such that we artificially introduce loss in that arm and thereby compensate for the stronger σ^+ transition. This happens at the cost of one third of the photons. After the recombination of both arms, we obtain a (ideally) maximally entangled state. Before impinging onto the polarization-projection setup, the original polarization state is restored by a second set of $\lambda/4$, $\lambda/2$ and $\lambda/4$ wave plates (not shown in the figure) which are adjusted accordingly.

The resulting measured density matrix is displayed in fig. 6.13. The asymmetry in the diagonal elements is drastically reduced, indicating balanced probabilities for photon detection from both transitions, and we obtain $F_{\text{Bell}} = (98.2 \pm 0.2)\%$ and $P = (96.7 \pm 1.4)\%$, or $F_{\text{Bell}} = (93.4 \pm 0.2)\%$ and $P = (87.8 \pm 1.3)\%$ without background subtraction. Note that fidelity and purity in this measurement are also in accordance with the process fidelity, which we attribute to a slightly more stable operation of the converter.

As before, the infidelity is mainly caused by depolarization of the photonic part of the entangled atom-photon pair and by decoherence of the atom caused by magnetic-field noise (see 6.2.2.4).

6.5. Atom-to-photon state transfer in the NIR

In section 5.3 we demonstrated the conception and realization of an experimental protocol for atom-to-photon quantum-state transfer as it could be employed in quantum-communication schemes. Despite the technological progress that has been initiated by that development, the protocol suffers from its unfavorable wavelength regime which renders its practical applicability possible only for very short communication lengths. Fortunately, a small modification of the named protocol provides the solution to the problem. Exploiting the emission of 854 nm generated during the transfer process, which were previously treated as an unwanted side effect, allows us to map the atomic state onto he polariza-

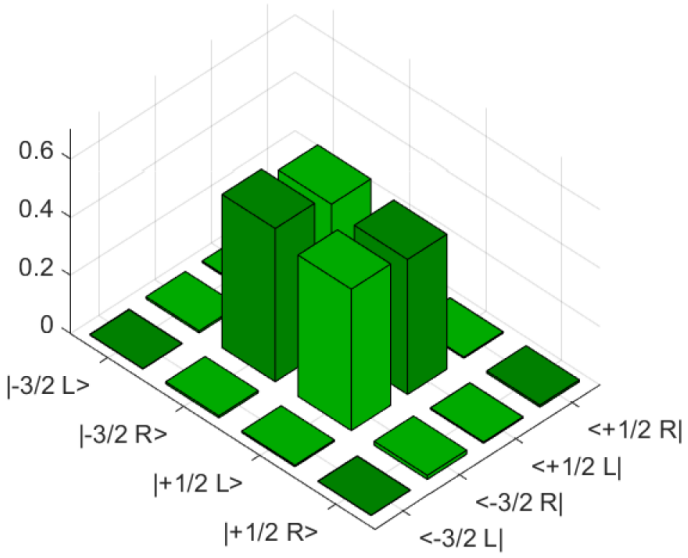

Figure 6.13.: Moduli of the elements of the atom-photon density matrix in the telecom range after implementing the CGC compensation described in the main text. Compared to fig. 6.12, the diagonal elements are clearly more balanced, resulting in a significant increase in the overlap fidelity with the maximally entangled Bell state.

tion of a photon with a much more suitable wavelength. In addition, quantum frequency conversion (cf. sec. 6.3) can be employed to reduce the transmission losses even more and make the transfer protocol appropriate for long-haul quantum communication. The experimental protocol, a novel alternative scheme for the quantum-process tomography, the experimental results, and an estimation of the error budget are presented in the following sections.

6.5.1. Experimental sequence

The experimental sequence is depicted in fig. 6.14. To characterize the state-transfer quantum process, we prepare a set of four different atomic input states, two eigenstates

$$|S_{1/2}, -1/2\rangle \text{ and } |S_{1/2}, +1/2\rangle \text{ , and the two superpositions}$$
$$\frac{|S_{1/2}, -1/2\rangle + |S_{1/2}, +1/2\rangle}{\sqrt{2}} \text{ and } \frac{|S_{1/2}, -1/2\rangle + i\,|S_{1/2}, +1/2\rangle}{\sqrt{2}} \text{ .}$$

The preparation of atomic input states starts with optical pumping. Depending on the desired state, the ion is either pumped into $|S_{1/2}, -1/2\rangle$, as shown in fig. 6.14 a) (for the preparation of $|-1/2\rangle$ and the two superpositions), or into $|S_{1/2}, +1/2\rangle$ by adjusting the pump frequencies accordingly.

Once the pumping, lasting for 50 µs, is accomplished, an optional RF $\frac{\pi}{2}$ pulse of variable phase and a pulse length of 5 µs is applied for the generation of the superposition

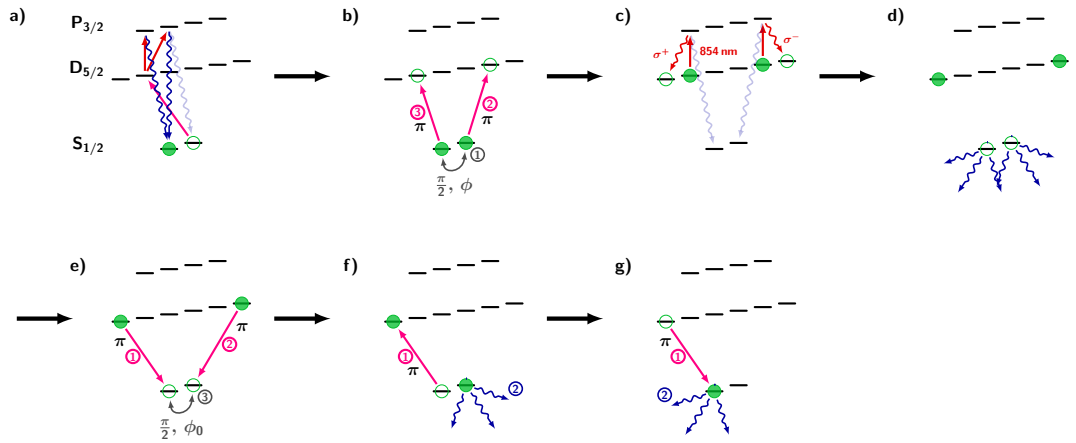

Figure 6.14.: Experimental sequence for the atom-photon state transfer protocol. **(a)** The sequence starts with optical pumping of the ion into the pure state $|S_{1/2}, -1/2\rangle$. **(b)** The state to be mapped into the photon is generated by a coherent RF $\frac{\pi}{2}$ pulse with variable phase ϕ (in the case of an initial superposition) or encoded into one of the eigenstates $|S_{1/2}, \pm 1/2\rangle$ by optical pumping (see (a)), and is subsequently coherently transferred into the $D_{5/2}$-manifold sub-levels $|\pm 3/2\rangle$. In an implementation of the protocol into a real quantum network, the steps (a) and (b) would be skipped as the states would already be stored in the ion. **(c)** Applying a horizontally polarized 854 nm laser pulse under 90° to the quantization axis excites the ion to the $P_{3/2}$ state along the π transition, from where it decays into the outermost $D_{5/2}$ sub-states, generating an entangled atom-photon pair. Decay into $S_{1/2}$ (being most likely) is eliminated by fluorescence detection adjacent to the generation (**(d)**). **(e)** Atomic-state projection onto an atomic superposition is carried out by coherently transferring the atomic state back to $S_{1/2}$ and applying an RF $\frac{\pi}{2}$ pulse with a fixed phase ϕ_0, followed by two state-shelving pulses and two fluorescence detections (**(f)** and **(g)**).

states. Two consecutive resonant 729 nm pulses of 10 µs length coherently transfer the population in the ground state into the respective state in the $|D_{5/2}, \pm 3/2\rangle$ sub-space. A horizontally-polarized laser pulse at 854 nm (3 µs), incident under 90° to the quantization axis, excites the ion to the short-lived $P_{3/2}$ manifold. Direction and polarization of the 854 nm ensures excitation solely along the π transitions $|D_{5/2}, -3/2\rangle \rightarrow |P_{3/2}, -3/2\rangle$ and $|D_{5/2}, +3/2\rangle \rightarrow |P_{3/2}, +3/2\rangle$. Upon absorption of a laser photon, the ion decays into the outermost $D_{5/2}$ levels under emission of a single photon at 854 nm. Due to the coupling of photon polarization and atomic transition, the decay results in the generation of an entangled atom-photon state, where the complex population amplitudes of the initial atomic state enter into the entangled state.

Decay occurring on the $P_{3/2} \rightarrow S_{1/2}$ transition is detected by fluorescence generation for 20 µs that discriminates these events with 99% probability. If a fluorescence photon is detected, the data is discarded and the sequence is restarted. Decay into one of the inner $D_{5/2}$ sub-levels is eliminated in a later stage by projection of the atom onto one of the states $|\pm 5/2\rangle$.

To map the initial atomic state onto the polarization state of the 854 nm photon, it is nec-

essary to project the atom onto a symmetric superposition state to erase the information on the initial qubit from the atomic sub-system and fully transfer the state onto the photonic part. This is realized by coherently transferring the atomic state back into $S_{1/2}$ assisted by two 729 nm pulses ($2 \times 10\,\mu s$) and applying an RF basis-rotation $\frac{\pi}{2}$ pulse. State projection is conducted by shelving of the $|-1/2\rangle$ population into the $D_{5/2}$ manifold and subsequent fluorescence generation (50 µs). If the ion stays dark during the fluorescence detection, the population is transferred back from $D_{5/2}$ into the ground state and another fluorescence detection takes place. If the ion stays dark during both read-outs, the data is discarded and the sequence is restarted, thus eliminating unwanted decay into the inner $D_{5/2}$ sub-levels. If the ion becomes bright in one of the two fluorescence detections, the state has successfully been projected and the initial atomic state is mapped onto the photon.

In the actual sequence, two additional shelving pulses, $|S_{1/2}, -1/2\rangle \rightarrow |D_{5/2}, -5/2\rangle$ and $|S_{1/2}, +1/2\rangle \rightarrow |D_{5/2}, +5/2\rangle$ and another fluorescence detection (where the sequence is only continued if the ion stays dark), are included after step (e) in fig. 6.14 to be more robust against imperfect 729 nm pulses. State discrimination is then conducted by consecutively transferring the population of $|\pm 5/2\rangle$ back to the ground state and analyze the population by fluorescence detection.

Following the pulse sequence, the ion is Doppler cooled for 10 µs before the sequence is restarted. During Doppler cooling, 854 nm laser light is applied to repump remaining population in $D_{5/2}$ back to $S_{1/2}$. The cooling can be reduced to the rather short duration of 10 µs since the probability for two consecutive fluorescence generations (i.e. for two consecutive photon-detection events) is small and the effective cooling time is much larger than the 10 µs. In sum, conditioning the state-analysis process on the detection of an 854 nm photon, we achieve an overall sequence-repetition rate of 8.3 kHz including the analysis pulses and fluorescence detections.

6.5.2. Quantum-process tomography

In this section, we will explore an alternative approach for the evaluation of a quantum process (i.e. the state-mapping process in the case of this experiment), which has originally been proposed in [157], in addition to the usual quantum-process–matrix formulation. The numerical implementation in the form of the underlying MATLAB script has been written by Stephan Kucera. One should note that both formulations are fully equivalent, as it will be briefly depicted in this section and is shown in detail in [157], and we will apply both for the characterization of the state mapping.

Generally speaking, a quantum process ε can be describes by its action onto an input state $\vec{\lambda}$, obeying to the prescription $\vec{\lambda} \xrightarrow{\varepsilon} \vec{\lambda}' = \mathbf{M}\vec{\lambda} + \vec{c}$. Here, $\mathbf{M}$ is a 3×3 matrix describing the rotation and compression of the three-dimensional input-state Bloch vector, leading to the resulting state $\vec{\lambda}'$, and $\vec{c}$ corresponds to a translation in the state space. Compression of the output-state vector $\vec{\lambda}'$ with respect to the input state $\vec{\lambda}$ corresponds to decoherence introduced by the quantum process ε and is reflected in the singular values s_i of $\mathbf{M}$.

A MATLAB script is used to find the best-matching values of $\mathbf{M}$ and $\vec{c}$ to describe the transformation from a set of prepared input states into a set of measured output states. Due to the Larmor precession of the initial atomic superposition (given that the atom is not prepared in one of the energy eigenstates), the atomic phase oscillates with time and allows for the scanning of different input states. As before, the photon-arrival time is translated into the phase of the input state, and the probability for projection of the photon state onto the two possible outcomes for the different photonic measurement bases (H/V, D/A, and R/L) is derived from the detection events via Bayesian estimation. Starting from an initial guess for $\mathbf{M}$ and $\vec{c}$, the script runs an iterative optimization algorithm to find the photonic output states that best reproduces the measured results for a set of known atomic input states, which are assumed to be ideally prepared. For each iteration, the program examines if the step produces a physical state and if an improvement regarding the probability to reproduce the measured results has been achieved. If both conditions are fulfilled, the new state is adopted, otherwise it is revoked[10]. As mentioned before, the method is also described in Stephan Kucera's thesis [124] and summarized in more detail in Philipp Müller's dissertation thesis [81].

In the experimental implementation, we prepare the ion in both energy eigenstates $|\mathrm{D}_{5/2}, \pm 3/2\rangle$, and in the (temporally oscillating) superposition $|-3/2\rangle + e^{i\varphi(t)}|+3/2\rangle$ between these two states. Despite not necessarily required, we also include the measurement for the superposition $|-3/2\rangle + e^{i\varphi(t)}e^{i\frac{\pi}{2}}|+3/2\rangle$ with an additional phase of $\frac{\pi}{2}$ into the measurement as a proof of principle to demonstrate the possibility to purposefully imprint a phase onto the mapped photonic state.

We infer the mean overlap fidelity of atomic input and photonic output state (not taking into account a known state rotation, which can easily be compensated for) from the singular values of $\mathbf{M}$ according to

$$\bar{F} = \frac{\bar{s}+1}{2}\,, \tag{6.15}$$

where $\bar{s} = \sum_{i=1}^{3} s_i$ denotes the mean of the singular values s_i.

After some maths, we find the relation between $\mathbf{M}$ and $\vec{c}$ and the quantum-process matrix χ [81]:

$$c_i = 4\mathcal{R}(\chi_{1i})\,, \tag{6.16}$$

$$M_{ij} = (2\chi_{11} - 1)\,\delta_{ij} + 2\mathcal{R}(\chi_{ij}) - 2\sum_{k=1}^{3}\epsilon_{ijk}\mathcal{I}(\chi_{1k})\,. \tag{6.17}$$

Here, ϵ_{ijk} is the Levi-Civita symbol, δ_{ij} is the Kronecker delta, and $\mathcal{R}(...)$ and $\mathcal{I}(...)$ denote the real and imaginary parts. χ_{mn} describe the components of the quantum-process matrix

[10] Though there is a certain probability defined within the script that a new state is adopted nonetheless, even if it shows no improvement towards the previous state. This has been implemented to prevent the optimization to be trapped in a local extremum.

χ defined by

$$\rho_{\text{out}} = \sum_{m,n=1}^{4} \chi_{mn} \hat{\sigma}_m \rho_{\text{in}} \hat{\sigma}_n^\dagger \,, \tag{6.18}$$

with the Pauli matrices $\hat{\sigma}_{2,3,4}$ and $\sigma_1 = \mathbb{1}$.
The characterization methods presented here will be applied to the experimental results shown in the next section.

6.5.3. Experimental results

We benchmark the state-mapping process by preparing four atomic input states (two eigenstates and two superposition states with initial phases 0° and 90°). For each input state, we perform full state tomography on the mapped photonic polarization state to deduce the Matrix **M**, extracting the rotation and deformation (compression) of the input state, and the translation of that state in the Bloch-sphere representation given by the three-dimensional vector $\vec{c}$.

Due to the Larmor precession of the superposition states, the instant of the photon emission determines the additional time-dependent phase of the transferred state, i.e. an additional polarization rotation. This is reflected in an oscillation of the conditioned photon-arrival-time distribution, similar to the wave-packet shown in section 6.2.2.1, when the photon is projected onto a linear polarization. Summing the photon detections into events with equal (reduced) phase, we obtain the histogram shown in fig. 6.15. As expected, the

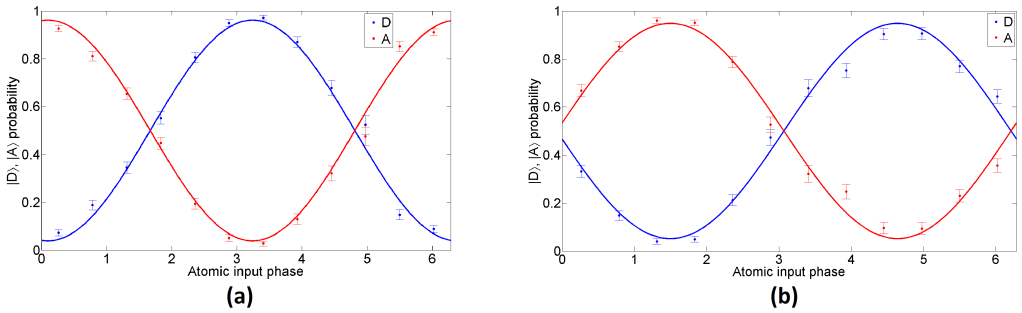

Figure 6.15.: Conditioned photon-detection histogram for projection of the 854 nm photon onto the linear bases D and A and projection of the atom onto a fixed superposition state for different atomic input states. **(a)** Initializing the atom in the superposition state with a starting phase of 0°. **(b)** Starting phase set to 90°. The oscillation occurs due to the Larmor precession of the atomic superposition state. The phase shift of the mapped photonic state caused by the different initial atomic superposition phases is nicely visible.

initial superposition phase is directly mapped onto polarization phase of the photon, proving our ability of state transfer. Additionally, the photon is measured in the circular bases for full state tomography.

In the experimental realization, we achieve a sequence-repetition rate of 8.33 kHz. Caused by the branching ratios between the decay along the 854 nm, 850 nm and 393 nm transition, an excitation cycle results in a probability η_{854} of 5.87% for the emission of a single 854 nm photon. Further reduction of the 854 nm-photon–emission probability on the desired decay path of $\eta_{\mathrm{CGC}} = 2/3$ occurs due to the Clebsch-Gordan coefficients that cause decay into other but the outermost $D_{5/2}$ Zeeman sub-levels which will be projected out in a later step. Additional photon-loss contributions are the collection efficiency η_{HALO} of the HALO of 6%, the single-mode–fiber coupling η_{FC} of 40% and a transmission efficiency η_{trans} from the ion to the detection setup, which has been estimated to be 80% for the 854 nm state transfer, as well as a factor η_{Phot} of about 65% that accounts for the fact that we only use 200 ns of the photon wave-packet. With the (average) quantum efficiencies η_{APD} of 30% for the APDs, we expect an overall detection efficiency of $\eta(854\,\mathrm{nm}) = \eta_{854} \cdot \eta_{\mathrm{CGC}} \cdot \eta_{\mathrm{Phot}} \cdot \eta_{\mathrm{HALO}} \cdot \eta_{\mathrm{FC}} \cdot \eta_{\mathrm{trans}} \cdot \eta_{\mathrm{APD}} \approx 0.15\%$ for the atom-to-photon state transfer. In the actual experiment, we obtain a total of 48616 signal events (i.e. detected photons after correcting for the background) in $3 \cdot 10^8$ experimental runs, corresponding to a transfer efficiency of 0.16%, being slightly higher than our estimated value, which we attribute to higher-than-expected overall transmission efficiency. With the repetition rate of 8.33 kHz, we get a state-transfer success rate of 1.35 detected successful mapping events per second. From the experimental results, we extract 485 background events in the measured 854 nm photon wave-packet, yielding a signal-to-background ratio of $SBR_{854} = 48616/485 = 100(5)$.

Performing the state-transfer tomography presented in the previous section, we obtain $\mathbf{M}$ and $\vec{c}$ using the MATLAB script described in [124], which is depicted in a Bloch/Poincaré-sphere representation in fig. 6.16 (a). The plot represents the rotation, damping and translation of the input states after the mapping process. From the singular values $s_1 = 0.983$, $s_2 = 0.919$, and $s_3 = 0.881$, we calculate the mean overlap fidelity of the mapped state with the ideal state following eq. (6.15) as $\bar{F} = (96.4 \pm 1.0)\%$. From $\mathbf{M}$ and $\vec{c}$ we infer the process matrix χ shown in fig. 6.16 (b). The identity component χ_{11}, defined as the process fidelity, is 94.5%. From the connection between χ_{11} and $\bar{F}$, given by eq. 5.10, we expect a mean fidelity of 96.4%, which is in good agreement with the result obtained from the singular values of $\mathbf{M}$. Furthermore we estimate the mean purity $\bar{P}$ of the mapped state from $F_{\mathrm{max}} = \frac{1}{2}(1+\sqrt{2P-1})$ as $\bar{P} \geq \frac{(2F-1)^2+1}{2} \approx (93.1 \pm 1.9)\%$.

The results presented here were obtained after correcting for detector dark counts as we want to evaluate the viability of the quantum interface independent of the detection setup. Including the background into the evaluation, we obtain $\bar{F} = (94.9 \pm 1.2)\%$, $\bar{P} \geq (90.3 \pm 2.1)\%$, and $\chi_{11} = 93.8\%$.

As the error estimation proves to be rather tricky, we employ an additional approach for the determination of the mean mapped-state overlap fidelity. In particular, we reconstruct the mapped photonic state for each fixed and known atomic input state and calculate the overlap fidelities between the respective input and output states. From that, we obtain a mean overlap fidelity including the error interval from the standard deviation.

Using this method, we get a mean overlap fidelity of $\langle F \rangle = (97.2 \pm 1.7)\%$, corresponding

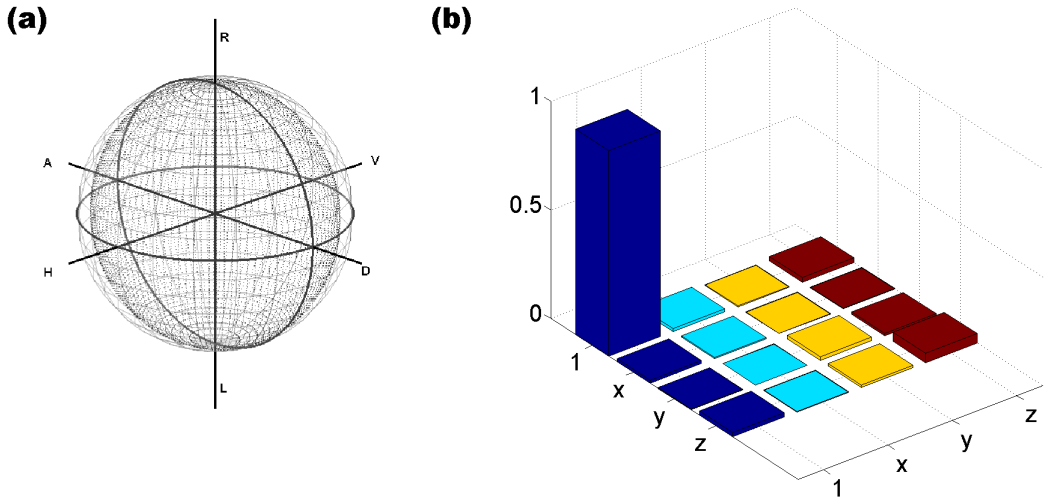

Figure 6.16.: (a) Visualization of the combined effect of **M** and $\vec{c}$, describing the state-mapping process, onto the photonic output state. The plot shows the rotation, translation and compression (decoherence) of the mapped states with respect to the atomic input states which we assume to be pure. **(b)** Quantum-process–matrix representation of the mapping process from the atomic input state onto the polarization state of the emitted 854 nm photon. The unity component χ_{11} is identified as the process fidelity.

to a mean state purity of $\bar{P} \geq (94.6 \pm 3.2)\%$, which is, withing the error bars, in good agreement with the previously determined numbers. Reverse calculation of the process fidelity χ_{11}, using

$$\chi_{11} = \frac{3\langle F \rangle - 1}{2}\,, \tag{6.19}$$

exhibits a value of $\chi_{11} = (95.8 \pm 2.6)\%$, where the error is derived from error propagation. Without background correction, we get $\langle F \rangle = (96.9 \pm 1.6)\%$, $\bar{P} \geq (89.5 \pm 4.5)\%$, and $\chi_{11} = (95.4 \pm 2.4)\%$.

Directly calculating the mean purity $\langle P \rangle = \langle tr(\rho^2) \rangle$ for the different input states, we obtain $\langle P \rangle = (90.6 \pm 4.7)\%$, which at first glance appears too low to explain the observed mean fidelity. However, taking the rather large error margin into account, the numbers are in accordance again.

6.5.4. Error budget

To identify potential for further improvement of the interface, an estimation of the error sources and their influence onto the quantum process has to me made. In this experiment, the infidelities are attributed to three main contributions:

(i) polarization-dependent losses on the photonic beam path from the emitting ion to the detection/projection setup,

(ii) magnetic-field noise that leads to decoherence of the atomic Zeeman qubit, and

(iii) atomic back-decay and re-excitation into and from the initial sub-levels in $D_{5/2}$,

which shall be discussed in the following.
(i) The effect of depolarization has already been discussed in 6.2.2.4. Polarization-dependent losses bias the atom-photon state towards one of the polarization eigenaxes, allowing an observer to extract the photon state to a certain degree, reducing the overlap with the maximally entangled state. Since the potentially polarizing elements are the same for both experiments, we can estimate the same amount of reduction of 1.8% of the Bell-state overlap fidelity. Including the QFC process, the depolarization is comparable to the one presented in in 6.2.2.4, resulting in a fidelity reduction of 1.3%.
(ii) The atomic coherence time is derived from a set of Ramsey-type measurements on the ground-state RF transition. From the ground-state coherence time, 800 µs, we calculate the effective coherence time for the involved superpositions[11] as 400 µs. For the overall mapping-process duration of 53 µs, this corresponds to an expected fidelity reduction of 0.9%.
(iii) The contribution of the back-decay is estimated by a rate-equation model. Assuming we start from the coherent atomic superposition $\alpha|D_{5/2}, -3/2\rangle + \beta|D_{5/2}, +3/2\rangle$, which we denote as $|i\rangle_c$. α and β are the (complex and normalized) amplitudes describing the state. Excitation along the π transition into $|P_{3/2}, \pm 3/2\rangle$ results in decay along one of three possible paths (where we subsume decay into any other $D_{5/2}$ sub-level than the outermost, which primarily occurs into $|\pm 3/2\rangle$, as one path to obtain an upper bound for the decoherence): 1) Decay into the "garbage" state $S_{1/2}$ (and less likely also into $D_{3/2}$), where the ion is decoupled from the driving field. We call that state $|f\rangle_g$. These events represent the majority of decay processes and are eliminated in a later state-discrimination phase. 2) The (desired) decay into $|\pm 5/2\rangle$, generating entanglement between the polarization state of the emitted 854 nm photon and the coherent atomic state $|f\rangle_c = \alpha'|D_{5/2}, -5/2\rangle + \beta'|D_{5/2}, +5/2\rangle$. 3) Adverse effects appear when the ion decays back to its initial state, i.e. $|\pm 3/2\rangle$, or, to a smaller degree, into $|\pm 1/2\rangle$. This causes an incoherent contribution to the initial superposition, $|i\rangle_i$. Upon re-excitation, the ion again undergoes decay along one of the three channels. As the ion now starts from an incoherent state, decay to $|\pm 5/2\rangle$ consequently transfers the atom into an incoherent final state $|f\rangle_i$. Repeated decay to $|i\rangle_i$ leads to re-excitation followed by subsequent decay, and so on. The probabilities for the three processes are determined by the branching ratio between the transitions at 393 nm and 854 nm and the respective CGCs of the individual sub-transitions within one transition.

To find a quantitative solution for the temporal dynamics of the system, i.e. the amount of decoherence caused by transfer of the incoherent initial part into the final state versus the percentage of the photon wave-packet that is taken into consideration, we formulate the problem in terms of rate equations for the five initial and final states $|i\rangle_c$, $|i\rangle_i$, $|f\rangle_c$, $|f\rangle_i$, and $|f\rangle_g$.

[11] The coherence time for the eigenstates is not of relevance as they do not decohere from magnetic-field noise.

Taking that the driving field excites the ion to the short-lived upper state with rate R, and the total decay rate of said excited state is Γ. Γ consists of three rates, Γ_g, describing the decay into $S_{1/2}$, Γ_f for the decay into $|f\rangle_c$ and $|f\rangle_i$, and Γ_i, representing the decay back into the initial starting levels. If we assume that $p(|\bullet\rangle_\bullet)$ describes the populations of the respective states, the formulation of the corresponding rate equations is fairly instructive:

$$\frac{d}{dt}p(|i\rangle_c) = -Rp(|i\rangle_c) \tag{6.20}$$
$$\frac{d}{dt}p(|i\rangle_i) = R\frac{\Gamma_i}{\Gamma}p(|i\rangle_c) + R\frac{\Gamma_i}{\Gamma}p(|i\rangle_i) - Rp(|i\rangle_i) \tag{6.21}$$
$$\frac{d}{dt}p(|f\rangle_c) = R\frac{\Gamma_f}{\Gamma}p(|i\rangle_c) \tag{6.22}$$
$$\frac{d}{dt}p(|f\rangle_i) = R\frac{\Gamma_f}{\Gamma}p(|i\rangle_i) \tag{6.23}$$
$$\frac{d}{dt}p(|f\rangle_g) = R\frac{\Gamma_g}{\Gamma}p(|i\rangle_c) + R\frac{\Gamma_g}{\Gamma}p(|i\rangle_i)\,. \tag{6.24}$$

Initially starting from a fully coherent state, i.e. $p(|i\rangle_c)(t=0) = 1$, the equations (6.20)-(6.24) yield the solutions

$$p(|i\rangle_c) = e^{-Rt} \tag{6.25}$$
$$p(|i\rangle_i) = e^{-R(1-\Gamma_i/\Gamma)t} - e^{-Rt} \tag{6.26}$$
$$p(|f\rangle_c) = \frac{\Gamma_f}{\Gamma}\left(1 - e^{-Rt}\right) \tag{6.27}$$
$$p(|f\rangle_i) = \frac{\Gamma_f}{\Gamma\left(1-\Gamma_i/\Gamma\right)}\left(e^{-Rt}\left(1-\frac{\Gamma_i}{\Gamma}\right) + \frac{\Gamma_i}{\Gamma} - e^{-R(1-\Gamma_i/\Gamma)t}\right) \tag{6.28}$$
$$p(|f\rangle_g) = \frac{\Gamma_g}{\Gamma\left(1-\Gamma_i/\Gamma\right)}\left(1 - e^{-R(1-\Gamma_i/\Gamma)t}\right)\,. \tag{6.29}$$

Fig. 6.17 displays the solutions for the relevant populations $p(|f\rangle_c)$, $p(|f\rangle_i)$, and $p(|i\rangle) = p(|i\rangle_c) + p(|i\rangle_i)$, where we inserted the experimental parameters $\Gamma_g/\Gamma = 0.9413$, $\Gamma_i/\Gamma = 0.0196$, $\Gamma_c/\Gamma = 0.0391$, and $R \approx 1/200\,\text{ns} = 5\,\text{MHz}$[12]. We see that after $1/e$ of the photonic wave-packet, the percentage of the incoherent part to the entire final state (i.e. $|D_{5/2}, \pm 5/2\rangle$) is 0.8%, corresponding to a reduction of 0.4% in the expected mapped-state overlap fidelity.

In total, we obtain an expected mapped-state fidelity of $100\% - 1.8\% - 0.4\% - 0.9\% = 96.9\%$, which nicely agrees with the experimentally observed values.

[12]The precise value is not too important for this calculation as we interested in the decoherence for a certain fraction of the photonic wave-packet.

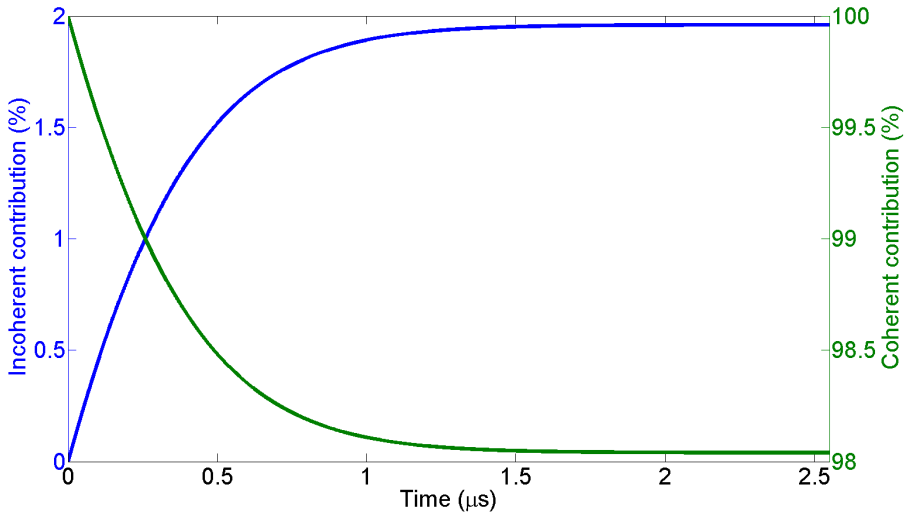

(a)

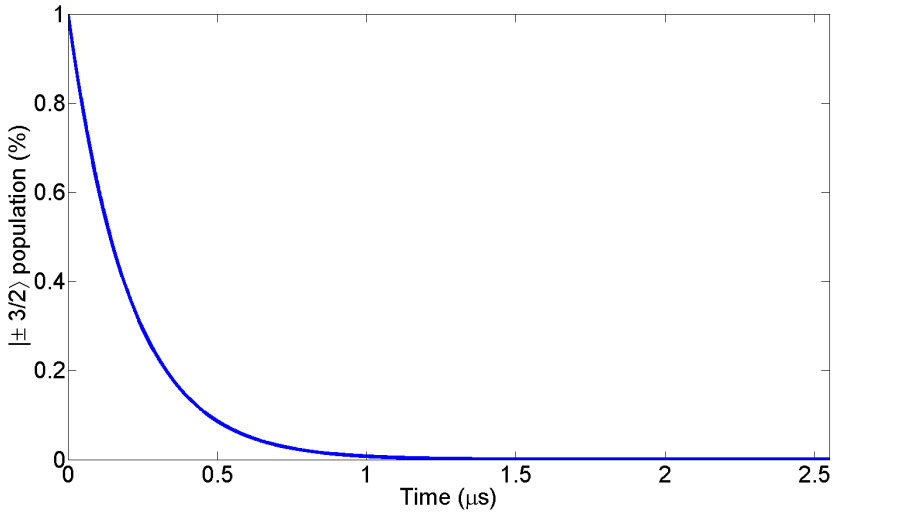

(b)

Figure 6.17.: Coherent (blue) and incoherent (green, caused by back-decay and re-excitation) contribution to the final atomic superposition $|f\rangle_c = \alpha'|D_{5/2}, -5/2\rangle + \beta'|D_{5/2}, +5/2\rangle$ (see main text) after the state-mapping process. Also shown is the population of the initial (coherent) superposition state (black), which is exponentially depleted due to the exciting laser. After $1/e$ of the photonic wavepacket (corresponding to a decrease of $1/e$ in the initial-state population), we expect an incoherent percentage of 0.8% to the final state.

7. Prospect: Towards local atomic two-qubit gates

The combination of our universal quantum interface for the generation of atom-photon entanglement and the bi-directional atom-to-photon and photon-to-atom quantum-state transfer with the possibility of polarization-state preserving quantum frequency conversion facilitates the distribution of quantum information or quantum entanglement over some kilometers of distance with reasonably low losses. However, this is only one building block for the implementation of a quantum-memory–based quantum-repeater network.

The realization of the memory-based quantum repeaters additionally requires local (de-) entangling two-atom gates to perform the atomic Bell-state measurements needed for the entanglement-swapping process. Our approach for these gates lies in the Mølmer-Sørensen (MS) gate, operating on the motional sideband transitions of the trapped ions. The theory concerning the MS gate, the experimental implementation, and the discussion of experimental challenges are the topic of section 7.2.

On top of the entangling two-qubit gate, we need the ability for single-ion addressing to selectively perform single-qubit rotations on the individual atoms for practical reasons. For that purpose, an addressing beam at 729 nm was set up. Focusing that beam through the HALO allows us to reach spot sizes below the inter-ion distance, thus enabling us to drive one ion while the other one stays nearly unaltered. The simple approach for an addressed single-ion rotation is presented in section 7.1.1, where the addressing beam is directly used for resonant state manipulations. However, this approach exhibits some drawbacks, as it requires interferometric stability between the addressing beam and the global 729 nm beam under 45°, which is, though not impossible, technically demanding.

Therefore, we developed an alternative ansatz to circumvent the necessity for interferometric stability by operating the addressing beam off-resonantly to the atomic transition, introducing a single-atom phase shift, which can then be used to effectively perform a rotating pulse on one ion while the other ion returns into its initial state after the pulse sequence. This technique is discussed in section 7.1.2.

7.1. Single-ion addressing and single-qubit gates

Characterization of the two-ion entangling gate requires local operations on the individual atoms to perform joint atom-atom-state measurements in different two-atom bases. For that purpose, an additional 729 nm beam, directed onto the ion through the HALO (0°),

was set up (cf. fig. 2.5). The achieved focal spot size owing to the HALO of about 2 µm lies below the typical inter-ion distance of 5 µm, thus allowing for the separate addressing of the ions. Switching between the ions is facilitated by an acousto-optic deflector[1] (AOD), set up in single-pass configuration in the beam line and tilted by 22.5° to match the orientation of the trap axis. Depending on the applied RF frequency, the beam is deflected under a different angle. Choosing the appropriate frequencies thus switches between the two (or more) ions. The additional frequency offset due to the addressing is compensated by applying the opposite frequency difference onto the "detuning" AOM in the beam path (not shown in the picture), which is used to match the laser frequency to the atomic transition frequency (or set a detuning to the transition).

In the following two sections, two approaches for the single-ion addressing are presented.

7.1.1. Addressed single-qubit σ_x rotations

The intuitive method for single-ion addressing is the direct manipulation of an individual ion while leaving the other ion nearly unaffected. This method brings some drawbacks that will be discussed in the next section. However, they pose a good option for testing the addressing itself and the resolution power of our optical setup, i.e. by which amount the state of the non-addressed ion is unintentionally disturbed during the process.

We first trap a single ion and perform a usual frequency scan to deduce the atomic resonance. In the second step, we trap a second ion and run a frequency scan of the AOD frequency for fixed laser power (the frequency shift being compensated by the additional detuning AOM), effectively corresponding to a scan of the beam focus along the trap axis.

The experimental result for that scan is shown in fig. 7.1. From the slightly different height and shape of the curves, we see that the alignment was still not optimal (we suspect that the tilting angle of the AOD did not perfectly match the tilting of the trap), but the results still exhibit a rather good suppression of unwanted excitation of the unaddressed ion. Also it has to be mentioned that the AOD was not fully symmetrized, that is the power was slightly higher for lower frequencies. The $D_{5/2}$-population ratios are (77.1±0.5)% (ion 1) to (1.99±0.05)% (ion 2) for the excitation of ion 1 and (67.5±0.5)% (ion 2) to (0.60±0.01)% (ion 1) for the excitation of ion 2.

One approach to reduce erroneous excitation of the wrong ion further is to switch the beam to the other ion after a pulse of desired pulse area on the target ion and apply a second pulse with a shifted phase by 180° and rotate the undesired population back to 0. If $\varepsilon_{1,2}$ are the unwanted-coupling parameter (i.e. the $D_{5/2}$ population of the other ion after a π pulse on the target ion, assuming both ions initially start in $S_{1/2}$), the population mismatch on the target ion after both pulses only scales with $\varepsilon_1\varepsilon_2$ and is therefore negligible in most experimental situations.

[1] Gooch & Housego, R46080-3-LTD

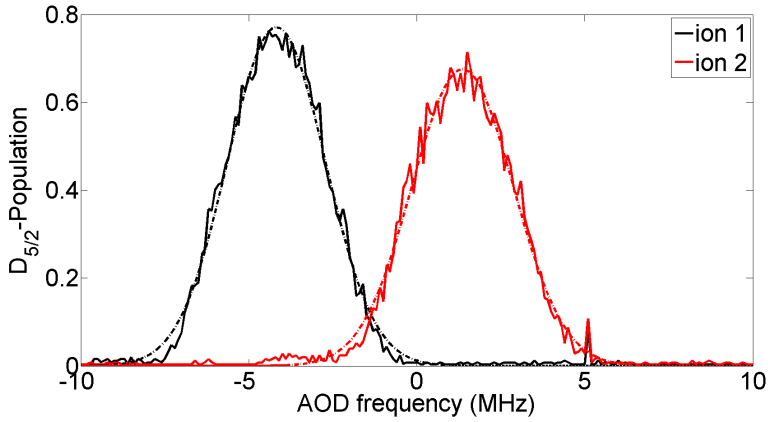

Figure 7.1.: Frequency scan of the acousto-optical deflector for fixed power and pulse length and a string of two trapped ions, oriented along the trap axis. The deflection angle of the AOD changes with the applied RF frequency, allowing for scanning of the spatial orientation of the laser beam after passing the AOD. Choosing the AOD frequency accordingly allows for the individual addressing of single ions. The dark/bright decisions are extracted from the camera picture used to distinguish between both ions. The dashed-dotted lines are Gaussian fits to the data.

7.1.2. Addressed single-qubit σ_z,σ_x rotations

The addressing methods presented in the previous section, though being elegant, possess one fundamental disadvantage. The resonant coupling imprints the laser phase onto the atomic state. Working with more than one 729 nm laser beam, as it is the case in the present experiments, reveals the necessity for phase stabilization between these beams at the position of the ion, which proves to be experimentally demanding. Instead, we pursue a different solution to this problem by using only the global beam (i.e. the beam that simultaneously drives both ions) under 45° to the HALO and quantization axis on resonance and realize single-ion manipulations by local off-resonant single-ion pulses using the 0° beam. These off-resonant pulses induce a phase shift which are then utilized to obtain the desired rotations.

For example, if we want to perform a π pulse on ion 1 while leaving ion 2 in its original state, we first apply a global $\frac{\pi}{2}$ pulse on both ions, then a local off-resonant pulse on ion 2, whose detuning, power and duration are chosen such that the resulting phase shift is exactly 180° with respect to ion 1, and subsequently apply a second $\frac{\pi}{2}$ pulse on both ions. Ion 1 will then undergo a full π pulse. Ion 2, however, will be rotated back to its initial state due to its acquired phase shift to the driving field, effectively corresponding to a usual π pulse on ion 1 and no rotation on ion 2, but not requiring phase stability between the different 729 nm beams.

The experimental realization of that sequence, starting with both ions in the ground state, is presented in fig. 7.2. We see that ion 1 is fully flipped ($D_{5/2}$ population: $p_{D_{5/2}} = (97.2 \pm 0.3)\%$) when ion 2 returns into its initial state ($D_{5/2}$ population: $p_{D_{5/2}} = (4.5 \pm$

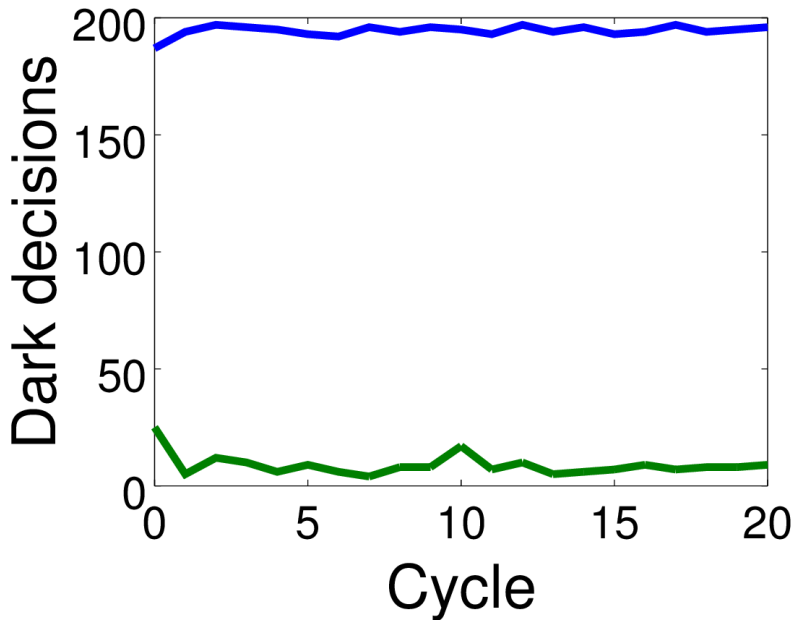

Figure 7.2.: $D_{5/2}$ population of ion 1 (blue) and ion 2 (green) after a sequence of two resonant global $\frac{\pi}{2}$ pulses, enclosing a local single-ion σ_z phase-rotation pulse. Detuning, power and duration of the σ_z pulse are adjusted to induce a 180° phase shift on ion 2.

0.3)%).

To make sure that the observed effect actually stems from the single-ion σ_z gate, we run two additional measurements. First we switch off the single-ion phase-rotation pulse, resulting in the data illustrated in fig. 7.3 (a). To verify that we do not transfer population with the local σ_z pulse, we perform another measurement where the second global $\frac{\pi}{2}$ pulse is skipped, which should result in half the population being in $D_{5/2}$ for both ions if the local pulse does not affect the population, but only the phase. Indeed, this is what we observe, as presented in fig. 7.3 (b).

These methods can be employed in future experiments to fully characterize the action of the Mølmer-Sørensen gate using standard two-qubit state tomography.

7.2. The Mølmer-Sørensen gate

A fully comprehensive quantum repeater or quantum network requires the implementation of local entangling and de-entangling multi-qubit gates. A versatile protocol to meet these requisites is provided by the so-called Mølmer-Sørensen gate [173, 174], named after Klaus Mølmer and Anders Sørensen, who proposed a robust entangling two-qubit gate which is, within certain restrictions, independent of the joint motional state. The MS gate is widely incorporated by many groups in the ion-trapping community [175, 176, 177, 178,

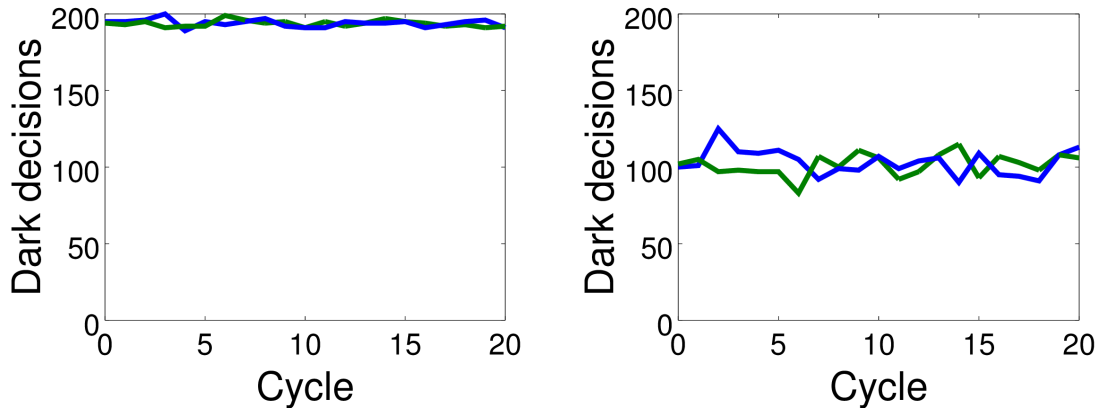

Figure 7.3.: (a) Same measurement as in fig. 7.2, but switching off the local σ_z gate. **(b)** Switching on the local phase-rotation pulse, but skipping the second global $\frac{\pi}{2}$ pulse. Details are found in the main text.

179] and is built upon the simultaneous off-resonant excitation of two motional-sideband transitions, thus coupling the electronic atom-states with their collective states of motion.

Section 7.2.1 treats the theory behind the Mølmer-Sørensen gate. A numerical simulation is presented in section 7.2.2, followed by the derivation of the experimental parameters in section 7.2.3. Finally, the experimental results are shown in section 7.2.4 and experimental error sources and imperfections are discussed.

7.2.1. Theory

The theory behind the Mølmer-Sørensen gate was first developed by its namesakes Klaus Mølmer and Anders Sørensen, published in two consecutive articles [173] and [174], and is also nicely elaborated in [176] and [180], which are the primary sources this section is based upon.

The principle of the entangling gate relies on the coupling of two (or more) ions via their joint state of motion in the ion trap, driven by a bi-chromatic laser field tuned close to the motional-sideband transitions between a ground state $|g\rangle$ and a (meta-stable) excited state $|e\rangle$. The key element is the irradiation of the ion chain by light that can not be absorbed by the individual ions, but requires mutual excitation of two ions from $|g\rangle$ to $|e\rangle$, which corresponds to an effective two-photon transition.

The energy of the isolated i-ions system is given by the energy of the collective center-of-mass motion of vibration frequency ν[2] and the internal electronic energy, described by

[2]Note that the vibrational frequency, despite denoted by the letter ν, is not a technical, but an angular frequency.

the Hamiltonian

$$\hat{H}_0 = \hbar\nu\left(\hat{a}^\dagger\hat{a} + \frac{1}{2}\right) + \frac{\hbar\omega_{eg}}{2}\sum_i \hat{\sigma}_{zi}\,, \tag{7.1}$$

where $\hat{a}^\dagger$ and $\hat{a}$ are the generation and annihilation operators of motional quanta, ω_{eg} denotes the resonance frequency between the states $|g\rangle$ to $|e\rangle$, and $\hat{\sigma}_{zi}$ describe the Pauli matrices on ion i.

The ions are exposed to a bichromatic light field with frequencies ω_j ($j = 1, 2$), tuned close to the motional-sideband transitions as depicted in fig. 7.4. Assuming equal interac-

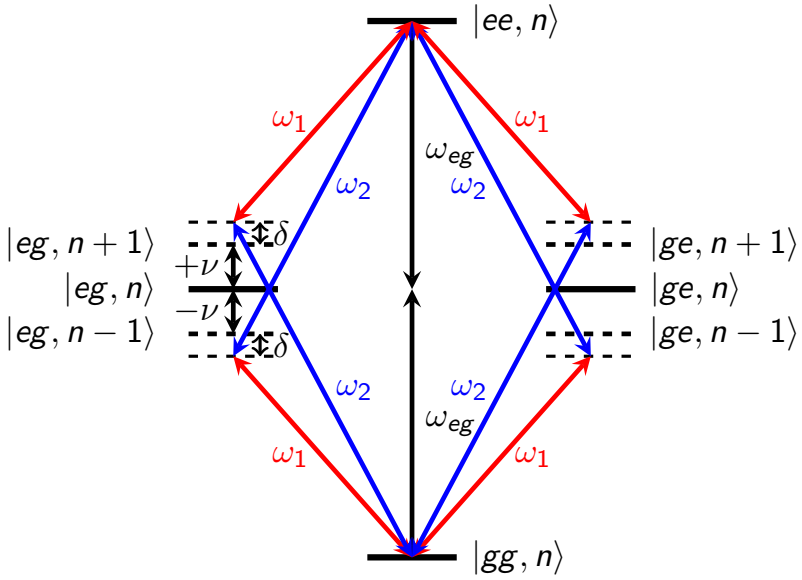

Figure 7.4.: Depiction of the transition paths in a Mølmer-Sørensen-type entangling two-ion gate. Choosing detuning, coupling strength and pulse duration appropriately, interference between the individual paths leads to decoupling from the motional state and ideally leaves the ions in an entangled state between the joint states $|gg\rangle$ and $|ee\rangle$ (see main text).

tion strengths $\Omega_1 = \Omega_2 = \Omega$ for both frequency components, the field induces the interaction Hamiltonian

$$\hat{H}_{\text{int}} = \sum_{i,j}\frac{\hbar\Omega}{2}\left(\hat{\sigma}_+^{(i)}(t)e^{i(\eta(\hat{a}^\dagger(t)+\hat{a}(t))-\omega_j t)} + H.c.\right) \tag{7.2}$$

with the Lamb-Dicke parameter η for the two-ion axial COM mode. The time-dependent Pauli operator $\hat{\sigma}_+^{(i)}(t)$ on ion i is defined by

$$\hat{\sigma}_\pm^{(i)}(t) = (\hat{\sigma}_x^{(i)}(t) \pm i\hat{\sigma}_y^{(i)}(t))/2 = (\hat{\sigma}_x^{(i)} \pm i\hat{\sigma}_y^{(i)})e^{\pm i\omega_{eg}t}/2 \tag{7.3}$$

and consequently $\left(\hat{\sigma}_+^{(i)}(t)\right)^\dagger = \hat{\sigma}_-^{(i)}(t)$. Its action onto a two-ion state is described by

$$\hat{\sigma}_+^{(1)}|g\bullet\rangle = |e\bullet\rangle\,, \qquad \hat{\sigma}_-^{(1)}|e\bullet\rangle = |g\bullet\rangle\,, \tag{7.4}$$

$$\hat{\sigma}_+^{(2)}|\bullet g\rangle = |\bullet e\rangle\,, \qquad \hat{\sigma}_-^{(2)}|\bullet e\rangle = |\bullet g\rangle\,. \tag{7.5}$$

Analogously, the time-dependent vibrational generation and annihilation operators are written as

$$\hat{a}^\dagger(t) = \hat{a}^\dagger e^{i\nu t}\,, \qquad \hat{a}(t) = \hat{a}e^{-i\nu t}\,. \tag{7.6}$$

Using the Taylor expansion

$$e^{\pm i(\eta(\hat{a}^\dagger(t)+\hat{a}(t)))} \approx 1 \pm i\eta\left(\hat{a}^\dagger(t)+\hat{a}(t)\right) = 1 \pm i\eta\left(\hat{a}^\dagger e^{i\nu t}+\hat{a}e^{-i\nu t}\right)\,, \tag{7.7}$$

(7.2) becomes

$$\hat{H}_{\text{int}} \approx \sum_{i,j}\frac{\hbar\Omega}{2}\left(\hat{\sigma}_+^{(i)}e^{i(\omega_{eg}-\omega_j)t}\left(1+i\eta(\hat{a}^\dagger e^{i\nu t}+\hat{a}e^{-i\nu t})\right)+H.c.\right)\,. \tag{7.8}$$

With $\omega_{eg}-\omega_1 = \nu+\delta$ (cf. fig. 7.4) and $\omega_{eg}-\omega_2 = -(\nu+\delta)$, applying the rotating-wave approximation (RWA) to omit all terms except those in $e^{i\delta t}$ yields[3]

$$\hat{H}_{\text{int}} \approx \frac{\eta}{2}\sum_i \Omega\left(ie^{i\delta t}\hat{\sigma}_+^{(i)}\hat{a}+ie^{-i\delta t}\hat{\sigma}_+^{(i)}\hat{a}^\dagger+H.c.\right)\,. \tag{7.9}$$

This Hamiltonian is used to determine the system dynamics (as explicated in sec. A.5).

From (7.9), we deduce the evolution of different initial states under the influence of the Mølmer-Sørensen gate for an interaction time T as

$$|gg\rangle \to \cos\left(\frac{\tilde{\Omega}T}{2}\right)|gg\rangle + i\sin\left(\frac{\tilde{\Omega}T}{2}\right)|ee\rangle \tag{7.10}$$

$$|ee\rangle \to \cos\left(\frac{\tilde{\Omega}T}{2}\right)|ee\rangle + i\sin\left(\frac{\tilde{\Omega}T}{2}\right)|gg\rangle \tag{7.11}$$

$$|ge\rangle \to \cos\left(\frac{\tilde{\Omega}T}{2}\right)|ge\rangle - i\sin\left(\frac{\tilde{\Omega}T}{2}\right)|eg\rangle \tag{7.12}$$

$$|eg\rangle \to \cos\left(\frac{\tilde{\Omega}T}{2}\right)|eg\rangle - i\sin\left(\frac{\tilde{\Omega}T}{2}\right)|ge\rangle \tag{7.13}$$

with $\tilde{\Omega} = \frac{(\eta\Omega)^2}{2\delta}$ (see also [174]).

It has to be noted that the results obtained above do not depend on the mean motional quantum number n, showing that the Mølmer-Sørensen gate works even if no ground-state cooling is implemented.

[3] A treatment including light shifts and a possible offset of the laser carrier frequency to the atomic resonance is given in A.5.

7.2.2. Numerical simulations

Being able to predict the outcome of a measurement in advance bears the advantage that potential discrepancies between measured and expected results can be recognized immediately. Moreover, imperfections that degrade the gate fidelity might (and did) appear in an experimental environment. It is therefore intuitive to carry out a simulation of the experiment prior to the actual measurement (and then of course, if the experimental results are not in agreement with the simulation, try to adapt the simulation to reproduce the experimental results and thus gain an insight on possible error sources).

The theoretical and numerical foundation for the simulation of the Mølmer-Sørensen gate are elaborated in section A.5. Based on the methods developed there, the simulated results are presented in this section. To anticipate the experimental results from the next section, we experience a decrease of the visibility which we (also) attribute to the adverse effect of servo bumps in the laser spectrum that couple to the carrier transition and significantly reduce the gate fidelity. To estimate this effect, we include the carrier coupling into the simulation as described in detail in app. A.5.

These servo bumps appear at the edge of the feedback-loop bandwidth for the frequency stabilization, typically at about 1 MHz, where signal phase shift leads to noise amplification instead of suppression. Since the noise background of diode lasers is rather high compared to, e.g., solid-state systems like Ti:Sa lasers, these servo bumps may represent a non-negligible contribution to the gate dynamics. The servo bumps were measured by a beat measurement with a stabilized Ti:Sa laser[4], tuned to match the frequency of the qubit laser. The beat signal is detected with a fast photo diode and frequency-analyzed by an RF spectrum analyzer[5]. The beat spectrum in a linear scale is shown in fig. 7.5. The servo-bump suppression with respect to the carrier is 28 (14.5 dB), which, taking into account the larger coupling strength of the carrier transition, shows the significant contribution of the servo bumps. This value seems very small (which would correspond to strong servo bumps) and might be caused by an inadvertent change of the locking parameters (as we discovered a loose contact in the cable connections afterwards), but values of 25 dB to 30 dB (in the power spectrum) are typical for the diode-laser servo bumps.

Following the procedure described in appendix A.5, we simulate the effect of the Mølmer-Sørensen gate onto a two-ion crystal with both ions starting in the ground state, both without and including the carrier coupling due to the servo bumps. As in the experiment, we scan both, gate time and the detuning of the bichromatic beam from the motional sidebands as well as the gate time and the overall offset from the central frequency of the laser and the atomic carrier resonance.

First we investigate the ideal situation without disturbances, i.e. without coupling to the carrier. Fig. 7.6 shows a gate-duration scan for different frequency spreads of the bichromatic beam, where its center frequency always coincides with the atomic resonance. In that context, *Detuning* denotes the frequency deviation of the laser frequencies from the

[4]Sirah, Matisse TX
[5]Agilent, N9320B

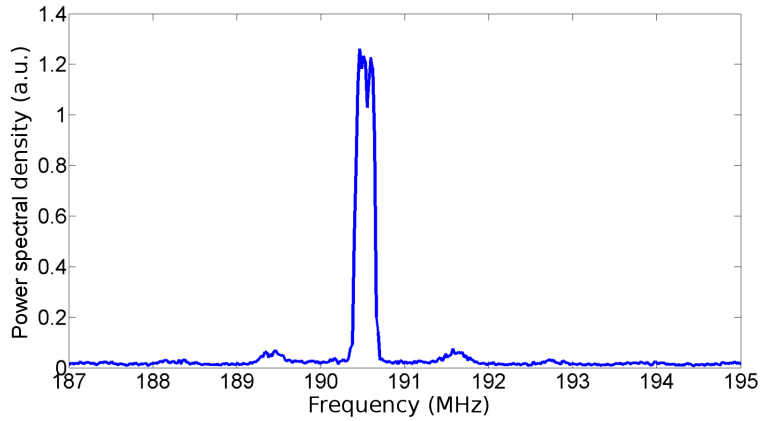

Figure 7.5.: Spectral-density beat signal of the reference Ti:Sa laser with the qubit laser. The laser beams are overlapped at a beam splitter and detected by a fast photo diode. The output of the photo diode is fed into a spectrum analyzer (resolution bandwidth: 100 kHz, video bandwidth: 10 kHz, spectral span: 10 MHz). The servo bumps from the frequency-stabilization feedback at the typical frequency of 1.1 MHz from the carrier are clearly visible. The lasers were detuned by 190.5 MHz to each other to assist the data analysis.

theoretically derived optimal value for the frequency detuning from the carrier transition $\nu + \delta$ (cf. sec. 7.2.3). The fully-entangling gate operation is reached after a gate time of 62.5 µs, indicated by the vanishing dark-bright and bright-dark population (i.e. the cases

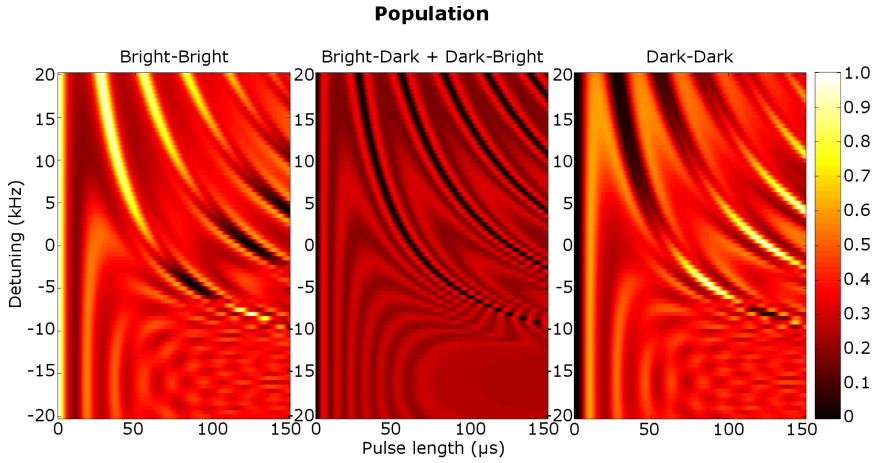

Figure 7.6.: Numerical simulation of a gate-duration scan of the Mølmer-Sørensen gate for different detunings and a constant offset of 0 kHz. Here, detuning denotes the frequency deviation of the laser frequencies from the expected ideal values $\nu + \delta$ (see main text and sec. 7.2.3). Shown are the populations for both ions remaining in the ground state $S_{1/2}$ (bright-bright), exactly one ion being excited into $D_{5/2}$ (bright-dark + dark-bright), and both ions being excited (dark-dark).

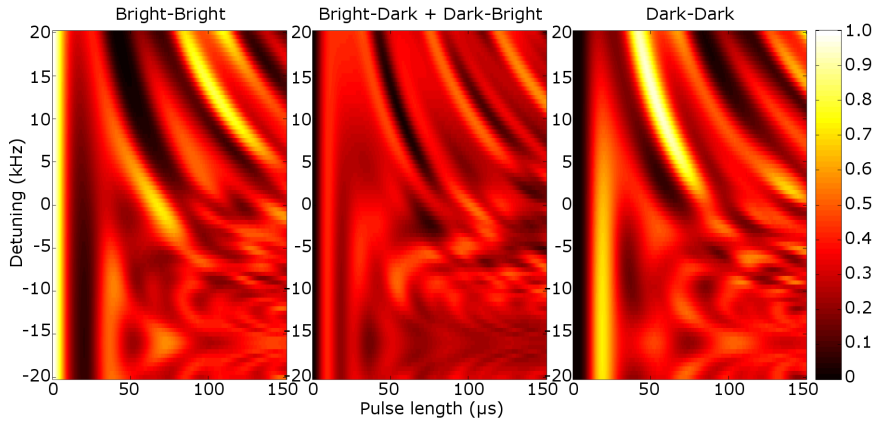

Figure 7.7.: Simulated populations for a Mølmer-Sørensen pulse-length scan for varying detunings (offset = 0 kHz), taking into account the coupling to the atomic carrier transition due to the laser servo bumps. For the servo-bump suppression of -30 dB assumed here, the gate fidelity is already considerably reduced.

where exactly one ion was excited).

Taking carrier coupling into account, the outcome of the simulation changes substantially. For a servo-bump suppression of 30 dB (i.e. a factor of 10^{-3}), we obtain the distribution shown in fig. 7.7. The gate fidelity is severely decreased. The best parameter set is identifies for zero *detuning* from $\nu + \delta$ and zero *offset* (i.e. the difference between the sum of the frequencies of both laser sidebands from the atomic carrier transition) for a gate duration of 78.7 µs, though the coherence might be affected further[6]. The dark-dark and bright-bright populations (both ions in $D_{5/2}$ and both ions in $S_{1/2}$, respectively) are reduced to 34.1% and 34.2%, respectively, while the parasitic dark-bright and bright-dark populations are increased to 24.8%. As we will se in section 7.2.4, these numbers approximately correspond to what we observe in the actual experimental realization.

Increasing the carrier coupling to -20 dB leads to the results shown in fig. 7.8. It is apparent that the gate robustness towards variations of detuning, offset or gate time is remarkably reduced, while the gate infidelity remains roughly at the previous low level.

Additionally, we run a set of measurements where we vary the offset instead of the detuning while scanning the gate time, again for no carrier coupling and -20 dB and -30 dB servo-bump suppression, for a constant detuning of 0 kHz. The corresponding simulation results are found in the figures 7.9, 7.10 and 7.11.

[6]Note that the data presented here shows only the populations

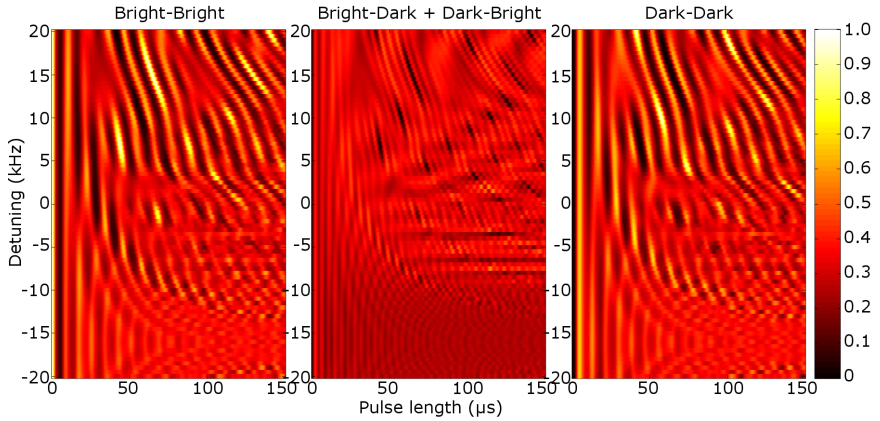

Figure 7.8.: Simulation of the population distribution for the Mølmer-Sørensen gate, scanning pulse length and detuning while keeping the offset constant at 0 kHz. The laser servo-bumps intesity at the atomic carrier frequency are suppressed by a factor of -20 dB with respect to the target frequency.

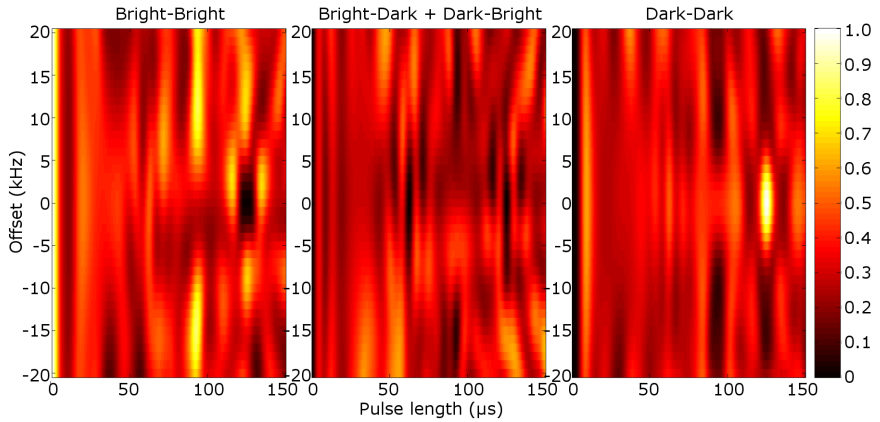

Figure 7.9.: Simulation of the Mølmer-Sørensen gate without coupling to the carrier, scanning gate duration and offset for a fixed zero detuning.

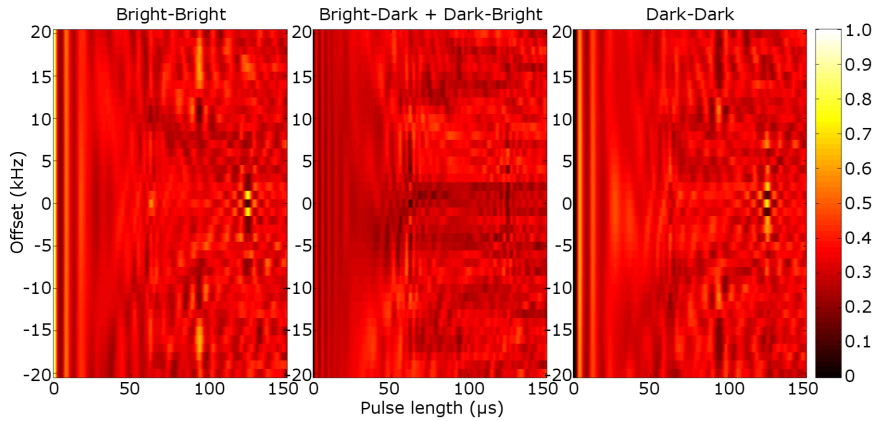

Figure 7.10.: Simulation of the Mølmer-Sørensen gate, scanning gate duration and offset for a fixed zero detuning, for a servo-bumps suppression of -30 dB.

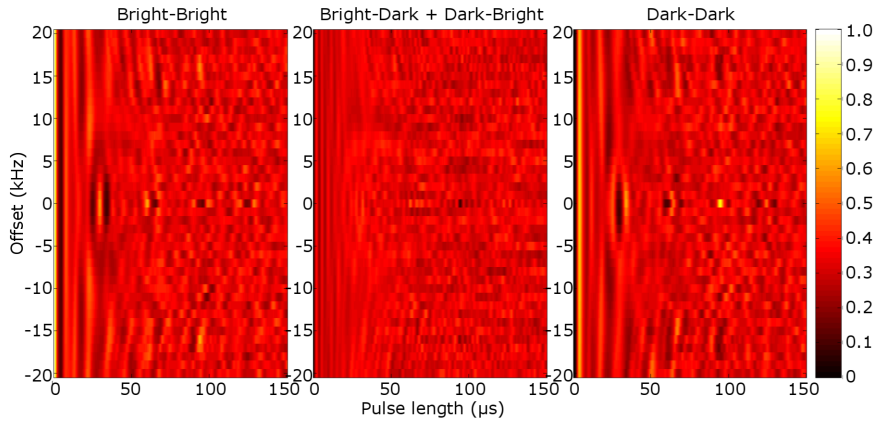

Figure 7.11.: Simulation of the Mølmer-Sørensen gate, scanning gate duration and offset for a fixed zero detuning, for a servo-bumps suppression of -20 dB.

7.2.3. Experimental parameters

The realization of an atom-atom–entangling gate operation mediated by the harmonic-oscillator mode in the trap potential requires decoupling of the internal atomic states from their motion while simultaneously maintaining the entanglement between both particles. Following the theoretical treatment in [24, 180], this gate action is achieved after a gate duration of

$$\tau_{MS} = 2\pi/|\delta| \,, \tag{7.14}$$

where the detuning[7] δ from the motional sidebands is determined by the experimental conditions. The optimal detuning is derived according to the formula

$$\eta\Omega \approx \frac{\delta}{4} \,, \tag{7.15}$$

where Ω is the experimentally determined Rabi frequency on the carrier, and η denotes the two-ion Lamb-Dicke parameter. The latter is defined by

$$\eta = \frac{2\pi}{\lambda} \cos\beta \sqrt{\frac{\hbar}{2M\omega_T}} \tag{7.16}$$

and exhibits a value of $\eta = 0.044$. β denotes the angle between the incident light beam and the orientation of the oscillation axis and is calculated in our experimental configuration as 49.2° for the axial mode. M is the effective mass of the particle (i.e. twice the mass of a single $^{40}Ca^{+}$ ion) and ω_T indicates the frequency of the harmonic-oscillator mode, which is 1.1956 MHz for the axial COM mode for our experimental parameters.

In general, off resonant excitation of the carrier transition leads to fast oscillations of the resulting state when $\Omega \ll \nu + \delta$ no longer holds, which strongly depend onto the laser phase [176]. However, adiabatically switching on and off the laser pulse provides independence of the gate from the current laser phase, which is achieved by Blackman-shaping the intensity profile of the laser pulse, where the rise and fall time covers a few cycles of the frequency describing the laser detuning from the carrier, $(\nu + \delta)/2\pi$, which we typically choose to be 4 µs.

7.2.4. Experimental results

The experimental sequence used for the measurements presented in the following is shown in figure 7.12. Both ions are initialized in the $|-1/2\rangle$ Zeeman sub-level of the ground state to ensure starting from a pure two-qubit state. Subsequently, the intensity-shaped (see sec. 7.2.3) bichromatic laser pulse, tuned close to the red and blue axial COM sideband of the $|S_{1/2}, -1/2\rangle \rightarrow |D_{5/2}, -5/2\rangle$ transition, of varying pulse duration and detuning or offset (cf. 7.2.2) is applied, followed by fluorescence-based atomic state analysis. The fluorescence is

[7] Be aware that the notation in these publications differs from the one used in this work.

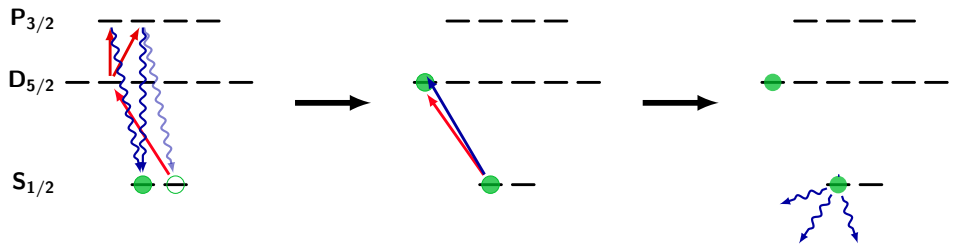

Figure 7.12.: Experimental sequence for the Mølmer-Sørensen gate. The sequence starts with optical pumping into $|S_{1/2}, -1/2\rangle$, followed by the actual intensity-shaped bichromatic Mølmer-Sørensen pulse. Subsequently, the two-atom state is read out by fluorescence generation, detected by an EMCCD camera to distinguish between both ions, or a PMT, distinguishing between dark (dark-dark) and bright (dark-bright, bright-dark, bright-bright) events.

detected either with the EMCCD camera, allowing for resolved single-ion state detection, or with the PMT, which was much faster, but only allowed, due to practical reasons, to distinguish between the dark-dark and all remaining states. The experiments presented in this section are analyzed using the latter method.

The bichromatic light field is generated by imprinting two frequencies onto a single laser beam passing through an AOM in single-pass configuration. Alternatively, the application of two RF frequencies at the AOM can be seen as an amplitude-modulated beam. Caution has to be taken on the nonlinearity of the AOM. We run an optimization process beforehand to compensate for the nonlinearities and avoid unwanted sidebands in the photonic spectrum.

In the experimental realization, in accordance to the simulations (or rather vice versa), we run two different measurements to deduce the optimal parameters for the entangling gate and to determine the gate quality. In both cases, the pulse duration is scanned. In the first scenario, the detuning, i.e. the deviation of the actual laser frequencies from the expected optimal value $\nu + \delta$ for the detuning from the atomic carrier transition, is scanned. In the second scenario, the detuning is kept fixed at the expected value and the offset is varied.

Usually, we first scan offset and pulse length for the expected optimal detuning calculated from the Lamb-Dicke parameter and the measured Rabi frequency. A typical experimental run is shown in fig. 7.13. From this measurement, the optimal offset, which occurs due to light shifts of the atomic carrier transition[8], is extracted and used for the following measurements. The reduced visibility compared to the ideal situation depicted in fig. 7.9 is already apparent. Rather, the experimental results show, to a certain degree, a resemblance with the simulation including the servo bumps, which are suppressed by 30 dB (cf. fig. 7.10), although some features like the fast-oscillating pattern do not appear in the

[8]To be precise, due to off-resonant coupling of the laser field onto other transitions that couple to the $|-1/2\rangle$ Zeeman sub-level of the ground state, hence affecting also the center frequency of the atomic target transition.

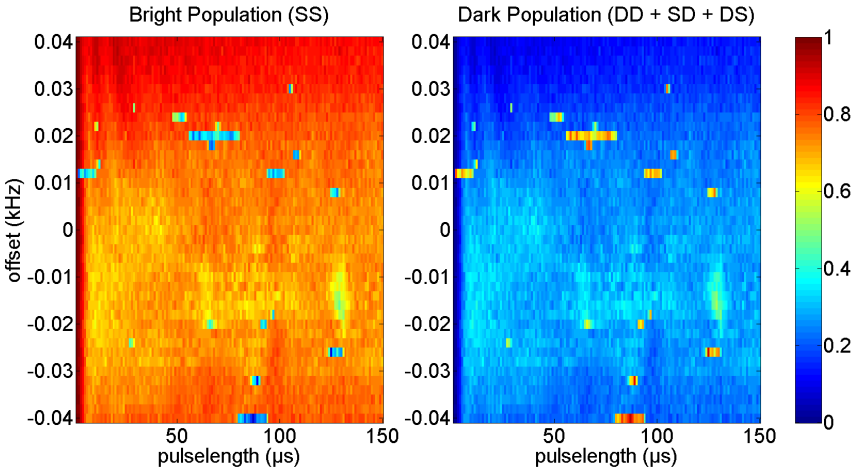

Figure 7.13.: Gate-duration scan of the bichromatic Mølmer-Sørensen pulse for varying offsets and the theoretically expected detuning. The measured carrier-transition Rabi frequency for the laser power used in the experiment was $2\pi \cdot 197\,\mathrm{kHz}$ and the zero-point for the detuning was chosen accordingly (cf. sec. 7.2.3). The horizontal lines appearing in some stages of the measurement correspond to periods where the ions were hot. Compared to fig. 7.9, the contrast of the typical features is reduced, which we trace back to unwanted coupling to the atomic carrier transition caused by the laser background spectrum (servo bumps).

measurement. This indicates that other, not yet fully understood disturbances appear in parallel.

Setting the offset to the previously determined value, the detuning (together with the gate duration) is scanned in the next step. The outcome of this scan is presented in fig. 7.14. Again, the contrast of the typical features is substantially reduced as in the numerical simulations considering the servo-bump distortion (see fig. 7.10), from which we infer that laser noise represents one of the major error sources in the experiment.

This chapter addressed first experiments towards a local atomic two-ion gates as a missing corner stone for the implementation of a basic quantum repeater in the laboratory. In section 7.1, I demonstrated a technique for the addressing of single ions within a chain of ions (in our case a two-ion chain)[9]. In the next section, I presented the results of our implementation of a Mølmer-Sørensen gate and discussed possible causes for the observed gate infidelity, which we attribute to a large spectral noise background of the quadrupole laser[10], resulting in coupling to the atomic carrier transition during the gate operation. In that context, simulations including carrier coupling were conducted which show qualitative agreement with the experimental results, supporting our hypothesis. Knowing (and

[9] Which is not neccessary for the entangling two-ion gate itself, but facilitate the characterization of said gate.
[10] Newer findings showed that residual magnetic-field noise might be a second relevant source of fidelity reduction [186].

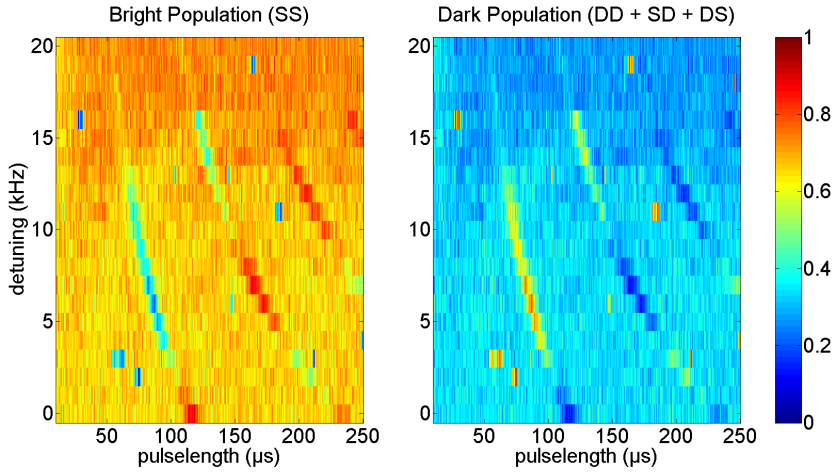

Figure 7.14.: For the optimal offset deduced from a measurement as the one shown in fig. 7.13, the Mølmer-Sørensen measurement is ran again, scanning gate duration and detuning, i.e. the deviation from the theoretically expected value. Unsurprisingly, the contrast is reduced as well, qualitatively resembling the simulation shown in fig. 7.7.

hopefully shortly eliminating) the sources for the gate infidelity represents a crucial step towards the realization of an entangling two-ion gate and thus towards the demonstration of a functional laboratory-scale quantum repeater.

8. Conclusion and outlook

Summary

The experiments described in this work represent a fundamental step towards the physical implementation of a basic quantum-repeater–based quantum network incorporating single trapped $^{40}Ca^{+}$ ions as network nodes and quantum memories for the repeaters. An essential building block for these networks are quantum interfaces between the atomic network nodes, formed by the $^{40}Ca^{+}$ ions, and the photonic quantum channels interconnecting the nodes or the quantum-repeater units in between. For a fully versatile quantum interface, three conditions have to be fulfilled:

- Mapping of a photonic state, for example stored in the polarization degree of freedom, onto an atomic state, typically by photon absorption. This process either has to occur with near-unity probability or a heralding event that signals a successful state mapping is required.
- Reverse state transfer from the atomic quantum memory onto a single photon via indirect interaction (such as teleportation) or direct photon emission.
- The generation of atom-photon entanglement.

In this thesis, I presented the conception and experimental realization of two interface protocols. The first protocol (cf. chapter 5) builds upon the absorption of (single) photons at 854 nm, triggering the emission of a heralding photon at 393 nm. Through suitable preparation of the ion, the photonic polarization state is mapped into the atomic qubit by the absorption process, and the success of the mapping is indicated by the detection of the heralding photon.This protocol can be utilized to also implement the remaining two interface operations. If the qubit is not stored in the photon polarization but in the initial atomic state, and the state of the absorbed infrared photon is known, the atomic state is transferred into the polarization state of the emitted heralding photon, which then serves as carrier of quantum information if the atomic state is projected onto a known superposition. If the atomic state is not projected, we end up with an entangled state between the atom and the polarization of the 393 nm photon, satisfying the third interface condition.

It is apparent that this interface scheme is only suitable for short distances due to the comparably high transmission losses for the working wavelength and the high cost of high-quality optics for blue, which limits the practical applicability of this scheme. For that reason, an alternative method for the implementation of an atom-photon quantum interface has been developed and demonstrated in the course of this work that allows for the

atom-to-photon state transfer onto an infrared photon at 854 nm. The wavelength in the NIR spectral region facilitates the implementation of QFC to convert the photon into the telecom regime, making this state-transfer scheme much more appropriate for the intended application of long-range quantum communication.

As the remaining task for a universal quantum interface, an implementation for atom-photon entanglement at 854 nm was demonstrated. The primary advantage of the new entanglement-generation protocol compared to the original proposal, working at 393 nm, is the possibility to include quantum frequency conversion, based on difference-frequency generation in a periodically-poled Lithium-niobate waveguide, to down-convert the NIR photons into the telecom O-band at 1310 nm, thus coupling the $^{40}Ca^{+}$ ion, with its transitions not lying in the desired wavelength region, to the low-loss telecom regime, resulting in a significant reduction of fiber-transmission losses. Experimental results including polarization-preserving QFC were presented, revealing high-efficiency, low-background conversion with near-unity quantum-process fidelity (i.e. the original quantum state is, within the error margin, not affected by the conversion process). These results represent a crucial step towards long-haul fiber-based quantum communication and quantum networks.

All protocols demonstrated here require precise control over the quantum state of the ions and methods for coherent manipulation of the state and specific preparation of the atomic qubit in a pure initial state. Both is achieved by frequency-selective optical pumping utilizing the narrow quadrupole transition between the ground state and the meta-stable $D_{5/2}$ state, and coherent Rabi rotations by means of coupling to a narrow-band laser at 729 nm, tuned on resonance with the respective Zeeman transitions between ground and meta-stable state. Alternatively, the atomic state is encoded into a Zeeman qubit in the ground state, split due to an external magnetic DC field of about 3 G, and manipulated by a radio-frequency coil below the trap that addresses the transition between both spin states in $S_{1/2}$. We demonstrated coherent control over the internal state of the ion, high-efficiency pure-state preparation and full atomic state tomography.

The storage time of quantum information in the atomic qubit is limited by magnetic decoherece, i.e. due to unknown fluctuations of the Zeeman-qubit energy levels caused by fluctuations of the ambient magnetic field that we do not control. A brief depiction of a method for active feed-forward compensation of the periodical perturbation of the residual magnetic field, originating primarily from the 50 Hz (and higher harmonics) from the power lines is given[1]. A three- to four-fold improvement of the coherence time was achieved by this method.

Finally, first steps towards local entangling two-ion gate operations were presented, required for the realization of a quantum-memory–based quantum repeater network. First, our method for selective single-ion addressing in a two-ion chain was shown, followed by a theoretical description and our experimental implementation of a Mølmer-Sørensen-type two-ion quantum gate. A comparison between theoretical and experimental results

[1] A detailed description is found in [133]

was given and possible sources for the observed gate infidelity were discussed.

The theoretical fundamentals treated in this thesis comprised, apart from a discussion of the properties of the $^{40}Ca^{+}$ ion, a comprehensive description of spatial dependency of the dipole emission and absorption properties. The latter is of particular importance for the understanding of the single-mode fiber coupling and the photon-to-atom quantum-state mapping.

Outlook

Of course, an experiment like ours is never finished and improvements and further extension are a continuous process. Therefore, the progress does not end with this thesis. Various ideas have already been developed within our team what will be set up and which experiments will be conducted in the next steps.

One of the first measures that will follow is the replacement of the current qubit laser at 729 nm with a new Ti:Sa system that exhibits a lower spectral background (cf. supplemental information of [181]), hopefully facilitating the realization of a working Mølmer-Sørensen gate, which would bring the realization of remote state teleportation into reach. Alternatively, we could extend the existing laser system and employ a so-called injection-locking scheme [182, 183], where the light leaving the laser diode is first spectrally filtered by an optical cavity before it is amplified by the tapered amplifier. Eventually, positive experiences of other groups regarding Ti:Sa systems and the technically demanding implementation of injection locking made us opting for the Ti:Sa solution.

To ensure line-narrowing and spectral purity of the laser, also other noise sources have to be eliminated. An often underestimated effect are thermal and acoustical distortions of the optical fibers, locally changing the refractive index and thus inducing phase noise. A method to counteract this noise by double-pass fiber-noise measurement and cancellation has already been established by other groups, described e.g. in [184, 185]. We plan to implement this technique for further linewidth narrowing.

Other work in progress includes the replacement of the currently used magnetic-field coils for the definition of the quantization axis by permanent magnets to reduce noise on the ambient field. We expect an increase of coherence time from this measure. Yet, preliminary results indicate that there are further magnetic fluctuations affecting the experiment that cannot be suppressed this way [186].

In addition, it is planned to incorporate an optical cavity around the Paul trap to increase the absorption efficiency in single-photon–absorption experiments. Higher absorption efficiencies enable new experiments, like distant-ion entanglement employing our photon-pair source (see next section), which so far were impractical due to estimated measurement times in the order from several weeks to months.

The prospects for milestones in the near future (i.e. in the next one or two years) are depicted in the following. The implementation of an operating Mølmer-Sørensen gate for local two-ion Bell-state measurements forms the foundation for future experiments. Once

that is achieved, the second trap apparatus will be put into operation. Constituting atom-photon entanglement simultaneously in both traps, the respective photons from both remote ions are collected and overlapped at a photonic Bell-state–measurement (BSM) setup, consisting of a non-polarizing beam splitter (nPBS) and a polarizing beam splitter (PBS) at each output arm of the nPBS. A single-photon detector is placed at each of the four output ports of the polarizing beam splitters. Depending on which of the possible detection-event combinations is detected, the two-photon state is projected onto the according Bell state[2] and hence the original atom-photon entanglement is swapped onto entanglement between the two distant ions [48, 187, 188]. This projective Bell-state measurement will firstly be conducted utilizing atom-photon entanglement (APE) at 393 nm before it is planned to switch to APE at 854 nm, including QFC in a next step.

Combining both techniques eventually allows us to teleport the quantum state, stored in the data ion, onto a second target ion situated in a distant trap [189, 190, 51, 191]. For that purpose, a third ancilla ion, stored in the same trap as the data ion, is employed. The quantum state is initially encoded into the internal state of the data ion, where it is protected until the connection to the target ion is established. The latter is realized by conducting a projective BSM between ancilla and target ion as explained before, creating entanglement between these two. Subsequently, a local projective BSM between ancilla and data ion by applying the Mølmer-Sørensen gate finally transfers the quantum information from the data onto the target ion without revealing its original state.

[2] With this setup, the detection of two out of four Bell states, namely the two orthogonal $|\Psi\rangle$ states, is possible.

A. Appendix

A.1. Dipole-emission properties and photon collection

The understanding of the dipole-emission properties of single atoms is crucial for the atom-photon-interface protocols presented in this thesis, as it allows an evaluation of the viability of said protocols. Additionally, the collection of light emitted into different spatial modes acts as a possible source of infidelity in the experiment, therefore it is important to understand the influence of the spatial emission. These effects are discussed in the following.

A.1.1. Spatial dependence of the photon polarization

In the following we will derive the relation between the photon polarization measured by a observer as a function of atomic-dipole orientation and direction of observation, as depicted in section 4.2.2

We have to distinguish between two reference frames, the atomic, which we define such that $\hat{e}_z^{(\mathrm{at})}$ is oriented along the quantization axis (and, for the sake of consistency, $\hat{e}_x^{(\mathrm{at})}$ lies in the table plane), and the photonic system for which $\hat{e}_z^{(\mathrm{ph})} \parallel \vec{k}$, where the wave vector $\vec{k}$ describes the propagation direction of the photon. The transformation between both bases is depicted in fig. 4.4.

The polarization amplitude as seen from an observer, whose orientation towards the atomic (laboratory) z-axis is defined by the angles θ and ϕ, for an atomic dipole which oscillates in the direction $\hat{e}^{(\mathrm{at})}$, is given by the projections onto the horizontal and vertical polarization in the photonic reference frame, i.e.

$$\vec{A}_H^{(\mathrm{ph})} = \left(\hat{e}^{(\mathrm{at})} \cdot \hat{e}_H^{(\mathrm{ph})}\right) \hat{e}_H^{(\mathrm{ph})}\,, \qquad \vec{A}_V^{(\mathrm{ph})} = \left(\hat{e}^{(\mathrm{at})} \cdot \hat{e}_V^{(\mathrm{ph})}\right) \hat{e}_V^{(\mathrm{ph})}\,. \tag{A.1}$$

From fig. 4.4 it is apparent that $\hat{e}_H^{(\mathrm{ph})}$ and $\hat{e}_V^{(\mathrm{ph})}$ correspond to the spherical unit vectors

$$\hat{e}_H^{(\mathrm{ph})} = \hat{e}_x^{(\mathrm{ph})} = \hat{e}_\theta^{(\mathrm{at})} = \begin{pmatrix} \cos\theta\,\cos\varphi \\ \cos\theta\,\sin\varphi \\ -\sin\theta \end{pmatrix}, \text{ and } \quad \hat{e}_V^{(\mathrm{ph})} = \hat{e}_y^{(\mathrm{ph})} = \hat{e}_\varphi^{(\mathrm{at})} = \begin{pmatrix} -\sin\varphi \\ \cos\varphi \\ 0 \end{pmatrix} \tag{A.2}$$

in the atomic reference frame. Furthermore, we define the remaining unit vectors in the laboratory system as

$$\hat{e}_z^{(\mathrm{at})} \hat{=} \hat{e}_0^{(\mathrm{at})} = \begin{pmatrix} 0 \\ 0 \\ 1 \end{pmatrix}, \hat{e}_x^{(\mathrm{at})} = \begin{pmatrix} 1 \\ 0 \\ 0 \end{pmatrix}, \hat{e}_x^{(\mathrm{at})} = \begin{pmatrix} 0 \\ 1 \\ 0 \end{pmatrix} \tag{A.3}$$

and

$$\hat{e}_{+}^{(\mathrm{at})} = -\frac{1}{\sqrt{2}} \begin{pmatrix} 1 \\ i \\ 0 \end{pmatrix} , \hat{e}_{-}^{(\mathrm{at})} = \frac{1}{\sqrt{2}} \begin{pmatrix} 1 \\ -i \\ 0 \end{pmatrix} , \tag{A.4}$$

where $\hat{e}_{0}^{(\mathrm{at})}$ corresponds to a π transition and $\hat{e}_{\pm}^{(\mathrm{at})}$ to the $\sigma^{\pm}$ transitions.

For analogous definitions in the photonic frame, we rewrite the horizontal and vertical polarization components as

$$\hat{e}_{H}^{(\mathrm{ph})} = \hat{e}_{x}^{(\mathrm{ph})} = -\frac{1}{\sqrt{2}} \left(\hat{e}_{+}^{(\mathrm{ph})} - \hat{e}_{-}^{(\mathrm{ph})} \right) , \text{and} \quad \hat{e}_{V}^{(\mathrm{ph})} = \hat{e}_{y}^{(\mathrm{ph})} = i \, \frac{1}{\sqrt{2}} \left(\hat{e}_{+}^{(\mathrm{ph})} + \hat{e}_{-}^{(\mathrm{ph})} \right) . \tag{A.5}$$

$\hat{e}_{\pm}^{(\mathrm{ph})}$ describe the circular polarizations R and L[1].

To obtain an expression for the transformation from the atomic into the photonic reference frame, we deploy [144]

$$\hat{e}_{q'}^{(\mathrm{at})} = e^{iq'\,\varphi} \sum_{q=-1}^{1} d^{1}_{q',q}(-\theta)\, \hat{e}_{q}^{(\mathrm{ph})} \tag{A.6}$$

with the Wigner (small) d matrices $d^{j}_{q',q}(\vartheta)$. Additionally, some useful properties of the Wigner d matrices (or the components thereof) should be kept in mind:

$$d^{j}_{q',q}(\vartheta) = (-1)^{q-q'}\, d^{j}_{q,q'}(\vartheta) \ , \quad \text{and} \quad d^{j}_{q',q}(\vartheta) = d^{j}_{-q,-q'}(\vartheta) \, . \tag{A.7}$$

With that at hand, the projections onto the photonic H and V polarizations for different atomic dipole orientations are then calculated. First we examine the π transition, which is described by a dipole oscillating along $\hat{e}_{0}^{(\mathrm{at})}$. The (un-normalized) direction-dependent polarization amplitude $\vec{A}_{\pi}^{(\mathrm{ph})}$ for the atomic π transition is decomposed into the two orthogonal horizontal (H) and vertical (V) contributions $\vec{A}_{H,\pi}^{(\mathrm{ph})}$ and $\vec{A}_{V,\pi}^{(\mathrm{ph})}$, which are computed according to

$$\vec{A}_{H/V,\pi}^{(\mathrm{ph})} = \left(\hat{e}_{0}^{(\mathrm{at})} \cdot \hat{e}_{H/V}^{(\mathrm{ph})} \right) \hat{e}_{H/V}^{(\mathrm{ph})} \tag{A.8}$$

Using eq. (A.6), we write $\hat{e}_{0}^{(\mathrm{at})}$ in the photonic basis as

$$\begin{aligned} \hat{e}_{0}^{(\mathrm{at})} &= d^{1}_{0,-1}(-\theta)\, \hat{e}_{-}^{(\mathrm{ph})} + d^{1}_{0,0}(-\theta)\, \hat{e}_{0}^{(\mathrm{ph})} + d^{1}_{0,1}(-\theta)\, \hat{e}_{+}^{(\mathrm{ph})} \\ &= -\frac{\sin\theta}{\sqrt{2}}\, \hat{e}_{-}^{(\mathrm{ph})} + \cos\theta\, \hat{e}_{0}^{(\mathrm{ph})} + \frac{\sin\theta}{\sqrt{2}}\, \hat{e}_{+}^{(\mathrm{ph})} \, . \end{aligned} \tag{A.9}$$

[1] Where the definition of left- and right-hand circular may vary throughout the literature due to the different definitions of the reference frame, pointing along the propagation direction of the photon or the observation direction anti-parallel to it.

Inserting eqs. (A.5) and (A.9) into (A.8), we obtain

$$\begin{aligned}\vec{A}^{(\mathrm{ph})}_{H,\pi} &= \left(\left(-\frac{\sin\theta}{\sqrt{2}}\,\hat{e}^{(\mathrm{ph})}_{-} + \cos\theta\,\hat{e}^{(\mathrm{ph})}_{0} + \frac{\sin\theta}{\sqrt{2}}\,\hat{e}^{(\mathrm{ph})}_{+} \right) \cdot \left(-\frac{1}{\sqrt{2}} \left(\hat{e}^{(\mathrm{ph})}_{+} - \hat{e}^{(\mathrm{ph})}_{-} \right) \right) \right) \hat{e}^{(\mathrm{ph})}_{H} \\ &= -\sin\theta\,\hat{e}^{(\mathrm{ph})}_{H}\end{aligned} \tag{A.10}$$

and

$$\begin{aligned}\vec{A}^{(\mathrm{ph})}_{V,\pi} &= \left(\left(-\frac{\sin\theta}{\sqrt{2}}\,\hat{e}^{(\mathrm{ph})}_{-} + \cos\theta\,\hat{e}^{(\mathrm{ph})}_{0} + \frac{\sin\theta}{\sqrt{2}}\,\hat{e}^{(\mathrm{ph})}_{+} \right) \cdot \left(i\,\frac{1}{\sqrt{2}} \left(\hat{e}^{(\mathrm{ph})}_{+} + \hat{e}^{(\mathrm{ph})}_{-} \right) \right) \right) \hat{e}^{(\mathrm{ph})}_{V} \\ &= \left(-i\,\frac{\sin\theta}{2} + i\,\frac{\sin\theta}{2} \right) \hat{e}^{(\mathrm{ph})}_{V} = 0\,.\end{aligned} \tag{A.11}$$

In sum, the full polarization amplitude is given by

$$\vec{A}^{(\mathrm{ph})}_{\pi} = \vec{A}^{(\mathrm{ph})}_{H,\pi} + \vec{A}^{(\mathrm{ph})}_{V,\pi} = -\sin\theta\,\hat{e}^{(\mathrm{ph})}_{H}\,. \tag{A.12}$$

Analogously, the transformations for $\hat{e}^{(\mathrm{at})}_{\pm}$ ($\sigma^{\pm}$ transitions) are derived as

$$\begin{aligned}\hat{e}^{(\mathrm{at})}_{+} &= e^{i\varphi} \left(d^{1}_{-1,1}(-\theta)\,\hat{e}^{(\mathrm{ph})}_{-} + d^{1}_{0,1}(-\theta)\,\hat{e}^{(\mathrm{ph})}_{0} + d^{1}_{1,1}(-\theta)\,\hat{e}^{(\mathrm{ph})}_{+} \right) \\ &= e^{i\varphi} \left(\frac{1-\cos\theta}{2}\,\hat{e}^{(\mathrm{ph})}_{-} - \frac{\sin\theta}{\sqrt{2}}\,\hat{e}^{(\mathrm{ph})}_{0} + \frac{1+\cos\theta}{2}\,\hat{e}^{(\mathrm{ph})}_{+} \right)\end{aligned} \tag{A.13}$$

and

$$\begin{aligned}\hat{e}^{(\mathrm{at})}_{-} &= e^{-i\varphi} \left(d^{1}_{-1,-1}(-\theta), \hat{e}^{(\mathrm{ph})}_{-} + d^{1}_{0,-1}(-\theta)\,\hat{e}^{(\mathrm{ph})}_{0} + d^{1}_{1,-1}(-\theta)\,\hat{e}^{(\mathrm{ph})}_{+} \right) \\ &= e^{-i\varphi} \left(\frac{1+\cos\theta}{2}\,\hat{e}^{(\mathrm{ph})}_{-} + \frac{\sin\theta}{\sqrt{2}}\,\hat{e}^{(\mathrm{ph})}_{0} + \frac{1-\cos\theta}{2}\,\hat{e}^{(\mathrm{ph})}_{+} \right)\,,\end{aligned} \tag{A.14}$$

respectively. The resulting polarization amplitudes become

$$\begin{aligned}\vec{A}^{(\mathrm{ph})}_{H,\sigma^+} &= \left(\hat{e}^{(\mathrm{at})}_{+} \cdot \hat{e}^{(\mathrm{ph})}_{H} \right) \hat{e}^{(\mathrm{ph})}_{H} \\ &= \left(-\frac{e^{i\varphi}}{\sqrt{2}} \left(\frac{1-\cos\theta}{2}\,\hat{e}^{(\mathrm{ph})}_{-} - \frac{\sin\theta}{\sqrt{2}}\,\hat{e}^{(\mathrm{ph})}_{0} + \frac{1+\cos\theta}{2}\,\hat{e}^{(\mathrm{ph})}_{+} \right) \cdot \left(\hat{e}^{(\mathrm{ph})}_{+} - \hat{e}^{(\mathrm{ph})}_{-} \right) \right) \hat{e}^{(\mathrm{ph})}_{H} \\ &= -\frac{e^{i\varphi}}{\sqrt{2}} \left(-\frac{1+\cos\theta}{2} + \frac{1-\cos\theta}{2} \right) \hat{e}^{(\mathrm{ph})}_{H} = \frac{e^{i\varphi}}{\sqrt{2}}\,\cos\theta\,\hat{e}^{(\mathrm{ph})}_{H}\end{aligned} \tag{A.15}$$

and

$$\begin{aligned}\vec{A}^{(\mathrm{ph})}_{V,\sigma^+} &= \left(\hat{e}^{(\mathrm{at})}_{+} \cdot \hat{e}^{(\mathrm{ph})}_{V} \right) \hat{e}^{(\mathrm{ph})}_{V} \\ &= \left(\frac{ie^{i\varphi}}{\sqrt{2}} \left(\frac{1-\cos\theta}{2}\,\hat{e}^{(\mathrm{ph})}_{-} - \frac{\sin\theta}{\sqrt{2}}\,\hat{e}^{(\mathrm{ph})}_{0} + \frac{1+\cos\theta}{2}\,\hat{e}^{(\mathrm{ph})}_{+} \right) \cdot \left(\hat{e}^{(\mathrm{ph})}_{+} + \hat{e}^{(\mathrm{ph})}_{-} \right) \right) \hat{e}^{(\mathrm{ph})}_{V} \\ &= \frac{ie^{i\varphi}}{\sqrt{2}} \left(\frac{1+\cos\theta}{2} + \frac{1-\cos\theta}{2} \right) \hat{e}^{(\mathrm{ph})}_{V} = \frac{ie^{i\varphi}}{\sqrt{2}}\,\hat{e}^{(\mathrm{ph})}_{V}\,,\end{aligned} \tag{A.16}$$

and thus the combined polarization amplitude is deduced as

$$\vec{A}^{(\mathrm{ph})}_{\sigma^+} = \vec{A}^{(\mathrm{ph})}_{H,\sigma^+} + \vec{A}^{(\mathrm{ph})}_{V,\sigma^+} = \frac{e^{i\varphi}}{\sqrt{2}} \left(\cos\theta\, \hat{e}^{(\mathrm{ph})}_H + i\, \hat{e}^{(\mathrm{ph})}_V \right) . \tag{A.17}$$

In an analogue way, employing eq. (A.14), we obtain

$$\vec{A}^{(\mathrm{ph})}_{H,\sigma^-} = \left(\hat{e}^{(\mathrm{at})}_- \cdot \hat{e}^{(\mathrm{ph})}_H \right) \hat{e}^{(\mathrm{ph})}_H = \frac{e^{-i\varphi}}{\sqrt{2}} \cos\theta\, \hat{e}^{(\mathrm{ph})}_H , \quad \text{and} \tag{A.18}$$

$$\vec{A}^{(\mathrm{ph})}_{V,\sigma^-} = \left(\hat{e}^{(\mathrm{at})}_- \cdot \hat{e}^{(\mathrm{ph})}_V \right) \hat{e}^{(\mathrm{ph})}_V = -\frac{ie^{-i\varphi}}{\sqrt{2}} \hat{e}^{(\mathrm{ph})}_V , \tag{A.19}$$

and in sum

$$\vec{A}^{(\mathrm{ph})}_{\sigma^-} = \vec{A}^{(\mathrm{ph})}_{H,\sigma^-} + \vec{A}^{(\mathrm{ph})}_{V,\sigma^-} = \frac{e^{-i\varphi}}{\sqrt{2}} \left(\cos\theta\, \hat{e}^{(\mathrm{ph})}_H - i\, \hat{e}^{(\mathrm{ph})}_V \right) . \tag{A.20}$$

What we have dismissed so far is the normalization condition for unpolarized light (i.e. light with equal fractions from all three polarizations) that must form a perfect spherical wave in emission which exhibits a probability of 1 to observe the emitted photon when integrated over the full solid angle 4π. This yields the constraint

$$\frac{1}{3} |\vec{A}_\pi|^2 + \frac{1}{3} |\vec{A}_{\sigma^+}|^2 + \frac{1}{3} |\vec{A}_{\sigma^-}|^2 \stackrel{!}{=} \frac{1}{4\pi} \quad \forall\, \theta, \varphi , \tag{A.21}$$

which is only satisfied when the polarization amplitudes $\vec{A}_\pi$, $\vec{A}_{\sigma^+}$ and $\vec{A}_{\sigma^-}$ are normalized by a factor of $\sqrt{\frac{3}{8\pi}}$. We then get the normalized polarization amplitudes

$$\vec{A}^{(\mathrm{ph})}_{\pi} = -\sqrt{\frac{3}{8\pi}} \sin\theta\, \hat{e}^{(\mathrm{ph})}_H , \tag{A.22}$$

$$\vec{A}^{(\mathrm{ph})}_{\sigma^+} = \sqrt{\frac{3}{8\pi}} \frac{e^{i\varphi}}{\sqrt{2}} \left(\cos\theta\, \hat{e}^{(\mathrm{ph})}_H + i\, \hat{e}^{(\mathrm{ph})}_V \right) , \text{and} \tag{A.23}$$

$$\vec{A}^{(\mathrm{ph})}_{\sigma^-} = \sqrt{\frac{3}{8\pi}} \frac{e^{-i\varphi}}{\sqrt{2}} \left(\cos\theta\, \hat{e}^{(\mathrm{ph})}_H - i\, \hat{e}^{(\mathrm{ph})}_V \right) . \tag{A.24}$$

A.1.2. Free-space collection

Estimation of the success probability for an experimental sequence in the context of this work requires the knowledge about the collection efficiencies of the single photons. Here we investigate the free-space collection, as already briefly treated in sec. 4.2.3, i.e. the direct collection of photons without the coupling into a single-mode fiber. In that case, it is sufficient to consider only the intensities (as opposed to the single-mode coupled case, discussed in section 4.2.4 and appendix A.1.3, where the complex field has to be regarded).

Single photons from the ion are collected by the HALO lens stack which covers an opening angle of $2\alpha = 2 \cdot 23.75°$, corresponding to 4.23% of the full solid angle. Together with

the directionality of the dipole emission from section 4.2.2 and appendix A.1.1, we are then able to calculate the expected photon-collection efficiency.

To determine the collection efficiency, we define the "intensity" $I^{(\mathrm{ph})} = |A^{(\mathrm{ph})}|^2$ of the normalized field as the square modulus of the polarization amplitude. It has to be stated that $I^{(\mathrm{ph})}$ denotes a probability intensity, which is proportional to the usual intensity, but exhibits a different physical dimension (probability per solid angle rather than power per area), where the integration over the full solid angle reveals a probability of 1.

For pure π emission, we get

$$I_\pi(\theta,\varphi) = |\vec{A}_\pi|^2 = \Big| -\sqrt{\frac{3}{8\pi}}\,\sin\theta\,\hat{e}_H^{(\mathrm{ph})}\Big|^2 = \frac{3}{8\pi}\,\sin^2\theta \tag{A.25}$$

and the free-space or multi-mode collection efficiency is given by

$$\eta_\pi^{MM} = \int_{\theta=0}^{\alpha}\int_{\varphi=0}^{2\pi} I_\pi(\theta,\varphi)\,\sin\theta\,d\theta\,d\varphi = 2\pi\,\frac{3}{8\pi}\int_{\theta=0}^{\alpha=23.75^\circ}\sin^3\theta\,d\theta \approx 0.53\%\,. \tag{A.26}$$

In the case of a σ transition with

$$\begin{aligned} I_{\sigma^\pm}(\theta,\varphi) &= |\vec{A}_{\sigma^\pm}|^2 = \Big|\sqrt{\frac{3}{8\pi}}\,\frac{e^{\pm i\varphi}}{\sqrt{2}}\,\Big(\cos\theta\,\hat{e}_H^{(\mathrm{ph})} \pm i\,\hat{e}_V^{(\mathrm{ph})}\Big)\Big|^2 \\ &= \frac{3}{8\pi}\cdot\frac{1}{2}\,\Big(\cos\theta\,\hat{e}_H^{(\mathrm{ph})} \pm i\,\hat{e}_V^{(\mathrm{ph})}\Big)\Big(\cos\theta\,\hat{e}_H^{(\mathrm{ph})} \mp i\,\hat{e}_V^{(\mathrm{ph})}\Big) = \frac{3}{8\pi}\,\frac{1}{2}\,\left(\cos^2\theta+1\right) \end{aligned} \tag{A.27}$$

the collection efficiency reads

$$\eta_\sigma^{MM} = \int_{\theta=0}^{\alpha}\int_{\varphi=0}^{2\pi} I_\sigma(\theta,\varphi)\,\sin\theta\,d\theta\,d\varphi = \frac{3}{8}\int_{\theta=0}^{\alpha=23.75^\circ}\left(\cos^2\theta+1\right)\,\sin\theta\,d\theta \approx 6.09\%\,. \tag{A.28}$$

A.1.3. Single-mode coupling

For photons coupled into a single-mode fiber, it is not sufficient to consider only the intensity, but the complex field, i.e. intensity and phase of the light field, hast to be taken into account. Here we investigate the coupling efficiency for photons emitted by the ion and collected hy the HALO lens system, assuming a fiber mode that perfectly matches the top-hat shaped HALO light mode. A calculation of the coupling efficiency including a Gaussian fiber mode is given in the next section.

All calculations in this section are conducted in the laboratory (atomic) reference frame, thus the superscripts $^{(\mathrm{at})}$ and $^{(\mathrm{ph})}$ are omitted.

When the light emitted by the ion is collimated by the HALO, the field wavefront becomes flat and we transform the electrical-field amplitudes[2] for the dipole transitions from

[2]Be aware that this quantity does not exhibit the physical unit of, but is directly proportional to the actual electrical field.

spherical coordinates,

$$\vec{E}_\pi = -\frac{ie^{ikr}}{r}\sqrt{\frac{3}{8\pi}}\sin\theta\,\hat{e}_\theta\,, \tag{A.29}$$

$$\vec{E}_{\sigma^\pm} = \frac{ie^{ikr}}{r}\sqrt{\frac{3}{8\pi}}\frac{e^{\pm i\varphi}}{\sqrt{2}}\left(\cos\theta\,\hat{e}_\theta \pm i\,\hat{e}_\varphi\right)\,, \tag{A.30}$$

with $k = 1/\lambda$ being the absolute value of the wave vector, into cylindrical coordinates (z, φ, ϱ). If the ion is placed in the focus of the HALO with focal length f, the distance r from the ion to the collimation-lens plane is $r = \sqrt{f^2+\varrho^2}$, where ϱ is the distance from the z axis, i.e. from the quantization axis. After collimation, the wavefront of the photonic wave packet will be flat, i.e. the terms in e^{ikr} in (A.29) and (A.30) will be constant and without loss of generality set to 1. Light formerly polarized in the $\hat{e}_\theta$ direction is polarized in $\hat{e}_\varrho$ direction, while the polarization component parallel to $\hat{e}_\varphi$ remains unaltered. With

$$\cos\theta = \frac{f}{\sqrt{f^2+\varrho^2}} \qquad \text{and} \qquad \sin\theta = \frac{\varrho}{\sqrt{f^2+\varrho^2}} \tag{A.31}$$

the field amplitudes become

$$\vec{E}_\pi = -\frac{i}{\sqrt{f^2+\varrho^2}}\sqrt{\frac{3}{8\pi}}\frac{\varrho}{\sqrt{f^2+\varrho^2}}\,\hat{e}_\varrho \tag{A.32}$$

and

$$\vec{E}_{\sigma^\pm} = \frac{i}{\sqrt{f^2+\varrho^2}}\sqrt{\frac{3}{8\pi}}\frac{e^{\pm i\varphi}}{\sqrt{2}}\left(\frac{f}{\sqrt{f^2+\varrho^2}}\,\hat{e}_\varrho \pm i\,\hat{e}_\varphi\right) \tag{A.33}$$

with

$$\hat{e}_\varrho = \begin{pmatrix}\cos\varphi\\ \sin\varphi\\ 0\end{pmatrix} \text{ and } \hat{e}_\varphi = \begin{pmatrix}-\sin\varphi\\ \cos\varphi\\ 0\end{pmatrix}\,. \tag{A.34}$$

The coupling efficiency into the single-mode fiber is attained by the overlap between the electrical-field mode $\vec{E}$ and the fiber mode $\vec{G}$ [100],

$$\eta^{SM} = \frac{\left|\int_{\varrho=0}^{\varrho_0}\int_{\varphi=0}^{2\pi}\vec{E}\cdot\vec{G}\,\varrho\cos(\theta(\varrho))d\varrho d\varphi\right|^2}{\int_{\varrho=0}^{\infty}\int_{\varphi=0}^{2\pi}\left|\vec{E}\right|^2\varrho\cos(\theta(\varrho))d\varrho d\varphi\int_{\varrho=0}^{\infty}\int_{\varphi=0}^{2\pi}\left|\vec{G}\right|^2\varrho\cos(\theta(\varrho))d\varrho d\varphi}\,, \tag{A.35}$$

where the factor $\cos(\theta(\varrho)) = \frac{f}{\sqrt{f^2+\varrho^2}}$ accounts for the projection of the spherical surface element onto the surface element of the measurement plane. ϱ_0 is the maximal diameter of the collimated light, determined by $\varrho_0 = \tan(\alpha)\cdot f$. For the effective focal length $f = 25\,\text{mm}$, we get $\varrho_0 = 11\,\text{mm}$.

In a first approach, the approximately Gaussian shape of the fiber mode is disregarded and we assume a fiber that matches the HALO mode. The fiber mode is modeled as

$$\vec{G} = \Theta(\varrho_0 - \varrho) \begin{pmatrix} \alpha \\ \beta \\ 0 \end{pmatrix} \quad , \quad |\alpha|^2 + |\beta|^2 = 1 \tag{A.36}$$

with the Heaviside function $\Theta(\varrho_0 - \varrho)$, resulting in the fiber-coupling efficiencies

$$\eta_\pi^{SM} = \frac{\left| \int_{\varrho=0}^{\varrho_0} \int_{\varphi=0}^{2\pi} \frac{1}{\sqrt{f^2+\varrho^2}} \frac{\varrho}{\sqrt{f^2+\varrho^2}} \begin{pmatrix} \cos\varphi \\ \sin\varphi \\ 0 \end{pmatrix} \Theta(\varrho_0 - \varrho) \begin{pmatrix} \alpha \\ \beta \\ 0 \end{pmatrix} \frac{f\,\varrho}{\sqrt{f^2+\varrho^2}} d\varrho d\varphi \right|^2}{\int_{\varrho=0}^{\infty} \int_{\varphi=0}^{2\pi} \frac{\varrho^2}{(f^2+\varrho^2)^2} \frac{f\,\varrho}{\sqrt{f^2+\varrho^2}} d\varrho d\varphi \int_{\varrho=0}^{\varrho_0} \int_{\varphi=0}^{2\pi} \frac{f\,\varrho}{\sqrt{f^2+\varrho^2}} d\varrho d\varphi} = 0 \tag{A.37}$$

and

$$\eta_{\sigma^\pm}^{SM} = \frac{\left| \int_{\varrho=0}^{\varrho_0} \int_{\varphi=0}^{2\pi} \frac{1}{\sqrt{f^2+\varrho^2}} e^{\pm i\varphi} \left(\frac{f}{\sqrt{f^2+\varrho^2}} \begin{pmatrix} \cos\varphi \\ \sin\varphi \\ 0 \end{pmatrix} \pm i \begin{pmatrix} -\sin\varphi \\ \cos\varphi \\ 0 \end{pmatrix} \right) \begin{pmatrix} \alpha \\ \beta \\ 0 \end{pmatrix} \frac{f\,\varrho}{\sqrt{f^2+\varrho^2}} d\varrho d\varphi \right|^2}{\underbrace{\int_{\varrho=0}^{\infty} \int_{\varphi=0}^{2\pi} \left(\frac{f^2}{(f^2+\varrho^2)^2} + \frac{1}{f^2+\varrho^2} \right) \frac{f\,\varrho}{\sqrt{f^2+\varrho^2}} d\varrho d\varphi}_{=\frac{8\pi}{3}} \underbrace{\int_{\varrho=0}^{\varrho_0} \int_{\varphi=0}^{2\pi} \frac{f\,\varrho}{\sqrt{f^2+\varrho^2}} d\varrho d\varphi}_{=2\pi\left(f\sqrt{f^2+\varrho_0^2}-f^2\right)}} . \tag{A.38}$$

Solving eq. (A.38) yields

$$\eta_{\sigma^\pm}^{SM} \approx \frac{|0.0136\,\mathrm{m}|^2}{\frac{8\pi}{3} \cdot 0.00363\mathrm{m}^2} \approx 6.09\% \,. \tag{A.39}$$

We see that the collection of σ light is unaltered compared to the multi-mode collection, while the collection of π photons is suppressed. Hence, when the collection of photons emitted on a σ transition is desired, while π photons are unwanted, single-mode collection does significantly increase the polarization purity of the fiber-coupled photons.

It is of particular interest to analyze the situation of a superposition of two atomic dipoles emerging from a σ^+ and a σ^- transition, respectively.

The field amplitude for the emitted field becomes

$$\begin{aligned} \vec{E}_\sigma &= \frac{1}{\sqrt{2}} \left(\vec{E}_{\sigma^+} + e^{i\phi} \vec{E}_{\sigma^-} \right) \\ &= \frac{i}{\sqrt{f^2+\varrho^2}} \sqrt{\frac{3}{32\pi}} \left(\frac{f\left(e^{i\varphi} + e^{i\phi} e^{-i\varphi}\right)}{\sqrt{f^2+\varrho^2}} \hat{e}_\varrho + \left(i e^{i\varphi} - i e^{i\phi} e^{-i\varphi} \right) \hat{e}_\varphi \right) , \end{aligned} \tag{A.40}$$

where ϕ describes the relative phase between the dipoles. Inserting (A.40) into (A.35) and numerically solving the equation reveals the coupling efficiency

$$\eta_\sigma^{SM} \approx 6.09\% \,. \tag{A.41}$$

We see that the collection efficiency stays unchanged and is independent of ϕ.

A.1.4. Mode matching

In a realistic estimation of the single-mode coupling efficiency, the fiber mode $\vec{G}$ used in eq. (A.36) has to be modified to exhibit a Gaussian shape: [145]

$$\vec{G} = \frac{\sqrt{2}}{w_0\sqrt{\pi}} e^{i\psi} \exp\left(-\frac{\varrho^2}{w^2(z)}\right) \begin{pmatrix} \alpha \\ \beta \\ 0 \end{pmatrix} \,. \tag{A.42}$$

ψ denotes the Gouy phase, w_0 is the beam waist, and $w(z)$ describes the beam radius in the measurement plane. In our situation, $w(z)$ coincides with the maximum beam radius ϱ_0.

As $\vec{G}$ remains independent of φ, it is directly apparent that

$$\eta_\pi^{SM} = \frac{\left| \int_{\varrho=0}^{\varrho_0} \int_{\varphi=0}^{2\pi} \vec{E}_\pi \cdot \vec{G} \, \frac{f\,\varrho}{\sqrt{f^2+\varrho^2}} d\varrho d\varphi \right|^2}{\int_{\varrho=0}^{\infty} \int_{\varphi=0}^{2\pi} \left|\vec{E}_\pi\right|^2 \frac{f\,\varrho}{\sqrt{f^2+\varrho^2}} d\varrho d\varphi \int_{\varrho=0}^{\infty} \int_{\varphi=0}^{2\pi} \left|\vec{G}\right|^2 \frac{f\,\varrho}{\sqrt{f^2+\varrho^2}} d\varrho d\varphi} = 0 \tag{A.43}$$

as the integral in the numerator vanishes.

The computation of the coupling efficiency for a σ transition is slightly more involved. The integral in the numerator yields

$$\begin{aligned} &\left| \int_{\varrho=0}^{\varrho_0} \int_{\varphi=0}^{2\pi} \vec{E}_{\sigma^\pm} \cdot \vec{G} \, \frac{f\,\varrho}{\sqrt{f^2+\varrho^2}} d\varrho d\varphi \right|^2 \\ &= \frac{3}{w_0^2\, 8\pi^2} \left| \int_{\varrho=0}^{\varrho_0} \int_{\varphi=0}^{2\pi} \frac{e^{\pm i\varphi}}{\sqrt{f^2+\varrho^2}} \left(\frac{f}{\sqrt{f^2+\varrho^2}} \begin{pmatrix} \cos\varphi \\ \sin\varphi \\ 0 \end{pmatrix} \pm i \begin{pmatrix} -\sin\varphi \\ \cos\varphi \\ 0 \end{pmatrix} \right) \cdot \right. \\ &\left. \exp\left(-\frac{\varrho^2}{\varrho_0^2}\right) \begin{pmatrix} \alpha \\ \beta \\ 0 \end{pmatrix} \, \frac{f\,\varrho}{\sqrt{f^2+\varrho^2}} \, d\varrho d\varphi \right|^2 \\ &\approx \frac{3}{w_0^2\, 8\pi^2} \cdot 0.00609^2 \,\mathrm{m}^2 \,. \end{aligned} \tag{A.44}$$

Both terms in the denominator become

$$\begin{aligned}
&\int_{\varrho=0}^{\infty}\int_{\varphi=0}^{2\pi}\left|\vec{E}_{\sigma^\pm}\right|^2\frac{f\,\varrho}{\sqrt{f^2+\varrho^2}}d\varrho d\varphi\\
&=\int_{\varrho=0}^{\infty}\int_{\varphi=0}^{2\pi}\left|\frac{ie^{\pm i\varphi}}{\sqrt{f^2+\varrho^2}}\sqrt{\frac{3}{16\pi}}\left(\frac{f}{\sqrt{f^2+\varrho^2}}\begin{pmatrix}\cos\varphi\\ \sin\varphi\\ 0\end{pmatrix}\pm i\begin{pmatrix}-\sin\varphi\\ \cos\varphi\\ 0\end{pmatrix}\right)\right|^2\frac{f\,\varrho}{\sqrt{f^2+\varrho^2}}\,d\varrho d\varphi\\
&=\frac{3}{16\pi}\int_{\varrho=0}^{\infty}\int_{\varphi=0}^{2\pi}\left(\frac{f^2}{(f^2+\varrho^2)^2}+\frac{1}{f^2+\varrho^2}\right)\frac{f\,\varrho}{\sqrt{f^2+\varrho^2}}\,d\varrho d\varphi\\
&=\frac{3}{16\pi}\cdot\frac{8\pi}{3}=\frac{1}{2}
\end{aligned}\tag{A.45}$$

and

$$\begin{aligned}
&\int_{\varrho=0}^{\infty}\int_{\varphi=0}^{2\pi}\left|\vec{G}\right|^2\frac{f\,\varrho}{\sqrt{f^2+\varrho^2}}d\varrho d\varphi=\frac{2}{w_0^2\pi}\int_{\varrho=0}^{\infty}\int_{\varphi=0}^{2\pi}\exp\left(-2\,\frac{\varrho^2}{\varrho_0^2}\right)\frac{f\,\varrho}{\sqrt{f^2+\varrho^2}}d\varrho d\varphi\\
&=\frac{4}{w_0^2}\int_{\varrho=0}^{\infty}\exp\left(-2\,\frac{\varrho^2}{\varrho_0^2}\right)\frac{f\,\varrho}{\sqrt{f^2+\varrho^2}}d\varrho\approx\frac{4}{w_0^2}\cdot 0.000029\,\mathrm{m}^2
\end{aligned}\tag{A.46}$$

respectively. Merging eqs. (A.44), (A.45) and (A.46) unfolds the coupling efficiency

$$\eta_{\sigma^\pm}^{SM}=\frac{\frac{3}{w_0^2\,8\pi^2}\cdot 0.00609^2\,\mathrm{m}^2}{\frac{1}{2}\cdot\frac{4}{w_0^2}\cdot 0.000029\,\mathrm{m}^2}=\frac{3}{16\pi^2}\,\frac{0.00609^2}{0.000029}\approx 2.43\%\,.\tag{A.47}$$

Compared to the idealized fiber, the coupling efficiency is reduced to 40% of the optimal value, which nicely agrees with our measurements. However, it becomes apparent that the assumption of a top-hat shaped fiber mode is not sufficient for reproducing the experimental results and a more realistic model like a Gaussian mode has to be employed.

A.2. Single-qubit state reconstruction

A single qubit, e.g. the polarization state of a single photon or the internal or motional state of a single trapped atom, can not be measured directly due to the projective nature of a quantum-mechanical measurement. However, if it is possible to create multiple copies of the qubit (e.g. by very well controlled state preparation), a set of tomography measurements in different bases allows for the reconstruction of the qubit state. [156] provides a convenient and straightforward recipe for a single-qubit state reconstruction for single photons, which can easily be adapted to other quantum systems. For the sake of consistency, we adopt the photonic nomenclature of the bases $|R\rangle$, $|L\rangle$, $|H\rangle$, $|V\rangle$, $|D\rangle$, $|A\rangle$. In the context of an atomic qubit with internal eigenstates $|0\rangle$ and $|1\rangle$, $|R\rangle$ and $|L\rangle$ become $|1\rangle$ and $|0\rangle$, and $|H\rangle$, $|V\rangle$, $|D\rangle$, and $|A\rangle$ become the respective superposition states of $|0\rangle$ and $|1\rangle$.

The state tomography is facilitated by measurements in different projection bases, and the number of detection events is recorded for each basis (assuming an equal number of experimental runs for each basis). For the single-qubit tomography, it is sufficient to measure in 4 different bases, e.g. $|R\rangle + |L\rangle$, $|H\rangle$, $|\bar{D}\rangle = (|H\rangle - |V\rangle)/\sqrt{2}$, and $|R\rangle$.

From the number of detection events in these bases,

$$n_0 = n_{|R\rangle+|L\rangle} = \frac{\mathcal{N}}{2}\left(\langle R|\hat{\rho}|R\rangle + \langle L|\hat{\rho}|L\rangle\right) \tag{A.48}$$

$$n_1 = n_{|H\rangle} = \mathcal{N}\left(\langle H|\hat{\rho}|H\rangle\right) \tag{A.49}$$

$$n_2 = n_{|\bar{D}\rangle} = \mathcal{N}\left(\langle \bar{D}|\hat{\rho}|\bar{D}\rangle\right) \tag{A.50}$$

$$n_3 = n_{|R\rangle} = \mathcal{N}\left(\langle R|\hat{\rho}|R\rangle\right) \tag{A.51}$$

with the (to be determined) single-qubit density matrix $\hat{\rho}$ and a normalization factor $\mathcal{N}$ that accounts for the detection efficiency (in the case of photonic qubits).

With the Stokes parameters defined by

$$S_0 = 2n_0\,, \qquad S_1 = 2(n_1 - n_0)$$
$$S_0 = 2(n_2 - n_0)\,, \qquad S_0 = 2(n_3 - n_0)\,,$$

we deduce the density matrix via the relation

$$\hat{\rho} = \frac{1}{2}\sum_{i=0}^{3}\frac{S_i}{S_0}\hat{\sigma}_i \tag{A.52}$$

with the Pauli operators $\hat{\sigma}_{1,2,3}$ and the identity operator $\hat{\sigma}_0$.

A.3. Linear entangled-state reconstruction

The two-qubit state tomography has already been briefly depicted in section 5.4 and shall be explained in more detail in this section.

In general, a two-qubit state is described by the density matrix

$$\hat{\rho} = \frac{1}{4} \sum_{i_1, j_2 = 0}^{3} r_{i_1} \, r_{j_2} \, \hat{\sigma}_{i_1} \otimes \hat{\sigma}_{j_2} \, , \qquad\qquad r_{i_1}, r_{j_2} \in \mathbb{R} \, . \tag{A.53}$$

$\hat{\sigma}_{i_k}$ denotes the i-th Pauli matrix for the k-th qubit and $\otimes$ denotes the tensor product. [156] provides a recipe for the determination of the $4^2 = 16$ real parameters r_{i_1}, r_{i_2}, that fully describe the state. In analogy to the single-qubit case, we need a set of 16 measurements $\hat{\mu}_{i_1} \otimes \hat{\mu}_{j_2}$ $(i_1, j_2 = 0, 1, 2, 3)$.

Given a yet unknown two-qubit density matrix $\hat{\rho}$, the expected coincidence counts $n_k = n_{i,j}$ in the joint measurement basis $\hat{\mu}_k = \hat{\mu}_{i_1} \otimes \hat{\mu}_{j_2}$ $(k = 1, ..., 16)$ are given by the expression

$$n_k = \mathcal{N} \, tr(\hat{\rho} \hat{\mu}_k) \tag{A.54}$$

or

$$n_k = \mathcal{N} \, \langle \psi_k | \hat{\rho} | \psi_k \rangle \, , \tag{A.55}$$

where the experimentally determined constant $\mathcal{N}$ accounts for the detection efficiencies and $\hat{\mu}_k = |\psi_k\rangle\langle\psi_k|$. Table A.3, taken from [156], shows one possible set of measurement bases in the photonic nomenclature.For measurements of atomic qubits, the states have to be adapted, e.g. with $|R\rangle = |1\rangle$, $|L\rangle = |0\rangle$ and the linear bases defined accordingly.

k	$\lvert\psi_k\rangle$	k	$\lvert\psi_k\rangle$
1	$\lvert H\rangle \otimes \lvert H\rangle$	9	$\lvert D\rangle \otimes \lvert R\rangle$
2	$\lvert H\rangle \otimes \lvert V\rangle$	10	$\lvert D\rangle \otimes \lvert D\rangle$
3	$\lvert V\rangle \otimes \lvert V\rangle$	11	$\lvert R\rangle \otimes \lvert D\rangle$
4	$\lvert V\rangle \otimes \lvert H\rangle$	12	$\lvert H\rangle \otimes \lvert D\rangle$
5	$\lvert R\rangle \otimes \lvert H\rangle$	13	$\lvert V\rangle \otimes \lvert D\rangle$
6	$\lvert R\rangle \otimes \lvert V\rangle$	14	$\lvert V\rangle \otimes \lvert L\rangle$
7	$\lvert D\rangle \otimes \lvert V\rangle$	15	$\lvert H\rangle \otimes \lvert L\rangle$
8	$\lvert D\rangle \otimes \lvert H\rangle$	16	$\lvert R\rangle \otimes \lvert L\rangle$

Table A.1.: List of the two-qubit measurement bases for the state tomography.

From the experimentally obtained numbers n_k for measurements in these bases, the underlying density matrix is calculated from

$$\hat{\rho} = \sum_{k=1}^{16} \hat{M}_k n_k / \sum_{k=1}^{4} n_k \, , \tag{A.56}$$

where the matrices $\hat{M}_k$ are found as

$$\hat{M}_1 = \frac{1}{2}\begin{pmatrix} 2 & -(1-i) & -(1+i) & 1 \\ -(1+i) & 0 & i & 0 \\ -(1-i) & -i & 0 & 0 \\ 1 & 0 & 0 & 0 \end{pmatrix} \tag{A.57}$$

$$\hat{M}_2 = \frac{1}{2}\begin{pmatrix} 0 & -(1-i) & 0 & 1 \\ -(1+i) & 2 & i & -(1+i) \\ 0 & -i & 0 & 0 \\ 1 & -(1+i) & 0 & 0 \end{pmatrix} \tag{A.58}$$

$$\hat{M}_3 = \frac{1}{2}\begin{pmatrix} 0 & 0 & 0 & 1 \\ 0 & 0 & i & -(1+i) \\ 0 & -i & 0 & -(1-i) \\ 1 & -(1-i) & -(1+i) & 2 \end{pmatrix} \tag{A.59}$$

$$\hat{M}_4 = \frac{1}{2}\begin{pmatrix} 0 & 0 & -(1+i) & 1 \\ 0 & 0 & i & 0 \\ -(1-i) & -i & 2 & -(1-i) \\ 1 & 0 & -(1+i) & 0 \end{pmatrix} \tag{A.60}$$

$$\hat{M}_5 = \frac{1}{2}\begin{pmatrix} 0 & 0 & 2i & -(1+i) \\ 0 & 0 & (1-i) & 0 \\ -2i & (1+i) & 0 & 0 \\ -(1-i) & 0 & 0 & 0 \end{pmatrix} \tag{A.61}$$

$$\hat{M}_6 = \frac{1}{2}\begin{pmatrix} 0 & 0 & 2i & -(1+i) \\ 0 & 0 & (1-i) & 2i \\ 0 & (1+i) & 0 & 0 \\ -(1-i) & -2i & 0 & 0 \end{pmatrix} \tag{A.62}$$

$$\hat{M}_7 = \frac{1}{2}\begin{pmatrix} 0 & 0 & 0 & -(1+i) \\ 0 & 0 & -(1-i) & 2 \\ 0 & -(1+i) & 0 & 0 \\ -(1-i) & 2 & 0 & 0 \end{pmatrix} \tag{A.63}$$

$$\hat{M}_8 = \frac{1}{2}\begin{pmatrix} 0 & 0 & 2 & -(1+i) \\ 0 & 0 & -(1-i) & 0 \\ 2 & -(1+i) & 0 & 0 \\ -(1-i) & 0 & 0 & 0 \end{pmatrix} \tag{A.64}$$

$$\hat{M}_9 = \begin{pmatrix} 0 & 0 & 0 & i \\ 0 & 0 & -i & 0 \\ 0 & i & 0 & 0 \\ -i & 0 & 0 & 0 \end{pmatrix} \tag{A.65}$$

$$\hat{M}_{10} = \begin{pmatrix} 0 & 0 & 0 & 1 \\ 0 & 0 & 1 & 0 \\ 0 & 1 & 0 & 0 \\ 1 & 0 & 0 & 0 \end{pmatrix} \tag{A.66}$$

$$\hat{M}_{11} = \begin{pmatrix} 0 & 0 & 0 & i \\ 0 & 0 & i & 0 \\ 0 & -i & 0 & 0 \\ -i & 0 & 0 & 0 \end{pmatrix} \tag{A.67}$$

$$\hat{M}_{12} = \frac{1}{2} \begin{pmatrix} 0 & 2 & 0 & -(1+i) \\ 2 & 0 & -(1+i) & 0 \\ 0 & -(1-i) & 0 & 0 \\ -(1-i) & 0 & 0 & 0 \end{pmatrix} \tag{A.68}$$

$$\hat{M}_{13} = \frac{1}{2} \begin{pmatrix} 0 & 0 & 0 & -(1+i) \\ 0 & 0 & -(1+i) & 0 \\ 0 & -(1-i) & 0 & 2 \\ -(1-i) & 0 & 2 & 0 \end{pmatrix} \tag{A.69}$$

$$\hat{M}_{14} = \frac{1}{2} \begin{pmatrix} 0 & 0 & 0 & -(1-i) \\ 0 & 0 & -(1-i) & 0 \\ 0 & -(1+i) & 0 & -2i \\ -(1+i) & 0 & 2i & 0 \end{pmatrix} \tag{A.70}$$

$$\hat{M}_{15} = \frac{1}{2} \begin{pmatrix} 0 & -2i & 0 & -(1-i) \\ 2i & 0 & (1-i) & 0 \\ 0 & (1+i) & 0 & 0 \\ -(1+i) & 0 & 0 & 0 \end{pmatrix} \tag{A.71}$$

$$\hat{M}_{16} = \begin{pmatrix} 0 & 0 & 0 & 1 \\ 0 & 0 & -1 & 0 \\ 0 & -1 & 0 & 0 \\ 1 & 0 & 0 & 0 \end{pmatrix} . \tag{A.72}$$

A.4. Maximum-likelihood estimation

The tomographic reconstruction (based on the treatment in [156]) of the density matrix might produce a state that is not physical. The maximum-likelihood estimation is employed to find the closest physical state that reproduces the measured data with the highest probability.

First, we construct a density matrix that is physical. This physical density matrix $\hat{\varrho}_P(t_1, ..., t_{16})$ is of the form

$$\hat{\varrho}_P(t_1, ..., t_{16}) = \frac{\hat{T}^\dagger \hat{T}}{tr(\hat{T}^\dagger \hat{T})} \tag{A.73}$$

with

$$\hat{T}(t_1, ..., t_{16}) = \begin{pmatrix} t_1 & 0 & 0 & 0 \\ t_5 + it_6 & t_2 & 0 & 0 \\ t_{11} + it_{12} & t_7 + it_8 & t_3 & 0 \\ t_{15} + it_{16} & t_{13} + it_{14} & t_9 + it_{10} & t_4 \end{pmatrix} . \tag{A.74}$$

In the next step, we derive a likelihood function to determine the probability that the current density matrix reproduces the set of measured data, i.e. how well the density matrix describes the underlying physical state.

Assuming a Gaussian probability distribution of the coincidence counts, we obtain the probability to measure the set of experimental coincidence counts for the measurements in the 16 bases, $n_1, ..., n_{16}$, for the current density matrix $\hat{\varrho}_P(t_1, ..., t_{16})$

$$\mathcal{P}(t_1, ..., t_{16}) = \frac{1}{N} \prod_{\nu=1}^{16} \exp\left(- \frac{\left(\mathcal{N}\langle\psi_\nu|\hat{\varrho}_P(t_1, ..., t_{16})|\psi_\nu\rangle - n_\nu\right)^2}{2\mathcal{N}\langle\psi_\nu|\hat{\varrho}_P(t_1, ..., t_{16})|\psi_\nu\rangle} \right) , \tag{A.75}$$

where $\frac{1}{N}$ accounts for the normalization, $\mathcal{N}\langle\psi_\nu|\hat{\varrho}_P(t_1, ..., t_{16})|\psi_\nu\rangle$ is the model-state–dependent coincidence-counts expectation value, and $\mathcal{N} = \sum_{\nu=1}^{4} n_\nu$. Here we used that the standard deviation is approximately $\sqrt{\mathcal{N}\langle\psi_\nu|\hat{\varrho}_P(t_1, ..., t_{16})|\psi_\nu\rangle}$.

To find the optimal set of optimization parameters $t_1, ..., t_{16}$, we maximize the function (A.75). Since the latter is computationally slow, it is more efficient to minimize the (negative) logarithm of $\mathcal{P}(t_1, ..., t_{16})$,

$$\mathcal{L}(t_1, ..., t_{16}) = \sum_{\nu=1}^{16} \frac{\left(\mathcal{N}\langle\psi_\nu|\hat{\varrho}_P(t_1, ..., t_{16})|\psi_\nu\rangle - n_\nu\right)^2}{2\mathcal{N}\langle\psi_\nu|\hat{\varrho}_P(t_1, ..., t_{16})|\psi_\nu\rangle} . \tag{A.76}$$

Our implementation of this method works with the joint atom-photon expectation values w_ν for measurements in the ν-th basis. The uncertainties u_ν of w_ν are derived from error propagation of the individual uncertainties in the conditioned expectation values $w_{ij}^{\text{ion}} = tr(\sigma_i \otimes \varrho_j)$, where $\sigma_{1,2,3}$ denotes the Pauli matrices (without the identity) and ϱ_j describes the atomic density matrix conditioned on the detection of the photon in state

j ($|H\rangle$,$|D\rangle$,$|V\rangle$,$|A\rangle$,$|R\rangle$, and $|L\rangle$), derived from a finite difference quotient, and the uncertainty of the photon-detection probability $p_{\mathrm{ph},k}$ in the k-th basis, derived from Bayesian statistics. A summary of the entries of w_ν is given in tab. A.4.

ν	σ_{ion}	σ_{photon}	w_ν
1	σ_0 ($\mathbb{1}$)	σ_0	1
2	σ_0 ($\mathbb{1}$)	σ_1 (H/V)	$p_{\mathrm{ph},H}$ - $p_{\mathrm{ph},V}$
3	σ_0 ($\mathbb{1}$)	σ_2 (D/A)	$p_{\mathrm{ph},D}$ - $p_{\mathrm{ph},A}$
4	σ_0 ($\mathbb{1}$)	σ_3 (R/L)	$p_{\mathrm{ph},R}$ - $p_{\mathrm{ph},L}$
5	σ_1 (σ_x)	σ_0	$w^{\mathrm{ion}}_{x,H} \cdot p_{\mathrm{ph},H} + w^{\mathrm{ion}}_{x,V} \cdot p_{\mathrm{ph},V}$
6	σ_1 (σ_x)	σ_1 (H/V)	$w^{\mathrm{ion}}_{x,H} \cdot p_{\mathrm{ph},H}$ - $w^{\mathrm{ion}}_{x,V} \cdot p_{\mathrm{ph},V}$
7	σ_1 (σ_x)	σ_2 (D/A)	$w^{\mathrm{ion}}_{x,D} \cdot p_{\mathrm{ph},D}$ - $w^{\mathrm{ion}}_{x,A} \cdot p_{\mathrm{ph},A}$
8	σ_1 (σ_x)	σ_3 (R/L)	$w^{\mathrm{ion}}_{x,R} \cdot p_{\mathrm{ph},R}$ - $w^{\mathrm{ion}}_{x,L} \cdot p_{\mathrm{ph},L}$
9	σ_2 (σ_y)	σ_0	$w^{\mathrm{ion}}_{y,H} \cdot p_{\mathrm{ph},H} + w^{\mathrm{ion}}_{y,V} \cdot p_{\mathrm{ph},V}$
10	σ_2 (σ_y)	σ_1 (H/V)	$w^{\mathrm{ion}}_{y,H} \cdot p_{\mathrm{ph},H}$ - $w^{\mathrm{ion}}_{y,V} \cdot p_{\mathrm{ph},V}$
11	σ_2 (σ_y)	σ_2 (D/A)	$w^{\mathrm{ion}}_{y,D} \cdot p_{\mathrm{ph},D}$ - $w^{\mathrm{ion}}_{y,A} \cdot p_{\mathrm{ph},A}$
12	σ_2 (σ_y)	σ_3 (R/L)	$w^{\mathrm{ion}}_{y,R} \cdot p_{\mathrm{ph},R}$ - $w^{\mathrm{ion}}_{y,L} \cdot p_{\mathrm{ph},L}$
13	σ_3 (σ_z)	σ_0	$w^{\mathrm{ion}}_{z,H} \cdot p_{\mathrm{ph},H} + w^{\mathrm{ion}}_{z,V} \cdot p_{\mathrm{ph},V}$
14	σ_3 (σ_z)	σ_1 (H/V)	$w^{\mathrm{ion}}_{z,H} \cdot p_{\mathrm{ph},H}$ - $w^{\mathrm{ion}}_{z,V} \cdot p_{\mathrm{ph},V}$
15	σ_3 (σ_z)	σ_2 (D/A)	$w^{\mathrm{ion}}_{z,D} \cdot p_{\mathrm{ph},D}$ - $w^{\mathrm{ion}}_{z,A} \cdot p_{\mathrm{ph},A}$
16	σ_3 (σ_z)	σ_3 (R/L)	$w^{\mathrm{ion}}_{z,R} \cdot p_{\mathrm{ph},R}$ - $w^{\mathrm{ion}}_{z,L} \cdot p_{\mathrm{ph},L}$

Table A.2.: List of the joint atom-photon expectation values w_ν for measurements in different bases.

With these, we modify the expression for the likelihood function (A.76) accordingly and obtain

$$\mathcal{L}(t_1,...,t_{16}) = \sum_{\nu=1}^{16} \frac{\left(\langle\psi_\nu|\hat{\varrho}_P(t_1,...,t_{16})|\psi_\nu\rangle - w_\nu\right)^2}{u_\nu} = \sum_{\nu=1}^{16} \frac{\left(tr(\sigma_\nu \otimes \hat{\varrho_P}) - w_\nu\right)^2}{u_\nu}\,, \tag{A.77}$$

with $\sigma_\nu = \sigma_{\mathrm{ion},i} \otimes \sigma_{\mathrm{photon},j}$ when i and j are chosen appropriately, i.e. according to tab. A.4.

A.5. Numerical simulation of the Mølmer-Sørensen gate

The numerical simulation closely orients on the theoretical framework developed in sec. 7.2.1. To reproduce a more realistic scenario, we introduce (undesired) coupling to the carrier transition caused by the servo-bump sidebands in the laser spectrum. Hence, the interaction Hamiltonian from eq. (7.2) is modified accordingly and we obtain

$$\hat{H}_{\text{int}} = \sum_{i,j} \frac{\hbar\Omega}{2} \left(\hat{\sigma}_+^{(i)}(t) e^{i(\eta(\hat{a}^\dagger(t)+\hat{a}(t))-\omega_j t)} + \underbrace{\frac{\hat{\sigma}_+^{(i)}\Omega_C}{\hbar\Omega}}_{\text{Carrier coupling}} + H.c. \right), \tag{A.78}$$

where Ω_C is the Rabi frequency describing the coupling of the laser servo bumps to the atomic carrier transition. As before, we apply the Taylor decomposition

$$e^{\pm i(\eta(\hat{a}^\dagger(t)+\hat{a}(t)))} \approx 1 \pm i\eta \left(\hat{a}^\dagger(t) + \hat{a}(t)\right) = 1 \pm i\eta \left(\hat{a}^\dagger e^{i\nu t} + \hat{a} e^{-i\nu t}\right) \tag{A.79}$$

to approximate the Hamiltonian as

$$\hat{H}_{\text{int}} \approx \sum_{i,j} \frac{\hbar\Omega}{2} \left(\hat{\sigma}_+^{(i)} e^{i(\omega_{eg}-\omega_j)t} \left(1 + i\eta(\hat{a}^\dagger e^{i\nu t} + \hat{a} e^{-i\nu t})\right) + \frac{\hat{\sigma}_+^{(i)}\Omega_C}{\hbar\Omega} + H.c. \right). \tag{A.80}$$

We include another extension compared to section 7.2.1 to allow for a global detuning of the center frequency $(\omega_1 + \omega_2)/2$ to the atomic carrier-transition frequency ω_{eg}, e.g. due to light shift of the addressed transition, denoted by Δ, as depicted in fig. A.1.

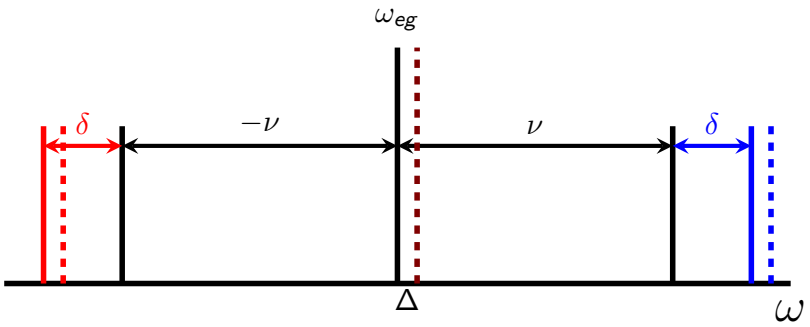

Figure A.1.: Schematic depiction of the relevant atomic transitions and the frequencies of the bichomatic laser field. The atomic carrier-transition frequency is denoted by ω_{eg}, and the two axial sidebands appear at frequencies $\pm\nu$ from the carrier. The bichromatic light field again is additionally detuned by $\pm\delta$ to the red and blue axial sideband, and its center frequency, ideally exactly at the carrier-transition frequency, can exhibit an offset Δ from the carrier, caused for instance by light-shift effects.

With that, we get

$$\omega_{eg} - \omega_1 = \nu + \delta + \Delta \tag{A.81}$$
$$\omega_{eg} - \omega_2 = -(\nu + \delta) + \Delta \tag{A.82}$$

and hence

$$\hat{H}_{\text{int}} \approx \sum_i \frac{\hbar\Omega}{2} \left(\hat{\sigma}_+^{(i)} \left(e^{i(\nu+\delta+\Delta)t} + e^{i(-(\nu+\delta)+\Delta)t} \right) \left(1 + i\eta(\hat{a}^\dagger e^{i\nu t} + \hat{a} e^{-i\nu t}) \right) + \frac{\hat{\sigma}_+^{(i)} \Omega_C}{\hbar\Omega} + H.c. \right) . \tag{A.83}$$

Rewriting (A.83) yields

$$\begin{aligned} \hat{H}_{\text{int}} \approx \sum_i \frac{\hbar\Omega}{2} \Bigg(& \hat{\sigma}_+^{(i)} \big(e^{i(\nu+\delta+\Delta)t} + e^{i(-(\nu+\delta)+\Delta)t} + i\eta\hat{a}^\dagger e^{i(2\nu+\delta+\Delta)t} + i\eta\hat{a}^\dagger e^{i(\Delta-\delta)t} \\ & + i\eta\hat{a} e^{i(\delta+\Delta)t} + i\eta\hat{a} e^{i(-(2\nu+\delta)+\Delta)t} \big) + \frac{\hat{\sigma}_+^{(i)} \Omega_C}{\hbar\Omega} + H.c. \Bigg) . \end{aligned} \tag{A.84}$$

Applying the rotating-wave approximation, we omit all terms but those in $\Delta \pm \delta$ to obtain

$$\hat{H}_{\text{int}} \approx \sum_i \left(\frac{\hbar\Omega}{2} \left(\hat{\sigma}_+^{(i)} \left(i\eta\hat{a}^\dagger e^{i(\Delta-\delta)t} + i\eta\hat{a} e^{i(\delta+\Delta)t} \right) + H.c. \right) + \frac{1}{2}\hat{\sigma}_+^{(i)}\Omega_C + \frac{1}{2}\hat{\sigma}_-^{(i)}\Omega_C \right) , \tag{A.85}$$

using that $\Omega_C = \Omega_C^\dagger$. Defining

$$A_{i,1}(t) = \Omega\, e^{i(\delta+\Delta)t} , \tag{A.86}$$
$$A_{i,2}(t) = \Omega\, e^{i(\delta-\Delta)t} , \tag{A.87}$$

(A.85) is formulated as

$$\begin{aligned} \hat{H}_{\text{int}}/\hbar \approx \sum_i \Bigg(& \frac{i\eta}{2} \left(A_{i,1}(t)\hat{\sigma}_+^{(i)}\hat{a} + A_{i,2}(t)\hat{\sigma}_+^{(i)}\hat{a}^\dagger - A_{i,1}^\dagger(t)\hat{\sigma}_-^{(i)}\hat{a}^\dagger - A_{i,2}^\dagger(t)\hat{\sigma}_-^{(i)}\hat{a} \right) \\ & + \frac{\Omega_C}{2} \left(\hat{\sigma}_+^{(i)} + \hat{\sigma}_-^{(i)} \right) \Bigg) . \end{aligned} \tag{A.88}$$

Using

$$\hat{\sigma}_+^{(1)} = 2|g\bullet\rangle\langle e\bullet| , \qquad \hat{\sigma}_-^{(1)} = 2|e\bullet\rangle\langle g\bullet| , \tag{A.89}$$
$$\hat{\sigma}_+^{(2)} = 2|\bullet g\rangle\langle\bullet e| , \qquad \hat{\sigma}_-^{(2)} = 2|\bullet e\rangle\langle\bullet g| \tag{A.90}$$

and defining the servo-bump Hamiltonian

$$\begin{aligned}\hat{H}_{\mathrm{SB}}/\hbar &= \frac{\Omega_C}{2}\left(\hat{\sigma}_+^{(1)} + \hat{\sigma}_-^{(1)} + \hat{\sigma}_+^{(2)} + \hat{\sigma}_-^{(2)}\right) \\ &= \Omega_C\left(|g\bullet\rangle\langle e\bullet| + |e\bullet\rangle\langle g\bullet| + |\bullet g\rangle\langle\bullet e| + |\bullet e\rangle\langle\bullet g|\right),\end{aligned} \tag{A.91}$$

we evaluate the action of the interaction Hamiltonian

$$\begin{aligned}\hat{H}_{\mathrm{int}}/\hbar \approx i\eta\Big(&A_{1,1}(t)\hat{a}|g\bullet\rangle\langle e\bullet| + A_{1,2}(t)\hat{a}^\dagger|g\bullet\rangle\langle e\bullet| - A_{1,1}^\dagger(t)\hat{a}^\dagger|e\bullet\rangle\langle g\bullet| - A_{1,2}^\dagger(t)\hat{a}|e\bullet\rangle\langle g\bullet| \\ &- A_{2,1}(t)\hat{a}|\bullet g\rangle\langle\bullet e| - A_{2,2}(t)\hat{a}^\dagger|\bullet g\rangle\langle\bullet e| + A_{2,1}^\dagger(t)\hat{a}^\dagger|\bullet e\rangle\langle\bullet g| + A_{2,2}^\dagger(t)\hat{a}|\bullet e\rangle\langle\bullet g|\Big) \\ &+\Omega_C\left(|g\bullet\rangle\langle e\bullet| + |e\bullet\rangle\langle g\bullet| + |\bullet g\rangle\langle\bullet e| + |\bullet e\rangle\langle\bullet g|\right)\end{aligned} \tag{A.92}$$

onto a general initial state

$$|\psi\rangle = \sum_{n=0}^{\infty}\left(\alpha_n|gg,n\rangle + \beta_n|eg,n\rangle + \gamma_n|ge,n\rangle + \delta_n|ee,n\rangle\right), \tag{A.93}$$

where n denotes the number of motional quanta in the system.

The system dynamics is described by Schrödinger's equation in the rotating atomic reference frame

$$\hat{H}_{\mathrm{int}}/\hbar|\psi\rangle = i\frac{\partial}{\partial t}|\psi\rangle\,. \tag{A.94}$$

The temporal derivative of the initial state is given by

$$\frac{\partial}{\partial t}|\psi\rangle = \sum_{n=0}^{\infty}\left(\dot{\alpha}_n|gg,n\rangle + \dot{\beta}_n|eg,n\rangle + \dot{\gamma}_n|ge,n\rangle + \dot{\delta}_n|ee,n\rangle\right). \tag{A.95}$$

Using

$$\hat{a}|\bullet\bullet,n\rangle = \sqrt{n}|\bullet\bullet,n-1\rangle\,, \tag{A.96}$$

$$\hat{a}^\dagger|\bullet\bullet,n\rangle = \sqrt{n+1}|\bullet\bullet,n+1\rangle\,, \tag{A.97}$$

application of $\hat{H}_{\mathrm{int}}/\hbar$ to $|\psi\rangle$ then, after some maths, reveals the differential equations for the coefficients $\alpha_n, \beta_n, \gamma_n$ and δ_n, describing the temporal evolution, including the carrier coupling, from comparison of the respective coefficients:

$$\dot{\alpha}_n = \eta\Big(A_{1,1}(t)\beta_{n+1}\sqrt{n+1} + A_{1,2}(t)\beta_{n-1}\sqrt{n} + A_{2,1}(t)\gamma_{n+1}\sqrt{n+1}$$

$$
\begin{aligned}
&+ A_{2,2}(t)\gamma_{n-1}\sqrt{n}\Big) - i\Gamma_C\Big(\beta_n + \gamma_n\Big)\,,\\
\dot{\beta}_n &= \eta\Big(- A^{\dagger}_{1,1}(t)\alpha_{n-1}\sqrt{n} - A^{\dagger}_{1,2}(t)\alpha_{n+1}\sqrt{n+1} + A_{2,1}(t)\delta_{n+1}\sqrt{n+1}\\
&+ A_{2,2}(t)\delta_{n-1}\sqrt{n}\Big) - i\Gamma_C\Big(\alpha_n + \delta_n\Big)\,,\\
\dot{\gamma}_n &= \eta\Big(A_{1,1}(t)\delta_{n+1}\sqrt{n+1} + A_{1,2}(t)\delta_{n-1}\sqrt{n} - A^{\dagger}_{2,1}(t)\alpha_{n-1}\sqrt{n}\\
&- A^{\dagger}_{2,2}(t)\alpha_{n+1}\sqrt{n+1}\Big) - i\Gamma_C\Big(\delta_n + \alpha_n\Big)\,,\\
\dot{\delta}_n &= \eta\Big(- A^{\dagger}_{1,1}(t)\gamma_{n-1}\sqrt{n} - A^{\dagger}_{1,2}(t)\gamma_{n+1}\sqrt{n+1} - A^{\dagger}_{2,1}(t)\beta_{n-1}\sqrt{n}\\
&- A^{\dagger}_{2,2}(t)\beta_{n+1}\sqrt{n+1}\Big) - i\Gamma_C\Big(\beta_n + \gamma_n\Big)\,.
\end{aligned}
$$

A.6. Mølmer-Sørensen gate on the radial sidebands

Sometimes it might be desirable to perform the Mølmer-Sørensen gate not on the axial sidebands[3], but on the radial sidebands, e.g. to eliminate axial sidebands in the spectrum, thus reducing erroneous coupling to neighboring transitions. However, this approach exhibits some experimental challenges, as instead of one sideband (or two if we consider both, the red and blue sideband), we drive four (or eight) transitions simultaneously, two motional eigenmodes (center-of-mass (COM) and rocking) for two radial trap frequencies, which all have to undergo the same dynamics, i.e. for which the motion has to be decoupled from the internal atomic state after the entangling-gate time.

To fulfill that condition, a more elaborate pulse sequence, where the complex Rabi frequency becomes time-dependent, has to be implemented. Starting from the idea proposed in [192], the calculation for the optimal pulse shape is carried out.

We assume that the Rabi frequency $\Omega(t)$ and the four Lamb-Dicke parameters η_m, $m \in \{1,2,3,4\}$, for the four radial modes are equal on both ions. Furthermore assuming the four radial frequencies ω_m to be equal for both ions (i.e. $\omega_m^{(1)} = \omega_m^{(2)}$), according to the treatment in [193], a bichromatic pulse at the detuning δ from the carrier frequency ω_0 of pulse duration τ results in the following interaction Hamiltonian:

$$\hat{U}(\tau) = \exp\left(\sum_{i=1}^{2}\hat{\phi}_i(\tau)\sigma_x^{(i)} + i\sum_{i\neq j}\chi_{i,j}(\tau)\sigma_x^{(i)}\sigma_x^{(j)}\right) . \tag{A.98}$$

The first term is the qubit-motion coupling on ion i, where

$$\hat{\phi}_i(\tau) = \sum_{m=1}^{4}\left(\alpha_m(\tau)\hat{a}_m^\dagger - \alpha_m^*(\tau)\hat{a}_m\right) , \tag{A.99}$$

$\hat{a}_m^\dagger(\hat{a}_m)$ being the raising (lowering) operator for the m-th radial mode, and $\hat{\sigma}_x^i$ is the Pauli-X operator of the i-th qubit. The factors $\alpha_m(\tau)$ are calculated as

$$\alpha_m(\tau) = i\eta_m\int_0^\tau \Omega(t)\,\sin(\delta t)\,e^{i\omega_m t}dt . \tag{A.100}$$

The second term of (A.98) describes the entangling interaction between qubits i and j, with

$$\chi_{i,j}(\tau) = 2\sum_{m=1}^{4}\eta_m^2\int_{t=0}^{\tau}\int_{t'=0}^{t}\Omega(t')\Omega(t)\sin(\delta t')\sin(\delta t)\sin\left(\omega_m(t-t')\right)dt'dt . \tag{A.101}$$

The time-dependent Rabi frequency $\Omega(t)$ is used as a control parameter for the optimization of the gate.
In order to achieve an entangling XX gate, we have to realize a pulse shape that fulfills

$$\hat{U}(\tau) = \exp\left(i\pi\hat{\sigma}_x^{(1)}\hat{\sigma}_x^{(2)}/4\right) . \tag{A.102}$$

[3]Which in our case are addressed by the beam under 45°.

This requires $\chi_{1,2}(\tau) = \pi/4$ and $\alpha_m(\tau) = 0$. Thus, we have to separate the time-dependent Rabi frequency $\Omega(t)$ into $2 \cdot 2 + 1 = 5$ equally long segments of duration $\tau/5$ with Rabi frequencies Ω_k, $k = 1, 2, 3, 4, 5$. We obtain

$$
\begin{aligned}
\alpha_m(\tau) &= i\eta_m \sum_{k=1}^{5} \int_{\frac{k-1}{5}\tau}^{\frac{k}{5}\tau} \Omega_k \sin(\delta t)\, e^{i\omega_m t} dt \\
&= i\eta_m \sum_{k=1}^{5} \left(\int_{\frac{k-1}{5}\tau}^{\frac{k}{5}\tau} \Omega_k \sin(\delta t) \cos(\omega_m t) dt \right. \\
&\left. + i \int_{\frac{k-1}{5}\tau}^{\frac{k}{5}\tau} \Omega_k \sin(\delta t) \sin(\omega_m t) dt \right) \\
&= i\eta_m \sum_{k=1}^{5} \left(\Omega_k \left[- \frac{\omega_m \sin(\omega_m t)\sin(\delta t) + \delta \cos(\omega_m t)\cos(\delta t)}{\delta^2 - \omega_m^2} \right]_{t=\frac{k-1}{5}\tau}^{\frac{k}{5}\tau} \right. \\
&\left. + \Omega_k \left[\frac{\omega_m \cos(\omega_m t)\sin(\delta t) - \delta \sin(\omega_m t)\cos(\delta t)}{\delta^2 - \omega_m^2} \right]_{t=\frac{k-1}{5}\tau}^{\frac{k}{5}\tau} \right) \\
&= i\eta_m \sum_{k=1}^{5} \Omega_k \left(- \frac{\omega_m \sin(\omega_m \frac{k}{5}\tau)\sin(\delta \frac{k}{5}\tau) + \delta \cos(\omega_m \frac{k}{5}\tau)\cos(\delta \frac{k}{5}\tau)}{\delta^2 - \omega_m^2} \right. \\
&+ \frac{\omega_m \sin(\omega_m \frac{k-1}{5}\tau)\sin(\delta \frac{k-1}{5}\tau) + \delta \cos(\omega_m \frac{k-1}{5}\tau)\cos(\delta \frac{k-1}{5}\tau)}{\delta^2 - \omega_m^2} \\
&+ \frac{\omega_m \cos(\omega_m \frac{k}{5}\tau)\sin(\delta \frac{k}{5}\tau) - \delta \sin(\omega_m \frac{k}{5}\tau)\cos(\delta \frac{k}{5}\tau)}{\delta^2 - \omega_m^2} \\
&\left. - \frac{\omega_m \cos(\omega_m \frac{k-1}{5}\tau)\sin(\delta \frac{k-1}{5}\tau) - \delta \sin(\omega_m \frac{k-1}{5}\tau)\cos(\delta \frac{k-1}{5}\tau)}{\delta^2 - \omega_m^2} \right) \\
&:= i\eta_m \sum_{k=1}^{5} \Omega_k a_{k,m} \\
&\stackrel{!}{=} 0
\end{aligned}
\tag{A.103}
$$

and

$$
\chi_{1,2} = 2 \sum_{m=1}^{4} \eta_m^2 \left(\int_{t=0}^{\frac{1}{5}\tau} \int_{t'=0}^{t} \Omega_1 \Omega_1 \sin(\delta t') \sin(\delta t) \sin\big(\omega_m (t - t')\big) dt' dt \right.
$$

$$+\sum_{k=2}^{5}\int_{t=\frac{k-1}{5}\tau}^{\frac{k}{5}\tau}\left(\sum_{l=1}^{k-1}\int_{t'=\frac{l-1}{5}\tau}^{\frac{l}{5}\tau}\Omega_k\Omega_l\sin(\delta t')\sin(\delta t)\sin\big(\omega_m(t-t')\big)dt'dt\right.$$
$$\left.+\int_{t'=\frac{k-1}{5}\tau}^{t}\Omega_k\Omega_k\sin(\delta t')\sin(\delta t)\sin\big(\omega_m(t-t')\big)dt'dt\right)\Bigg)$$

$$=2\sum_{m=1}^{4}\eta_m^2\Bigg(\int_{t=0}^{\frac{1}{5}\tau}-\Omega_1\Omega_1\sin(\delta t)\Big[\frac{\sin(\omega_m t+(\delta-\omega_m)t')}{2(\delta-\omega_m)}+\frac{\sin(\omega_m t-(\delta+\omega_m)t')}{2(\delta+\omega_m)}\Big]_{t'=0}^{t}dt$$

$$+\sum_{k=2}^{5}\int_{t=\frac{k-1}{5}\tau}^{\frac{k}{5}\tau}\Bigg(\sum_{l=1}^{k-1}-\Omega_k\Omega_l\sin(\delta t)\Big[\frac{\sin(\omega_m t+(\delta-\omega_m)t')}{2(\delta-\omega_m)}+\frac{\sin(\omega_m t-(\delta+\omega_m)t')}{2(\delta+\omega_m)}\Big]_{t'=\frac{l-1}{5}\tau}^{\frac{l}{5}\tau}$$
$$-\Omega_k\Omega_k\sin(\delta t)\Big[\frac{\sin(\omega_m t+(\delta-\omega_m)t')}{2(\delta-\omega_m)}+\frac{\sin(\omega_m t-(\delta+\omega_m)t')}{2(\delta+\omega_m)}\Big]_{t'=\frac{k-1}{5}\tau}^{t}\Bigg)dt\Bigg)$$

$$=2\sum_{m=1}^{4}\eta_m^2\Bigg(\int_{t=0}^{\frac{1}{5}\tau}-\Omega_1\Omega_1\sin(\delta t)\Big\{\frac{\sin(\delta t)}{2(\delta-\omega_m)}+\frac{\sin(-\delta t)}{2(\delta+\omega_m)}-\frac{\sin(\omega_m t)}{2(\delta-\omega_m)}-\frac{\sin(\omega_m t)}{2(\delta+\omega_m)}\Big\}dt$$

$$+\sum_{k=2}^{5}\int_{t=\frac{k-1}{5}\tau}^{\frac{k}{5}\tau}\Bigg(\sum_{l=1}^{k-1}-\Omega_k\Omega_l\sin(\delta t)\Big\{\frac{\sin(\omega_m t+(\delta-\omega_m)\frac{l}{5}\tau)}{2(\delta-\omega_m)}+\frac{\sin(\omega_m t-(\delta+\omega_m)\frac{l}{5}\tau)}{2(\delta+\omega_m)}$$
$$-\frac{\sin(\omega_m t+(\delta-\omega_m)\frac{l-1}{5}\tau)}{2(\delta-\omega_m)}-\frac{\sin(\omega_m t-(\delta+\omega_m)\frac{l-1}{5}\tau)}{2(\delta+\omega_m)}\Big\}$$
$$-\Omega_k\Omega_k\sin(\delta t)\Big\{\frac{\sin(\delta t)}{2(\delta-\omega_m)}+\frac{\sin(-\delta t)}{2(\delta+\omega_m)}-\frac{\sin(\omega_m t+(\delta-\omega_m)\frac{k-1}{5}\tau)}{2(\delta-\omega_m)}$$
$$-\frac{\sin(\omega_m t-(\delta+\omega_m)\frac{k-1}{5}\tau)}{2(\delta+\omega_m)}\Big\}\Bigg)dt\Bigg). \quad \text{(A.104)}$$

With

-

$$\int_{t=0}^{\frac{1}{5}\tau}\sin(\delta t)\sin(\delta t)dt=\left[\frac{t}{2}-\frac{\sin(2\delta t)}{4\delta}\right]_{t=0}^{\frac{1}{5}\tau}=\frac{\tau}{10}-\frac{\sin(\frac{2}{5}\delta\tau)}{4\delta}, \quad \text{(A.105)}$$

- $$\int_{t=0}^{\frac{1}{5}\tau} \sin(\delta t)\sin(\omega_m t)dt = \left[\frac{\omega_m \sin(\delta t)\cos(\omega_m t) - \delta\cos(\delta t)\sin(\omega_m t)}{\delta^2-\omega_m^2}\right]_{t=0}^{\frac{1}{5}\tau} \quad (A.106)$$
$$= \frac{\omega_m \sin(\delta\frac{\tau}{5})\cos(\omega_m\frac{\tau}{5}) - \delta\cos(\delta\frac{\tau}{5})\sin(\omega_m\frac{\tau}{5})}{\delta^2-\omega_m^2},$$

- $$\int_{t=\frac{k-1}{5}\tau}^{\frac{k}{5}\tau} \sin(\delta t)\sin(\omega_m t+(\delta-\omega_m)X)dt\ ,\ X=\frac{l}{5}\tau,\frac{l-1}{5}\tau,\frac{k-1}{5}\tau$$
$$= \frac{1}{2}\left[\frac{\sin((\delta-\omega_m)(t-X))}{\delta-\omega_m} - \frac{\sin((\delta+\omega_m)t+(\delta-\omega_m)X)}{\delta+\omega_m}\right]_{t=\frac{k-1}{5}\tau}^{\frac{k}{5}\tau} \quad (A.107)$$
$$= \frac{1}{2}\left\{\frac{\sin((\delta-\omega_m)(\frac{k}{5}\tau-X))}{\delta-\omega_m} - \frac{\sin((\delta+\omega_m)\frac{k}{5}\tau+(\delta-\omega_m)X)}{\delta+\omega_m}\right.$$
$$\left. - \frac{\sin((\delta-\omega_m)(\frac{k-1}{5}\tau-X))}{\delta-\omega_m} + \frac{\sin((\delta+\omega_m)\frac{k-1}{5}\tau+(\delta-\omega_m)X)}{\delta+\omega_m}\right\},$$

- $$\int_{t=\frac{k-1}{5}\tau}^{\frac{k}{5}\tau} \sin(\delta t)\sin(\omega_m t-(\delta+\omega_m)X)dt$$
$$= \frac{1}{2}\left[\frac{\sin((\delta-\omega_m)t+(\delta+\omega_m)X)}{\delta-\omega_m} - \frac{\sin((\delta+\omega_m)(t-X))}{\delta+\omega_m}\right]_{t=\frac{k-1}{5}\tau}^{\frac{k}{5}\tau}$$
$$= \frac{1}{2}\left\{\frac{\sin((\delta-\omega_m)\frac{k}{5}\tau+(\delta+\omega_m)X)}{\delta-\omega_m} - \frac{\sin((\delta+\omega_m)(\frac{k}{5}\tau-X))}{\delta+\omega_m}\right. \quad (A.108)$$
$$- \frac{\sin((\delta-\omega_m)\frac{k-1}{5}\tau+(\delta+\omega_m)X)}{\delta-\omega_m}$$
$$\left. + \frac{\sin((\delta+\omega_m)(\frac{k-1}{5}\tau-X))}{\delta+\omega_m}\right\},$$

- $$\int_{t=\frac{k-1}{5}\tau}^{\frac{k}{5}\tau} \sin(\delta t)\sin(\delta t)dt = \left[\frac{t}{2} - \frac{\sin(2\delta t)}{4\delta}\right]_{t=\frac{k-1}{5}\tau}^{\frac{k}{5}\tau} = \frac{k}{10}\tau - \frac{\sin(\frac{2k}{5}\delta\tau)}{4\delta} - \frac{k-1}{10}\tau + \frac{\sin(\frac{2(k-1)}{5}\delta\tau)}{4\delta} \quad (A.109)$$

we get

$$
\begin{aligned}
\chi_{1,2} = 2\sum_{m=1}^{4}\eta_m^2\Bigg(&-\Omega_1\Omega_1\Bigg\{\frac{1}{2(\delta-\omega_m)}\Big[\int_{t=0}^{\frac{1}{5}\tau}\sin(\delta t)\sin(\delta t)dt\Big]-\frac{1}{2(\delta+\omega_m)}\Big[\int_{t=0}^{\frac{1}{5}\tau}\sin(\delta t)\sin(\delta t)dt\Big]\\
&-\frac{1}{2(\delta-\omega_m)}\Big[\int_{t=0}^{\frac{1}{5}\tau}\sin(\delta t)\sin(\omega_m t)dt\Big]-\frac{1}{2(\delta+\omega_m)}\Big[\int_{t=0}^{\frac{1}{5}\tau}\sin(\delta t)\sin(\omega_m t)dt\Big]\Bigg\}\\
&+\sum_{k=2}^{5}\Bigg(\sum_{l=1}^{k-1}-\Omega_k\Omega_l\Bigg\{\frac{1}{2(\delta-\omega_m)}\Big[\int_{t=\frac{k-1}{5}\tau}^{\frac{k}{5}\tau}\sin(\delta t)\sin(\omega_m t+(\delta-\omega_m)\frac{l}{5}\tau)dt\Big]\\
&+\frac{1}{2(\delta+\omega_m)}\Big[\int_{t=\frac{k-1}{5}\tau}^{\frac{k}{5}\tau}\sin(\delta t)\sin(\omega_m t-(\delta+\omega_m)\frac{l}{5}\tau)dt\Big]\\
&-\frac{1}{2(\delta-\omega_m)}\Big[\int_{t=\frac{k-1}{5}\tau}^{\frac{k}{5}\tau}\sin(\delta t)\sin(\omega_m t+(\delta-\omega_m)\frac{l-1}{5}\tau)dt\Big]\\
&-\frac{1}{2(\delta+\omega_m)}\Big[\int_{t=\frac{k-1}{5}\tau}^{\frac{k}{5}\tau}\sin(\delta t)\sin(\omega_m t-(\delta+\omega_m)\frac{l-1}{5}\tau)dt\Big]\Bigg\}\\
&-\Omega_k\Omega_k\Bigg\{\frac{1}{2(\delta-\omega_m)}\Big[\int_{t=\frac{k-1}{5}\tau}^{\frac{k}{5}\tau}\sin(\delta t)\sin(\delta t)dt\Big]-\frac{1}{2(\delta+\omega_m)}\Big[\int_{t=\frac{k-1}{5}\tau}^{\frac{k}{5}\tau}\sin(\delta t)\sin(\delta t)dt\Big]\\
&-\frac{1}{2(\delta-\omega_m)}\Big[\int_{t=\frac{k-1}{5}\tau}^{\frac{k}{5}\tau}\sin(\delta t)\sin(\omega_m t+(\delta-\omega_m)\frac{k-1}{5}\tau)dt\Big]\\
&-\frac{1}{2(\delta+\omega_m)}\Big[\int_{t=\frac{k-1}{5}\tau}^{\frac{k}{5}\tau}\sin(\delta t)\sin(\omega_m t-(\delta+\omega_m)\frac{k-1}{5}\tau)dt\Big]\Bigg\}\Bigg)\Bigg)\\
= 2\sum_{m=1}^{4}\eta_m^2\Bigg(&-\Omega_1\Omega_1\Bigg\{\frac{1}{2(\delta-\omega_m)}\Big[\frac{\tau}{10}-\frac{\sin(\frac{2}{5}\delta\tau)}{4\delta}\Big]-\frac{1}{2(\delta+\omega_m)}\Big[\frac{\tau}{10}-\frac{\sin(\frac{2}{5}\delta\tau)}{4\delta}\Big]\\
&-\frac{1}{2(\delta-\omega_m)}\Big[\frac{\omega_m\sin(\delta\frac{\tau}{5})\cos(\omega_m\frac{\tau}{5})-\delta\cos(\delta\frac{\tau}{5})\sin(\omega_m\frac{\tau}{5})}{\delta^2-\omega_m^2}\Big]
\end{aligned}
$$

$$
- \frac{1}{2(\delta+\omega_m)}\left[\frac{\omega_m \sin\left(\delta\frac{\tau}{5}\right)\cos\left(\omega_m\frac{\tau}{5}\right) - \delta\cos\left(\delta\frac{\tau}{5}\right)\sin\left(\omega_m\frac{\tau}{5}\right)}{\delta^2-\omega_m^2}\right]\Bigg\}
$$

$$
+\sum_{k=2}^{5}\left(\sum_{l=1}^{k-1} -\Omega_k\Omega_l\Bigg\{\right.
$$

$$
\frac{1}{2(\delta-\omega_m)}\left[\frac{1}{2}\left(\frac{\sin\left((\delta-\omega_m)(\frac{k}{5}\tau-\frac{l}{5}\tau)\right)}{\delta-\omega_m} - \frac{\sin\left((\delta+\omega_m)\frac{k}{5}\tau+(\delta-\omega_m)\frac{l}{5}\tau\right)}{\delta+\omega_m}\right.\right.
$$

$$
\left.\left. - \frac{\sin\left((\delta-\omega_m)(\frac{k-1}{5}\tau-\frac{l}{5}\tau)\right)}{\delta-\omega_m} + \frac{\sin\left((\delta+\omega_m)\frac{k-1}{5}\tau+(\delta-\omega_m)\frac{l}{5}\tau\right)}{\delta+\omega_m}\right)\right]
$$

$$
+\frac{1}{2(\delta+\omega_m)}\left[\frac{1}{2}\left(\frac{\sin\left((\delta-\omega_m)\frac{k}{5}\tau+(\delta+\omega_m)\frac{l}{5}\tau\right)}{\delta-\omega_m} - \frac{\sin\left((\delta+\omega_m)(\frac{k}{5}\tau-\frac{l}{5}\tau)\right)}{\delta+\omega_m}\right.\right.
$$

$$
\left.\left. - \frac{\sin\left((\delta-\omega_m)\frac{k-1}{5}\tau+(\delta+\omega_m)\frac{l}{5}\tau\right)}{\delta-\omega_m} + \frac{\sin\left((\delta+\omega_m)(\frac{k-1}{5}\tau-\frac{l}{5}\tau)\right)}{\delta+\omega_m}\right)\right]
$$

$$
-\frac{1}{2(\delta-\omega_m)}\left[\frac{1}{2}\left(\frac{\sin\left((\delta-\omega_m)(\frac{k}{5}\tau-\frac{l-1}{5}\tau)\right)}{\delta-\omega_m} - \frac{\sin\left((\delta+\omega_m)\frac{k}{5}\tau+(\delta-\omega_m)\frac{l-1}{5}\tau\right)}{\delta+\omega_m}\right.\right.
$$

$$
\left.\left. - \frac{\sin\left((\delta-\omega_m)(\frac{k-1}{5}\tau-\frac{l-1}{5}\tau)\right)}{\delta-\omega_m} + \frac{\sin\left((\delta+\omega_m)\frac{k-1}{5}\tau+(\delta-\omega_m)\frac{l-1}{5}\tau\right)}{\delta+\omega_m}\right)\right]
$$

$$
-\frac{1}{2(\delta+\omega_m)}\left[\frac{1}{2}\left(\frac{\sin\left((\delta-\omega_m)\frac{k}{5}\tau+(\delta+\omega_m)\frac{l-1}{5}\tau\right)}{\delta-\omega_m} - \frac{\sin\left((\delta+\omega_m)(\frac{k}{5}\tau-\frac{l-1}{5}\tau)\right)}{\delta+\omega_m}\right.\right.
$$

$$
\left.\left. - \frac{\sin\left((\delta-\omega_m)\frac{k-1}{5}\tau+(\delta+\omega_m)\frac{l-1}{5}\tau\right)}{\delta-\omega_m} + \frac{\sin\left((\delta+\omega_m)(\frac{k-1}{5}\tau-\frac{l-1}{5}\tau)\right)}{\delta+\omega_m}\right)\right]\Bigg\}
$$

$$
-\Omega_k\Omega_k\Bigg\{
$$

$$
\left(\frac{1}{2(\delta-\omega_m)} - \frac{1}{2(\delta+\omega_m)}\right)\left[\frac{k}{10}\tau - \frac{\sin\left(\frac{2k}{5}\delta\tau\right)}{4\delta} - \frac{k-1}{10}\tau + \frac{\sin\left(\frac{2(k-1)}{5}\delta\tau\right)}{4\delta}\right]
$$

$$
-\frac{1}{2(\delta-\omega_m)}\left[\frac{1}{2}\left(\frac{\sin\left((\delta-\omega_m)(\frac{k}{5}\tau-\frac{k-1}{5}\tau)\right)}{\delta-\omega_m} - \frac{\sin\left((\delta+\omega_m)\frac{k}{5}\tau+(\delta-\omega_m)\frac{k-1}{5}\tau\right)}{\delta+\omega_m}\right.\right.
$$

$$
\left.\left. - \frac{\sin\left((\delta-\omega_m)(\frac{k-1}{5}\tau-\frac{k-1}{5}\tau)\right)}{\delta-\omega_m} + \frac{\sin\left((\delta+\omega_m)\frac{k-1}{5}\tau+(\delta-\omega_m)\frac{k-1}{5}\tau\right)}{\delta+\omega_m}\right)\right]
$$

$$
-\frac{1}{2(\delta+\omega_m)}\left[\frac{1}{2}\left(\frac{\sin\left((\delta-\omega_m)\frac{k}{5}\tau+(\delta+\omega_m)\frac{k-1}{5}\tau\right)}{\delta-\omega_m} - \frac{\sin\left((\delta+\omega_m)(\frac{k}{5}\tau-\frac{k-1}{5}\tau)\right)}{\delta+\omega_m}\right.\right.
$$

$$
\left.\left. - \frac{\sin\left((\delta-\omega_m)\frac{k-1}{5}\tau+(\delta+\omega_m)\frac{k-1}{5}\tau\right)}{\delta-\omega_m} + \frac{\sin\left((\delta+\omega_m)(\frac{k-1}{5}\tau-\frac{k-1}{5}\tau)\right)}{\delta+\omega_m}\right)\right]\Bigg\}
$$

$$
\left.\right)\Bigg)
$$

$$:= 2\sum_{m=1}^{4}\eta_m^2\left(-\Omega_1^2 b_m + \sum_{k=2}^{5}\left(\sum_{l=1}^{k-1} -\Omega_k\Omega_l c_{k,l,m} - \Omega_k^2 d_{k,m}\right)\right) \stackrel{!}{=} \frac{\pi}{4}\,, \tag{A.110}$$

where we used the substitutions

$$\begin{aligned} a_{k,m} :=& -\frac{\omega_m \sin\left(\omega_m \frac{k}{5}\tau\right)\sin\left(\delta\frac{k}{5}\tau\right) + \delta\cos\left(\omega_m\frac{k}{5}\tau\right)\cos\left(\delta\frac{k}{5}\tau\right)}{\delta^2-\omega_m^2} \\ &+ \frac{\omega_m \sin\left(\omega_m \frac{k-1}{5}\tau\right)\sin\left(\delta\frac{k-1}{5}\tau\right) + \delta\cos\left(\omega_m\frac{k-1}{5}\tau\right)\cos\left(\delta\frac{k-1}{5}\tau\right)}{\delta^2-\omega_m^2} \\ &+ \frac{\omega_m \cos\left(\omega_m \frac{k}{5}\tau\right)\sin\left(\delta\frac{k}{5}\tau\right) - \delta\sin\left(\omega_m\frac{k}{5}\tau\right)\cos\left(\delta\frac{k}{5}\tau\right)}{\delta^2-\omega_m^2} \\ &- \frac{\omega_m \cos\left(\omega_m \frac{k-1}{5}\tau\right)\sin\left(\delta\frac{k-1}{5}\tau\right) - \delta\sin\left(\omega_m\frac{k-1}{5}\tau\right)\cos\left(\delta\frac{k-1}{5}\tau\right)}{\delta^2-\omega_m^2}\,, \end{aligned} \tag{A.111}$$

$$\begin{aligned} b_m :=& \frac{1}{2(\delta-\omega_m)}\left[\frac{\tau}{10} - \frac{\sin\left(\frac{2}{5}\delta\tau\right)}{4\delta}\right] - \frac{1}{2(\delta+\omega_m)}\left[\frac{\tau}{10} - \frac{\sin\left(\frac{2}{5}\delta\tau\right)}{4\delta}\right] \\ &- \frac{1}{2(\delta-\omega_m)}\left[\frac{\omega_m\sin\left(\delta\frac{\tau}{5}\right)\cos\left(\omega_m\frac{\tau}{5}\right) - \delta\cos\left(\delta\frac{\tau}{5}\right)\sin\left(\omega_m\frac{\tau}{5}\right)}{\delta^2-\omega_m^2}\right] \\ &- \frac{1}{2(\delta+\omega_m)}\left[\frac{\omega_m\sin\left(\delta\frac{\tau}{5}\right)\cos\left(\omega_m\frac{\tau}{5}\right) - \delta\cos\left(\delta\frac{\tau}{5}\right)\sin\left(\omega_m\frac{\tau}{5}\right)}{\delta^2-\omega_m^2}\right], \end{aligned} \tag{A.112}$$

$$\begin{aligned} c_{k,l,m} :=& \frac{1}{2(\delta-\omega_m)}\left[\frac{1}{2}\left(\frac{\sin\left((\delta-\omega_m)(\frac{k}{5}\tau-\frac{l}{5}\tau)\right)}{\delta-\omega_m} - \frac{\sin\left((\delta+\omega_m)\frac{k}{5}\tau+(\delta-\omega_m)\frac{l}{5}\tau\right)}{\delta+\omega_m}\right.\right. \\ &\left.\left. - \frac{\sin\left((\delta-\omega_m)(\frac{k-1}{5}\tau-\frac{l}{5}\tau)\right)}{\delta-\omega_m} + \frac{\sin\left((\delta+\omega_m)\frac{k-1}{5}\tau+(\delta-\omega_m)\frac{l}{5}\tau\right)}{\delta+\omega_m}\right)\right] \\ &+ \frac{1}{2(\delta+\omega_m)}\left[\frac{1}{2}\left(\frac{\sin\left((\delta-\omega_m)\frac{k}{5}\tau+(\delta+\omega_m)\frac{l}{5}\tau\right)}{\delta-\omega_m} - \frac{\sin\left((\delta+\omega_m)(\frac{k}{5}\tau-\frac{l}{5}\tau)\right)}{\delta+\omega_m}\right.\right. \\ &\left.\left. - \frac{\sin\left((\delta-\omega_m)\frac{k-1}{5}\tau+(\delta+\omega_m)\frac{l}{5}\tau\right)}{\delta-\omega_m} + \frac{\sin\left((\delta+\omega_m)(\frac{k-1}{5}\tau-\frac{l}{5}\tau)\right)}{\delta+\omega_m}\right)\right] \\ &- \frac{1}{2(\delta-\omega_m)}\left[\frac{1}{2}\left(\frac{\sin\left((\delta-\omega_m)(\frac{k}{5}\tau-\frac{l-1}{5}\tau)\right)}{\delta-\omega_m} - \frac{\sin\left((\delta+\omega_m)\frac{k}{5}\tau+(\delta-\omega_m)\frac{l-1}{5}\tau\right)}{\delta+\omega_m}\right.\right. \\ &\left.\left. - \frac{\sin\left((\delta-\omega_m)(\frac{k-1}{5}\tau-\frac{l-1}{5}\tau)\right)}{\delta-\omega_m} + \frac{\sin\left((\delta+\omega_m)\frac{k-1}{5}\tau+(\delta-\omega_m)\frac{l-1}{5}\tau\right)}{\delta+\omega_m}\right)\right] \\ &- \frac{1}{2(\delta+\omega_m)}\left[\frac{1}{2}\left(\frac{\sin\left((\delta-\omega_m)\frac{k}{5}\tau+(\delta+\omega_m)\frac{l-1}{5}\tau\right)}{\delta-\omega_m} - \frac{\sin\left((\delta+\omega_m)(\frac{k}{5}\tau-\frac{l-1}{5}\tau)\right)}{\delta+\omega_m}\right.\right. \\ &\left.\left. - \frac{\sin\left((\delta-\omega_m)\frac{k-1}{5}\tau+(\delta+\omega_m)\frac{l-1}{5}\tau\right)}{\delta-\omega_m} + \frac{\sin\left((\delta+\omega_m)(\frac{k-1}{5}\tau-\frac{l-1}{5}\tau)\right)}{\delta+\omega_m}\right)\right], \end{aligned} \tag{A.113}$$

and

$$
\begin{aligned}
d_{k,m} := & \left(\frac{1}{2(\delta-\omega_m)} - \frac{1}{2(\delta+\omega_m)}\right)\left[\frac{k}{10}\tau - \frac{\sin\left(\frac{2k}{5}\delta\tau\right)}{4\delta} - \frac{k-1}{10}\tau + \frac{\sin\left(\frac{2(k-1)}{5}\delta\tau\right)}{4\delta}\right] \\
& - \frac{1}{2(\delta-\omega_m)}\left[\frac{1}{2}\left(\frac{\sin\left((\delta-\omega_m)(\frac{k}{5}\tau - \frac{k-1}{5}\tau)\right)}{\delta-\omega_m} - \frac{\sin\left((\delta+\omega_m)\frac{k}{5}\tau + (\delta-\omega_m)\frac{k-1}{5}\tau\right)}{\delta+\omega_m}\right.\right. \\
& \left.\left. - \frac{\sin\left((\delta-\omega_m)(\frac{k-1}{5}\tau - \frac{k-1}{5}\tau)\right)}{\delta-\omega_m} + \frac{\sin\left((\delta+\omega_m)\frac{k-1}{5}\tau + (\delta-\omega_m)\frac{k-1}{5}\tau\right)}{\delta+\omega_m}\right)\right] \\
& - \frac{1}{2(\delta+\omega_m)}\left[\frac{1}{2}\left(\frac{\sin\left((\delta-\omega_m)\frac{k}{5}\tau + (\delta+\omega_m)\frac{k-1}{5}\tau\right)}{\delta-\omega_m} - \frac{\sin\left((\delta+\omega_m)(\frac{k}{5}\tau - \frac{k-1}{5}\tau)\right)}{\delta+\omega_m}\right.\right. \\
& \left.\left. - \frac{\sin\left((\delta-\omega_m)\frac{k-1}{5}\tau + (\delta+\omega_m)\frac{k-1}{5}\tau\right)}{\delta-\omega_m} + \frac{\sin\left((\delta+\omega_m)(\frac{k-1}{5}\tau - \frac{k-1}{5}\tau)\right)}{\delta+\omega_m}\right)\right] \\
= & \left(\frac{1}{2(\delta-\omega_m)} - \frac{1}{2(\delta+\omega_m)}\right)\left[\frac{1}{10}\tau - \frac{\sin\left(\frac{2k}{5}\delta\tau\right)}{4\delta} + \frac{\sin\left(\frac{2(k-1)}{5}\delta\tau\right)}{4\delta}\right] \\
& - \frac{1}{2(\delta-\omega_m)}\left[\frac{1}{2}\left(\frac{\sin\left((\delta-\omega_m)\frac{1}{5}\tau\right)}{\delta-\omega_m} - \frac{\sin\left((\delta+\omega_m)\frac{k}{5}\tau + (\delta-\omega_m)\frac{k-1}{5}\tau\right)}{\delta+\omega_m} + \frac{\sin\left(2\delta\frac{k-1}{5}\tau\right)}{\delta+\omega_m}\right)\right] \\
& - \frac{1}{2(\delta+\omega_m)}\left[\frac{1}{2}\left(\frac{\sin\left((\delta-\omega_m)\frac{k}{5}\tau + (\delta+\omega_m)\frac{k-1}{5}\tau\right)}{\delta-\omega_m} - \frac{\sin\left((\delta+\omega_m)\frac{1}{5}\tau\right)}{\delta+\omega_m} - \frac{\sin\left(2\delta\frac{k-1}{5}\tau\right)}{\delta-\omega_m}\right)\right].
\end{aligned}
\tag{A.114}
$$

Eq. (A.110) yields

$$
\begin{aligned}
\chi_{1,2} = 2\sum_{m=1}^{4}\eta_m^2\Bigg(& -\Omega_1^2 b_m + \Big[-\Omega_2\Omega_1 c_{2,1,m} - \Omega_2^2 d_{2,m}\Big] \\
& + \Big[-\Omega_3\Omega_1 c_{3,1,m} - \Omega_3\Omega_2 c_{3,2,m} - \Omega_3^2 d_{3,m}\Big] \\
& + \Big[-\Omega_4\Omega_1 c_{4,1,m} - \Omega_4\Omega_2 c_{4,2,m} - \Omega_4\Omega_3 c_{4,3,m} - \Omega_4^2 d_{4,m}\Big] \\
& + \Big[-\Omega_5\Omega_1 c_{5,1,m} - \Omega_5\Omega_2 c_{5,2,m} - \Omega_5\Omega_3 c_{5,3,m} - \Omega_5\Omega_4 c_{5,4,m} - \Omega_5^2 d_{5,m}\Big]\Bigg)
\end{aligned}
\tag{A.115}
$$

$$
\begin{aligned}
&= \Omega_1^2\Big(-2\sum_m \eta_m^2 b_m\Big) + \Omega_2\Omega_1\Big(-2\sum_m \eta_m^2 c_{2,1,m}\Big) + \Omega_2^2\Big(-2\sum_m \eta_m^2 d_{2,m}\Big) \\
&+ \Omega_3\Omega_1\Big(-2\sum_m \eta_m^2 c_{3,1,m}\Big) + \Omega_3\Omega_2\Big(-2\sum_m \eta_m^2 c_{3,2,m}\Big) + \Omega_3^2\Big(-2\sum_m \eta_m^2 d_{3,m}\Big) \\
&+ \Omega_4\Omega_1\Big(-2\sum_m \eta_m^2 c_{4,1,m}\Big) + \Omega_4\Omega_2\Big(-2\sum_m \eta_m^2 c_{4,2,m}\Big) + \Omega_4\Omega_3\Big(-2\sum_m \eta_m^2 c_{4,3,m}\Big) + \Omega_4^2\Big(-2\sum_m \eta_m^2 d_{4,m}\Big) \\
&+ \Omega_5\Omega_1\Big(-2\sum_m \eta_m^2 c_{5,1,m}\Big) + \Omega_5\Omega_2\Big(-2\sum_m \eta_m^2 c_{5,2,m}\Big) + \Omega_5\Omega_3\Big(-2\sum_m \eta_m^2 c_{5,3,m}\Big) + \Omega_5\Omega_4\Big(-2\sum_m \eta_m^2 c_{5,4,m}\Big) \\
&+ \Omega_5^2\Big(-2\sum_m \eta_m^2 d_{5,m}\Big) .
\end{aligned}
\tag{A.116}
$$

Substituting

$$
\begin{aligned}
&\gamma_{1,1} = \Big(-2\sum_m \eta_m^2 b_m\Big), \gamma_{2,1} = \Big(-2\sum_m \eta_m^2 c_{2,1,m}\Big), \gamma_{2,2} = \Big(-2\sum_m \eta_m^2 d_{2,m}\Big), \\
&\gamma_{3,1} = \Big(-2\sum_m \eta_m^2 c_{3,1,m}\Big), \gamma_{3,2} = \Big(-2\sum_m \eta_m^2 c_{3,2,m}\Big), \gamma_{3,3} = \Big(-2\sum_m \eta_m^2 d_{3,m}\Big), \\
&\gamma_{4,1} = \Big(-2\sum_m \eta_m^2 c_{4,1,m}\Big), \gamma_{4,2} = \Big(-2\sum_m \eta_m^2 c_{4,2,m}\Big), \gamma_{4,3} = \Big(-2\sum_m \eta_m^2 c_{4,3,m}\Big), \gamma_{4,4} = \Big(-2\sum_m \eta_m^2 d_{4,m}\Big), \\
&\gamma_{5,1} = \Big(-2\sum_m \eta_m^2 c_{5,1,m}\Big), \gamma_{5,2} = \Big(-2\sum_m \eta_m^2 c_{5,2,m}\Big), \gamma_{5,3} = \Big(-2\sum_m \eta_m^2 c_{5,3,m}\Big), \gamma_{5,4} = \Big(-2\sum_m \eta_m^2 c_{5,4,m}\Big), \\
&\gamma_{5,5} = \Big(-2\sum_m \eta_m^2 d_{5,m}\Big),
\end{aligned}
\tag{A.117}
$$

we rewrite

$$
\begin{aligned}
\chi_{1,2} &= \gamma_{1,1}\Omega_1^2 + \gamma_{2,1}\Omega_2\Omega_1 + \gamma_{2,2}\Omega_2^2 + \gamma_{3,1}\Omega_3\Omega_1 + \gamma_{3,2}\Omega_3\Omega_2 + \gamma_{3,3}\Omega_3^2 + \gamma_{4,1}\Omega_4\Omega_1 + \gamma_{4,2}\Omega_4\Omega_2 \\
&\quad + \gamma_{4,3}\Omega_4\Omega_3 + \gamma_{4,4}\Omega_4^2 + \gamma_{5,1}\Omega_5\Omega_1 + \gamma_{5,2}\Omega_5\Omega_2 + \gamma_{5,3}\Omega_5\Omega_3 + \gamma_{5,4}\Omega_5\Omega_4 + \gamma_{5,5}\Omega_5^2 \\
&\quad \stackrel{!}{=} \frac{\pi}{4} .
\end{aligned}
\tag{A.118}
$$

The four conditions for α_m are

$$
\alpha_m = i\eta_m\Big(\Omega_1 a_{1,m} + \Omega_2 a_{2,m} + \Omega_3 a_{3,m} + \Omega_4 a_{4,m} + \Omega_5 a_{5,m}\Big) \stackrel{!}{=} 0 \;\forall\, m \in \{1,2,3,4\} \tag{A.119}
$$

or

$$
i\eta_m\Big(\Omega_1 a_{1,m} + \Omega_2 a_{2,m} + \Omega_3 a_{3,m} + \Omega_4 a_{4,m}\Big) \stackrel{!}{=} -i\eta_m\Omega_5 a_{5,m} \;\forall\, m \in \{1,2,3,4\} . \tag{A.120}
$$

Eq. (A.120) can be written in the form

$$\underbrace{\begin{pmatrix} a_{1,1} & a_{2,1} & a_{3,1} & a_{4,1} \\ a_{1,2} & a_{2,2} & a_{3,2} & a_{4,2} \\ a_{1,3} & a_{2,3} & a_{3,3} & a_{4,3} \\ a_{1,4} & a_{2,4} & a_{3,4} & a_{4,4} \end{pmatrix}}_{:=A} \begin{pmatrix} \Omega_1 \\ \Omega_2 \\ \Omega_3 \\ \Omega_4 \end{pmatrix} = -\Omega_5 \begin{pmatrix} a_{5,1} \\ a_{5,2} \\ a_{5,3} \\ a_{5,4} \end{pmatrix} . \tag{A.121}$$

Thus

$$\begin{pmatrix} \Omega_1 \\ \Omega_2 \\ \Omega_3 \\ \Omega_4 \end{pmatrix} = -\Omega_5 \, A^{-1} \cdot \begin{pmatrix} a_{5,1} \\ a_{5,2} \\ a_{5,3} \\ a_{5,4} \end{pmatrix} . \tag{A.122}$$

We define

$$A^{-1} := G = \begin{pmatrix} g_{1,1} & g_{2,1} & g_{3,1} & g_{4,1} \\ g_{1,2} & g_{2,2} & g_{3,2} & g_{4,2} \\ g_{1,3} & g_{2,3} & g_{3,3} & g_{4,3} \\ g_{1,4} & g_{2,4} & g_{3,4} & g_{4,4} \end{pmatrix} \tag{A.123}$$

to obtain

$$\begin{aligned} \Omega_1 &= -\left(g_{1,1}a_{5,1} + g_{2,1}a_{5,2} + g_{3,1}a_{5,3} + g_{4,1}a_{5,4}\right)\Omega_5 \\ \Omega_2 &= -\left(g_{1,2}a_{5,1} + g_{2,2}a_{5,2} + g_{3,2}a_{5,3} + g_{4,2}a_{5,4}\right)\Omega_5 \\ \Omega_3 &= -\left(g_{1,3}a_{5,1} + g_{2,3}a_{5,2} + g_{3,3}a_{5,3} + g_{4,3}a_{5,4}\right)\Omega_5 \\ \Omega_4 &= -\left(g_{1,4}a_{5,1} + g_{2,4}a_{5,2} + g_{3,4}a_{5,3} + g_{4,4}a_{5,4}\right)\Omega_5 \end{aligned} \tag{A.124}$$

Inserting (A.124) into (A.118) yields

$$
\begin{aligned}
\chi_{1,2} = \Omega_5^2 \Big(& \gamma_{1,1} \cdot \left(g_{1,1}a_{5,1} + g_{2,1}a_{5,2} + g_{3,1}a_{5,3} + g_{4,1}a_{5,4}\right)^2 \\
& + \gamma_{2,1} \cdot \left(g_{1,2}a_{5,1} + g_{2,2}a_{5,2} + g_{3,2}a_{5,3} + g_{4,2}a_{5,4}\right) \cdot \left(g_{1,1}a_{5,1} + g_{2,1}a_{5,2} + g_{3,1}a_{5,3} + g_{4,1}a_{5,4}\right) \\
& + \gamma_{2,2} \cdot \left(g_{1,2}a_{5,1} + g_{2,2}a_{5,2} + g_{3,2}a_{5,3} + g_{4,2}a_{5,4}\right)^2 \\
& + \gamma_{3,1} \cdot \left(g_{1,3}a_{5,1} + g_{2,3}a_{5,2} + g_{3,3}a_{5,3} + g_{4,3}a_{5,4}\right) \cdot \left(g_{1,1}a_{5,1} + g_{2,1}a_{5,2} + g_{3,1}a_{5,3} + g_{4,1}a_{5,4}\right) \\
& + \gamma_{3,2} \cdot \left(g_{1,3}a_{5,1} + g_{2,3}a_{5,2} + g_{3,3}a_{5,3} + g_{4,3}a_{5,4}\right) \cdot \left(g_{1,2}a_{5,1} + g_{2,2}a_{5,2} + g_{3,2}a_{5,3} + g_{4,2}a_{5,4}\right) \\
& + \gamma_{3,3} \cdot \left(g_{1,3}a_{5,1} + g_{2,3}a_{5,2} + g_{3,3}a_{5,3} + g_{4,3}a_{5,4}\right)^2 \\
& + \gamma_{4,1} \cdot \left(g_{1,4}a_{5,1} + g_{2,4}a_{5,2} + g_{3,4}a_{5,3} + g_{4,4}a_{5,4}\right) \cdot \left(g_{1,1}a_{5,1} + g_{2,1}a_{5,2} + g_{3,1}a_{5,3} + g_{4,1}a_{5,4}\right) \\
& + \gamma_{4,2} \cdot \left(g_{1,4}a_{5,1} + g_{2,4}a_{5,2} + g_{3,4}a_{5,3} + g_{4,4}a_{5,4}\right) \cdot \left(g_{1,2}a_{5,1} + g_{2,2}a_{5,2} + g_{3,2}a_{5,3} + g_{4,2}a_{5,4}\right) \\
& + \gamma_{4,3} \cdot \left(g_{1,4}a_{5,1} + g_{2,4}a_{5,2} + g_{3,4}a_{5,3} + g_{4,4}a_{5,4}\right) \cdot \left(g_{1,3}a_{5,1} + g_{2,3}a_{5,2} + g_{3,3}a_{5,3} + g_{4,3}a_{5,4}\right) \\
& + \gamma_{4,4} \cdot \left(g_{1,4}a_{5,1} + g_{2,4}a_{5,2} + g_{3,4}a_{5,3} + g_{4,4}a_{5,4}\right)^2 \\
& - \gamma_{5,1} \cdot \left(g_{1,1}a_{5,1} + g_{2,1}a_{5,2} + g_{3,1}a_{5,3} + g_{4,1}a_{5,4}\right) \\
& - \gamma_{5,2} \cdot \left(g_{1,2}a_{5,1} + g_{2,2}a_{5,2} + g_{3,2}a_{5,3} + g_{4,2}a_{5,4}\right) \\
& - \gamma_{5,3} \cdot \left(g_{1,3}a_{5,1} + g_{2,3}a_{5,2} + g_{3,3}a_{5,3} + g_{4,3}a_{5,4}\right) \\
& - \gamma_{5,4} \cdot \left(g_{1,4}a_{5,1} + g_{2,4}a_{5,2} + g_{3,4}a_{5,3} + g_{4,4}a_{5,4}\right) \\
& + \gamma_{5,5} \Big) \\
& := \Gamma\, \Omega_5^2 \,,
\end{aligned}
\tag{A.125}
$$

with

$$
\begin{aligned}
\Gamma = & \gamma_{1,1} \cdot \left(g_{1,1}a_{5,1} + g_{2,1}a_{5,2} + g_{3,1}a_{5,3} + g_{4,1}a_{5,4}\right)^2 \\
& + \gamma_{2,1} \cdot \left(g_{1,2}a_{5,1} + g_{2,2}a_{5,2} + g_{3,2}a_{5,3} + g_{4,2}a_{5,4}\right) \cdot \left(g_{1,1}a_{5,1} + g_{2,1}a_{5,2} + g_{3,1}a_{5,3} + g_{4,1}a_{5,4}\right) \\
& + \gamma_{2,2} \cdot \left(g_{1,2}a_{5,1} + g_{2,2}a_{5,2} + g_{3,2}a_{5,3} + g_{4,2}a_{5,4}\right)^2 \\
& + \gamma_{3,1} \cdot \left(g_{1,3}a_{5,1} + g_{2,3}a_{5,2} + g_{3,3}a_{5,3} + g_{4,3}a_{5,4}\right) \cdot \left(g_{1,1}a_{5,1} + g_{2,1}a_{5,2} + g_{3,1}a_{5,3} + g_{4,1}a_{5,4}\right) \\
& + \gamma_{3,2} \cdot \left(g_{1,3}a_{5,1} + g_{2,3}a_{5,2} + g_{3,3}a_{5,3} + g_{4,3}a_{5,4}\right) \cdot \left(g_{1,2}a_{5,1} + g_{2,2}a_{5,2} + g_{3,2}a_{5,3} + g_{4,2}a_{5,4}\right) \\
& + \gamma_{3,3} \cdot \left(g_{1,3}a_{5,1} + g_{2,3}a_{5,2} + g_{3,3}a_{5,3} + g_{4,3}a_{5,4}\right)^2 \\
& + \gamma_{4,1} \cdot \left(g_{1,4}a_{5,1} + g_{2,4}a_{5,2} + g_{3,4}a_{5,3} + g_{4,4}a_{5,4}\right) \cdot \left(g_{1,1}a_{5,1} + g_{2,1}a_{5,2} + g_{3,1}a_{5,3} + g_{4,1}a_{5,4}\right) \\
& + \gamma_{4,2} \cdot \left(g_{1,4}a_{5,1} + g_{2,4}a_{5,2} + g_{3,4}a_{5,3} + g_{4,4}a_{5,4}\right) \cdot \left(g_{1,2}a_{5,1} + g_{2,2}a_{5,2} + g_{3,2}a_{5,3} + g_{4,2}a_{5,4}\right) \\
& + \gamma_{4,3} \cdot \left(g_{1,4}a_{5,1} + g_{2,4}a_{5,2} + g_{3,4}a_{5,3} + g_{4,4}a_{5,4}\right) \cdot \left(g_{1,3}a_{5,1} + g_{2,3}a_{5,2} + g_{3,3}a_{5,3} + g_{4,3}a_{5,4}\right)
\end{aligned}
$$

$$
\begin{aligned}
&+ \gamma_{4,4} \cdot \left(g_{1,4}a_{5,1} + g_{2,4}a_{5,2} + g_{3,4}a_{5,3} + g_{4,4}a_{5,4}\right)^2 \\
&- \gamma_{5,1} \cdot \left(g_{1,1}a_{5,1} + g_{2,1}a_{5,2} + g_{3,1}a_{5,3} + g_{4,1}a_{5,4}\right) \\
&- \gamma_{5,2} \cdot \left(g_{1,2}a_{5,1} + g_{2,2}a_{5,2} + g_{3,2}a_{5,3} + g_{4,2}a_{5,4}\right) \\
&- \gamma_{5,3} \cdot \left(g_{1,3}a_{5,1} + g_{2,3}a_{5,2} + g_{3,3}a_{5,3} + g_{4,3}a_{5,4}\right) \\
&- \gamma_{5,4} \cdot \left(g_{1,4}a_{5,1} + g_{2,4}a_{5,2} + g_{3,4}a_{5,3} + g_{4,4}a_{5,4}\right) \\
&+ \gamma_{5,5} \,,
\end{aligned}
\tag{A.126}
$$

and hence

$$
\begin{aligned}
\chi_{1,2} = \Gamma\,\Omega_5^2 &\stackrel{!}{=} \frac{\pi}{4} \\
\Rightarrow \quad \boxed{\Omega_5 = \sqrt{\frac{\pi}{4\Gamma}}} &\,.
\end{aligned}
\tag{A.127}
$$

(A.127) results in

$$\boxed{\Omega_1 = -\left(g_{1,1}a_{5,1} + g_{2,1}a_{5,2} + g_{3,1}a_{5,3} + g_{4,1}a_{5,4}\right)\sqrt{\frac{\pi}{4\Gamma}}} \tag{A.128}$$

$$\boxed{\Omega_2 = -\left(g_{1,2}a_{5,1} + g_{2,2}a_{5,2} + g_{3,2}a_{5,3} + g_{4,2}a_{5,4}\right)\sqrt{\frac{\pi}{4\Gamma}}} \tag{A.129}$$

$$\boxed{\Omega_3 = -\left(g_{1,3}a_{5,1} + g_{2,3}a_{5,2} + g_{3,3}a_{5,3} + g_{4,3}a_{5,4}\right)\sqrt{\frac{\pi}{4\Gamma}}} \tag{A.130}$$

$$\boxed{\Omega_4 = -\left(g_{1,4}a_{5,1} + g_{2,4}a_{5,2} + g_{3,4}a_{5,3} + g_{4,4}a_{5,4}\right)\sqrt{\frac{\pi}{4\Gamma}}}\,. \tag{A.131}$$

Bibliography

[1] P. E. Ceruzzi. *A History of Modern Computing*. MIT Press, Cambridge MA (2003).

[2] F. Faggin, M. E. Hoff, S. Mazor, M. Shima. *The history of the 4004*. IEEE Micro **16**, 10–20 (1996).

[3] J. Abbate. *Inventing the Internet*. MIT Press, Cambridge MA (1999).

[4] W. Diffie, M. Hellman. *New Directions in Cryptography*. IEEE Transactions on Information Theory **22**, 644–654 (1978).

[5] R. Rivest, A. Shamir, L. Adleman. *A Method for Obtaining Digital Signatures and Public-Key Cryptosystems*. Communications of the ACM **21**, 120–126 (1978).

[6] M. Planck. *Zur Theorie des Gesetzes der Energieverteilung im Normalspektrum*. Verhandlungen der Deutschen physikalischen Gesellschaft **17**, 237–245 (1900).

[7] W. Heisenberg. *Über quantentheoretische Umdeutung kinematischer und mechanischer Beziehungen*. Zeitschrift für Physik **33**, 879–893 (1925).

[8] M. Born, P. Jordan. *Zur Quantenmechanik*. Zeitschrift für Physik **34**, 858 (1925).

[9] E. Schrödinger. *Über das Verhältnis der Heisenberg-Born-Jordanschen Quantenmechanik zu der meinen*. Annalen der Physik **79**, 734–756 (1926).

[10] R. P. Feynman. *Simulating physics with computers*. Int. J. Theor. Phys. **21**, 467 (1982).

[11] R. P. Feynman. *Quantum mechanical computers*. Found. Phys. **16**, 507 (1986).

[12] D. Deutsch, R. Josza. *Rapid solution of problems by quantum computation*. Proc. R. Soc. Lond. A **439**, 553 (1992).

[13] P. Shor. *Algorithms for quantum computation: discrete logarithms and factoring*. Proc. 35th Ann. Symp. Found. Comp. Sci. (1994).

[14] L. K. Grover. *Quantum Mechanics Helps in Searching for a Needle in a Haystack*. Phys. Rev. Lett. **79**, 325 (1997).

[15] T. H. Johnson, S. R. Clark, D. Jaksch. *What is a quantum simulator?* EPJ Quantum Technology **1**, 10 (2014).

[16] J. W. Britton, B. C. Sawyer, A. C. Keith, C.-C. J. Wang, J. K. Freericks, H. Uys, M. J. Biercuk, J. J. Bollinger. *Engineered two-dimensional Ising interactions in a trapped-ion quantum simulator with hundreds of spins*. Nature **484**, 489–492 (2012).

[17] S. Lloyd. *Universal Quantum Simulators*. Science **273**, 1073–1078 (1996).

[18] K. Kim, M.-S. Chang, S. Korenblit, R. Islam, E. E. Edwards, J. K. Freericks, G.-D. Lin, L.-M. Duan, C. Monroe. *Quantum simulation of frustrated Ising spins with trapped ions*. Nature **465**, 590–593 (2010).

[19] J. Zhang, G. Pagano, P. W. Hess, A. Kyprianidis, P. Becker, H. Kaplan, A. V. Gorshkov, Z.-X. Gong, C. Monroe. *Observation of a many-body dynamical phase transition with a 53-qubit quantum simulator*. Nature **551** (2017).

[20] D. Deutsch. *Quantum Theory, the Church-Turing Principle and the Universal Quantum Computer*. Proc. R. Soc. A: Math., Phys. Eng. Sci. **400**, 97 (1985).

[21] E. Martín-López, A. Laing, T. Lawson, R. Alvarez, X.-Q. Zhou, J. L. O'Brien. *Experimental realization of Shor's quantum factoring algorithm using qubit recycling*. Nat. Phot. **6**, 773–776 (2012).

[22] C. Figgatt, D. Maslov, K. A. Landsman, N. M. Linke, S. Debnath, C. Monroe. *Complete 3-Qubit Grover Search on a Programmable Quantum Computer*. arXiv:1703.10535 (2017).

[23] D. Leibfried, B. DeMarco, V. Meyer, D. Lucas, M. Barrett, J. Britton, W. M. Itano, B. Jelenkovic, C. Langer, T. Rosenband, D. J. Wineland. *Experimental demonstration of a robust, high-fidelity geometric two ion-qubit phase gate*. Nature **422**, 412 (2003).

[24] J. Benhelm, G. Kirchmair, C. F. Roos, R. Blatt. *Towards fault-tolerant quantum computing with trapped ions*. Nat. Phys. **4**, 463 (2008).

[25] Y. Wang, M. Um, J. Zhang, S. An, M. Lyu, J.-N. Zhang, L.-M. Duan, D. Yum, K. Kim. *Single-qubit quantum memory exceeding 10-minute coherence time*. arXiv:1701.04195 (2017).

[26] T. Monz, P. Schindler, J. T. Barreiro, M. Chwalla, D. Nigg, W. A. Coish, M. Harlander, W. Hänsel, M. Hennrich, R. Blatt. *14-Qubit Entanglement: Creation and Coherence*. Phys. Rev. Lett. **106**, 130506 (2011).

[27] P. Schindler, D. Nigg, T. Monz, J. T. Barreiro, E. Martinez, S. X. Wang, S. Quint, M. F. Brandl, V. Nebendahl, C. F. Roos, M. Chwalla, M. Hennrich, R. Blatt. *A quantum information processor with trapped ions*. New J. Phys. **15**, 123012 (2013).

[28] S. Gulde, M. Riebe, G. P. T. Lancaster, C. Becher, J. Eschner, H. Häffner, F. Schmidt-Kaler, I. L. Chuang, R. Blatt. *Implementation of the Deutsch-Jozsa algorithm on an ion-trap quantum computer*. Nature **421**, 48–50 (2003).

[29] J. Chiaverini, J. Britton, D. Leibfried, E. Knill, M. D. Barrett, R. B. Blakestad, W. M. Itano, J. D. Jost, C. Langer, R. Ozeri, T. Schätz, D. J. Wineland. *Implementation of the semiclassical quantum Fourier transform in a scalable system*. Science **308**, 997–1000 (2005).

[30] D. Hanneke, J. P. Home, J. D. Jost, J. M. Amini, D. Leibfried, D. J. Wineland. *Realization of a programmable two-qubit quantum processor*. Nat. Phys. **6**, 13–61 (2009).

[31] N. Daniilidis, D. J. Gorman, L. Tian, H. Häffner. *Quantum information processing with trapped electrons and superconducting electronics*. New Journal of Physics **15**, 073017 (2013).

[32] D. Hite, Y. Colombe, A. Wilson, D. Allcock, D. Leibfried, D. Wineland, D. Pappas. *Surface science for improved ion traps*. MRS Bulletin **38**, 826–833 (2013).

[33] D. P. L. Aude Craik, N. M. Linke, T. P. Harty, C. J. Ballance, D. M. Lucas, A. M. Steane, D. T. C. Allcock. *Microwave control electrodes for scalable, parallel, single-qubit operations in a surface-electrode ion trap*. Applied Physics B **114**, 3–10 (2014).

[34] A. Bermudez, X. Xu, R. Nigmatullin, J. O'Gorman, V. Negnevitsky, P. Schindler, T. Monz, U. G. Poschinger, C. Hempel, J. Home, F. Schmidt-Kaler, M. Biercuk, R. Blatt, S. Benjamin, M. Müller. *Assessing the Progress of Trapped-Ion Processors Towards Fault-Tolerant Quantum Computation*. Phys. Rev. X **7**, 041061 (2017).

[35] P. F. Herskind, S. X. Wang, M. Shi, Y. Ge, M. Cetina, I. L. Chuang. *Microfabricated surface ion trap on a high-finesse optical mirror*. Opt. Lett. **36**, 3045–3047 (2011).

[36] G. R. Brady, A. R. Ellis, D. L. Moehring, D. Stick, C. Highstrete, K. M. Fortier, M. G. Blain, R. A. Haltli, A. A. Cruz-Cabrera, R. D. Briggs, J. R. Wendt, T. R. Carter, S. Samora, S. A. Kemme. *Integration of fluorescence collection optics with a microfabricated surface electrode ion trap*. Applied Physics B **103**, 801–808 (2011).

[37] D. L. Moehring, C. Highstrete, D. Stick, K. M. Fortier, R. Haltli, C. Tigges, M. G. Blain. *Design, fabrication and experimental demonstration of junction surface ion traps*. New J. Phys. **13**, 075018 (2011).

[38] T. Karin, I. Le Bras, A. Kehlberger, K. Singer, N. Daniilidis, H. Häffner. *Transport of charged particles by adjusting rf voltage amplitudes*. Appl. Phys. B **106**, 117–125 (2012).

[39] C. Monroe, J. Kim. *Scaling the Ion Trap Quantum Processor*. Science **339**, 1164 (2013).

[40] K. Wright, J. M. Amini, D. L. Faircloth, C. Volin, S. C. Doret, H. Hayden, C.-S. Pai, L. D. W., D. Denison, T. Killian, S. R. E., A. W. Harter. *Reliable transport through a microfabricated X -junction surface-electrode ion trap*. New J. Phys. **15**, 033004 (2013).

[41] A. Mokhberi, R. Schmied, S. Willitsch. *Optimised surface-electrode ion-trap junctions for experiments with cold molecular ions*. New J. Phys. **19**, 043023 (2017).

[42] H. Buhrman, H. Röhrig. *Distributed Quantum Computing*, 1–20. Springer Berlin Heidelberg (2003).

[43] V. S. Denchev, G. Pandurangan. *Distributed quantum computing: A new frontier in distributed systems or science fiction?* SIGACT News **39**, 77–95 (2008).

[44] H. J. Kimble. *The quantum internet*. Nature **453**, 1023 (2008).

[45] A. Stute, B. Casabone, B. Brandstätter, K. Friebe, T. E. Northup, R. Blatt. *Quantum-state transfer from an ion to a photon*. Nat. Phot. **7**, 219–222 (2013).

[46] D. N. Matsukevich, A. Kuzmich. *Quantum State Transfer Between Matter and Light*. Science **306**, 663–666 (2004).

[47] B. Vermersch, P.-O. Guimond, H. Pichler, P. Zoller. *Quantum State Transfer via Noisy Photonic and Phononic Waveguides*. Phys. Rev. Lett. **118**, 133601 (2017).

[48] J. Hofmann, M. Krug, N. Ortegel, L. Gérard, M. Weber, W. Rosenfeld, H. Weinfurter. *Heralded Entanglement Between Widely Separated Atoms*. Science **337**, 72 (2012).

[49] Z.-S. Yuan, Y.-A. Chen, B. Zhao, S. Chen, J. Schmiedmayer, J.-W. Pan. *Experimental demonstration of a BDCZ quantum repeater node*. Nature **549**, 1098–1101 (2008).

[50] M. D. Barrett, J. Chiaverini, T. Schaetz, J. Britton, W. M. Itano, J. D. Jost, E. Knill, C. Langer, D. Leibfried, R. Ozeri, D. J. Wineland. *Deterministic quantum teleportation of atomic qubits*. Nature **429**, 737 (2004).

[51] M. Riebe, H. Häffner, C. F. Roos, W. Hänsel, J. Benhelm, G. Lancaster, T. Körber, C. Becher, F. Schmidt-Kaler, D. James, R. Blatt. *Deterministic quantum teleportation with atoms*. Nature **429**, 734–737 (2004).

[52] C. Nölleke, A. Neuzner, A. Reiserer, C. Hahn, G. Rempe, S. Ritter. *Efficient Teleportation Between Remote Single-Atom Quantum Memories*. Phys. Rev. Lett. **110**, 140403 (2013).

[53] S.-K. Liao, W.-Q. Cai, W.-Y. Liu, L. Zhang, Y. Li, J.-G. Ren, J. Yin, Q. Shen, Y. Cao, Z.-P. Li, F.-Z. Li, X.-W. Chen, L.-H. Sun, J.-J. Jia, J.-C. Wu, X.-J. Jiang, J.-F. Wang, Y.-M. Huang, Q. Wang, Y.-L. Zhou, L. Deng, T. Xi, L. Ma, T. Hu, Q. Zhang, Y.-A. Chen, N.-L. Liu, X.-B. Wang, Z.-C. Zhu, C.-Y. Lu, R. Shu, C.-Z. Peng, J.-Y. Wang, J.-W. Pan. *Satellite-to-ground quantum key distribution*. Nature **549**, 43–47 (2017).

[54] D. K. Oi, A. Ling, G. Vallone, P. Villoresi, S. Greenland, E. Kerr, M. Macdonald, H. Weinfurter, H. Kuiper, E. Charbon, R. Ursin. *CubeSat quantum communications mission*. EPJ Quantum Technology **4**, 6 (2017).

[55] H. Takenaka, A. Carrasco-Casado, M. Fujiwara, M. Kitamura, M. Sasaki, M. Toyoshima. *Satellite-to-ground quantum-limited communication using a 50-kg-class microsatellite*. Nat. Phot. **11**, 502–508 (2017).

[56] G. A. Kao, C. K.and Hockham. *Dielectric-fibre surface waveguides for optical frequencies*. Proceedings IEE **113**, 1151–1158 (1966).

[57] C. H. Bennett, G. Brassard. *Quantum cryptography: Public key distribution and coin tossing*. Proceedings of IEEE International Conference on Computers, Systems and Signal Processing **175**, 8 (1984).

[58] A. K. Ekert. *Quantum cryptography based on Bell's theorem*. Phys. Rev. Lett. **67**, 661–663 (1991).

[59] N. Jain, L. Lydersen, C. Wittmann, C. Wiechers, D. Elser, C. Marquardt, V. Makarov, G. Leuchs. *Inducing a detector efficiency mismatch to hack a commercial quantum key distribution system*. CLEO/Europe and EQEC 2011 Conference Digest (2011).

[60] P. H. Leung, K. A. Landsman, C. Figgatt, N. M. Linke, C. Monroe, K. R. Brown. *Robust two-qubit gates in a linear ion crystal using a frequency-modulated driving force*. arXiv:1708.08039 (2017).

[61] J. D. Wong-Campos, S. A. Moses, K. G. Johnson, C. Monroe. *Demonstration of Two-Atom Entanglement with Ultrafast Optical Pulses*. Phys. Rev. Lett. **119**, 230501 (2017).

[62] C. J. Ballance, T. P. Harty, N. M. Linke, M. A. Sepiol, D. M. Lucas. *High-Fidelity Quantum Logic Gates Using Trapped-Ion Hyperfine Qubits*. Phys. Rev. Lett. **117**, 060504 (2016).

[63] D. E. Browne, M. B. Plenio, S. F. Huelga. *Robust Creation of Entanglement between Ions in Spatially Separate Cavities*. Phys. Rev. Lett. **91**, 067901 (2003).

[64] S. Ritter, C. Nölleke, C. Hahn, A. Reiserer, A. Neuzner, M. Uphoff, M. Mücke, E. Figueroa, J. Bochmann, G. Rempe. *An elementary quantum network of single atoms in optical cavities*. Nature **484**, 195 (2012).

[65] A. Reiserer, N. Kalb, G. Rempe, S. Ritter. *An elementary quantum network of single atoms in optical cavities*. Nature **508**, 237–240 (2014).

[66] T. G. Tiecke, J. D. Thompson, N. P. de Leon, L. R. Liu, V. Vuletić, M. D. Lukin. *Nanophotonic quantum phase switch with a single atom*. Nature **508**, 241–244 (2014).

[67] P. Maunz, S. Olmschenk, D. Hayes, D. N. Matsukevich, L.-M. Duan, C. Monroe. *Heralded Quantum Gate between Remote Quantum Memories*. Phys. Rev. Lett. **102**, 250502 (2009).

[68] C. Kurz, J. Huwer, M. Schug, P. Müller, J. Eschner. *A high-rate source for single photons in a pure quantum state*. New J. Phys. **15**, 055005 (2013).

[69] Y. O. Dudin, A. G. Radnaev, R. Zhao, J. Z. Blumoff, T. A. B. Kennedy, A. Kuzmich. *Entanglement of Light-Shift Compensated Atomic Spin Waves with Telecom Light*. Phys. Rev. Lett. **105**, 260502 (2010).

[70] V. Krutyanskiy, M. Meraner, J. Schupp, B. P. Lanyon. *Polarisation-preserving photon frequency conversion from a trapped-ion-compatible wavelength to the telecom C-band*. Appl. Phys. B **123**, 228 (2017).

[71] T. Walker, K. Miyanishi, R. Ikuta, H. Takahashi, S. V. Kashanian, Y. Tsujimoto, K. Hayasaka, T. Yamamoto, N. Imoto, M. Keller. *Long-distance single photon transmission from a trapped ion via quantum frequency conversion*. arXiv:1711.09644 (2017).

[72] N. Maring, P. Farrera, K. Kutluer, M. Mazzera, G. Heinze, H. de Riedmatten. *Direct frequency comb spectroscopy in the extreme ultraviolet*. Nature **551**, 485–488 (2017).

[73] M. Bock. *In preparation*. Ph.D. thesis, Universität des Saarlandes (2019).

[74] A. Lenhard, J. Brito, M. Bock, C. Becher, J. Eschner. *Coherence and entanglement preservation of frequency-converted heralded single photons*. Opt. Express **25**, 11187–11199 (2017).

[75] C. Schuck. *Interfacing Single Ions and Single Photons for Quantum Networks*. Ph.D. thesis, ICFO, Barcelona (2009).

[76] F. Rohde. *Remote ion traps for quantum networking: Two-photon interference and correlations*. Ph.D. thesis, ICFO, Barcelona (2009).

[77] J. Huwer. *Experimental tools for quantum networking operations with single photons and single ions*. Ph.D. thesis, Universität des Saarlandes, Saarbrücken (2013).

[78] M. Schug. *Single photons from single ions: quantum interference and distant ion interaction*. Ph.D. thesis, Universität des Saarlandes (2015).

[79] C. Kurz. *Quantum networking with single ions and single photons interfaced in free space*. Ph.D. thesis, Universität des Saarlandes (2015).

[80] A. Lenhard. *Quantum Photonic Interfaces between Atomic and Telecommunication Wavelengths*. Ph.D. thesis, Universität des Saarlandes (2015).

[81] P. Müller. *Towards quantum networks with single ions: on the way and off the trail*. Ph.D. thesis, Universität des Saarlandes (2019).

[82] C. Kurz, P. Eich, M. Schug, P. Müller, J. Eschner. *Programmable atom-photon quantum interface*. Phys. Rev. A **93**, 062348 (2016).

[83] J. G. Bohnet, B. C. Sawyer, J. W. Britton, M. L. Wall, A. M. Rey, M. Foss-Feig, J. J. Bollinger. *Quantum spin dynamics and entanglement generation with hundreds of trapped ions*. Science **352**, 1297 (2016).

[84] H. Che, K. Deng, Z. T. Xu, W. H. Yuan, J. Zhang, Z. H. Lu. *Efficient Raman sideband cooling of trapped ions to their motional ground state*. Phys. Rev. A **96**, 013417 (2017).

[85] A. Ozawa, J. Davila-Rodriguez, J. R. Bounds, H. A. Schuessler, T. W. Hänsch, T. Udem. *Single ion fluorescence excited with a single mode of an UV frequency comb*. Nat. Commun. **8**, 44 (2017).

[86] C. Bruzewicz, R. McConnell, J. Sedlacek, J. Stuart, W. Loh, J. Sage, J. Chiaverini. *High-Fidelity, Single-Shot, Quantum-Logic-Assisted Readout in a Mixed-Species Ion Chain*. arXiv:1706.05102 (2017).

[87] H. Kaufmann, T. Ruster, C. T. Schmiegelow, M. A. Luda, V. Kaushal, J. Schulz, D. von Lindenfels, F. Schmidt-Kaler, U. G. Poschinger. *Scalable creation of long-lived multipartite entanglement*. arXiv:1707.03695 (2017).

[88] S. Begley, M. Vogt, G. K. Gulati, H. Takahashi, M. Keller. *Optimized Multi-Ion Cavity Coupling*. Phys. Rev. Lett. **116**, 223001 (2016).

[89] B. P. Lanyon, C. Maier, M. Holzäpfel, T. Baumgratz, C. Hempel, P. Jurcevic, I. Dhand, A. S. Buyskikh, A. J. Daley, M. Cramer, M. B. Plenio, R. Blatt, C. F. Roos. *Efficient tomography of a quantum many-body system*. Nat. Phys., advance online publication (2017).

[90] T. Manovitz, A. Rotem, R. Shaniv, I. Cohen, Y. Shapira, N. Akerman, A. Retzker, R. Ozeri. *Fast dynamical decoupling of the Molmer-Sorensen entangling gate*. Phys. Rev. Lett. **119**, 220505 (2017).

[91] F. Domínguez, M. J. Gutiérrez, I. n. Arrazola, J. Berrocal, J. M. Cornejo, J. J. Del Pozo, R. A. Rica, S. Schmidt, E. Solano, D. Rodríguez. *Motional studies of one and two laser-cooled trapped ions for electric-field sensing applications*. arXiv:1708.06786 (2017).

[92] D. J. Gorman, B. Hemmerling, E. Megidish, S. A. Moeller, P. Schindler, M. Sarovar, H. Haeffner. *Engineering vibrationally-assisted energy transfer in a trapped-ion quantum simulator*. arXiv:1709.04064 (2017).

[93] D. Castelvecchi. *Quantum computers ready to leap out of the lab in 2017*. Nature **541**, 9 (2017).

[94] R. Gerritsma, G. Kirchmair, F. Zähringer, J. Benhelm, R. Blatt, C. F. Roos. *Precision measurement of the branching fractions of the* $4p\,^2P_{3/2}$ *decay of Ca II*. Eur. Phys. J. D **50**, 13 (2008).

[95] M. Ramm, T. Pruttivarasin, M. Kokish, I. Talukdar, H. Häffner. *Precision Measurement Method for Branching Fractions of Excited $P_{1/2}$ States Applied to $^{40}Ca^{+}$*. Phys. Rev. Lett. **111**, 023004 (2013).

[96] V. P. Krainov, H. R. Reiss, B. M. Smirno. *Radiative Processes in Atomic Physics*. John Wiley & Sons (1997).

[97] R. E. Cohen. *Tables of the Clebsch-Gordan Coefficients*. U.S. Atomic Energy Commission (1958).

[98] D. Kielpinski, C. Monroe, D. J. Wineland. *Architecture for a large-scale ion-trap quantum computer*. Nature **417**, 709 (2002).

[99] J. I. Cirac, P. Zoller, H. J. Kimble, H. Mabuchi. *Quantum State Transfer and Entanglement Distribution among Distant Nodes in a Quantum Network*. Phys. Rev. Lett. **78**, 3221 (1997).

[100] L. Luo, D. Hayes, T. Manning, D. Matsukevich, P. Maunz, S. Olmschenk, J. Sterk, C. Monroe. *Protocols and techniques for a scalable atom-photon quantum network*. Fortschritte der Physik **57**, 1133 (2009).

[101] H. Häffner, F. Schmidt-Kaler, W. Hänsel, C. F. Roos, T. Körber, M. Chwalla, M. Riebe, J. Benhelm, U. D. Rapol, C. Becher, R. Blatt. *Robust entanglement*. Appl. Phys. B **81**, 151 (2005).

[102] F. Schmidt-Kaler, S. Gulde, M. Riebe, T. Deuschle, A. Kreuter, G. Lancaster, C. Becher, J. Eschner, H. Häffner, R. Blatt. *The coherence of qubits based on single Ca^{+} ions*. J. Phys. B: At. Mol. Opt. Phys. **36**, 623 (2003).

[103] T. Ruster, C. T. Schmieglow, H. Kaufmann, C. Warschburger, F. Schmidt-Kaler, U. G. Poschinger. *A long-lived Zeeman trapped-ion qubit*. Phys. Rev. Lett. **71**, 4287 (1993).

[104] J. Benhelm, G. Kirchmair, C. F. Roos, R. Blatt. *Experimental quantum-information processing with $^{43}Ca^{+}$ ions*. Phys. Rev. A **77**, 062306 (2008).

[105] S. Olmschenk, K. C. Younge, D. L. Moehring, D. N. Matsukevich, P. Maunz, C. Monroe. *Quantum Teleportation Between Distant Matter Qubits*. Phys. Rev. A **76**, 052314 (2007).

[106] T. P. Harty, M. A. Sepiol, A. D. T. C., B. C. K., J. E. Tarlton, D. M. Lucas. *High-Fidelity Trapped-Ion Quantum Logic Using Near-Field Microwaves*. Phys. Rev. Lett. **117**, 140501 (2016).

[107] M. Ghadimi, V. Blums, B. G. Norton, P. M. Fisher, S. C. Connell, A. J. M., C. Volin, H. Hayden, C.-S. Pai, D. Kielpinski, M. Lobino, E. W. Streed. *Scalable ion-photon quantum interface based on integrated diffractive mirrors*. npj Quantum Information **3**, 4 (2017).

[108] A. Stute, B. Casabone, B. Brandstätter, D. Habicher, H. G. Barros, P. O. Schmidt, T. E. Northup, R. Blatt. *Toward an ion-photon quantum interface in an optical cavity*. Appl. Phys. B **107**, 1145 (2012).

[109] W. Paul, H. Steinwedel. *Ein neues Massenspektrometer ohne Magnetfeld*. Zeitschrift Naturforschung Teil A **8**, 448 (1953).

[110] E. Fischer. *Three-dimensional stabilization of charged particles in a quadrupole field.* Z. Phys. **156**, 1 (1959).

[111] H. Häffner, C. Roos, R. Blatt. *Quantum computing with trapped ions*. Phys. Rep. **469**, 155 (2008).

[112] S. Debnath, N. M. Linke, C. Figgatt, K. A. Landsman, K. Wright, C. Monroe. *Demonstration of a small programmable quantum computer with atomic qubits*. Nature **536**, 63 (2012).

[113] T. Monz, D. Nigg, E. A. Martinez, M. F. Brandl, P. Schindler, R. Rines, S. X. Wang, I. L. Chuang, R. Blatt. *Realization of a scalable Shor algorithm*. Science **351**, 1068 (2016).

[114] R. L. Taylor, C. D. B. Bentley, J. S. Pedernales, L. Lamata, E. Solano, A. R. R. Carvalho, J. J. Hope. *A Study on Fast Gates for Large-Scale Quantum Simulation with Trapped Ions*. Sci Rep. **7**, 46197 (2017).

[115] J. T. Barreiro, M. Müller, P. Schindler, D. Nigg, T. Monz, M. Chwalla, M. Hennrich, C. F. Roos, P. Zoller, R. Blatt. *An open-system quantum simulator with trapped ions*. Nature **470**, 486 (2011).

[116] F. Gebert, Y. Wan, F. Wolf, C. N. Angstmann, J. C. Berengut, P. O. Schmidt. *Precision Isotope Shift Measurements in Calcium Ions Using Quantum Logic Detection Schemes*. Phys. Rev. Lett. **115**, 053003 (2015).

[117] T. Rosenband, D. B. Hume, P. O. Schmidt, C. W. Chou, A. Brusch, L. Lorini, W. H. Oskay, R. E. Drullinger, T. M. Fortier, J. E. Stalnaker, S. A. Diddams, W. C. Swann, N. R. Newbury, W. M. Itano, D. J. Wineland, J. C. Bergquist. *Frequency Ratio of Al^+ and Hg^+ Single-Ion Optical Clocks; Metrology at the 17th Decimal Place*. Science **319**, 1808 (2008).

[118] M. Chwalla. *Precision spectroscopy with $^{40}Ca^+$ ions in a Paul trap*. Ph.D. thesis, Leopold-Franzens-Universität, Innsbruck (2009).

[119] D. Leibfried. *Individual addressing and state readout of trapped ions utilizing rf micromotion*. Phys. Rev. A **60**, R3335 (1999).

[120] D. J. Berkeland, J. D. Miller, J. C. Bergquist, W. Itano, D. J. Wineland. *Minimization of ion micromotion in a Paul trap*. Journal of Applied Physics **83**, 5025 – 5033 (1998).

[121] S. Earnshaw. *On the nature of the molecular forces which regulate the constitution of the luminiferous ether*. Transactions of the Cambridge Philosophical Society **7** (1842).

[122] H. G. Dehmelt. *Radiofrequency spectroscopy of stored ions I: Storage*. Adv. At. Mol. Phys. **3**, 53 (1967).

[123] S. Quabis, R. Dorn, M. Eberler, O. Glöckl, G. Leuchs. *Focusing light to a tighter spot*. Opt. Commun. **179**, 1 (2000).

[124] S. Kucera. *In preparation*. Ph.D. thesis, Universität des Saarlandes (2018).

[125] F. Rohde, M. Almendros, C. Schuck, J. Huwer, M. Hennrich, J. Eschner. *A diode laser stabilization scheme for $^{40}Ca^{+}$ single-ion spectroscopy*. J. Phys. B: At. Mol. Opt. Phys. **43**, 11 (2010).

[126] C. Schuck, M. Almendros, F. Rohde, M. Hennrich, J. Eschner. *Two-color photoionization of calcium using SHG and LED light*. Applied Physics B **100**, 765–771 (2010).

[127] R. V. Pound. *Electronic frequency stabilization of microwave oscillators*. Rev. Sci. Instrum. **17**, 11 (1946).

[128] R. Drever, J. Hall, F. Kowalski, J. Hough, G. Ford, A. Munley, H. Ward. *Laser phase and frequency stabilization using an optical resonator*. Appl. Phys. B **31**, 2 (1983).

[129] E. D. Black. *An introduction to Pound-Drever-Hall laser frequency stabilization*. Am. J. Phys. **69**, 1 (2000).

[130] M. Almendros. *Towards Long-Distance Quantum Communication*. Ph.D. thesis, ICFO, Barcelona (2010).

[131] T. W. Hänsch, A. L. Shawlow. *Cooling of gases by laser radiation*. Opt. Commun. **13**, 68 (1975).

[132] N. F. Ramsey. *A Molecular Beam Resonance Method with Separated Oscillating Fields*. Phys. Rev. **78**, 695–699 (1950).

[133] M. Kreis. *Magnetfeldstabilisierung für Hochpräzise Einzelatom Spektroskopie*. Master's thesis, Universität des Saarlandes (2014).

[134] J. Eschner, G. Morigi, F. Schmidt-Kaler, R. Blatt. *Laser cooling of trapped ions*. J. Opt. Soc. Am. B **20**, 1003 (2003).

[135] S. Stenholm. *The semiclassical theory of laser cooling*. Rev. Mod. Phys. **58**, 699 (1986).

[136] F. Diedrich, J. C. Bergquist, W. M. Itano, D. J. Wineland. *Laser Cooling to the Zero-Point Energy of Motion*. Phys. Rev. Lett. **62**, 403 (1989).

[137] G. Morigi, J. Eschner, C. H. Keitel. *Ground State Laser Cooling Using Electromagnetically Induced Transparency*. Phys. Rev. Lett. **85**, 4458 (2000).

[138] M. L. Citron, H. R. Gray, C. W. Gabel, C. R. Stroud Jr. *Quantum Computations with Cold Trapped Ions*. Phys. Rev. A **16**, 1507 (1977).

[139] A. Lenhard, M. Bock, S. Kucera, J. Brito, P. Eich, P. Müller, C. Becher, J. Eschner. *Telecom-heralded single photon absorption by a single atom*. arXiv:1504.08303 (2015).

[140] U. G. Poschinger, G. Huber, F. Ziesel, M. Deiss, M. Hettrich, S. A. Schulz, G. Poulsen, M. Drewsen, R. J. Hendricks, K. Singer, F. Schmidt-Kaler. *Coherent Manipulation of a $^{40}Ca^{+}$ Spin Qubit in a Micro Ion Trap*. Journal of Physics B **42**, 154013 (2009).

[141] P. Müller, T. Tentrup, M. Bienert, G. Morigi, J. Eschner. *Spectral properties of single photons from quantum emitters*. Phys. Rev. A **96**, 023861 (2017).

[142] P. Müller, J. Eschner. *Single calcium-40 ion as quantum memory for photon polarization: a case study*. Appl. Phys. B **114**, 303 (2014).

[143] M. Schug, C. Kurz, P. Eich, J. Huwer, P. Müller, J. Eschner. *Quantum interference in the absorption and emission of single photons by a single ion*. Phys. Rev. A **90**, 023829 (2014).

[144] I. Hertel, C.-P. Schulz. *Atome, Moleküle und optische Physik 1*. Springer (2008).

[145] T. Kim, P. Maunz, J. Kim. *Efficient collection of single photons emitted from a trapped ion into a single-mode fiber for scalable quantum-information processing*. Phys. Rev. A **84**, 063423 (2011).

[146] W. Demtröder. *Experimentalphysik 3*. Springer (2005).

[147] R. Maiwald, D. Leibfried, J. Britton, J. C. Bergquist, G. Leuchs, D. J. Wineland. *Stylus ion trap for enhanced access and sensing*. Nat. Phys. **5**, 551 (2009).

[148] M. Fischer, M. Bader, R. Maiwald, A. Golla, M. Sondermann, G. Leuchs. *Efficient saturation of an ion in free space*. Appl. Phys. B **117**, 797–801 (2014).

[149] A. D. Boozer, A. Boca, R. Miller, T. E. Northup, H. J. Kimble. *Reversible State Transfer between Light and a Single Trapped Atom*. Phys. Rev. Lett. **98**, 193601 (2007).

[150] T. Wilk, S. C. Webster, A. Kuhn, G. Rempe. *Single-Atom Single-Photon Quantum Interface*. Science **317**, 488 (2007).

[151] M. K. Tey, Z. Chen, S. A. Aljunid, B. Chng, F. Huber, G. Maslennikov, C. Kurtsiefer. *Strong interaction between light and a single trapped atom without the need for a cavity*. Nat. Phys. **4**, 924 (2008).

[152] G. Vittorini, D. Hucul, I. V. Inlek, C. Crocker, C. Monroe. *Entanglement of distinguishable quantum memories*. Phys. Rev. A **90**, 040302 (2014).

[153] C. Kurz, M. Schug, P. Eich, J. Huwer, P. Müller, J. Eschner. *Experimental protocol for high-fidelity heralded photon-to-atom quantum state transfer*. Nat. Commun. **5**, 5527 (2014).

[154] J. Brito, S. Kucera, P. Eich, P. Müller, J. Eschner. *Doubly-heralded single-photon absorption by a single atom*. Appl. Phys. B 122:36 (2016).

[155] J. Brito. *Quantum interfaces based on single photons from parametric down-conversion*. Ph.D. thesis, Universität des Saarlandes (2016).

[156] D. James, P. G. Kwiat, W. J. Munro, A. G. White. *Measurement of qubits*. Phys. Rev. A **64**, 052312 (2001).

[157] I. L. Chuang, M. A. Nielsen. *Prescription for experimental determination of the dynamics of a quantum black box*. J. Mod. Opt. **44**, 2455 (1997).

[158] D. Hucul, I. V. Inlek, G. Vittorini, C. Crocker, S. Debnath, S. M. Clark, C. Monroe. *Modular entanglement of atomic qubits using photons and phonons*. Nat. Phys. **11**, 37–42 (2015).

[159] M. Bock, P. Eich, S. Kucera, M. Kreis, A. Lenhard, C. Becher, J. Eschner. *High-fidelity entanglement between a trapped ion and a telecom photon via quantum frequency conversion*. Nat. Commun. **9**, 1998 (2018).

[160] H.-J. Briegel, W. Dür, J. I. Cirac, P. Zoller. *Quantum Repeaters: The Role of Imperfect Local Operations in Quantum Communication*. Phys. Rev. Lett. **81**, 5932 (1998).

[161] M. Zwerger, B. P. Lanyon, T. E. Northup, C. A. Muschik, W. Dür, N. Sangouard. *Quantum repeaters based on trapped ions with decoherence-free subspace encoding*. Quantum Sci. Technol. **2**, 044001 (2017).

[162] D. Luong, L. Jiang, J. Kim, N. LÃ¼tkenhaus. *Overcoming lossy channel bounds using a single quantum repeater node*. Applied Physics B **122** (2015).

[163] L. M. Duan, M. D. Lukin, J. I. Cirac, P. Zoller. *Long-distance quantum communication with atomic ensembles and linear optics*. Nature **404**, 413–418 (2001).

[164] N. Sangouard, C. Simon, H. de Riedmatten, N. Gisin. *Quantum repeaters based on atomic ensembles and linear optics*. Rev. Mod. Phys. **83**, 33 (2011).

[165] H. Rütz, K.-H. Luo, H. Suche, C. Silberhorn. *Quantum Frequency Conversion between Infrared and Ultraviolet*. Phys. Rev. Applied **7**, 024021 (2017).

[166] A. Stute, B. Casabone, P. Schindler, T. Monz, P. O. Schmidt, B. Brandstätter, T. E. Northup, R. Blatt. *Tunable ion-photon entanglement in an optical cavity*. Nature **485**, 482 (2012).

[167] F. Bussiéres, C. Clausen, A. Tiranov, B. Korzh, B. V. Verma, S. W. Nam, F. Marsili, A. Ferrier, P. Goldner, H. Herrmann, C. Silberhorn, W. Sohler, M. Afzelius, N. Gisin. *Quantum teleportation from a telecom-wavelength photon to a solid-state quantum memory*. Nat. Phot. **8**, 775–778 (2014).

[168] B. E. A. Saleh, M. C. Teich. *Fundamentals of Photonics*. John Wiley and Sons, Hoboken, New Jersey, 2nd edition (2007).

[169] M. Bock, A. Lenhard, C. Chunnilall, C. Becher. *Highly efficient heralded single-photon source for telecom wavelengths based on a PPLN waveguide*. Opt. Express **24**, 23992–24001 (2016).

[170] Z. Y. Ou. *Efficient conversion between photons and between photon and atom by stimulated emission*. Phys. Rev. A **78**, 023819 (2008).

[171] R. Ikuta, Y. Kusaka, T. Kitano, H. Kato, T. Yamamoto, M. Koashi, N. Imoto. *Wide-band quantum interface for visible-to-telecommunication wavelength conversion*. Nat. Commun. **2**, 1544 (2011).

[172] M. T. Rakher, L. Ma, O. Slattery, X. Tang, K. Srinivasan. *Quantum transduction of telecommunications-band single photons from a quantum dot by frequency upconversion*. Nat. Phot. **4**, 786–791 (2010).

[173] K. Mølmer, A. Sørensen. *Multiparticle Entanglement of Hot Trapped Ions*. Phys. Rev. Lett. **82**, 1835–1838 (1999).

[174] A. Sørensen, K. Mølmer. *Quantum Computation with Ions in Thermal Motion*. Phys. Rev. Lett. **82**, 1971 (1999).

[175] P. Schindler, D. Nigg, T. Monz, J. T. Barreiro, E. Martinez, S. X. Wang, S. Quint, M. F. Brandl, V. Nebendahl, C. F. Roos, M. Chwalla, M. Hennrich, R. Blatt. *A quantum information processor with trapped ions*. New J. Phys. **15**, 123012 (2013).

[176] G. Kirchmair, J. Benhelm, R. Zähringer, F.and Gerritsma, C. F. Roos, R. Blatt. *Deterministic entanglement of ions in thermal states of motion*. New J. Phys. **11**, 023002 (2009).

[177] C. A. Sackett, D. Kielpinski, B. E. King, C. Langer, V. Meyer, C. J. Myatt, M. Rowe, Q. A. Turchette, W. M. Itano, D. J. Wineland, C. Monroe. *Experimental entanglement of four particles*. Nature **404**, 256–259 (2000).

[178] N. Navon, N. Akerman, S. Kotler, Y. Glickman, R. Ozeri. *Quantum process tomography of a Mølmer-Sørensen interaction*. Phys. Rev. A **90**, 010103 (2014).

[179] P. C. Haljan, K.-A. Brickman, L. Deslauriers, P. J. Lee, C. Monroe. *Spin-Dependent Forces on Trapped Ions for Phase-Stable Quantum Gates and Entangled States of Spin and Motion*. Phys. Rev. Lett. **94**, 153602 (2005).

[180] C. F. Roos. *Ion trap quantum gates with amplitude-modulated laser beams*. New J. Phys. **10**, 013002 (2008).

[181] V. Sudhir, R. Schilling, S. A. Fedorov, H. Schütz, D. J. Wilson, T. J. Kippenberg. *Quantum Correlations of Light from a Room-Temperature Mechanical Oscillator*. Phys. Rev. X **7**, 031055 (2017).

[182] N. M. Linke, C. J. Ballance, D. M. Lucas. *Injection locking of two frequency-doubled lasers with 3.2 GHz offset for driving Raman transitions with low photon scattering in Ca43+*. Opt. Lett. **38**, 5087–5089 (2013).

[183] N. Akerman, N. Navon, S. Kotler, Y. Glickman, R. Ozeri. *Universal gate-set for trapped-ion qubits using a narrow linewidth diode laser*. New Journal of Physics **17**, 113060 (2015).

[184] L.-S. Ma, P. Jungner, J. Ye, J. L. Hall. *Delivering the same optical frequency at two places: accurate cancellation of phase noise introduced by an optical fiber or other time-varying path*. Opt. Lett. **19**, 1777–1779 (1994).

[185] W. Bian, Y. Huang, H. Guan, P. Liu, L. Ma, K. Gao. *1 Hz linewidth Ti:sapphire laser as local oscillator for $^{40}Ca^{+}$ optical clocks*. Rev. Sci. Instr. **87**, 063121 (2016).

[186] O. Elshehy. *Permanent-magnet-based Zeeman field generation in an ion trap*. Master's thesis, Universität des Saarlandes (2018).

[187] D. N. Matsukevich, P. Maunz, D. L. Moehring, S. Olmschenk, C. Monroe. *Bell Inequality Violation with Two Remote Atomic Qubits*. Phys. Rev. Lett. **100**, 150404 (2008).

[188] B. Hensen, H. Bernien, A. E. Dréau, A. Reiserer, N. Kalb, M. S. Blok, J. Ruitenberg, R. F. L. Vermeulen, R. N. Schouten, C. Abellán, W. Amaya, V. Pruneri, M. W. Mitchell, M. Markham, D. J. Twitchen, D. Elkouss, S. Wehner, T. H. Taminiau, R. Hanson. *Loophole-free Bell inequality violation using electron spins separated by 1.3 kilometres*. Nature **526**, 682–686 (2015).

[189] C. H. Bennett, G. Brassard, C. Crépeau, R. Jozsa, A. Peres, W. K. Wootters. *Teleporting an unknown quantum state via dual classical and Einstein-Podolsky-Rosen channels*. Phys. Rev. Lett. **70**, 1895 (1993).

[190] M. Barrett, J. Chiaverini, T. Schaetz, J. Britton, W. M. Itano, J. D. Jost, E. Knill, C. Langer, D. Leibfried, R. Ozeri, D. J. Wineland. *Deterministic quantum teleportation of atomic qubits*. Nature **429**, 737–739 (2004).

[191] S. Lloyd, M. S. Shahriar, J. H. Shapiro, P. R. Hemmer. *Long Distance, Unconditional Teleportation of Atomic States via Complete Bell State Measurements*. Phys. Rev. Lett. **87**, 167903 (2001).

[192] K. Kim, M.-S. Chang, R. Islam, S. Korenblit, L.-M. Duan, C. Monroe. *Entanglement and Tunable Spin-Spin Couplings between Trapped Ions Using Multiple Transverse Modes*. Phys. Rev. Lett. **103**, 120502 (2009).

[193] T. Choi, S. Debnath, T. A. Manning, C. Figgatt, Z.-X. Gong, L.-M. Duan, C. Monroe. *Optimal Quantum Control of Multimode Couplings between Trapped Ion Qubits for Scalable Entanglement*. Phys. Rev. Lett. **112**, 190502 (2014).

Acknowledgments

A thesis like the present is never the work of a single person, but the result of the collective endeavor of a whole team of motivated people that all contributed to the success of our experiment. Without all these guys, it would not be possible to operate such a complex laboratory and produce the results that were part of this work.

First of all, I want to thank my boss Jürgen for giving me the opportunity to work in this fascinating field. He always took his time to discuss the various problems appearing in the lab, and his expertise and experience clearly were a huge help during my time in the group. Aside from the professional aspects, I have barely ever met a supervisor who is so supportive in every facet, e.g. when he saved my derrière when I completely forgot a submission deadline.

Next in line I would like to mention the "veterans" Michael and Christoph who were currently running the lab when I joined the ion team. They made my start really easy and helped me to quickly learn how to operate everything. I don't know if the transition would have been so inviscid for me without these two and working with them was a great experience and a lot of fun. Also, sharing the ride to the university with Christoph has led to a lot of fruitful discussions, not only about physics, and we very soon agreed on how traffic should be organized.

Philipp is probably one of the most pleasant persons to work with and always lend an ear to theoretical problems of any kind. But maybe more importantly, Philipp exhibits an astonishing knowledge about dialectology and phonetics and awakened my interest in these fields. Although the productivity might suffer when working in the same office as him, you definitely learn a lot (maybe not specifically what you need to learn at the moment, but one should not be too strict about that) and a high degree of entertainment is guaranteed.

A large amount of my time I worked with Matthias[1] Kreis. Despite the obvious lack in his knowledge about football, it was (mostly) always a pleasure to work with him, knowing I'm not alone in my struggle with the stubborn experiment. After a while, we developed a highly efficient way of non-verbal communication (where a simple panic-stricken scream was sufficient to give a detailed diagnosis of the symptoms and suspected sources of a malfunction). I wish him all the best with the heritage he is left with.

A constant source of confusion was our collaboration with Matthias Bock from the group of Christoph Becher because it was never fully clear which Matthias I was talking about when simply addressing to "Matthias". Nonetheless, I was always looking forward to the measurements conducted with Matthias, whose refreshing but sometimes almost annoying optimism[2] probably was the ideal compensation for my thoroughly nourished pessimism.

[1] A way too wide-spread name.

[2] I guess he would be the only person who was able to remain optimistic despite being passenger of an aircraft approaching the ground at 1000 km/h with no wings left and the entire rear part of the plane went missing – and proof everybody wrong as somehow everything works out just fine in the end.

Of course I should also mention the source guys Jan and Stephan, with whom I spent quite some days (and nights) in the lab. Jan's calm and target-oriented way of working was highly appreciated by the whole team. On the downside, he was not only calm, but rather silent as the night. More than once he almost gave me a heart attack when suddenly appearing straight behind me in a dark laboratory without making a single sound when entering the room and approaching. I also want to thank Stephan for his numerous help in the lab and the many productive discussions.

My special thanks, of course, goes to our secretary Ingeborg Michel, the backbone of the group, who kept everything running and had the amazing ability to solve even the most complicated administrative problems. Even more important, she provided access to the one coffee machine that produced drinkable coffee, which saved my day uncounted times.

At last, the most important people that made all this possible shall not go unnoticed. I want to thank my parents for their constant support during the whole time. Also I want to thank my girlfriend Sofie who has always been there for me, sustaining my moods and building me up again during bad times and making sure that I never fully lost my enthusiasm. Without them, I would not be where I am today.

And, although it's rather unusual to thank your pet, I definitely have to thank my dog Annie[3]. No one else could cheer me up so easily just by doing something stupid and looking adorable.

[3]Who is clearly not dangerous, though she mentioned on some occasions that she plans to bite Matthias someday, but that's a different story.